

**ENGINEERING THE KINETICS OF SELF ASSEMBLY OF FACETED NANOPARTICLES**

A Dissertation

Presented to the Faculty of the Graduate School

of Cornell University

In Partial Fulfillment of the Requirements for the Degree of

Doctor of Philosophy

by

Abhishek Kumar Sharma

August 2021



© 2021 Abhishek Kumar Sharma



# ENGINEERING THE KINETICS OF SELF ASSEMBLY OF FACETED NANOPARTICLES

Abhishek Kumar Sharma, Ph. D.

Cornell University 2021

Recent developments in synthesis techniques have enabled production of colloidal nanoparticles of with intricate shapes with unprecedented precision. When put under high osmotic pressure, faceted particles can self-assemble into intricate structures that find applications in photonic and photoelectric systems. Thus, it is of engineering interest to understand design principles governing nanoparticle self-assembly. Not only can such understanding be of practical importance, but it can also reveal general principles about the way how naturally occurring systems self-assemble into complex nanostructures.

In this thesis, I will discuss findings from our Monte Carlo simulations that reveal the influence of the shape of a nanoparticle on its self-assembly. We find that the way such nanoparticles are faceted has important consequences upon how quickly they self-assemble, providing us 'design rules' for the nanoparticle shape. For example, octahedral particles tend to align their facets in the disordered phase, but not in the ordered phase. Entropic preference to facet alignment in the disordered phase results in a large kinetic barrier for its disorder-order transition.

In our studies of a variety of shapes (such as cubes, truncated cubes and gyrobifastigia), we have found transitions that show departures from classical nucleation that motivate

development of new theories and simulation methods. Based on the geometric properties of the particle shape, such particles may also form mesophases – phases that have an intermediate degree of order between disordered and ordered phases. I will also illustrate examples of transitions to and from mesophases – and how their existence might hinder or accelerate disorder to order transitions. We studied how either a rotator mesophase or a liquid crystal forms a crystal; the former case illustrates a transition primarily involving particle reorientations with minimal translations, while the latter is an example of a transition with large particle translations with minimal reorientations. In both cases, we the structure and formation kinetics of the incipient crystalline nucleus could depart from the classical theory considerably. These results contribute to improving our current understanding of self-assembly of nanoparticles, with predictions that are suitable for experimental validation in near future.

## **BIOGRAPHICAL SKETCH**

Abhishek Kumar Sharma was born in New Delhi, India. At five years old, he wanted to be a pilot. He went to Navyug School Laxmi Bai Nagar for twelve years and pursued Science stream with Biology in high school. He was always the quiet kid with a noticeable stutter. In sixth grade he once mistook the date of a science exam (instead preparing for a Hindi language exam) yet ended up scoring the highest marks. This incident led to a paradoxically dismissive moniker of 'scientist'. At fifteen he was asked by a teacher what did he want to be later in life, and he said 'researcher'. He found excellent biology and physics teachers, and later went on to join Indian Institute of Technology (IIT) Delhi as an undergraduate.

At IIT Delhi he majored in Chemical Engineering with a minor area in Biochemical Engineering and Biotechnology. In Summer 2014 he joined Bioseparations and Bioprocessing Lab at the Department of Chemical Engineering as an undergraduate researcher. He worked primarily on downstream processing of biopharmaceuticals and co-invented a novel reactor design. At the same time, he was involved in an effort related to biofuels that made it to front page of a national daily. He was a G.S. Bhasin Scholar for one semester and IIT Delhi Merit Semester scholar for two semesters. During his time at IIT Delhi, he took interest in philosophy and journalism. The former brought him clarity as a thinker. He believes his training in philosophy made him a better scientist. In particular, he values the ability to find comfort in not being able to answer a question straightaway, instead focusing on understanding the question better.

In Fall 2016 he started as a PhD student at Cornell's Robert Frederick Smith School of Chemical and Biomolecular Engineering. Although coming in with very broad interests (and not a particularly good grade in undergraduate thermodynamics), his encounter with statistical thermodynamics in the core class made him interested in joining Escobedo Group where he primarily conducted simulations of polyhedral nanoparticles. He was also a part of a collaborative effort relating to polymeric photoresists with Ober Group at Material Science and Engineering at Cornell and Semiconductor Research Corporation. He pursued a minor area in Applied Mathematics. During his time at Cornell, he participated in a variety of student initiatives, including Graduate Alumni Reunion, Chemical Engineering Graduate Students' Association, CBE Women, Diversity and Inclusion Program, Science Blender Podcast, and CBE Symposium. He was awarded the Austin Hooey Graduate Research Excellence Award in Fall 2020. He also contributed to a publication for Daniel Research Team relating to antibiotic screening assays. During his time at CBE, his work resulted in three journal cover arts (Soft Matter, JPC B, ACS Infectious Diseases).

He plans to work with Juan de Pablo group at University of Chicago's Pritzker School of Molecular Engineering in July 2021 where he plans to conduct simulations pertaining to metamaterials. At this point, he believes being involved in the process of scientific discovery brings him great joy. Hence in the long term, he intends to pursue research as a career He intends to remain involved in scientific outreach and communication.

*To those who have found joy in the pursuit of knowledge*



## **ACKNOWLEDGMENTS**

First and foremost, I would like to acknowledge competent advising of Prof. Fernando Escobedo. I could not have imagined a better research arrangement where I could engage in a sincere scholarly discourse. In pre-pandemic times, I could simply do a ‘walk-in’ at his office and discuss latest findings. Timely facilitation of this sort really accelerated my research. I think knowing that my ideas would be judged fairly and given genuine attention made me more comfortable to share them. Running my ideas through Fernando always improved them given his experience in the research area. I have looked forward each meeting. Unfortunately, I have come to understand that my experience is quite idiosyncratic, and not shared by many graduate students who time and again find themselves at odds with their advisors’ expectations and goals. I firmly believe that graduate school is not supposed to be a harsh experience for anyone. I think Fernando is doing many things right when it comes to advising. I have never been afraid of sharing difficulties I face, never been afraid of being judged for showing weakness be it scholarly, physiological, or mental. I have never had to power through a sick day or mood swings. This created a stimulating environment where I can openly work on my mistakes instead of hiding them. Fernando also cares to learn who I am as a person other than a researcher. In contrast I have heard advisors dissuading graduate students from pursuing service. I think without his advising I would not be where I am today. The world would be a better place with more advisors like him.

I was surrounded by many other mentors at Olin Hall.

Susan Daniel was the Director of Graduate Studies when I was recruited by CBE. She truly created a welcoming environment for me, and I have very much enjoyed talking to her about science, academia, and culture. She prompted me to be more involved at CBE, which I regard as among the most influential prompts of my graduate school journey. Our highly enriching regular lunch meetings formed the framework for Let's Get Lunch by DIP.

I met Abe Stroock on the second day of classes with an intent to join his group. Even though I was deemed not a great fit for his group, he has been a key mentor in all aspects. I have enjoyed conversations with him about research and politics, which have led to important ideas that I live by – one of them being 'managing your advisor'. He was always generous with his time, and I would like to thank him for agreeing to be a part of my Special Committee.

I was not a great student of fluid mechanics as an undergraduate, thinking it was not for me. But Don Koch's graduate class and earnest answers to my questions made me learn it well so much so I would have liked to join his group if I had not already decided on working with Fernando. Over the years he has been my go-to person of theory advice, which has been important for many projects. I am thankful for him for agreeing to be a part of my Special Committee representing the Applied Mathematics minor.

I would also like to thank all the faculty members who have helped me learn many fascinating things over the years – Lynden Archer, Paul Steen, James Sethna, Kathryn

Mann and Paulette Clancy to name a few. I am also thankful for all the professors, TAs, and undergrads I had a chance to interact with as a teaching assistant for unit operations lab. In particular I would like to thank Prof. Brad Anton and Prof. Frank Lomax for giving me the opportunity to re-learn so many ChemE concepts – running the distillation column in continuous mode was one of the highlights of my time at Olin. I would also like to thank fellow TA Franklin Gong for picking up the slack when I fell sick.

I am also thankful to all the current members of the Escobedo group.

Prajwal Bangalore Prakash was instrumental in my onboarding with the polyhedra project. He had started the project one semester before I joined the lab, and his familiarity and collaboration on the two course projects really jump-started my research. I enjoy discussing research ideas with him. Outside work, I am grateful to him for driving me to the ER once. Mayank Misra taught me how to use BASH scripting – which enabled me to automate my workflow. I used this skill to create simulations that analyze themselves and trigger other simulations – vastly accelerating my research. Mayank's enterprising attitude is also exemplified in him developing the VMD code for visualizing polyhedral nanoparticles. It was a true collaboration between us, which led to beautiful renderings seen Chapter 2 onwards in this thesis. These renderings also allow for interactive viewing of the 3D configurations. Several of my findings are born out of incessant staring at them. Ankita Mukhtyar was a competent colleague who I got to share an office with for the first two years. I enjoyed discussing research problems and also exploring the restaurants of Ithaca with her. She, along with Chris Nowak and

Yangyang Sun, were helpful in explaining LAMMPS minutia during my occasional forays into MD. Unmukt Gupta and Yangyang Sun are also acknowledged for sharing their scripts. Isabela Quintela Matos was at times the first person to hear my new findings, and I certainly appreciated hearing about her results likewise. Andreia Fenley has been a sincere person who is always willing to have a conversation just about anything. Allen Yang was fun to collaborate with on the SRC project. Luis Nieves-Rosado, although joined the group a bit late into my time, had already been a great friend and I am looking forward to what he does next.

I am also thankful to NSF and SRC for funding my work over the years, and maintenance of computing resources by ICSE and CAC.

I owe thanks to many folks who worked on the project before me, many of whom I have never met but I am deeply indebted to. Bettina John wrote the original MC code that is the basis for all my simulations. Umang Agrawal's pioneering work with mesophases really revealed so much science, and nearly all the research questions I have pursued are related to his work in one way or another. I also had a chance to meet Mihir Khadilkar, and his help in generating initial configurations for certain phases is appreciated. Vikram Thapar passed me the baton on many projects relating to kinetics, and I was fortunate to be able to collaborate with him on my first paper.

Many people at CBE enabled a healthy workplace with their presence. Until March 2019 my office was in a small cabin inside the Daniel lab office. I appreciated the entire lab

fostering me not very differently from their own members. I made great friends in many of them. Many in Daniel lab are quiet folks, and I sincerely apologize if I was ever a disruption to them given, I can enjoy conversations too much to lose being mindful of others. I am particularly thankful to Tiffany Tang for being a great friend and colleague, especially helping me understand the nuances about coronaviruses during the pandemic. Lakshmi Nathan was a nice friend who facilitated my involvement with the Graduate Alumni Reunion and had thoughtful conversations about academia and careers. I am also grateful to Zeinab Mohamed for giving me the opportunity to contribute to one of her papers. Yehou Gnopo (Putnam Lab, but also worked from the Daniel lab office for a while) also became a very important friend with whom I connected not only as a researcher but also as an international student.

Several organizations within CBE enriched me as an individual – such as ChEGSA, DIP, CBE Women, and Science Blender. It was through these organizations I gained useful skills and cherished friendships that helped me stay sane through the highs and lows. Andrew Ruttinger, Alicia Aquino, Chris Klassen, Cindy Qiu, Hector Fuster, Natalia Lopez, Trevor Donadt, and so many more folks truly left a positive influence on me as a person. I enjoyed sharing numerous meals and snacks with many of these people. Karthik Nayani for one even helped me in making progress with the theory in Chapter 4 of this thesis.

The staff at CBE always made sure everything proceeded smoothly. Johanna, Breana, Stephanie, Carol, Joanna, Bianca, Annie, Brittney, Karen, and Cindy were all very helpful throughout my time at Olin.

I would also like to acknowledge all the help and care provided by Cornell Health and Cayuga Medical Associates over all the years.

Anyone who knows me knows I consume a lot of educational content on YouTube; hence this acknowledgement would be incomplete without thanking all the creators who nurtured my curiosity about the world for nearly a decade. Grant Sanderson (3Blue1Brown) was my entry point into appreciating math. His clear explanations and visualizations were a big influence for me. For instance – without his *Essence of Algebra* series I would not be able to come up with the facet alignment measure (Chapter 1). His *Essence of Calculus* series inspired me to visualize Taylor's series better and enabled certain derivations in Chapter 2. Brady Haran (Numberphile) introduced me to so much great math that inspired me to pursue a minor area in Applied Math. Michael Stevens (Vsauce), ViHart, MinutePhysics, and Derek Muller (Veritasium) were crucial in my undergraduate days as they introduced me to fascinating science and math. Later into my graduate school I would add Destin Sandlin, Steve Mould, Tom Scott, and PBS Infinite Series to that list. In addition, I would like to acknowledge John and Hank Green (vlogbrothers) as major influences on my thinking and appreciation of nuance when it comes to understanding of the world.

Although I picked podcast listening in the latter half of my PhD, I do think they contributed value to my thinking: Radiolab, Science Vs., Invisibilia, Hidden Brain to name a few.

I would also like to acknowledge all the musical artists whose art and words inspired me and kept me going throughout my time at Cornell: Beach House, The Beatles, Bon Iver, Broadcast, Brockhampton, Coldplay, Frank Ocean, Kanye West, Kendrick Lamar, Kid Cudi, Lorde, Mac Miller, Paramore, Portishead, Radiohead, Run The Jewels, Tame Impala and so many more.

Last but not the least, I would like to acknowledge my friends and family. Sahil Loomba and Harsh Parikh – who themselves were on their graduate school journey – remained in constant touch and always were great influences be it about work or about life. The trips I took with them were truly the highlights of my time. Harshit Agarwal has had a very similar journey to me, having started at the same undergraduate lab. We always had things we could relate with each other about. Friends from undergrad – Anshul, Rama, Saravan, Vidisha, Yoshita and more – were very much supportive over the years. I would also like to thank my family for their understanding that doing the graduate school and science in general brought me happiness.



## TABLE OF CONTENTS

Biographical Sketch .....	v
Acknowledgments .....	ix
Table of Contents .....	xvii
Preface .....	xxi
<b>Chapter 1: Solid-Phase Nucleation Free-Energy Barriers In Truncated Cubes: Interplay Of Localized Orientational Order And Facet Alignment.....</b>	<b>1</b>
1 Introduction.....	2
2 Methods .....	7
3 Results and Discussion .....	14
4 Conclusion .....	30
5 Acknowledgements.....	33
6 Supplementary Information .....	34
<b>Chapter 2: Nucleus-Size Pinning for Determination of Nucleation Free-Energy Barriers and Nucleus Geometry .....</b>	<b>37</b>
1 Introduction.....	38
2 Methods .....	43
3 Results and Discussion .....	57
4 Conclusions.....	69
5 Acknowledgements.....	72
6 Appendix: Interfacial Contribution to Free Energy Derivative.....	72

<b>Chapter 3: Disorder Foreshadows Order in Colloidal Cubes .....</b>	<b>81</b>
1 Introduction.....	82
2 Methods .....	86
3 Results and Discussion .....	92
4 Conclusions.....	113
5 Acknowledgements.....	115
6 Supplementary Information .....	116
<b>Chapter 4: Low Interfacial Free Energy Describes Bulk Ordering Transition in Colloidal Cubes.....</b>	<b>123</b>
1 Introduction.....	124
2 Methods .....	127
3 Results and Discussion .....	138
4 Conclusion and Outlook.....	160
5 Acknowledgements.....	162
6 Supporting Information .....	163
<b>Chapter 5: Kinetics of Rotator-Crystal Transition of Truncated Cubes .....</b>	<b>175</b>
1 Introduction.....	176
2 Methods .....	177
3 Results and Discussions .....	180
4 Conclusions and Future Work .....	202
5 Acknowledgements.....	204
<b>Chapter 6: Influence of Particle Aspect Ratio on Kinetics .....</b>	<b>205</b>
1 Introduction.....	205

2	Methods .....	208
3	Results and Discussion .....	212
4	Conclusions and Future Work .....	229
5	Acknowledgements.....	232
	<b>References .....</b>	<b>233</b>



## PREFACE

The context of this work lies in need to understand bottom-up assembly crucial for formation of the next generation of materials. We are approaching the limits of top-down design, such as falling short of Moore's law predictions for transistor density on a microchip. In contrast, many naturally occurring systems generate complexity through bottom-up design where simple small-scale units compose complex and functional macroscopic structures such as virus envelopes. One of the simplest synthetic paradigms for such bottom-up materials design are colloidal nanoparticles. Recent developments in customizable nanoparticles with complex shapes and surface chemistries has unlocked an uncharted design space. How must one relate the design of an individual nanoparticle with the emergent properties of a collection of the same? Can we control such behaviors? How quickly might such emergent properties arise (i.e. kinetics)? Simulations can provide useful answers to such questions by the virtue of microscopic knowledge. In this thesis, I have focused on asking the question of whether a particle's shape can influence its ordering kinetics.

The simulations do have their limitations. For one, it is hard to tell whether a given simulation is sampling the phase space ergodically. Most of the Monte Carlo simulations in this thesis comprise *local* single particle moves that may not be effective in glassy systems, or systems where cooperative motions might be important. Further, polydispersity in experimental systems would result in deviations from the modelling predictions that use strict monodispersity. Finally, the effect of enthalpic forces is non-

trivial, and how their interplay with entropic effects might turn out is hard to predict a priori. Nevertheless, by studying the entropic effects in isolation, these studies do form a good basis for adding in more complexities. These studies are also great model systems of creating theories and methods that would be applicable beyond this specific context of nanoparticles.

This is a papers-only thesis; hence it is primarily organized in relatively independent chapters that have been or will be published as peer-reviewed publications. Nevertheless, interesting connections between the chapters are drawn here wherever they exist. The chapters are mostly placed in chronological order.

Chapter 1 pertains to the nucleation of the solid phases for the particle shapes belonging to the truncated cubes family. This work picks up where a previous graduate student left off, adding novel techniques to understand trends in the ease of solid phase formation as they relate to facet alignment. The article was published and chosen as the cover article for 21<sup>st</sup> March 2018 issue of *Soft Matter* journal.

Chapter 2 develops and validates a method that improves upon a popular technique to study hard to nucleate particle shapes. As we test the method, we find unexpected behavior in the phase transition of gyrobifastigia, largely enabled by the new method. The article was published in *The Journal of Chemical Physics* in May 2018.

Chapter 3 focusses on the kinetics of disorder to order phase transition in cubic nanoparticles. This system was infamously hard to study under the established

understanding of kinetics of solid phase formation. We develop new techniques and borrow from methods developed in Chapter 1 to elucidate the novel kinetics. This study was published in *The Journal of Physical Chemistry B* in September 2018.

Chapter 4 follows up the preceding chapter by a two-pronged approach of simulation and theory to substantiate its conjectures regarding unusual kinetics of cubic nanoparticles. Physical properties of the system are measured by newly adapted methods. These measurements are used to inform predictions of a theoretical model to explain the anomalous observations. This study has been accepted for publication in *The Journal of Physical Chemistry B* in April 2021 and is featured on the Supplementary Cover of special issue *Carol K. Hall Festschrift*.

Chapter 5 is recent study that complements Chapter 1 in that it studies two candidate shapes from the same family, except that we focus on rotator to crystal transition. Novel methods are developed to study this transition, contrasting the two cases where the rotator phase and crystal phase may be placed on similar and dissimilar lattice. This study is a work-in-progress and will be published in near future in a more advanced form.

Chapter 6 builds upon the novel findings in Chapter 2 in two ways. First, we provide independent prediction of the aspect ratio of nuclei for gyrobifastigia through cleaving walls method from Chapter 4. Second, we study how this interesting behavior is influenced by the aspect ratio, finding interesting alterations in phase behavior and

kinetics. Like Chapter 5, this study will also be published in near future with more developed analysis.

The text in Chapters 1-4 is sourced from the final manuscripts for the respective publications. However, there would be several minor editorial changes in the published articles made by journal editorial staff. Such changes are not incorporated here.

Chapters 5 and 6 are still works in progress and are written in a communication style focused on succinctly reporting key results known at the present time. Hence, their introductions and conclusions would be expanded before they are published. Nevertheless, most of the relevant background for Chapter 5 and 6 is available in Chapters 1 and 2, respectively. If all goes well, you should be able to find published versions of these papers in next few years.

Each chapter is formatted as a standalone unit with its own numbering of equations, figures, and tables. Chapter 1 includes contribution from Vikram Thapar. Rest of the chapters are authored by me and Fernando.

# **CHAPTER 1: SOLID-PHASE NUCLEATION FREE-ENERGY BARRIERS IN TRUNCATED CUBES: INTERPLAY OF LOCALIZED ORIENTATIONAL ORDER AND FACET ALIGNMENT**

Abhishek K. Sharma\*, Vikram Thapar\*, and Fernando A. Escobedo

Smith School of Chemical and Biomolecular Engineering, Cornell University, Ithaca, NY  
14853

\*) These authors contributed equally to this work.

## **Abstract**

The nucleation of ordered phases from the bulk isotropic phase of octahedron-like particles has been studied via Monte Carlo simulations and umbrella sampling. Specifically, selected shapes that form ordered (plastic) phases with various symmetries (cubic and tetragonal) are chosen to unveil trends in the free-energy barrier heights  $\Delta G^*$  associated with disorder to order transitions. The shapes studied in this work have truncation parameter ( $s$ ) values of 0.58, 0.75, 0.8 and 1. The case of octahedron ( $s = 1.0$ ) is studied to provide a counterexample where the isotropic phase nucleates directly into a (Minkowski) crystal phase rather than a rotator phase. The simulated  $\Delta G^*$ 's for these systems are compared with those previously reported for hard spheres and truncated cubes with  $s = 0.5$  (cuboctahedron, CO) and  $s = 2/3$  (truncated octahedron, TO). The comparison shows that, for comparable degrees of supersaturation, all rotator

phases nucleate with smaller  $\Delta G^*$ 's than that of the hard sphere crystal, whereas the octahedra crystal nucleates with larger  $\Delta G^*$ 's. Our analysis of near-critical translationally ordered nuclei of octahedra shows a strong bias towards an orientational alignment which is incompatible with the tendency to form facet-to-facet contacts in the disordered phase, thus creating an additional entropic penalty for crystallization. For rotator phases of octahedra-like particles, we observe that the strength of localized orientational order correlates inversely with  $\Delta G^*$ . We also observe that for  $s > 0.66$  shapes and similar to octahedra, configurations with high facet alignment do not favor high orientational order, and thus  $\Delta G^*$  increase with truncation.

## **1 Introduction**

Recent studies<sup>1-10</sup> have made remarkable progress in understanding the self-assembly of anisotropic particles. By virtue of their geometry, anisotropic particles have configurations that depend upon the orientation of individual particles, i.e., possess orientational degrees of freedom. Examples of experimentally synthesizable anisotropic particles include branched particles<sup>11,12</sup>, faceted polyhedra<sup>13-19</sup>, patterned particles<sup>20-23</sup>, and rod and ellipsoid shaped particles<sup>24-27</sup>. Among them, polyhedral particles are being extensively studied as they have well defined geometries that are amenable to both synthesis and modeling. Over the years, simulations have proven very useful in exploring the rich phase behavior of polyhedral particles of a diversity of

shapes and for various extents of size polydispersity<sup>4-10</sup>. Using Monte Carlo simulations in the isothermal-isobaric ensemble, it has been shown<sup>4</sup> that some of the hard polyhedral particles that tessellate space undergo transitions from a disordered phase to a fully translationally and orientationally ordered phase via partially ordered phases termed as “mesophases”, which are defined as phases whose structural order is intermediate between disordered liquids and ordered crystals. Unlike spherical particles that form ordered phases having only translational order, the orientational degrees of freedom in anisotropic particles allow the formation of phases that may or may not be orientationally ordered. Thus, examples of mesophases of anisotropic particles include liquid crystals that are orientationally ordered but translationally disordered, and rotator plastic crystals that are translationally ordered but orientationally disordered.

One of the families of shapes that are readily synthesizable using a polyol process<sup>17,18</sup> is that of truncated cubes, defined by a truncation parameter,  $s$ , which varies from cubes ( $s = 0$ ) via cuboctahedra ( $s = 0.5$ ) to octahedra ( $s = 1$ ). In this family, shapes with  $s < 0.5$  are denoted as ‘cube-like’ while shapes with  $s > 0.5$  are denoted as ‘octahedron-like’. Recent computational studies<sup>7,10</sup> have rigorously examined the phase behavior of the truncated-cube family via simulation and revealed a rich diversity in crystal structures and plastic crystal mesophases. Specifically for octahedron-like particles, i.e., shapes with  $s > 0.5$ , the lattice symmetry of the plastic mesophases transforms from body-

centered tetragonal (BCT) to body-centered cubic (BCC) as the truncation is increased. This provides a simple illustration of how changes in faceting influences the stability of different lattice structures. Along with mapping the phase behavior, it would be interesting to explore how such changes in particle truncation and rotator lattice symmetry influence the kinetics of disorder-to-order phase transitions. Thapar and Escobedo<sup>8</sup> performed a computational study to explore the homogenous nucleation kinetics from disordered phase to rotator phase of two shapes of the truncated cube family, namely, truncated octahedra (TOs) ( $s = 2/3$ ) and cuboctahedra (COs) ( $s = 0.5$ ). It was shown that both these shapes nucleate the ordered phase faster than hard spheres (HSs) at comparable degrees of supersaturation. It is unclear, however, whether other particle shapes in the same truncated cube family follow a similar trend or whether particular truncations are optimal in facilitating the nucleation of the solid phase.

The homogeneous nucleation of an ordered phase from an isotropic phase at small or moderate degrees of supersaturation is a *rare event* – it requires a critically large domain within the isotropic phase to seed a stable ordered nucleus – an event far from the immediate phase space visited by the disordered phase. The unlikeliness of such a rare event makes its quantitative characterization using conventional brute force simulations computationally inefficient. Hence, many sophisticated sampling methods<sup>28,29,38,39,30–37</sup> have been developed to overcome this challenge. Among them, the umbrella sampling (US) method has been widely used to estimate the free energy

barrier height associated with nucleation<sup>40,41</sup>. The technique involves biasing the system such that the rare events are sampled more frequently with a reasonable computational effort. The US calculations are performed along a reaction coordinate that tracks the progress of the nucleation process. Most crystal nucleation studies of hard particles have successfully employed the size of the largest solid like cluster<sup>8,40-42</sup> in the system as reaction coordinate. Once the biased probabilities of forming clusters of different sizes are known, they are unbiased to obtain the free energy as a function of the reaction coordinate.

In this work, we apply US to estimate the nucleation barriers for the transition from a disordered phase to an ordered phase for hard octahedron-like ( $s > 0.5$ ) particles. Specifically, the shapes studied are octahedrons (Oct) and truncated cubes with truncation parameter  $s = 0.58$  (TC58),  $s = 0.75$  (TC75) and  $s = 0.8$  (TC80). TC58, which is the truncated cube with minimum asphericity,<sup>10</sup> forms a plastic body-centered tetragonal (PBCT) lattice, while the other two form a body-centered cubic (PBCC) rotator phase. All three shapes undergo a first-order phase transition from an isotropic phase to a plastic crystal phase, whereas for Oct the system undergoes a phase transition from isotropic phase to Minkowski crystal phase<sup>7</sup>. To allow meaningful comparisons, we use US to simulate these transitions at comparable degrees of super saturation, which quantifies the thermodynamic driving force to nucleation. For our

comparisons, we will also peruse rotator-phase nucleation data for shapes with  $s = 0.5$  (CO) and  $s = 2/3$  (TO) from a previous simulation study<sup>8</sup>.

Our selection of methods and analysis is appropriate for the systems of interest as the phase transitions involved were well described by classical nucleation pathways. It should be noted, however, that non-classical pathways could also occur, especially for anisotropic particles<sup>4</sup> where independent orientational and translational order may occur at different stages in the ordering process and lead to metastable or stable intermediary mesophases. This is important, for example, in isotropic-to-smectic phase transitions in hard rods<sup>43</sup> where two-step processes may occur with orientational order preceding translational order or vice versa. The occurrence of more complex ordering pathways are also well known in two-step freezing processes<sup>44–48</sup> where the particles form an intermediate dense liquid phase before translational order ensues. The existence of multistage mechanisms can be revealed by a detailed analysis of transition state configurations and transitional pathways.<sup>8,40</sup>

The rest of this paper is organized as follows. In Section 2 we describe the model used to simulate the hard polyhedral particles, our choice of order parameter, and other relevant simulation details. In Section 3 we show and discuss our simulation results for nucleation free-energy barriers. Finally, in Section 4 we provide some concluding remarks.

## 2 Methods

### 2.1 Model

In this work, we use a hard particle pair potential given by:

$$bU_{ij} = \begin{cases} 0 & \text{if flag} = 1 \\ \infty & \text{if flag} = 0 \end{cases} \quad (1)$$

where  $U_{ij}$  is the interaction potential between particle  $i$  and  $j$ , and  $\beta = 1/k_B T$  ( $k_B$  is Boltzmann constant and  $T$  is the temperature). The value of variable flag is set to 1 if particle  $i$  and  $j$  do not overlap with each other, otherwise flag = 0. The overlapping of a particle  $i$  with particle  $j$  is checked through the separating axis theorem<sup>49</sup> (which states that two convex shapes do not overlap, if there exists an axis on which their projections do not intersect).

### 2.2 Order Parameters

For all the transitions studied in this work, the order parameter used is the number of particles in the largest translationally ordered cluster,  $n_{tr}$ . The crux in estimating this order parameter is to determine whether a given particle is “solid-like”; i.e., translationally ordered. This is determined using the local bond order parameter analysis proposed by Steinhardt *et al.*<sup>50</sup> and used in several nucleation studies (e.g., for

hard spheres<sup>40-42</sup>, and for TOs and COs<sup>8</sup>). For every particle  $i$ , the local bond order parameter,  $q_{l,m}(i)$  is defined by:

$$q_{l,m}(i) = \frac{1}{N_b(i)} \sum_{j=1}^l Y_{l,m}(\theta_{i,j}, \phi_{i,j}) \quad (2)$$

where  $N_b(i)$  is the number of neighbors of particle  $i$  and  $Y_{l,m}(\vartheta, \phi)$  are the spherical harmonics,  $\vartheta_{ij}$  and  $\phi_{ij}$  are polar and azimuthal angles between particle  $i$  and its neighbor  $j$  respectively,  $l$  is the symmetry index and the value of  $m$  ranges from  $-l$  to  $l$ . In this work we use  $l = 6$ . The neighbors of particle  $i$  are those particles which are within the cutoff distance  $r_c$  of particle  $i$ ; here we chose  $r_c \approx 1.2$  times the distance to the first peak of the radial distribution function. The translational-order correlation between particle  $i$  and its neighbor  $j$ ,  $d_6(i, j)$  is given by:

$$d_6(i, j) = \frac{\sum_{m=-6}^6 q_{6,m}(i) q_{6,m}^*(j)}{\sum_{m=-6}^6 \left| q_{6,m}(i) \right|^{1/2} \left| q_{6,m}(j) \right|^{1/2}} \quad (3)$$

where the asterisk denotes the complex conjugate. Two particles  $i$  and  $j$  are defined as translationally connected if  $d_6(i, j) > d_c$ , which is the translational order correlation cutoff. In this case, we use a value of  $d_c = 0.7$  as used in our earlier studies<sup>8</sup>. A particle with at least  $\zeta_c = 7$  translational connections is classified as translationally ordered or solid-like. A solid-like cluster is identified by using a criterion that if two solid like

particles are within the cutoff distance,  $r_c$  then they belong to the same cluster. This definition of order parameter involves three tunable parameters:  $r_c$ ,  $d_c$ , and  $\zeta_c$ . In an earlier study,<sup>41</sup> it was demonstrated that umbrella sampling free-energy barrier calculations that used this definition of order parameter are robust and relatively insensitive to variations of these tunable parameters. Consistent with such studies,<sup>8,41</sup> our preliminary tests also showed that while variations in such parameters do alter the shape of the free energy landscape being sampled (e.g., the location of the critical nucleus size), the free energy difference between the transition state at the barrier top and the initial state remained largely unaffected.

As a complementary metric of order, for selected cases we also evaluated the global orientational order parameter,  $P_4$ , of the particles belonging to  $n_{tr}$ :

$$\begin{aligned}
 P_4 &= \max_n \frac{3}{14N} \sum_i P_4(\mathbf{u}_i \cdot \mathbf{n}) \\
 &= \max_n \frac{3}{14N} \sum_i (35 \cos^4 \tau_i(\mathbf{n}) - 30 \cos^2 \tau_i(\mathbf{n}) + 3)
 \end{aligned} \tag{4}$$

where,  $\mathbf{u}_i$  is the unit vector along a relevant particle axis and  $\mathbf{n}$  is a director unit vector which maximizes  $P_4$  (see details in John *et al.*<sup>51</sup>). The summation is performed over all three axes for all  $n_{tr}$  particles in the nucleus. In this formulation of  $P_4$ ,  $P_4 = 1$  corresponds to perfect orientational order.

In order to study local orientational order, we use the  $I_4$  orientational order parameter<sup>52</sup> that captures the relative orientation of a particle to an arbitrary reference coordinate frame. It uses spherical harmonics similar to  $q_6$  but for angles associated with individual particle axes orientations instead of the bond orientation between two neighboring particles. In its normalized form it is evaluated for a given particle  $j$  as:

$$I_{4,m}(j) = \frac{\sum_{i=1}^3 Y_{4,m}(\theta_i, \phi_i)}{\sqrt{\sum_{m=-4}^4 |\sum_{i=1}^3 Y_{4,m}(\theta_i, \phi_i)|^2}} \quad (5)$$

where  $Y_{4,m}(\theta_i, \phi_i)$  are spherical harmonics with symmetry index 4, and  $\theta_i$  and  $\phi_i$  are polar and azimuthal angles of the particle axis  $i$  to the reference coordinate frame.

Analogous to  $d_6$ , the dot product in  $I_4$  between two particles  $i$  and  $j$  is defined as:

$$d_4(i, j) = \sum_{m=-4}^4 I_{4,m}(i) \cdot I_{4,m}^*(j) \quad (6)$$

where the asterisk (\*) implies complex conjugate. The two particles are assumed to be aligned if  $d_4(i, j) > 0.7$ . We use  $I_4$  in conjunction with  $q_6$  such that two neighboring particles are bonded if  $d_4(i, j) > 0.7$  and  $d_6(i, j) > 0.7$  simultaneously. Similar to  $q_6$ , a particle with at least 7 translational connections is termed as solid-like, and if two solid like particles are within the cutoff distance,  $r_c$  then they belong to the same cluster.

### 2.3 Facet Alignment Measure

It has been speculated in previous studies<sup>19,53</sup> that neighboring faceted particles might tend to align their facets in order to minimize their excluded volume and maximize packing entropy. However, since calculation of the volume excluded by particles is a non-trivial, computationally intensive task, here we introduce a simpler surrogate metric that quantifies the extent of facet-to-facet matching, whose values are expected to correlate with the smallness of excluded volume. Indeed, we exploit the fact that a signature of local efficient packing of particles is that the nearest facets tend to align parallel to each other, in a way that if viewed normal to one of the facets would lead to a near complete overlap. Accordingly, we define a *facet alignment measure*  $\Delta(i, j)$  for any two neighboring particles  $i$  and  $j$ . In essence, it is the overlap area of the nearest facets (defined by the minimum centroid to centroid distance) when one is projected onto the other (**Figure 1**). Since this operation can be performed in two different ways (i.e., projecting the facet from  $i$  onto the plane of the facet from  $j$ , and vice versa), the maximum of the two areas is taken to be the final value of  $\Delta(i, j)$ , thus making the operation commutative. The larger the value of  $\Delta$ , the higher is the facet alignment.  $\Delta(i, j)$  is scaled with respect to the maximum possible value for a given system (i.e., the area of the largest facet). In our calculations, neighboring particles were defined based on a Voronoi construction<sup>54</sup>. Since for any particle shape with facets of disparate sizes, the larger surface-area facets are expected to have stronger tendency toward facet-to-

facet alignment, for  $s \geq 2/3$  only the hexagonal faces are considered for nearest facet calculations.

It is important to note that  $\Delta(i, j)$  is in principle independent of local orientational order in that they need not be correlated, i.e., there may be configurations with high facet-alignment but low orientational order and vice versa.

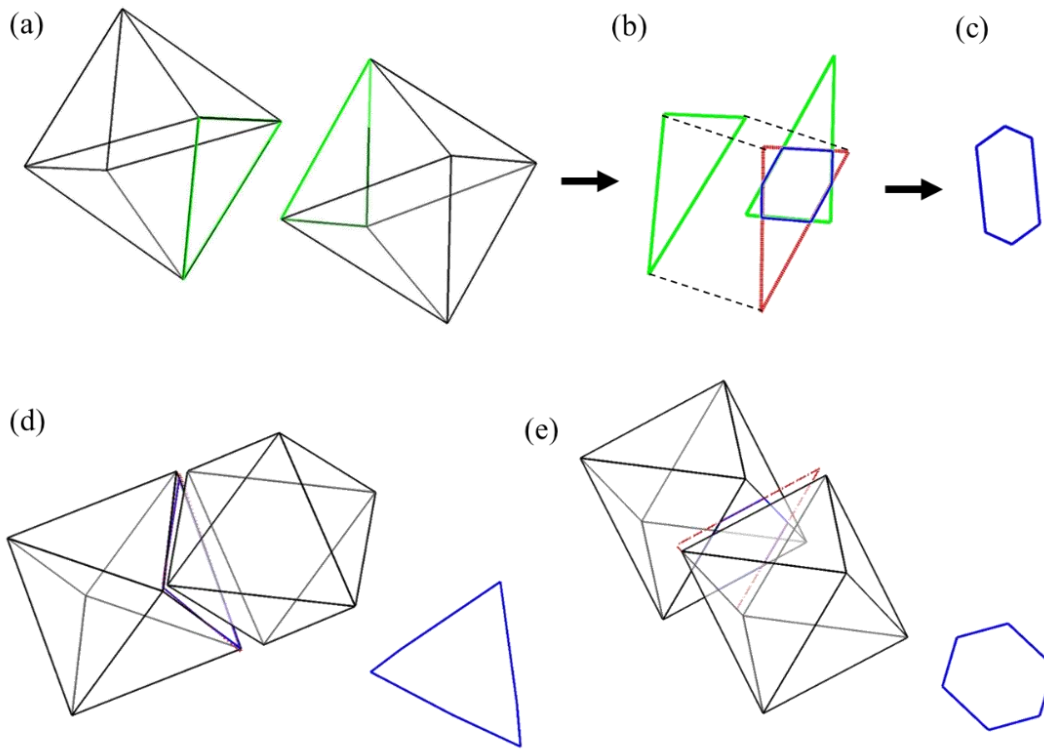


**Figure 1:** Definition of facet alignment measure  $\Delta$ , demonstrated for octahedra. (a) Nearest facets (green) are identified such that the centroid-to-centroid distance is the minimum. (b) One of the facets is projected (red) upon the plane of the other. The intersection of the projection with the other facet is obtained (blue). (c) The in-plane area of the intersection is calculated and normalized relative to the area of the triangular facet (the largest facet in the system). The calculation is repeated in the reverse order of facets and the higher value is taken. Sample configurations are shown for near-complete facet-to-facet alignment ( $\Delta \sim 1$ ) in (d) and

a staggered orientationally-ordered configuration present in the Minkowski crystal ( $\Delta \sim 2/3$ ) in (e).

## 2.4 Simulation Details

Metropolis Monte Carlo (MC) simulations were conducted in a cubic cell with periodic boundary conditions and  $N = 2744$  particles. The simulations are performed at constant reduced pressure,  $P^* = \beta P v$  ( $v$  is the volume of a shape) and constant temperature,  $T$ . Each MC cycle consisted of  $N$  translational moves,  $N$  rotational moves, and one volume move. All trial moves are accepted according to the Metropolis criterion<sup>55</sup>, which requires ruling out overlaps between any two particles (via the separating axes theorem<sup>49</sup>). Each value of pressure,  $P^*$  corresponds to a given value of degree of supersaturation ( $DSS$ ), which is estimated via:

$$DSS = \beta |\Delta\mu| \quad (7)$$

where  $\Delta\mu$  is difference in the chemical potential between the metastable liquid and the stable solid.  $|\Delta\mu|$  represents the thermodynamic driving force for nucleating the new phase. The details for estimating  $DSS$  are provided in earlier publications<sup>8</sup>.

Since we focus on  $DSS$  conditions where brute force MC simulations are impractical to estimate the free energy barrier height to nucleation,  $\Delta G^*$ , we employed umbrella sampling (US)<sup>30,31</sup> simulations to do so. US is performed by partitioning the phase space along the order parameter  $n_{tr}$  into a set of windows with overlapping boundaries. For

each window, MC simulations are performed with rigid reflexive walls at the boundaries and keeping the track of number of times system visits a given value of  $n_{tr}$ . While inside a given window,  $n_{tr}$  is allowed to change unbiased. To reduce computational cost, instead of evaluating the order parameters for every cycle<sup>40</sup>, we measure  $n_{tr}$  every 2 MC cycles. If the proposed move entails the change  $n_{tr}^{(o)} \rightarrow n_{tr}^{(n)}$  and  $n_{tr}^{(n)}$  falls outside the window, the entire 2 MC cycle trajectory is rejected, and the system is reset to the earlier configuration within the window which adds a visit to  $n_{tr}^{(o)}$ . The histogram of visits  $H(n_{tr})$  thus collected is unbiased and it was directly used to estimate free energies for each window via  $\beta G(n_{tr}) \sim \beta \ln H(n_{tr})$  and the full free-energy profile is then obtained by matching the free-energy values obtained at the boundaries between consecutive windows; free energy values are shifted so that it is zero for  $n_{tr} = 0$  as reference.

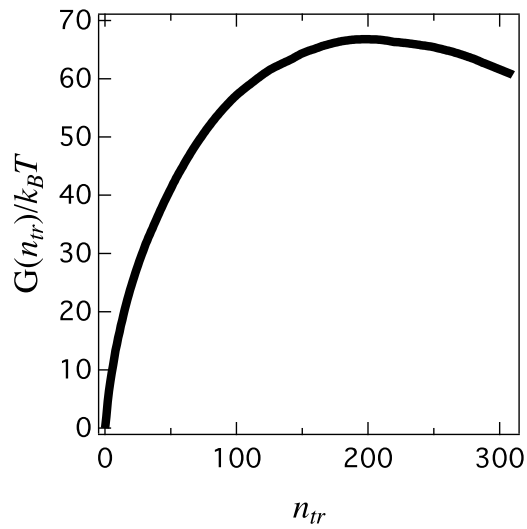
### 3 Results and Discussion

#### 3.1 Crystal nucleation of Octahedrons (Octs)

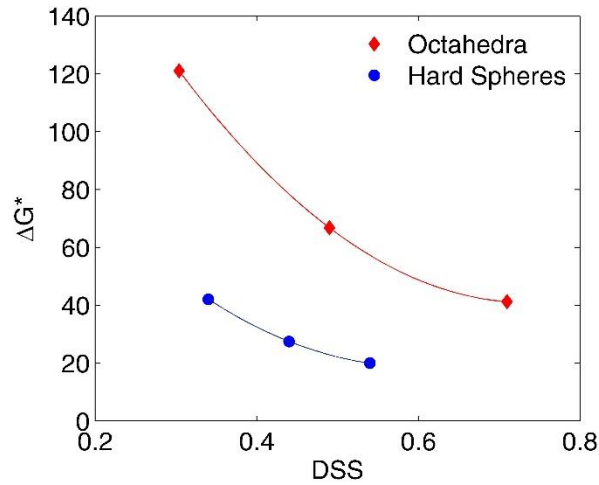
To study the isotropic to crystal nucleation in Oct, US calculations were performed at various degrees of supersaturation using the largest  $q_6$ -based translationally ordered cluster as the reaction coordinate. The free energy barriers are tabulated in Table 1. Figure 2 shows the free energy  $G(n_{tr})/k_B T$  versus  $n_{tr}$  for  $DSS=0.49$ , showing that free-energy barrier height,  $\Delta G^*$ , is approximately  $66.8 k_B T$ .

**Table 1:** Nucleation barriers for octahedra using umbrella sampling.

Reduced Pressure $(P^* = \beta p \sigma^3)$	Degree of Supersaturation $(\beta \Delta \mu)$	Order Parameter	Barrier Height $(\beta \Delta G^*)$	Critical Nucleus Size
10.64	0.30	$q_6$	121.0	416
11.33	0.49	$q_6$	66.8	196
12.0	0.71	$q_6$	41.2	103
11.33	0.49	$q_6 \cap I_4$	68.2	172



**Figure 2:** Free-energy profile,  $G(n_{tr})$  versus  $n_{tr}$  obtained using US simulations for Octs at  $P^* \approx 11.33$  ( $DSS = 0.49$ ).



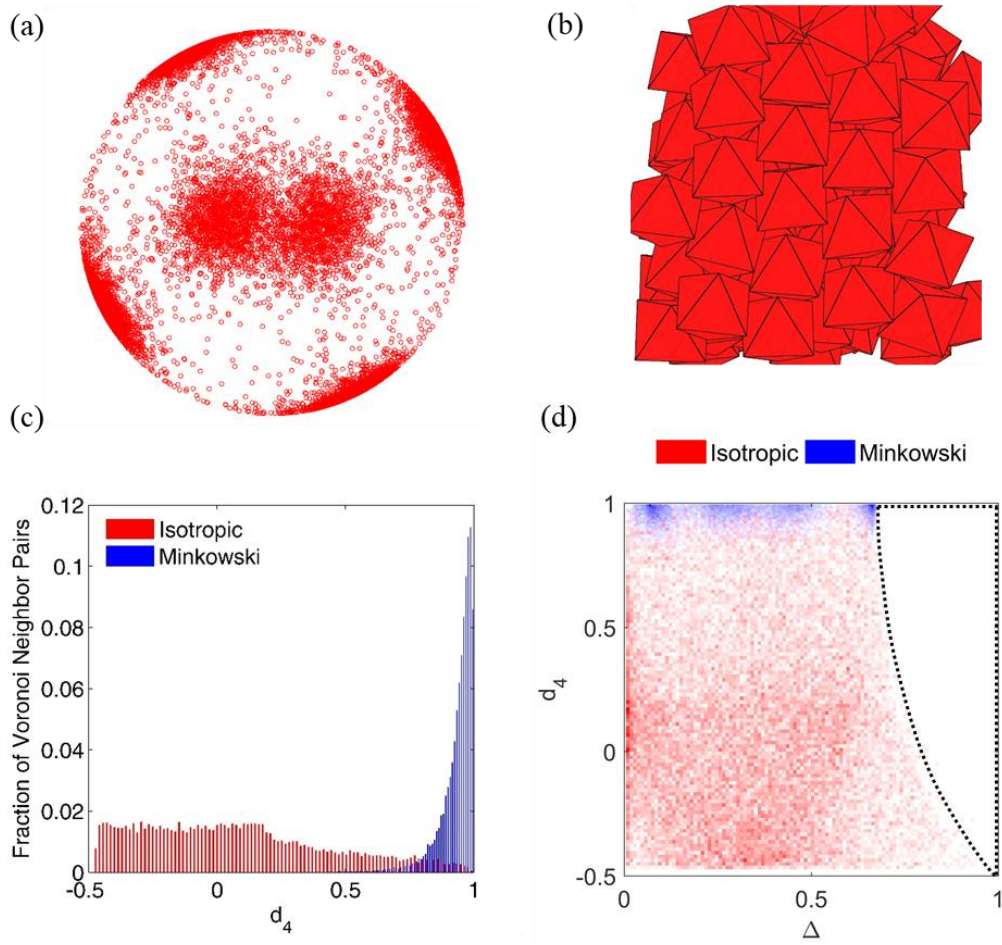
**Figure 3:** Free-energy barrier-height  $\Delta G^*/k_B T$  for octahedra and hard spheres<sup>43</sup> at different values of  $DSS$ . Spline interpolations are shown as solid lines.

Figure 3 shows a comparison of nucleation barriers of isotropic to Minkowski crystal transitions in octahedrons with those for the isotropic to FCC crystal transition of HSs<sup>41</sup>. The comparison shows that the nucleation barriers for octahedrons are much larger than HSs for comparable  $DSS$  values. In order to understand why octahedra may have more difficulty ordering than HSs, we look for some clues in the microstructure of the near-critical nucleus. For this we collected and analyzed configurations from the US window near the top of the barrier (i.e., for  $180 < n_{tr} < 200$  in Fig. 2). The orientation distribution function of the particles in these near-critical nuclei was obtained by plotting the components of all particle axes on the surface of a unit sphere. As shown in Fig. 4(a), the particle orientation distribution clearly shows well-defined clusters at six different locations, indicative of preferential orientational alignment. This is further

confirmed by the high value of global orientational order parameter  $P_4 \approx 0.46$  for the particles in the nucleus. Although the order parameter  $n_{tr}$  is solely derived from translational correlations in a system, these results show that the particles in the nucleus tend to also pack with orientational alignment. To further validate the claim that orientational order is a characteristic feature of this transition, we performed the US simulation using a conjunction of  $q_6$  and  $I_4$  used to define the ordered cluster to capture both orientational and translational order present (see Methods section). The resulting nucleation barrier for  $P^*=11.33$  was still found to be higher than that of hard spheres and close to what was determined using  $q_6$  alone (see Table 1). Thus, in contrast to the hard sphere case, orientational alignment is an essential feature of the crystalline nuclei in octahedra. Similar to the Minkowski crystal being nucleated, this orientational alignment has incomplete face-to-face alignment as seen in one of the snapshots of the portion of a  $n_{tr} = 189$  nucleus shown in Fig.4(b): The triangular faces are primarily staggered with respect to each other.

We now examine how local orientational order correlates to the face-to-face matching in the Minkowski crystal. For local orientational order we calculate  $d_4$  from Eq. (6) between neighboring particles. Parameter  $I_4$  (see Eq. 5) describes the preferential orientational alignment into six clusters of octahedral symmetry in Fig. 4(a). As shown in Fig. 4(c),  $d_4$  captures the orientational alignment present in the Minkowski crystal in contrast with the disordered phase. Figure 4(d) shows the variation of  $d_4$  with respect

to facet alignment measure  $\Delta$ . It is evident that for  $\Delta > 2/3$ , increasing alignment correlates with a decrease in orientational alignment. Thus, the presence of configurations with neighboring particles aligning their facets in the isotropic phase hinder the orientational alignment needed to grow the Minkowski crystal. In order to nucleate into and grow the Minkowski crystal, the spontaneous orientational fluctuations in the isotropic phase must stir configurations away from complete face-to-face alignment. This additional restriction in the nucleation pathway reduces the probability of particles to assemble into the crystalline structure, hence increasing free-energy barrier height for crystal nucleation in octahedra relative to hard spheres.



**Figure 4:** Nucleation of Minkowski crystal for octahedra at  $P^* = 11.33$ . (a) Particle orientation distribution function of near-critical nuclei with  $180 < n_{tr} < 200$ . The distribution is obtained over 20 different configurations. (b) Snapshot of a portion of the nucleus from one of these configurations with  $n_{tr} = 194$ . (c) Histogram of  $d_4$  values for Voronoi neighbor pairs in a Minkowski crystal and the disordered phase. Both systems had 2744 particles. (d) 2D Histogram plot of  $d_4$  values for Voronoi neighbor pairs vs. corresponding facet alignment measure values  $\Delta$  ( $\Delta = 1$  implies perfect alignment). The darker the color the higher the number of neighbors belonging to that region. For  $\Delta > 2/3$  possible orientational alignment is limited, the extent of which decreases with facet alignment, shown by presence of a forbidden (empty) region on the top right of the plot (enclosed by dashed lines). Most particles in the crystal phase are restricted to  $\Delta < 2/3$ , as that is the maximum possible value of  $\Delta$  for an orientationally aligned pair of particles, implying a staggered arrangement of nearest triangular facets.

### 3.2 Rotator-phase nucleation of TC58, TC75 and TC80

In this section we compare the nucleation barriers for isotropic-to-plastic solid transition for particles with various degrees of truncations and degrees of supersaturation. For these comparisons, we group our results into shapes lying into two ranges: the first for  $0.5 \leq s \leq 0.667$ , and the second for  $0.75 \leq s \leq 0.85$ . The main reason for this grouping is that they correspond to shapes that form different types of rotator phase structures: the first group forms BCT-lattice, weakly-orientationally ordered rotators, while the second group forms a BCC-lattice, moderately ordered rotator<sup>10</sup>. Figures 5 and 6 and Table 2 show our results for  $s = 0.58, 0.75$  and  $0.85$  as determined by US calculations using largest  $q_6$ -based translationally ordered cluster as the reaction coordinate.

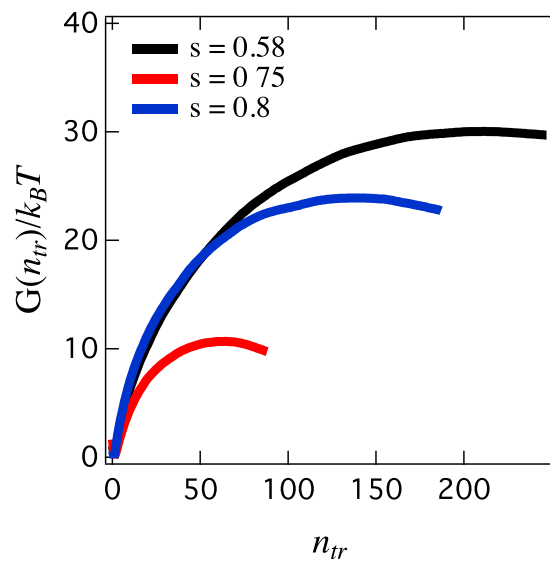


**Figure 5:** Free-energy profile,  $G(n_{tr})$  versus  $n_{tr}$  obtained using US simulations for TC58, TC75 and TC80 for comparable DSSs  $\approx 0.3$ , corresponding to  $P^* \approx 7.60, 9.34$  and  $10.17$ , respectively.

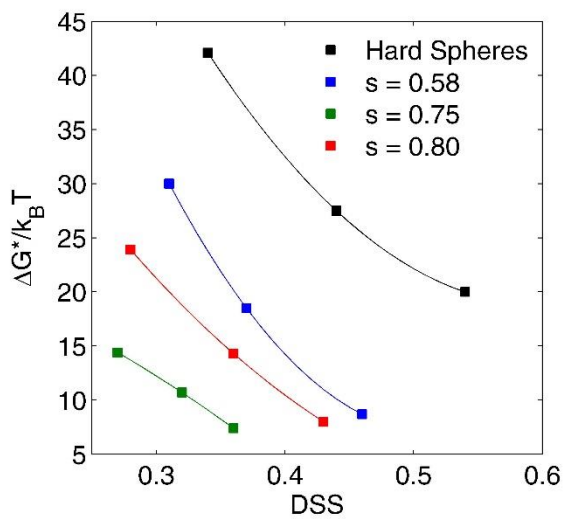


**Figure 6:** Free-energy barrier-height  $\Delta G^*/k_B T$  of TC58, TC75, TC80 and HS<sup>43</sup> at different values of DSS. Solid lines are cubic interpolations.

**Table 2:** Nucleation barriers for truncated cubes using umbrella sampling. Error bars estimated via block-data analysis.

Truncation (s)	Degree of Supersaturation ( $\beta\Delta\mu$ )	Barrier Height ( $\beta\Delta G^*$ )	Critical Nucleus Size
0.58	0.31	30.0±1.0	210
0.58	0.37	18.5±0.5	140
0.58	0.46	8.7±0.4	65
0.75	0.27	14.4±0.4	85
0.75	0.32	10.7±0.5	65
0.75	0.36	7.4±0.4	40
0.8	0.28	23.9±0.8	140
0.8	0.36	14.3±0.6	80
0.8	0.43	8±0.5	46

In order to compare nucleation free-energy barriers for shapes with different  $s$  for the same value of  $DSS = 0.34$  (Fig. 6), we perform cubic spline interpolation for the data obtained here and other available data reported in previous studies<sup>8</sup> for cuboctahedra ( $s=0.5$ ) and truncated octahedra ( $s=2/3$ ). This particular value of  $DSS$  is chosen because it leads to barriers of the order of  $\sim 20 k_B T$ , making them easier to estimate reliably via US (compared to very high or very small barriers which carry larger uncertainties).

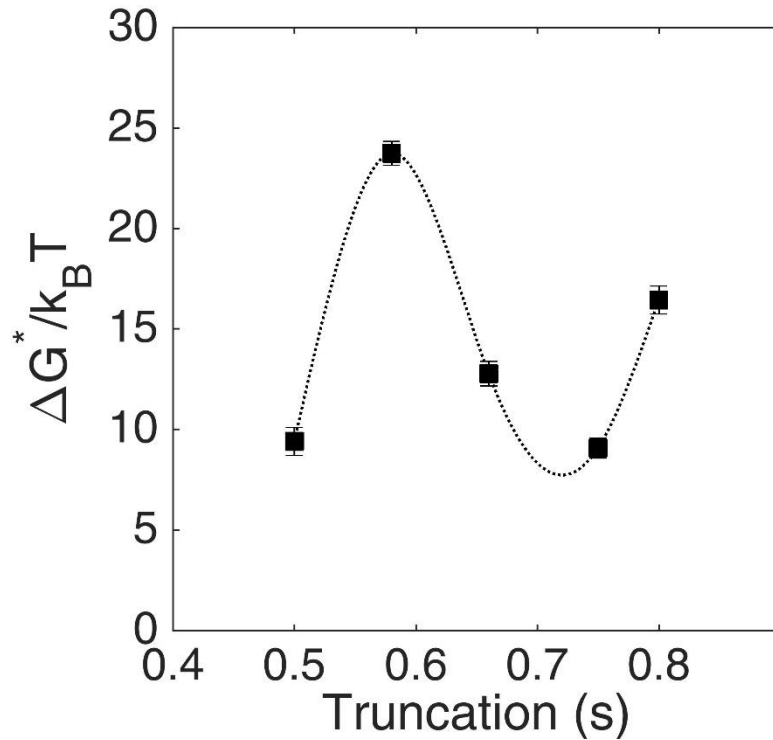


**Figure 7:** Free-energy barrier-height  $\Delta G^*/k_B T$  for isotropic to rotator phase transition for particle shapes with different truncations at  $DSS = 0.34$ . Data for CO and TO obtained from prior work<sup>8</sup>. For comparison,  $\Delta G^*$  for HS<sup>41</sup> at  $DSS = \mathbf{0.34}$  would be  $\sim 42 k_B T$ .

In an earlier publication<sup>8</sup> we highlighted the role of orientational order in catalyzing the nucleation of rotator phases in anisotropic particles, including CO and TO. The degree of orientational order is reflected in the presence of certain preferred orientations in the rotator phase. As long as such preferred orientations are a subset of those orientations promoted by the natural tendency for facet-to-facet contacts between particles, then the anisotropy of particle orientational distribution in the rotator phase can be seen as an indicator of the catalytic effect of local orientational order. As has been demonstrated,<sup>10</sup> all the rotator phases generated by particle shapes from the truncated cube family have non-uniform orientational distribution and hence it is expected that the nucleation barriers for all cases considered here are lower than that observed for HS<sup>40,41</sup>. However, the more diffuse (isotropic) the distribution of preferred orientations in the rotator phase is, the less the catalytic effect of orientational order is expected to be, for in the limit of particles approaching a fully isotropic orientational distribution, hard sphere like behavior would ensue.

We first examine the trends in  $\Delta G^*$  data for the group of shapes in  $0.5 \leq s \leq 0.667$ . Shapes similar to TC58 undergo a first order phase transition from isotropic to rotator phase with a very small extent of global orientational order<sup>10</sup> (similar to that of the isotropic phase). Specifically, for  $s = 0.58$  the preferred orientations are spread over 18 clusters on the unit sphere and hence the nature of its isotropic-solid phase transition would be close to that for HSs, where a globally translationally ordered and

orientationally disordered phase is nucleated. This is further confirmed by plotting the particle orientation distribution of nuclei for  $187 < n_{tr} < 217$  (near the top of the barrier for  $P^* \approx 7.60$ ), which is seen in Fig. 8(a) to be quite diffuse, and by the small value of  $P_4 \approx 0.07$  (the snapshot of a  $n_{tr} = 209$  near-critical nucleus is shown in Fig. 8(b)). Such results are also consistent with the TC58 having the smallest asphericity among all shapes considered here.<sup>10</sup> In comparison, the critical nuclei of COs and TOs have higher values for  $P_4 \approx 0.1$  and  $0.15$  respectively (associated with 6 preferred clusters, the lower value in CO implying a more ‘diffuse’ clustering). Thus, it is expected that the catalytic effect of orientational order is weaker in case of TC58 and thus its nucleation barriers be higher than those for CO and TO. Thus, the strength of local orientational order correlates with lower nucleation barrier heights.

We now consider the second group of shapes with  $s = 0.75$  and  $0.80$ . The rotator phases of TC75 and TC80 are termed as high-cubatic plastic crystal phases<sup>10</sup>, as they have non-negligible global orientational order. Similar orientational order is also observed for nuclei near top of the barrier for both TC75s and TC80s, which is also related to that observed in the Minkowski lattice of perfect octahedra. As shown for TC75 at  $P^* = 9.34$  and TC80 at  $P^* = 10.17$  in Fig. 8(c) and (d) respectively, the orientation distributions of these nuclei show inhomogeneous distribution with weak clustering at different regions, with TC75 exhibiting more scattered clusters compared to TC80. This clustering however is stronger than that of TOs as indicated by the moderate  $P_4$  values of  $0.39$  and

0.41 for TC75 and TC80, respectively. Snapshots of a portion of near-critical nucleus for TC75 ( $n_{tr} = 62$ ) and TC80 ( $n_{tr} = 148$ ) are also shown in Figs. 8(d) and 8(f) respectively.

If we apply here the same criteria, we used to explain trends in barrier heights for  $s \in [0.5, 0.66]$ , we would predict that the nucleation barriers for these shapes would be much lower than those of TO, with TC80 having a lower barrier than TC75. In contrast, we observe that TC80 has a higher free-energy barrier than TC75 for comparable  $DSS$ . To understand this discrepancy, we must explore the spontaneous fluctuations in local order present in the isotropic phase and how they affect the nucleation behavior. Similar to the case with the Minkowski crystal in octahedra, we anticipate that a similar discord between facet-to-facet matching and orientational order might be contributing to the rise of nucleation barriers. If we consider the distribution of facet alignment measure for both TC75 & TC80 (Figure 9), we clearly observe that the size of the forbidden region on the top-right is larger for TC80. Moreover, due to a more scattered distribution of preferred orientations for TC75, more high- $\Delta$  configurations are explored by the particles in the rotator phase. Thus, the nucleation barrier is smaller for TC75 than for TC80 due to a reduced hindrance to nucleation pathways from states of high facet-to-facet matching. Using a similar line of reasoning, we predict a monotonous increase in the nucleation barrier for  $s > 0.8$  as the lattice structure of the rotator phase essentially remains the same while the hindrance associated with the forbidden region

in the  $d_4$ - $\Delta$  diagram likely increases. As a limit, truncated octahedra ( $s=0.66$ ) do not have any significant forbidden region (see SI).

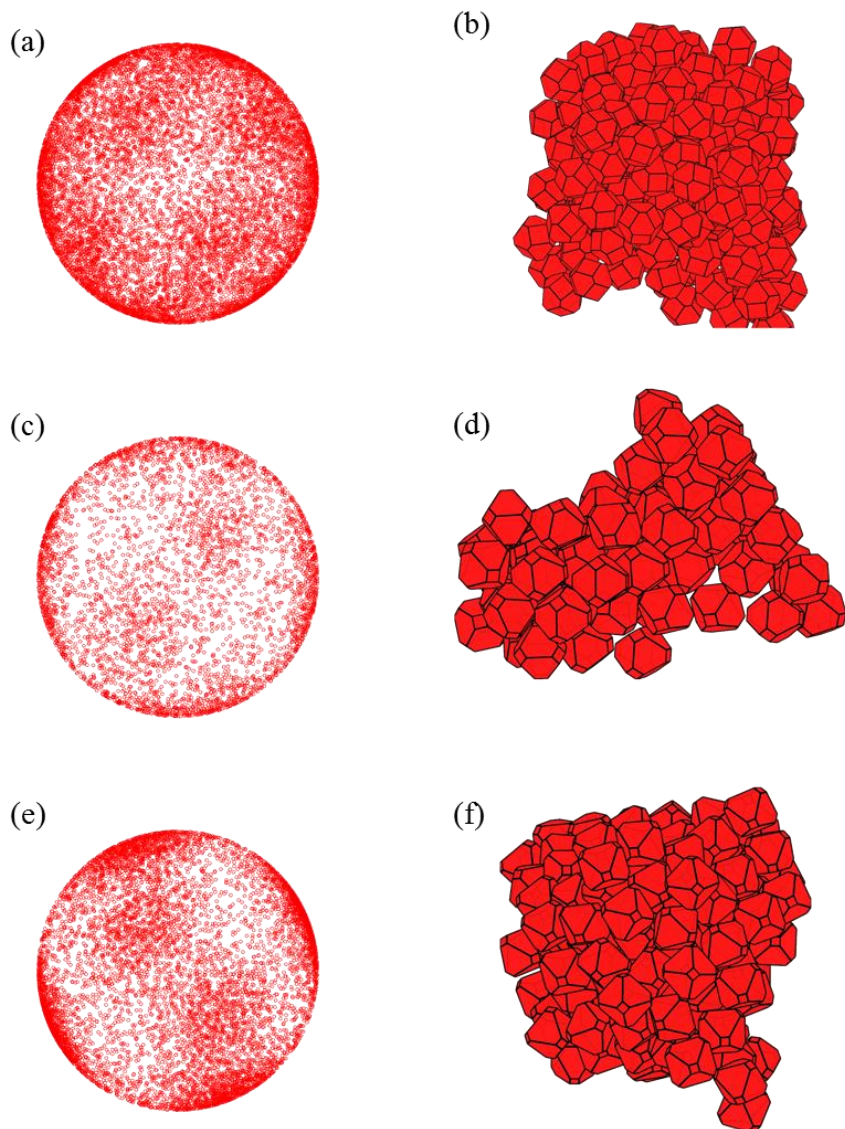


**Figure 8:** Particle orientation distribution map of near-critical nuclei for (a) TC58 at  $P^*=7.60$ , (c) TC75 at  $P^*=9.34$  and (e) TC80 at  $P^*=10.17$ . Each distribution is obtained over 20 different configurations. Snapshots of a portion of the nucleus are shown in (b) for TC58, (d) for TC75 and (f) for TC80.

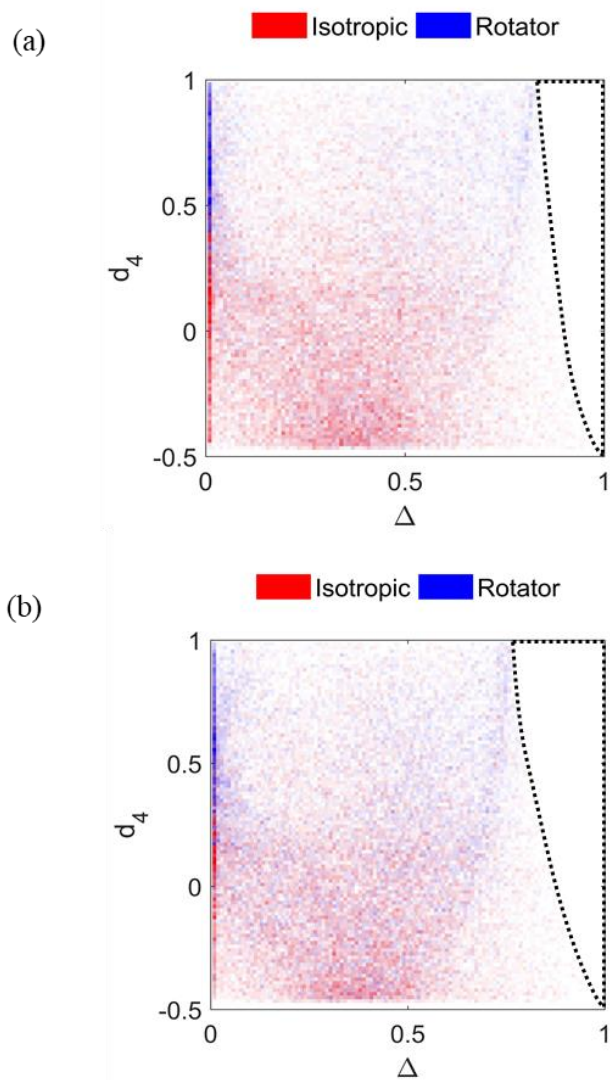


**Figure 9:** 2D Histogram plot for  $d_4$  values for Voronoi neighbor pairs vs. corresponding facet alignment measure values ( $\Delta$ ) for (a)  $s=0.75$  and (b)  $s=0.8$ , each for  $DSS \approx 0.34$ . The systems contained 2744 particles. The darker the color the higher the number of neighbors belonging to that region. Similar to perfect octahedra, we observe that there is a ‘forbidden’ region (empty area enclosed by dashed lines) on top right which implies that high facet alignment can restrict orientational alignment. The size of the forbidden region is significantly larger for  $s = 0.8$  in comparison to  $s = 0.75$ .

## 4 Conclusion

In this work, we performed MC simulations to study the nucleation of ordered phases of selected octahedron-like shapes from the truncated cube family. The analysis unveils non-trivial trends in nucleation free energy barriers  $\Delta G^*$  (as surrogates for describing nucleation kinetics) as a function of the extent of shape truncation. We demonstrate that for perfect octahedra the simulated nucleation barriers for nucleating the Minkowski crystal are much larger than those for solid-phase nucleation in HS for comparable degrees of supersaturation. Our analysis of configurations of neighboring particles reveals that this transition to crystal involves a mismatch between facet-to-facet alignment and local orientational order. Since facet-to-facet match-up increases local packing entropy, configurations with high degree of facet-to-facet alignment occur as spontaneous fluctuations in the isotropic phase, as quantified by a novel facet alignment metric. However, any two octahedra with near perfect facet matching will necessarily be orientationally misaligned and are hence inconsistent with the high orientational order needed to realize the Minkowski crystal lattice. Since there is a spontaneous tendency for a subpopulation of particles in the isotropic phase to have such high facet alignment, such configurations hinder the nucleation pathways, resulting in higher values of  $\Delta G^*$  as compared to systems where such hindrance is absent (like HSs).

It is the interplay between the tendency for facet alignment and local orientational order<sup>8</sup> among particles that underpins the attainment of translational-ordered packing and the observed trends in  $\Delta G^*$  for particle shapes with varying degrees of truncation. In essence, local facet alignment may or may not be conducive to configurations that on average match the stable ordered structure, hence aiding or deterring the nucleation process. For all truncations (except for perfect octahedra which do not form a stable rotator phase), the estimated  $\Delta G^*$  values for the isotropic-to-rotator phase transition are smaller than those for HSs at similar degrees of supersaturation, presumably due to the beneficial effect of local orientational order as described in earlier studies<sup>8</sup>. We also observe that such a catalytic effect of local orientational order correlates with the degree of overall orientational order in the incipient rotator phase (as detected, e.g., by the clustering of particle orientations along preferential directions), which leads to a maximum for  $\Delta G^*$  around TC58, whose critical nucleus has negligible orientational order. The near-isotropic particle orientation distribution in the solid nucleus of TC58 renders its  $\Delta G^*$  values closer to those of HS for comparable degrees of supersaturation. For  $s > 0.66$ , however, even as local orientational order increases with increasing truncation, the rotator-nucleation barriers increase. In these cases, we infer that, instead of facilitating, facet alignment hinders some of the nucleation pathways that lead to the local orientational order required to form the solid phase (akin to the effect in octahedra), leading to higher barriers to nucleation as truncation increases (and the

octahedron shape is approached). Despite the complex interplay between orientational and translational order in the systems studied, we found no evidence for multi-step non-classical nucleation pathways.

Future simulation studies could be aimed at calculating nucleation rates by either complementing  $\Delta G^*$  data with the evaluation of kinetic prefactors<sup>8,40,41</sup> or by implementing transition path sampling methods<sup>37</sup>. In addition, to further test the hypotheses regarding the interplay between localized orientational order and facet alignment, similar analyses can be performed for other particle geometries. We anticipate that the effects of localized orientational order and facet-to-facet matching are general and can help understand the dynamics with which faceted particles self-assemble. However, the metrics we have used in this study are system specific and will require suitable extensions and specialization for application to systems with particles with different geometries/symmetries. Finally, the effect on nucleation kinetics of shape and size polydispersity, a prevalent feature in experimental systems, should also be investigated. On the one hand, polydispersity may suppress some nucleation pathways as has been observed for hard spheres<sup>56</sup> (with large extent polydispersities eventually suppressing crystallization altogether<sup>57-58</sup>); on the other hand, in some systems a small degree of polydispersity could also lessen the facet-alignment-based hindrances that we have identified in this study.

This study adds to the body of work devoted to unveiling guidelines to engineer the self-assembly of anisotropic particles. Our analysis identifies some specific shapes that exhibit favorable kinetic for the homogeneous nucleation of translational order and the microscopic mechanisms that can be responsible for such behavior. For example, we have elucidated how local 2-particle correlations can aid or hinder collective phase transition phenomena. Such insights could be used to design fast self-assembling particles and external fields and additives that could act as catalysts for heterogeneous nucleation.

## **5 Acknowledgements**

Funding support from NSF award CBET-1402117 is gratefully acknowledged. This work used the Extreme Science and Engineering Discovery Environment (XSEDE), which is supported by the National Science Foundation grant number ACI-1053575. The authors are also grateful to Unmukt Gupta for valuable exchanges.

## 6 Supplementary Information

### 6.1 Calculation of Facet Alignment Measure

Here we describe the methodology used to implement facet alignment ( $\Delta$ ) for convex particles with convex facets (this can conveniently be generalized for concave cases).

For two particles, say particle 1 and particle 2, the facet alignment measure is defined in the following steps:

1. Search for a pair of facets (belonging to either particles)  $F_{1n}$  and  $F_{2n}$  that have the shortest centroid-to-centroid distance.

- 1.1. Centroid of a face is defined as the arithmetic mean of individual Cartesian coordinates all vertices of the face.

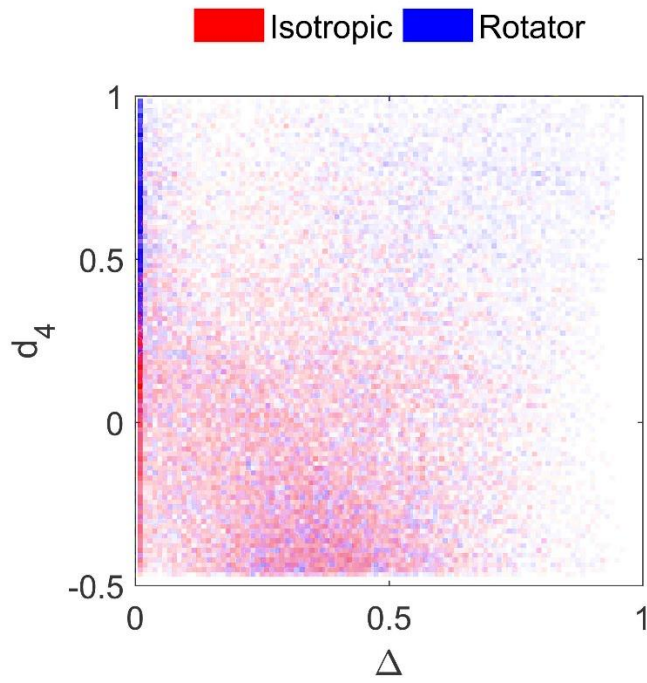
2. Project  $F_{1n}$  to the plane of  $F_{2n}$ .

- 2.1. Create a  $2 \times 3$  transformation matrix  $T$  to map vertices of  $F_{1n}$  onto a 2-D coordinate system defined in the plane of  $F_{2n}$ .

- 2.1.1. In order to define the transformation matrix, we need two orthogonal unit vectors that lie in the plane of  $F_{2n}$ . Arbitrarily choose one edge vector of the face as the first unit vector. To obtain the second unit vector, use the cross product of the first unit vector with the cross product of itself and another non-parallel edge vector.

- 2.2. Multiply  $T$  with each of the vertices ( $3 \times 1$  *matrix*) of  $F_{1n}$  to obtain the projected face  $F_{1n}^p$  in the plane of  $F_{2n}$ . Repeat the same for the vertices of  $F_{2n}$  to obtain its description in the 2-D coordinate system  $F_{2n}^p$ .
3. Find the intersection area  $A_{12}$  between  $F_{1n}^p$  and  $F_{2n}^p$ .
  - 3.1. For all edges belonging to face  $F_{1n}^p$ , find their intersections with all the edges of  $F_{2n}^p$ . Call the set of intersections  $I$ .
  - 3.2. Find all the vertices that belong inside both  $F_{1n}^p$  and  $F_{2n}^p$ . This can be done using *inpolygon* MATLAB built-in function. Call this set of vertices  $C$ .
  - 3.3. Take the union of  $C$  and  $I$  and evaluate the area  $A_{12}$  of the resulting polygon.
4. Repeat steps 2 & 3 by projecting  $F_{2n}$  to the plane of  $F_{1n}$  and obtain area  $A_{21}$ .
5. Find  $A_m = \max(A_{12}, A_{21})$ .
6. Evaluate  $\Delta = A_m/A_l$ , where  $A_l$  is the area of the largest facet present on the particle.

6.2  $d_4$  vs.  $\Delta$  Histogram for  $s=0.667$



It is noted that there is no significant range of  $\Delta$  that is not accessed by the rotator phase, thus the hindrance due to incompatible facet matching is minimal.

## CHAPTER 2: NUCLEUS-SIZE PINNING FOR DETERMINATION OF NUCLEATION FREE-ENERGY BARRIERS AND NUCLEUS GEOMETRY

Abhishek K. Sharma and Fernando A. Escobedo\*

School of Chemical and Biomolecular Engineering, Cornell University, Ithaca, NY 14853,  
USA

### Abstract

Classical Nucleation Theory (CNT) has recently been used in conjunction with a seeding approach to simulate nucleation phenomena at small-to-moderate supersaturation conditions when large free-energy barriers ensue. In this study, the conventional seeding approach [J.R. Espinosa, C. Vega, C. Valeriani, and E. Sanz, *J. Chem. Phys.* **144**, 034501 (2016)] is improved by a novel, more robust method to estimate nucleation barriers. Inspired by the interfacial pinning approach [U. R. Pedersen, *J. Chem. Phys.* **139**, 104102 (2013)] used before to determine conditions where two phases coexist, the seed of the incipient phase is pinned to a preselected size to iteratively drive the system toward the conditions where the seed becomes a critical nucleus. The proposed technique is first validated by estimating the critical nucleation conditions for the

disorder-to-order transition in hard spheres, and then applied to simulate and characterize the highly non-trivial (prolate) morphology of the critical crystal nucleus in hard gyrobifastigia. A generalization of CNT is used to account for nucleus asphericity and predict nucleation free-energy barriers for gyrobifastigia. These predictions of nuclei shape and barriers are validated by independent umbrella sampling calculations.

## 1 Introduction

First order phase transitions from metastable phases to stable phases often take place through a mechanism of nucleation and growth. In particular, crystal nucleation involves the formation of ordered domains of the stable phase (nuclei) that, once sufficiently large, can spontaneously grow to reach macroscopic size. The condition at which a given nucleus has an equal probability to grow and decay is termed as *critical*<sup>57,58</sup>. To a good approximation, this critical state corresponds to a saddle region in the transition pathway and hence where the nucleus attains its highest free energy. The nucleus must overcome this critical or transition state to form the stable phase, and the difference between the free energy of the critical state to the pure metastable state is called *nucleation barrier* ( $\Delta G^*$ ). Detailed knowledge of the mechanism of how such nuclei form and grow is of great practical importance, for this can open the door to rationally manipulate or bias these processes, e.g., to catalyze the assembly of nanoparticles into ordered structures<sup>8,59</sup>.

Computer simulations have emerged as a valuable complementary tool to experiments and theory to study the mechanism of nucleation and growth for a variety of phase transitions and systems. Since the formation of an ordered domain in a moderately metastable disordered phase is a rare event, using brute force simulations to sample representative nucleation trajectories is computationally impractical unless the nucleation free-energy barrier is small (say order of a few  $k_B T$ ). For example, for a nucleation barrier of  $20 k_B T$ , the chance of sampling the critical condition is nearly one in a billion trial configurations attempting to escape the metastable basin. Hence, a variety of rare-event sampling techniques have been developed and employed to understand nucleation kinetics, such as umbrella sampling<sup>40-42</sup>, forward flux sampling<sup>28,29,41,60,61</sup>, and metadynamics<sup>62-64</sup>. However, application of these techniques is limited in cases where nucleation barriers are steep and/or high where the ratcheting of configurations through milestones along the pathway from the disordered phase becomes inefficient and tedious. This is because when climbing steep free-energy profiles, the relative frequency with which the high free-energy states are visited is quite low in proportion to the low free-energy states, thus leading to poor sampling and inaccurate estimates of free energy differences. A way to overcome this limitation is the 'seeding approach'<sup>65-68</sup>. The approach essentially involves insertion of a preformed ordered domain (seed) into the disordered phase and observing its growth/decay behavior. Several simulations are then run for different degrees of supersaturation

trying to narrow down the conditions when a transition occurs between growth and decay behaviors<sup>67,68</sup>, i.e., the seed grows spontaneously above a critical supersaturation while decays spontaneously below it. Once the critical conditions are found, they are used in combination with classical nucleation theory (CNT) to evaluate the key parameters that characterize the nucleation process such as the nucleation free-energy barrier, interfacial energy, and the nucleation rate. This seeding approach has been successfully demonstrated for nucleation in L-J systems<sup>65</sup>, NaCl<sup>68</sup>, hard spheres<sup>67</sup>, water, lattice models<sup>69</sup>, and metals<sup>70</sup>. Besides homogenous nucleation, the method has been employed to study heterogeneous nucleation phenomena in nanoparticles<sup>71</sup>, including cases with a cubic seed<sup>72</sup>. While seeding appears to be a promising method to study nucleation at low-to-moderate supersaturations (and to complement the scope of other methods that can resolve nucleation behavior for moderate-to-high supersaturations without resorting to CNT), its applicability relies on the following preconditions/assumptions:

- (i) CNT can be used to estimate the free-energy barrier height. An appropriate order parameter to detect the seed and Classical (as opposed to non-classical) nucleation pathways are ingredients typically associated with this assumption.

- (ii) The seed growth-to-decay transition behavior is abrupt and detectable with limited sampling.
- (iii) The system can evolve from an initially arbitrary shaped seed (typically spherical) to the inherent seed shape in a timely fashion. The configurations obtained upon insertion and equilibration of the seed are representative of those that would occur spontaneously in the system.

Assumption (i) underpins the seeding method and the extension to be elaborated in this work. Assumption (ii) can be invalid for systems with a flat or diffusive free energy profile around the top of the barrier (implying a low Zeldovich factor), where the transition from growth-to-decay behavior is gradual, and when even a slightly post-critical nucleus has significant probability of dissolution. In such a scenario, it would be difficult to precisely pinpoint the critical condition altogether and extensive sampling required to quantify growth vs. decay behavior. We note here that conventional seeding studies have thus far only considered the ‘first occurrence’ of growth to decay to bracket the critical condition<sup>67,68</sup>. A more statistically rigorous implementation would entail, e.g., estimating growth/decay probabilities from more extensive sampling of trajectories, such that the critical condition<sup>58,66</sup> can be established by the equality of growth and decay probabilities. Assumption (iii) could be violated if the initially assumed seed shape is very different from the inherent seed geometry<sup>73-76</sup>. While equilibration

of the seed can take place over a shorter time scale than that for seed growth/melting as implemented in conventional seeding<sup>77</sup>, such a trend is system and seed-size dependent. Further, it may not be straightforward to establish whether seed equilibration is attained, which may affect the seed growth/decay behavior and lead to unreliable results for both the seed size and critical condition. In fact, even though we can ‘surgically’ insert an ordered seed into a disorder phase and then equilibrate<sup>67,68</sup> it, the initial structures of the core and interface may remain far from their ‘natural’ states over very long simulation periods. This is important because the configurations present at the interface can play a crucial role in the overall mechanism of nucleation and growth<sup>8</sup>.

In this study, we propose and demonstrate a variant of the seeding approach that improves the handling of the constraints (ii) and (iii) listed above. In essence, we introduce an iterative scheme (similar to interfacial pinning<sup>78–80</sup>) that converges to the critical nucleation conditions for a seed of a prescribed size without the need to assume the seed shape or to constrain the interface morphology. We call this method nucleus-size pinning (NSP) which we couple to a generalization of CNT to extend its scope to treat seeds of arbitrary geometry. Our main application of this approach is for the nucleation of an aspherical seed for hard gyrobifastigia (GBFs). GBF is a Johnson solid consisting of four square and four triangular faces whose equilibrium phase behavior has been studied earlier, being remarkable for its ability to form a space-filling crystal

and inability to form any mesophase<sup>4</sup>. GBF can be seen as a test-bed that provides a stringent test to simulation studies of crystal nucleation, given not only the anisotropy of its shape and of its crystal lattice, but also the large free-energy barriers that have been associated with their disorder-to-order phase transition.<sup>4</sup>

The rest of this paper is organized as follows. In Section 2.1 we present the generalization of CNT for arbitrary seed geometries. In Section 2.2 we describe the details of NSP method, followed by a description of simulation details and order parameters in Section 2.3 and 2.4, respectively. In Section 3.1, we first validate the applicability of NSP by replicating established nucleation barrier results for hard spheres,<sup>40,41,67</sup> and then in Section 3.2 we apply this method to GBF crystallization. Finally, in Section 4 we present our conclusions and an outlook for the method.

## 2 Methods

### 2.1 Generalized Classical Nucleation Theory

For a system with an ordered (solid) seed of volume  $V_s$  and surface area  $A_s$ , the extensive free energy of the system  $\phi_T$  in reference to a disordered (liquid) bulk phase is given as:

$$\phi_T = \phi_{bulk} + \phi_i \quad (1)$$

where  $\phi_i$  is the contribution of the interface between the seed and the liquid, and  $\phi_{bulk}$  is the difference between contributions of bulk solid and liquid phases for a volume  $V_s$ .  $\phi_i$  is proportional to  $A_s$ , while the bulk contributions are proportional to  $V_s$  or to the number of particles in the seed  $N_s$ , thus equation (1) becomes:

$$\phi_T = -\Delta\mu N_s + \gamma A_s \quad (2)$$

where  $\Delta\mu$  is the chemical potential difference between liquid and solid and  $\gamma$  is the interfacial free energy to maintain the solid-liquid interface. For systems where the liquid phase is metastable,  $\Delta\mu$  is positive (implying that  $\phi$  decreases with  $V_s$ , because the solid is thermodynamically more stable). For a given seed of fixed geometry,  $N_s$  is proportional to the volume  $V_s$ , which in turn is related to the length scale of the seed ( $L$ ) as:

$$N_s \propto V_s \propto L^3 \quad (3)$$

$$\rightarrow L \propto N_s^{\frac{1}{3}} \quad (4)$$

Similarly, for a given geometry, the surface area  $A_s$  is proportional to  $L^2$ . Upon rearranging terms,

$$A_s \propto L^2 \propto N_s^{\frac{2}{3}} \quad (5)$$

Equation (5) can be used to rewrite Eq. (2) with a proportionality constant ( $k_A$ ) as:

$$\phi_T = -\Delta\mu N_s + k_A N_s^{\frac{2}{3}} \quad (6)$$

In order to find the critical nucleus size  $N_s^*$ , the expression for the derivative of  $\phi_T$  with respect to  $N_s$  is given by:

$$\frac{d\phi_T}{dN_s} = -\Delta\mu + \frac{2k_A N_s^{-\frac{1}{3}}}{3} = 0 \quad (7)$$

$$N_s^* = \left(\frac{2k_A}{3\Delta\mu}\right)^3 \quad (8)$$

Which when substituted in equation (6) gives:

$$\phi_T^* = -\Delta\mu \left(\frac{2k_A}{3\Delta\mu}\right)^3 + k_A \left(\frac{2k_A}{3\Delta\mu}\right)^2 = \frac{4k_A^3}{27\Delta\mu^2} = \frac{N_s^* \Delta\mu}{2}$$

this critical free energy barrier will also be denoted later as  $\Delta G^*$  so that this equation is:

$$\phi_T^* \equiv \Delta G^* = N_s^* \Delta\mu / 2 \quad (9)$$

This expression is the same as the one associated with CNT and has been reported in earlier studies.<sup>67,68,81,82</sup> The key feature of Eq. (9) is its independence of seed geometry; as it only assumes the validity of the square-cube law relating the surface area and the volume. Thus, equation (9) can be used to calculate the nucleation barrier ( $\Delta G^*$ ) once a critical seed (of size  $N_s^*$ ) of appropriate geometry is obtained, which need not be spherical.

## 2.2 Nucleus-Size Pinning

In this section, we shall derive the iterative expression used by nucleus-size pinning for estimating of the critical supersaturation conditions. For concreteness, this derivation is targeted to estimating the critical pressure (at constant temperature) but it can be readily generalized for any thermodynamic field other than pressure (e.g., temperature) as described in our earlier publications<sup>78</sup>. For a pure component system at fixed temperature  $T$ , the fundamental thermodynamic equation can be written as:

$$d\mu = vdp \quad (10)$$

In an isothermal-isobaric (NPT) ensemble with  $N$  total particles at pressure  $p$  and temperature  $T$ , the probability  $p(N_s)$  of a state with  $N_s$  particles in the solid phase seed can be written as:

$$p(N_s) \propto \exp(-\phi_T(N_s)) \quad (11)$$

The total free energy can again be split up as:

$$\phi_T(N_s) = \phi_{bulk,solid}(N_s) - \phi_{bulk,liquid}(N_s) + \phi_i(N_s) \quad (12)$$

For critical nucleation conditions, the slope  $S_T = \frac{d\phi_T}{dN_s}$  should be zero, thus:

$$S_T = \frac{d\phi_{bulk,solid}}{dN_s} - \frac{d\phi_{bulk,liquid}}{dN_s} + \frac{d\phi_i}{dN_s} = 0 \quad (13)$$

But since at constant pressure and temperature:  $\phi_{bulk,j} = \mu_j N_s$ , equation (13)

becomes:

$$S_T = \mu_{solid} - \mu_{liquid} + \frac{d\phi_i}{dN_s} \quad (14)$$

Let  $p^*$  denote the critical pressure corresponding to a preset, target seed size  $N_{s,t}$ .

Assume that an initial isothermal isobaric simulation is conducted at a pressure  $p_A$  corresponding to a point A on the free energy curve where the seed of size is  $N_{s,A}$ . The

goal is to devise a scheme that, given simulation data at  $p_A$ , it returns a guess

pressure  $p_B$  that is closer to  $p^*$ , a process that can be iterated till converge to  $p^*$ , in a

manner analogous to interfacial pinning<sup>78-80</sup>. For this purpose, we approximate

selected terms in equation (14) by truncated Taylor expansions around point A to obtain

an extrapolation to a point of interest B as follows:

$$\mu_{j,B} = \mu_{j,A} + \frac{\partial \mu_{j,A}}{\partial p} \Delta p_{BA} \quad (15)$$

$$\frac{d\phi_{i,B}}{dN_s} = C_A \quad (16)$$

which are the first and zeroth order approximations respectively, with  $\mu_{j,A}$  and  $C_A$

being the values of properties at point A, and  $\Delta p_{BA} = p_B - p_A$ . Note that for equation

(16), we assume that for small changes in pressure the interfacial contribution to the

slope is not a strong function of pressure<sup>67</sup>, and hence can be approximated as a constant (whose value is  $C_A$ ). This assumption may be relaxed with the use of a suitable modification to CNT that describes the variation of interfacial free energy with pressure; a more detailed analysis of this assumption, including a CNT-based estimation of  $\gamma$  is given in the Appendix. Substituting equation (10) into equation (15):

$$\mu_{j,B} = \mu_{j,A} + \bar{v}_A \Delta p_{BA} \quad (17)$$

Where  $\bar{v}_A$  is the ensemble average of the specific volume at point A. Further:

$$\Delta\mu_{sl,B} = \mu_{solid,B} - \mu_{liquid,B} = \Delta\mu_{sl,A} + \Delta\bar{v}_{sl,A} \Delta p_{BA} \quad (18)$$

where  $\Delta\mu_{sl,A}$  and  $\Delta\bar{v}_{sl,A}$  are the differences in chemical potential and specific volume at point A, respectively. Substituting equations (16) and (18) into equation (14) we obtain an expression for  $S_{T,B}$ :

$$S_{T,B} = \Delta\mu_{sl,A} + C_A + \Delta\bar{v}_{sl,A} \Delta p_{BA} = S_{T,A} + \Delta\bar{v}_{sl,A} \Delta p_{BA} \quad (19)$$

For a given point A, if  $S_{T,A}$  and  $\Delta\bar{v}_{sl,A}$  are known, the needed change in pressure  $\Delta p_{BA}$  to reach the desired value of  $S_{T,B} = 0$  (critical condition) can be obtained as,

$$\Delta p_{BA} = -\frac{S_{T,A}}{\Delta\bar{v}_{sl,A}} \quad (20)$$

$$\rightarrow p_B = p_A - \frac{S_{T,A}}{\Delta\bar{v}_{sl,A}} \quad (21)$$

This estimate of  $p_B$  can be further improved by iterating the entire process, eventually converging towards  $p^*$ , the critical pressure. Such a convergence is expected for systems having a monotonically varying slope for free energy (with respect to nucleus size), as was the case for the systems studied in this work and is likely the case for many nucleation and growth phenomena.

At any given pressure, the value of  $\Delta\bar{v}_{sl}$  can be obtained using the equations of state for either phases. The slope  $S_T$  of the free energy profile can be obtained using an approach similar to interfacial pinning<sup>78–80</sup>. However, instead of pinning the position of the interface, we pin the nucleus size by biasing the system with a harmonic potential of the form:

$$\Delta U_H = \frac{\kappa}{2} (N_s - N_{s,t})^2 \quad (22)$$

We note that while this biasing potential is similar to the one traditionally used in umbrella sampling simulations, the purpose here is not to map the local free energy profile but rather to provide the balancing potential to pin the seed size and iteratively converge to the underlying free energy maxima. The ideal probability distribution associated with such a potential is a Gaussian distribution centered at  $N_s = N_{s,t}$ , noting that both  $N_{s,t}$  and the pinning force constant  $\kappa$  are user defined values. When applied to a given point A on the total free energy curve, the resulting probability distribution is given by:

$$p(N_s) \propto \exp(-(\phi_T + \Delta U_H)) \quad (23)$$

In the neighborhood of  $N_{s,t}$ ,  $\phi_T$  can be assumed to be a linear function with slope  $S_T$ . With this assumption, it can be shown that the  $p(N_s)$  is also a quasi-Gaussian distribution with a shifted mean value of  $N_s$  such that:

$$S_T = -\kappa(\langle N_s \rangle - N_{s,t}) \quad (24)$$

Thus, by calculating the average value of  $N_s$  in a biased simulation [under the external potential of Eq. (22)], we can determine the value  $S_T$  needed for the iterative scheme of equation (21) to obtain  $p^*$ . Convergence proceeds as the pressure correction becomes negligible and  $S_T$  approaches zero.

### 2.3 Simulation Details

#### 2.3.1 Model

For both hard spheres and gyrobifastigia we used hard pair potential given by:

$$\beta U_{ij} = \begin{cases} 0 & \text{if no overlap} \\ \infty & \text{if overlap} \end{cases} \quad (25)$$

For spheres, overlaps are detected by evaluating if the center-to-center distance  $r_{ij}$  is less than the diameter ( $\sigma$ ). For gyrobifastigia, overlaps are checked by employing the separating axis theorem.<sup>49</sup>

### 2.3.2 Metropolis Monte Carlo

Metropolis Monte Carlo (MC) simulations were performed in an isothermal-isobaric (NPT) ensemble where the number of particles, the pressure, and the temperature of the system were kept constant. As is customary<sup>40,41</sup>, for spheres the pressure was scaled as  $p = \beta p_a \sigma^3$ , where  $\beta = \frac{1}{k_B T}$ ,  $p_a$  is the unscaled pressure,  $k_B$  is the Boltzmann constant, and  $\sigma$  is the diameter of the sphere. For GBF, the pressure was scaled as  $p = \beta p_a a_c^3$ , where  $a_c$  is the radius of the circumscribing sphere. Simulations were conducted using periodic boundary conditions and cycles consisting of N translational, 2 isotropic volume moves, and for GBF, an additional N rotation moves. A volume move attempt involves the rescaling of the simulation box size while maintaining constant the reduced coordinates of the particles' centers of mass (and particle orientations for GBF).<sup>31</sup> For spheres the simulation box was cubic while for GBF the box was cuboidal in shape to accommodate an equal number of particle layers of the anisotropic solid-phase lattice vector. For hard spheres, the degree of supersaturation were taken and interpolated from the literature<sup>67</sup>. For GBF, the equations of state for the various phases were obtained and selected degrees of supersaturation DSS ( $= \beta \Delta \mu$ ) were evaluated upon integration of suitable branches of those equations of state, by using the same formulas discussed in earlier work<sup>4,8</sup>.

### 2.3.3 Nucleus-Size Pinning

The biased NPT MC simulations were performed in manner similar to those described in prior studies<sup>78</sup>. Following the conventional seeding<sup>66,67</sup> methods, an ordered spherical seed of a chosen size is inserted into a hole carved in a disordered phase by eliminating any overlapping particles. To avoid finite size effects, a system sufficiently larger than the seed size was simulated to ensure that the seed does not interact with its periodic images. For this purpose, the size and shape of the simulation box were altered, as necessary. Both the ordered seed and the disordered configurations were at equilibrated volume fractions corresponding to the pressure of interest as per the equations of state. To save computational time, the order parameter calculations were performed once every 100 MC cycles, upon which the modified Metropolis criteria with the biased potential was used to accept or reject the trajectory of the last 100 cycles (if rejected, the old trajectory was restored). Once key system properties such as the cluster size, the specific volume, and, in the case of GBF, the aspect ratio of the nucleus, have fully converged (usually in about  $3 \times 10^6$  MC cycles), the run is stopped and statistics for the cluster size are evaluated (note that this equilibration process eliminates potential artifacts from the original seed preparation). Using equation (21), a new estimate of the sought-after pressure is obtained, and a new iteration of the process is started.

For the method to work efficiently, the strength of harmonic potential ( $\kappa$ ) needs to be chosen carefully. If too high, the system would be too constrained to be able to explore diverse configurations and statistics thus obtained would not be representative. If too low, the assumptions regarding the local behavior of various system properties as implied by the Taylor series expansions in equations (15) and (16), may not be correct. An insufficiently strong potential can lead to multimodal  $p(N_s)$  distribution, with peaks on either side of the barrier. This is possible when the unbiased free energy profile exhibits a high variation in slope near the target nucleus size, allowing for solutions to equation (13) on either side of the peak. This issue can be remedied by increasing  $\kappa$  and a suitable value can be found using the following criterion<sup>78</sup>:

$$\kappa > \frac{1}{\sigma_{N_s}^2} \quad (26)$$

where  $\sigma_{N_s}^2$  is the variance in the  $N_s$  values for a short unbiased simulation around the target conditions. For the purpose of estimation of barrier heights, since the method uses CNT, the method is more indicated for lower degrees of supersaturation where larger nuclei ensue. Thus, it is a complementary technique to conventional methods such as umbrella sampling and forward flux sampling which tend to be inefficient at low DSS.

### 2.3.4 Umbrella Sampling (US)

To provide an independent estimation of the homogeneous solid-nucleation free-energies for GBFs for comparison to estimates from the proposed NSP method, we also implemented umbrella sampling (US) simulations<sup>8</sup>. Using as reaction coordinate the size of the greatest cluster of ordered particles ( $N_s$ ), the transition path from the disordered to the ordered state is divided into overlapping windows. Each window is simulated separately with reflective walls and  $N_s$  is recorded every 2 MC cycles. Reflective walls are implemented such that any trajectory moving outside the window at the end of 2 MC cycles is returned to the configuration prior to the 2 MC cycles, which is counted again. Statistics obtained from each window are used to obtain relative free energies for the  $N_s$  states within a window. Finally, individual sections are stitched together by matching values at the boundaries of the windows, keeping the value for the most frequent entry near  $N_s = 0$  as the reference. All US calculations were performed with a system of 1728 particles.

## 2.4 Order Parameters

### 2.4.1 Hard Spheres

As in previous crystal nucleation simulations of hard spheres<sup>40,41</sup>, we use the size of the largest translationally ordered cluster as the reaction coordinate. We use  $q_6$

Steinhardt<sup>50</sup> order parameter defined as follows: For every particle  $i$ , the local bond order parameter,  $q_{l,m}(i)$  is defined by

$$q_{l,m}(i) = \frac{1}{N_b(i)} \sum_{j=1}^l Y_{l,m}(\theta_{i,j}, \phi_{i,j}) \quad (27)$$

where  $N_b(i)$  is the number of neighbors of particle  $i$ ,  $Y_{l,m}(\vartheta, \phi)$  are the spherical harmonics,  $\vartheta_{ij}$  and  $\phi_{ij}$  are polar and azimuthal angles between particle  $i$  and its neighbor  $j$  respectively,  $l$  is the symmetry index and the value of  $m$  ranges from  $-l$  to  $l$ . In this work we use  $l = 6$ . The neighbors of particle  $i$  are those particles which are within the cutoff distance  $r_c = 1.4\sigma$  of particle  $i$ . The translational-order correlation between particle  $i$  and its neighbor  $j$ ,  $d_6(i, j)$  is given by:

$$d_6(i, j) = \frac{\sum_{m=-6}^6 q_{6,m}(i) q_{6,m}^*(j)}{\left(\sum_{k=-6}^6 |q_{6,k}(i)|^2\right)^{\frac{1}{2}} \left(\sum_{l=-6}^6 |q_{6,l}(j)|^2\right)^{\frac{1}{2}}} \quad (28)$$

where the asterisk (\*) denotes the complex conjugate. Two particles  $i$  and  $j$  are defined as translationally connected if  $d_6(i, j) > 0.7$ . A particle with at least 7 translational connections is classified as translationally ordered or solid-like. Solid clusters are identified by the condition that any two solid-like particles within the  $r_c$  belong to the same cluster. The tunable parameters in such order parameters need to be optimized using criteria described in prior studies<sup>8,41</sup>.

## 2.4.2 Gyrobifastigia

We found that the Steinhardt order parameters were not effective to capture the local translation symmetry present in the ABCD cubic lattice formed by GBFs<sup>4</sup>. Hence, we devised an orientational order parameter that proved to be suitable to capture the inherent crystal symmetry. It is based on the observation that in the crystal lattice all constituent particles have their long axes aligned. We can then define an orientational order correlation or a ‘dot-product’ similar to  $d_6$  as follows. For a given pair of neighboring particles  $i$  and  $j$  (i.e., within the cutoff distance  $r_c = 1.4a$ , where  $a$  is the side length of GBF), we define the orientational order correlation  $d_z(i, j)$  as:

$$d_z(i, j) = |z(i) \cdot z(j)| \quad (29)$$

where  $z(i)$  and  $z(j)$  are unit vectors pointing along the long axis of particles  $i$  and  $j$ .  $d_z(i, j)$  is essentially the magnitude of the cosine of the angle included between the two axis vectors, and hence varies from zero to 1 for orthogonal to aligned configurations, respectively. Note that the correlation is unaffected by whether the vectors are flipped  $180^\circ$  and the operation is commutative. Particles  $i$  and  $j$  are considered orientationally correlated if  $d_z(i, j) > d_{z,min} = 0.95$ , implying a  $\sim 18^\circ$  tolerance from perfect alignment. If a given particle has at least 4 aligned neighbors, it is considered solid-like. If two solid-like particles are orientationally correlated, then

they belong to the same cluster. The size of the largest orientationally ordered cluster is used as the reaction coordinate for the nucleation process.

### 3 Results and Discussion

#### 3.1 Nucleus-size Pinning for Hard Spheres

To validate the NSP method for a well-studied system, we apply it to hard spheres. The free energy barriers  $\Delta G^*$  for disorder to order transition for HS have been determined via a variety of methods such as US<sup>40</sup> and seeding<sup>67</sup>. Thus, our first objective was to test the barriers and critical nuclei sizes found by NSP by comparison with those reported in literature. The results for various target nuclei sizes are tabulated in Table 2 and shown in Figure 1(a). It can be seen that the NSP-estimated values provide a good interpolation to the reported estimates, hence showing a suitable consistency with prior data. It typically takes 5-6 iterations to obtain convergence within one percent relative error in the pressure value.

For  $N_t = 1300$ , the convergence of the algorithm was tested with different initial guesses for pressure (one higher and one lower than the reported value) as shown in Figure 1(b). The values obtained from either direction are asymptotically convergent. In practice, one may stop iterations as successive values are within the desired tolerance, and yet the estimates from the different starting points may differ by a non-negligible amount. This is possible if the profile is relatively flat (i.e., the corresponding Zeldovich

factor is low). Convergence to a narrower range of  $p^*$  could be improved by using a weaker biasing potential that can better resolve weaker slopes near the top of the barrier.

**Table 2:** Nucleus-size pinning for hard spheres.  $N$  is the total number of particles in the system,  $N_t$  is the target seed size, and  $p_i$  is the initial guess of the critical pressure (whose converged value is  $p^*$ ) and  $\kappa$  is the strength of the biasing potential as described in Eq. (22).

$N$	$N_t$	$p_i$	$\kappa$	$p^*$
55183	400	14	0.005	14.42
55183	600	14	0.0005	14.066
55143	800	14	0.0005	13.783
55116	1300	12.5	0.0005	13.37
55116	1300	14	0.0005	13.42

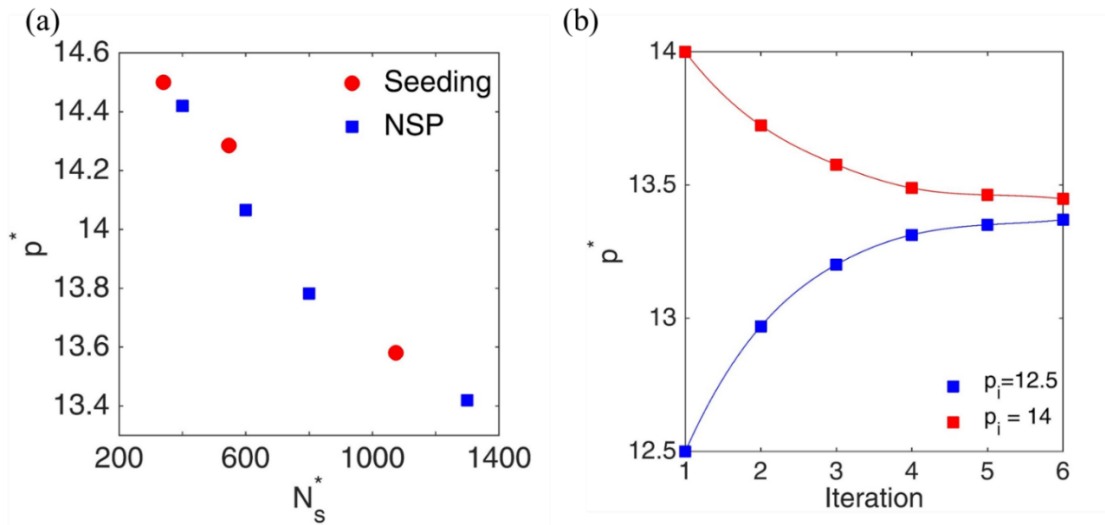


**Figure 2:** Nucleus-size pinning simulation results for hard spheres. (a) critical nucleation pressures ( $p^*$ ) for various critical nucleus sizes  $N_s^*$  as determined by NSP (blue) and by the seeding method of Espinosa et al.<sup>67</sup> (red). (b) Convergence towards the critical pressure for a target critical nucleus size of 1300 for different initial pressures of 12.5 (blue) and 14 (red). The values asymptotically converge towards a common critical pressure value, with the last step correction on each run being less than  $\Delta p^* \sim 0.02$ .

The associated free energy barriers can be calculated using equation (9), which shall be in agreement with reported results for seeding<sup>67</sup>. These estimates will become increasingly accurate for lower DSS as the critical nucleus becomes larger and the system approaches the macroscopic phase properties as assumed in the CNT approach.

### 3.2 Gyrobifastigia

#### 3.2.1 Umbrella Sampling

We performed US calculations to generate reference results for the crystal critical nucleus size ( $N_s^*$ ) and free-energy barrier ( $\beta\Delta G^*$ ) of GBF to test the predictions of NSP

(for  $N^*$ ) and its combination with the CNT (for  $\beta\Delta G^*$ ). These simulations generate the complete free energy profile along the reaction coordinate, from which one can readily obtain  $N_s^*$  and  $\beta\Delta G^*$ .

The results from US are tabulated in Table 2. Figure 2(a) shows the estimated free energy profiles for GBFs at various pressures. Figure 2(b) shows a comparison of nucleation barriers for GBFs and hard spheres<sup>41</sup>. It is observed that for the same DSS value GBF has a much higher  $\beta\Delta G^*$  than hard spheres. These large  $\Delta G^*$  for GBF may be due to the tendency of neighboring particles to pack in configurations that, while minimizing excluded volume<sup>83</sup> and maximizing packing entropy,<sup>53</sup> are inconsistent with the final ABCD crystal structure of GBFs. For example, two particles may tend to match their square facets while maintaining their long axes at a  $60^\circ$  angle (Figure 2(d)), excluding a volume (to other particles) larger than that in the ABCD lattice where the particle long-axes align (Figure 2(c)). Such misaligned configurations can lead to ‘dead ends’ in the nucleation pathway and require particles to first disassemble to further progress towards the crystalline global order<sup>59</sup>. Such poisoning can even preclude nucleation as is the case in the isotropic-nematic transition of colloidal rods;<sup>84</sup> we speculate that the coupling of orientational and translational order in GBFs helps the system overcome similar local configurational traps. Particle-alignment defects near the crystal interface likely increase the interfacial tension; in fact, our estimates shown in Fig. 8 in the Appendix indicate that  $\gamma$  of GBFs is nearly twice larger than that of hard

spheres. In addition, since for a given size, an aspherical seed has an associated larger surface area, a larger effective interfacial contribution to the free energy, and a higher barrier height would also be expected. Since estimating larger  $\beta\Delta G^*$  via US or another standard simulation method becomes more challenging, its calculation for GBFs for DSS =  $\beta\Delta\mu < 0.5$  would be an especially suitable application for the NSP method.

**Table 3:** Results for barrier height ( $\beta\Delta G^*$ ) and critical nucleus size ( $N_s^*$ ) from umbrella sampling (US) calculations for gyrobifastigia for various pressures ( $p$ ), along with their corresponding degrees of supersaturation ( $\beta\Delta\mu$ ).

Reduced Pressure ( $p$ )	DSS ( $\beta\Delta\mu$ )	$\beta\Delta G^*$	$N_s^*$
12.5	0.684	73.0	252
13	0.873	46.1	153
14	1.244	19.0	48
15	1.608	8.6	27

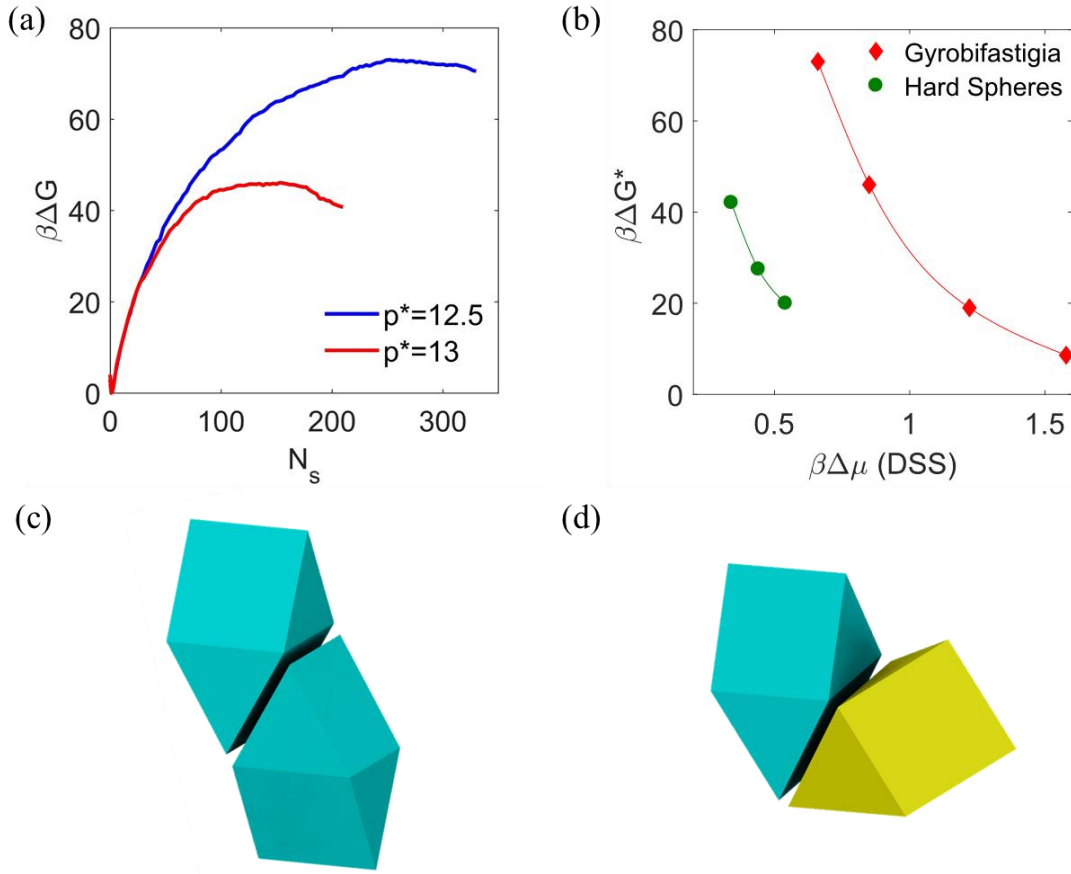


**Figure 3:** Nucleation free-energy barriers for gyrobifastigia using umbrella sampling. (a) Representative estimated free energy ( $\beta\Delta G$ ) vs. nucleus size ( $N_s$ ) (for different pressures ( $p^*$ )). (b) Nucleation barriers  $\beta\Delta G^*$  for gyrobifastigia (diamonds) and for hard spheres<sup>41</sup> (circles) at various DSSs. Configurations of gyrobifastigia particle pairs in (c) the ABCD crystal, and (d) a non-crystalline high local packing entropy state<sup>53,59</sup>.

Interestingly, the morphology of the nuclei formed for GBF is significantly aspherical as shown in Figure 3(a). This behavior likely stems from the difference in interfacial energies of the nucleus along directions parallel to the particles' long axes and perpendicular to it. A feature emerging out of the geometry of GBF lattice is that the

facets of the anisotropic nucleus are slanted at an angle of  $\tan^{-1}(2\sqrt{3}) \approx 73.9^\circ$  as revealed in Figure 3(a, inset).

We also investigated how the shape anisotropy of the crystal nucleus evolved as it grew beyond its critical size. While the nucleus aspect ratio could increase indefinitely with size to become filamentous in shape, it was conjectured that it maintained a quasi-octahedral shape, based on the characteristic slant of the nucleus facets. To test this conjecture, we simulated the growth of a post critical nucleus up to a size of  $N_s \approx 8000$  (over 50 times its critical size) at which point local features are smoothed out and macroscopic behavior could be considered emergent. We observed that the shape anisotropy persists even for such large nuclei and the aspect ratio remains about the same (Figure 3(b)). The presence of a nearly invariant nucleus geometry validates the use of the CNT equation (9) to estimate  $\Delta G^*$ . We thus estimate  $\Delta G^*$  from the known critical nucleus sizes (from US) using equation (9); the results and their error bars are shown in Figure 4. We find that CNT tends to overestimate  $\Delta G^*$  by a relatively constant deviation of  $\sim 10k_B T$  but the *relative* deviations decrease as DSS is reduced. These trends are expected, as the nuclei tend to have larger size for lower DSS and hence approach the macroscopic limiting behavior that CNT assumes. Note that one could use a  $\Delta G^*$  value obtained from US, ideally corresponding to large  $N_s^*$  (and small  $\Delta \Omega$ ), to fine-tune the order parameter definition (i.e., parameters  $r_c$  and  $d_{z,min}$  in Section 2.4.2) until the  $N_s^*$  calculated in the US simulation agrees with the  $N_s^*$  calculated via the CNT Eq. (9).

While in this way the US and CNT curves in Fig. 4 would be brought in closer agreement, this would not necessarily provide an independent test of the quality of the order parameter or of the general applicability of CNT.<sup>41</sup> Regardless of such refinements,  $\Delta G^*$  estimates from the critical nucleus size [via Eq. (9)] are expected to have large uncertainties for smaller nucleus sizes (when errors in estimates of interfacial particles can contribute significantly to the nucleus size) and become increasingly accurate as lower DSS values (and hence larger cluster sizes) are probed.

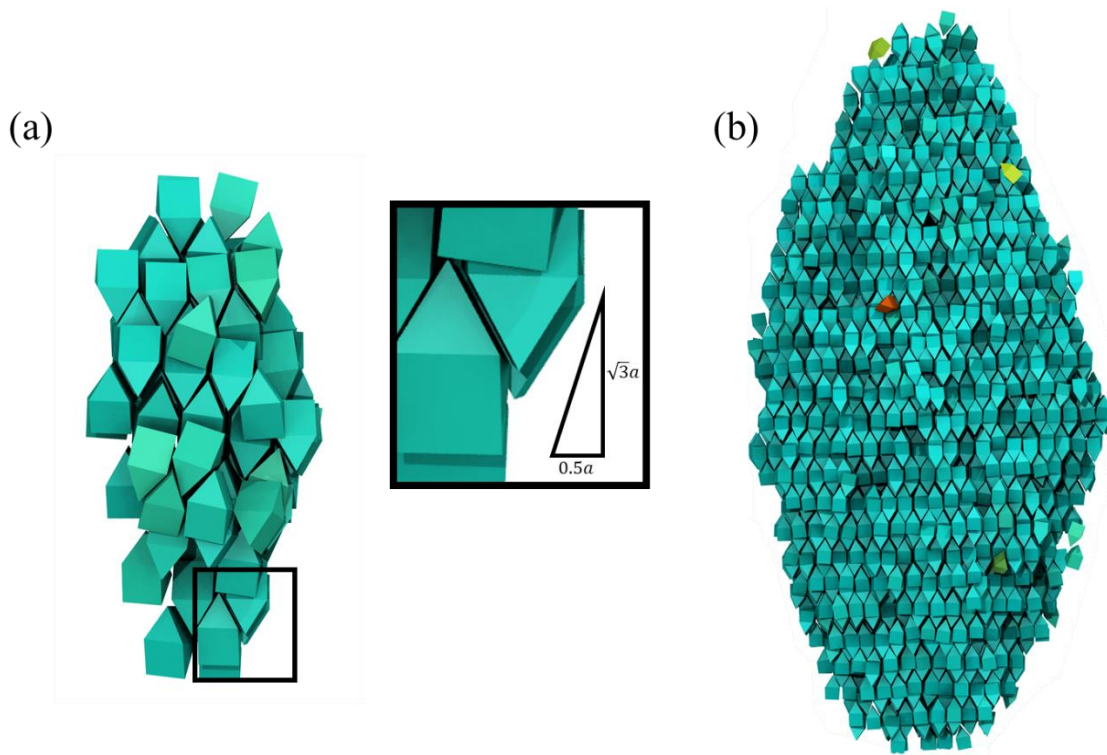


**Figure 4:** Morphology of nuclei for gyrobifastigia. (a) Near-critical nucleus ( $N_s^* \approx 150$ ) obtained by umbrella sampling at  $p^*=13$ , evidencing its aspherical, elongated shape along the particle long-axis. Inset: The nucleus is approximately faceted at a specific angle =  $\tan^{-1}(2\sqrt{3})$ . In the inset  $a$  is the side length of a gyrobifastigium. (b) A quasi-octahedron shaped (post-critical) nucleus corresponding to  $N_s \approx 8000$ . Particles are colored according to the deviation from the director of the nucleus – from blue to red as the alignment decreases.

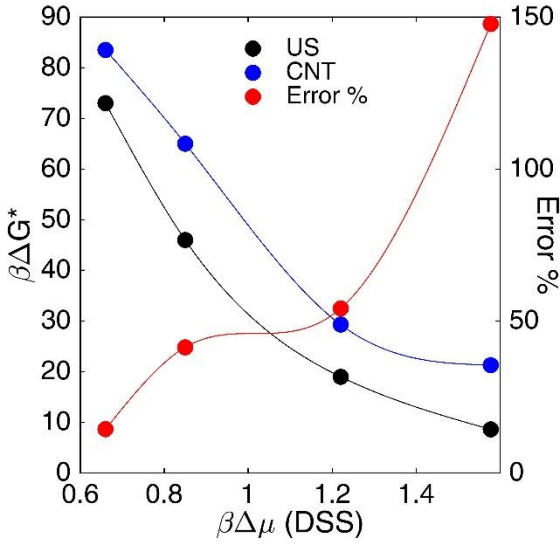


**Figure 5:** Comparison of CNT-estimated nucleation barriers ( $\beta\Delta G^*$ ) with those calculated using umbrella sampling (US) as a function of degree of supersaturation (DSS). The CNT values are obtained using equation (9) by inputting  $N_s^*$  values from umbrella sampling.

### 3.2.2 Nucleus-size Pinning for Gyrobifastigia

Having established the presence of anisotropic solid nuclei and the applicability of the CNT to GBF in the previous section, we now demonstrate how the NSP method can be implemented as an alternative and complement to US to study the shape and size of the critical nuclei, and to estimate nucleation barriers. The simulations were performed for a range of nucleus sizes that overlaps and extends beyond the upper bound explored before using US. The results are shown in Table 3. As shown in Fig. 5(a), the relationship between critical nucleation pressure and  $N_s^*$  as determined by NSP agrees well with that obtained from our US calculations performed earlier. Similarly, Fig. 5(b) shows that NSP

with CNT produces free-energy barrier heights which slightly overestimate those found by US, as was earlier observed (in Figure 4).

**Table 4:** Results from nucleus-size pinning method for GBF

$p_i$	$N$	$N_t$	$\kappa$	$p^*$	DSS = $\beta\Delta\mu$	$\beta\Delta G^*$
14	3373	100	0.01	13.34	0.977	48.875
11.5	1666	100	0.05	13.35	0.9813	49.065
14	1664	50	0.05	13.9004	1.1844	29.61
14	3373	150	0.01	12.9083	0.8155	61.163
14	3344	300	0.01	12.41	0.6275	94.125
14	3334	500	0.005	12.1205	0.5149	128.725

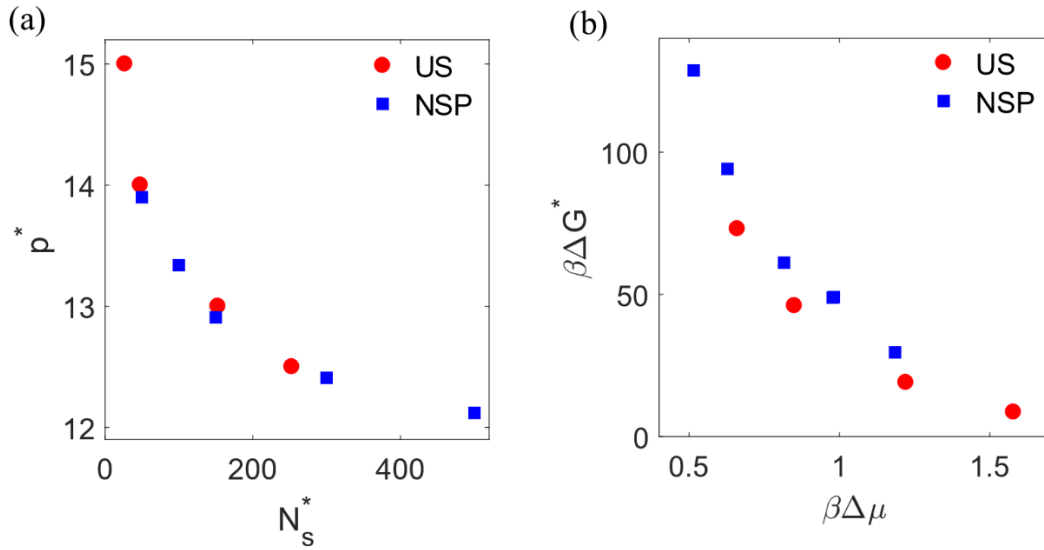


**Figure 6:** Comparison of NSP (blue) and umbrella sampling (US, red) for GBF (a) Comparison of critical conditions:  $p^*$  and  $N_s^*$  are the critical pressure and nucleus size, respectively. (b) Comparison of free energy barrier heights values ( $\beta\Delta G^*$ ) as a function of degree of supersaturation ( $\beta\Delta\mu$ ).

The converged values obtained from iterations started from different initial pressure guesses were quite close in the cases examined, presumably due to a sharper peak of the free energy profile as compared to the calculations for hard spheres discussed in Section 3.1. Since there is no constraint on the shape of the nucleus but only on its size, its shape should eventually tend to the ‘natural’ one. Indeed, Figure 6 shows that the shape of the GBF nuclei as determined by NSP have geometries consistent with those found earlier via US, becoming increasingly quasi-octahedron like as the size increases and having an aspect ratio of  $\sim 2$  (found from the principal moments of the nucleus inertial tensor, as a ratio of longest axis to the mean of the shorter ones). This aspect ratio would slightly increase for much larger nucleus sizes (it is still 2.1 for the one in

Fig. 3(b)) if the aberrations at the top and bottom vertices of the quasi-octahedron were to smooth out.

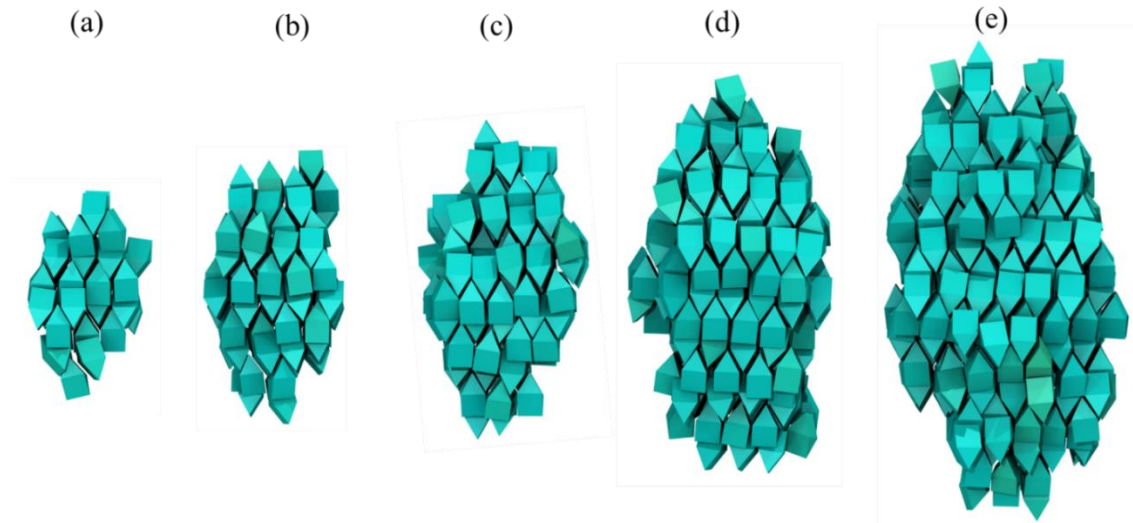


**Figure 7:** Various critical nuclei of GBF as obtained using the NSP method for  $N_s \approx$  (a) 50, (b) 100, (c) 150, (d) 300, and (e) 500, with aspect ratios close to 2.0 (1.9, 2.0, 1.9, 2.0, and 2.1 respectively). Particles are colored as in Fig. 3.

#### 4 Conclusions

In this study we introduced the nucleus-size pinning (NSP) method which, as an extension of the seeding technique<sup>67</sup>, is designed to iteratively converge to the critical state in a nucleation process. We first validated the method by reproducing the known results for hard spheres. We then demonstrated the robustness of the method by identifying non-trivial anisotropic growth of nuclei during disorder-to-order transition

in gyrobifastigia. By combining NSP with a formulation of classical nucleation theory that allows the treatment of an aspherical nucleus, we were able to determine nucleation barriers for gyrobifastigia in a range of small DSS where conventional methods would be very computationally expensive. The method allows the 'natural' seed geometry to be attained and the critical state to be readily identified, as demonstrated here for gyrobifastigium. The proposed method may even prove useful in studying the transition state in situations where a global order parameter rather than a local order parameter (as in classical nucleation) is used to describe the phase transition process. The proposed NSP approach can be easily applied to other systems for the determination of the critical states provided suitable order parameters are employed. For example, applications should be readily implementable to nucleation processes where the degree of metastability (or DSS) is defined by departures of temperature (as opposed to pressure) from the coexistence conditions. Moreover, NSP can help reveal important microstructural features of transition states, which might be non-trivial to hypothesize a-priori. Altogether, NSP provides a means to effectively and unambiguously target the simulation of the critical transition state in a nucleation process, one that complements existing rare event sampling techniques. The iterative process can be further automated such that the equilibration (at each iteration step) is checked via statistical tests for normality<sup>85</sup> and by pre-specifying a tolerance for global convergence.

While the NSP method provides a more robust way for establishing the conditions for cluster criticality than the traditional seeding approach, it retains certain limitations. First, it requires a valid model (such as CNT) to relate critical nucleus size to the nucleation free-energy barrier. Only in the presence of an applicable model can we determine other properties of interest such as interfacial energy. Nevertheless, even in the absence of such a model, the method is still able to describe the critical nuclei at different DSS, whose characterization may be of interest in various context, e.g., to identify differences in structural order between the core and interfacial regions of potential configurational bottlenecks associated with transition states<sup>33,34,86</sup>. Second, the convergence of the algorithm is dependent upon the ‘flatness’ of the target free energy profile. If there is a broad region (in comparison to the spread of the biasing harmonic potential) with nearly constant free energy around the barrier top, then the method can end up identifying any of those states as the critical one (within a user-specified tolerance). Note, however, that such flat barrier tops would pose challenges to many simulation methods and entail an intrinsic ambiguity to the definition of the critical nucleus. Third, and in common with other methods (like umbrella sampling), NSP requires the use of order parameters that are a good approximation to the reaction coordinate that best describes the transition process<sup>39</sup>. In fact, the choice of nucleation order parameter (e.g., the criteria to decide which particles are solid-like) affects not only the effective height of the free-energy barrier but also its flatness (as pertaining to

the second limitation listed before). Finally, variants of the NSP method can be implemented to improve the convergence of the iterative scheme, e.g., to more explicitly account for the dependence of interfacial free energy on supersaturation conditions (as discussed in the Appendix).

## 5 Acknowledgements

Funding support from NSF award CBET-1402117 is gratefully acknowledged. The authors are grateful to Prajwal B. Prakash and Unmukt Gupta for valuable discussions and sharing base simulation code.

## 6 Appendix: Interfacial Contribution to Free Energy Derivative

In Section 2.2 we assumed that the interfacial-energy contribution to the slope  $C_A$  in Eq. (16) can be neglected for small changes in pressure  $\Delta p^* < 1$ , an assumption which is consequential to the convergence properties of the NSP iterations to the critical conditions, but not to the final results. We note that this assumption is consistent with earlier studies that found the variation of interfacial energy ( $\gamma$ )  $\Delta\gamma$  to be small (i.e., less than 5%) for changes  $\Delta p^* < 1$ ,<sup>67</sup> and that in NSP iterations the usual step corrections in pressure are much smaller than  $\Delta p^* < 0.5$ . Nevertheless, in this section we re-examine this assumption by first rearranging Eq. (14) to obtain the interfacial contribution to the slope ( $S_i$ ) as:

$$S_i = \frac{d\phi_i}{dN_s} = S_T - (\mu_{solid} - \mu_{liquid}) = S_T - \Delta\mu_{sl} \quad (A1)$$

Thus, for a simulation performed at a given pressure, Eq. (A1) can be used to evaluate  $S_i$ , the interfacial contribution to the slope (note that this involves a contribution from interfacial tension and from nucleus geometry, either of which may vary with pressure). One such evaluation is illustrated in Table 4 and Fig. 7 for a series of iterations in case of hard spheres for a target cluster size of  $N_t = 1300$ :

**Table 4:** Calculation of interfacial contribution to the slope from data of total slope and chemical potential difference for various iterations of NSP for hard spheres with  $N_t = 1300$ .

Iteration	$p_i$	$\Delta\mu_{sl}$	$S_T$	$S_i$
1	14.00	-0.235	-0.054	0.180
2	13.72	-0.207	-0.029	0.178
3	13.58	-0.193	-0.017	0.176
4	13.49	-0.184	-0.005	0.179
5	13.46	-0.181	-0.003	0.178
6	13.45	-0.180	-0.003	0.178
7	13.44	-0.179	-0.003	0.176
8	13.42	-0.177	0.001	0.179

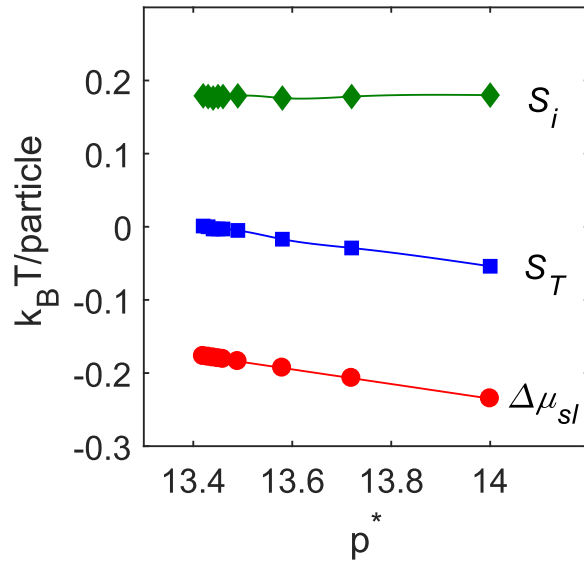


**Figure 7:** Key contributions to the variation of the slope  $S_T$  of the free energy as a function of pressure. The interfacial contribution  $S_i$  is nearly constant.

It can be seen in Fig. 7 that the major contribution to the variation of the total slope ( $S_T$ ) is through the variation of  $\Delta\mu_{sl} = DSS$ , while the interfacial contribution remains nearly constant  $\sim 0.178$ , consistent with the assumption of Eq. (16).

Alternative implementations of the NSP could explicitly take into account the variation of  $\gamma$  with pressure. For instance, one can use the known values of  $S_i = \frac{d\phi_i}{dN_s}$  at two or more nearby pressures (from the iterative steps) to obtain an extrapolation model  $S_i = S_i(p^*)$  and use such a model to improve the estimate of  $p^*$  for the next iteration.

As a related extension, we note that the NSP method and CNT can also be combined to extract the interfacial tension  $\gamma$  from  $S_i$ . Assuming for concreteness that the nucleus is

spherical, then  $k_A = \gamma \left( \frac{36\pi}{N_t \rho_S^2} \right)^{\frac{1}{3}}$  and  $S_i = \frac{2k_A}{3N^{\frac{1}{3}}}$ , from which it follows that:

$$\gamma = S_i \left( \frac{3N_t \rho_S^2}{32\pi} \right)^{\frac{1}{3}} \quad (\text{A2})$$

Equation (A2) can be used to estimate  $\gamma$  at successive steps in the NSP iteration process, as shown in Figure 8(a) for hard spheres. The results are in line with what has been reported in prior studies using other techniques<sup>40,67,87,88</sup>. The intermediate calculations, however, may be less reliable than that for the converged critical condition as a CNT fit may be more suitable near the top of the free-energy barrier than away from it<sup>40</sup>. Similar calculations for  $\gamma$  could be performed for aspherical nuclei, perusing explicit expressions for volume and surface area of a nucleus of known geometry. For example, for GBF if we approximate the nuclei as a prolate spheroid with an aspect ratio  $\sim 2$  (see Figure 6), the interfacial tension can be written as:

$$\gamma = \frac{S_i}{\frac{4\pi}{3\sqrt{3}}+1} \left( \frac{3N_t \rho_S^2}{8\pi} \right)^{\frac{1}{3}} \quad (\text{A3})$$

In the reduced units employed,  $\gamma$  values for GBFs (Fig. 8(b)) appear to be larger than those for hard-spheres (Fig. 8(a)) for comparable DSS, a difference that correlates with the difference in free energy barrier heights shown earlier in Fig. 2(b). The intermediate-

step  $\gamma$  estimates using this approach are also shown in Fig. 8(b). Note, however, that isolating an average, crystal-facet independent  $\gamma$  for the GBF nucleus, should be seen as rather approximate calculation, especially for small nuclei (large  $p^*$ ) where their shape may depart vastly from a spheroid (possibly causing the non-monotonous trend for  $p^* > 13$ ). Further, the errorbars were found to be rather large, i.e.,  $\sim \pm 0.05$  for the initial pressure  $p^* = 14$ , which should be representative of those of nearby points where equilibration was less converged. Within errorbars then, the data available does not allow us to ascertain whether for  $p^* > 13$  the  $\gamma$  trend is non-monotonous or simply approaches a plateau.

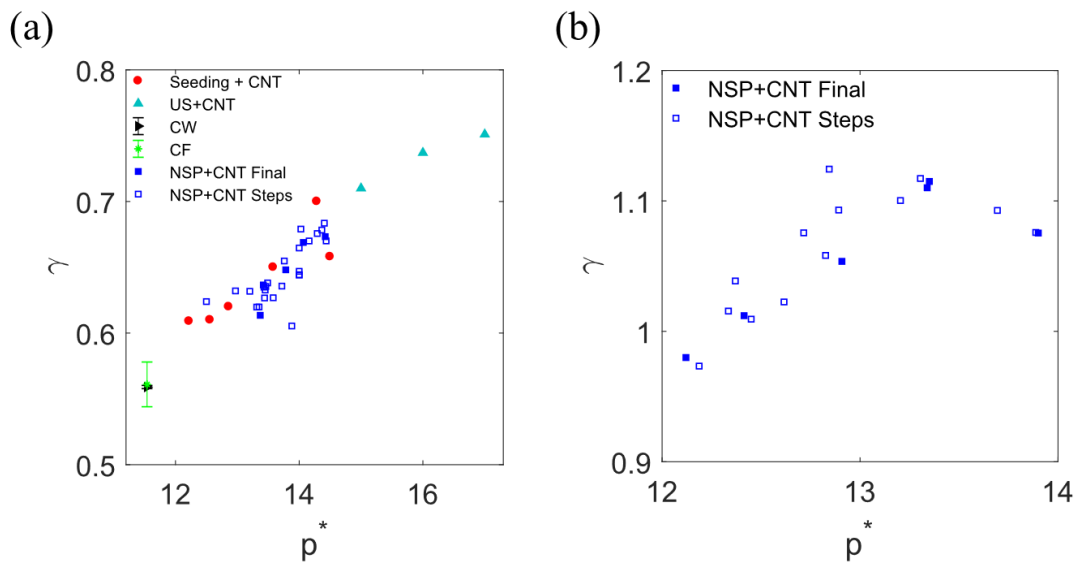


**Figure 8:** Interfacial tension ( $\gamma$ ) vs. pressures ( $p^*$ ) from various simulation methods. (a) Hard spheres, comparing NSP +CNT results for (converged) final pressure values and intermediate step values (excluding the first iteration), seeding method<sup>67</sup>, US+CNT<sup>40</sup>, cleaving walls (CW) approach<sup>88</sup>, and capillary fluctuation (CF) method<sup>87</sup>. (b) GBFs for NSP+CNT results.

Finally, once we have an estimate for  $S_i$ , and hence  $k_A$ , we can estimate  $N_S^*$  for the corresponding pressure using Eq. (8). Note that we can apply such a CNT-based approach to the estimate  $N_S^*$  in a single simulation, irrespective of whether convergence to the critical condition has been reached. We tested this idea in Fig. 9 for hard spheres and GBF, by comparing the NSP+CNT based estimates of  $N_S^*$  from intermediate steps and from the converged values and with data from other methods. We observe a good agreement in the results among the various techniques, suggesting that the validity of CNT for the systems under study.

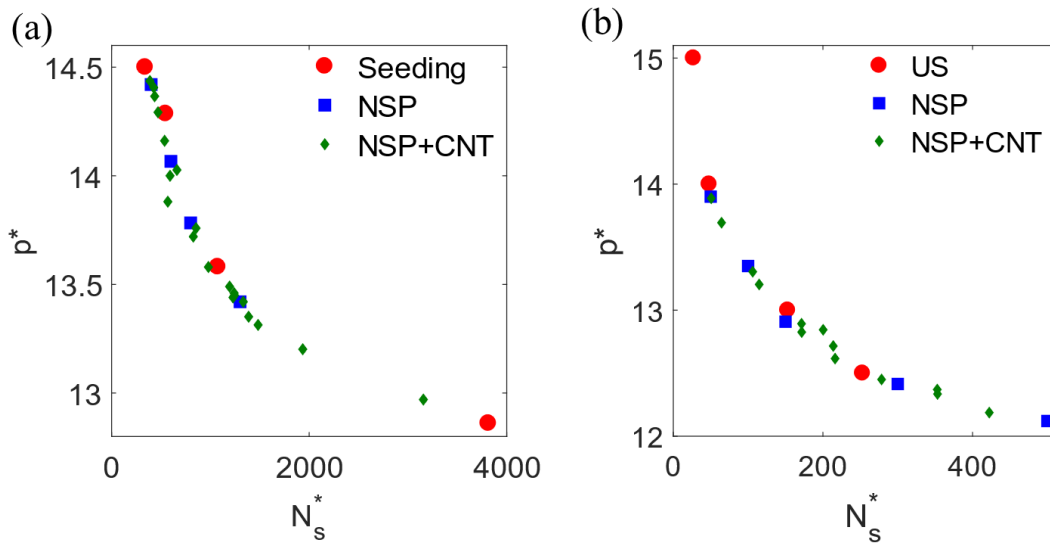


**Figure 9:** Comparison of estimates of critical conditions in the pressure ( $p^*$ ) vs. nucleus size ( $N_s^*$ ) plane, obtained from: Seeding<sup>67</sup>, US = Umbrella sampling, the NSP described in the main text, and the NSP+CNT approach described in Appendix. (a) Hard spheres. (b) Hard gyrobifastigia.

## CHAPTER 3: DISORDER FORESHADOWS ORDER IN COLLOIDAL CUBES

Abhishek K. Sharma and Fernando A. Escobedo\*

Robert Frederick Smith School of Chemical and Biomolecular Engineering,

Cornell University, Ithaca, NY 14853

### Abstract

Monte Carlo simulations are used to investigate the mechanism of the disorder-to-order phase transition for a bulk system of colloidal hard cubes. It is observed that the structure of the ordered state is foreshadowed in the disordered state through multiple spontaneously occurring ordered domains. Such domains arise due to the entropic preference for local facet alignment between particles and occur transiently and sparsely throughout the system even in the stable isotropic phase. At pressures (and degrees of supersaturation) where the isotropic phase becomes marginally metastable, a classical nucleation process is never observed; instead, the ordered domains increase in number and size, eventually reaching a critical point where they percolate the entire system and spontaneously consolidate to form the ordered phase. The critical number of particles and the per particle free energy barrier both decrease with pressure. Using

---

\* Email: fe13@cornell.edu

the total number of locally ordered particles as a global order parameter, it is predicted that for large systems the ordering transition would only be spontaneous above a critical pressure. Finally, a test designed to probe the ability of the system to favor a single monodomain solid from initially misaligned ordered domains, reveals that an active interdomain zone mediates the concerted reorientation of particles.

## **1 Introduction**

Microscopic colloidal particles can self-assemble into complex meso-scale structures<sup>89</sup> whose characteristics are dictated by individual features of the particles such as size, shape, and specific inter-particle interactions<sup>90</sup>. With recent advances in our ability to synthesize nanoparticles with precise control over those individual features, a concurrent interest has bloomed to understand the design principles to engineer desired behaviors out of such customized components.<sup>91</sup> Not only can such a design be of practical importance, but it can also reveal general principles about the way how naturally occurring systems self-assemble into exquisitely complex microstructures.<sup>92</sup>

It has long been known that entropic effects<sup>93</sup> alone can result in the self-assembly of hard spherical particles into a close-packed lattice.<sup>55</sup> Oblong hard particles and rods, which possess additional orientational degrees of freedom, result in the formation of different ordered states such as nematic phases with aligned particles, where the loss of orientational entropy is compensated by a gain in translational entropy<sup>83</sup>. A further

level of particle shape complexity has been explored by considering faceted particles such as polyhedra<sup>4,94</sup>, where their additional orientational degrees of freedom can lead to the formation of different types of crystals and *mesophases* (thus called for they are neither completely disordered (*isotropic*), nor completely ordered (*crystal*)). To control the emergence of these phases in polyhedral systems<sup>6,7</sup> it is important to study and characterize not only their thermodynamic behavior but also the mechanisms underlying disorder-to-order phase transitions. Similar to hard spheres,<sup>40,42</sup> the transitions involved are often first order transitions,<sup>10</sup> comprising nucleation and growth of the incipient phase from a metastable mother phase. Recent studies<sup>8,53,59</sup> have revealed several design rules for engineering the particle shape to control the ease of self-assembly. For example, it was observed<sup>8</sup> that for several polyhedra with small asphericity and high rotational symmetry, translationally-ordered rotator phases nucleate from the disordered state with a smaller free-energy barrier than that observed for hard spheres at a comparable degree of supersaturation. This effect was attributed to the presence of productive correlations between local orientational order and translational order, which catalyze the isotropic-to-rotator phase transition. Recently, it was reported<sup>59</sup> that even though similar local fluctuations in orientational order are ubiquitous for other polyhedral shapes, their effect is only catalytic when the final ordered phase comprises configurations with extensive facet alignment between neighboring particles. This is because the excluded volume for a pair of neighbor faceted

particles tends to be minimized, and the local packing entropy maximized, if their facets align. Because such high local entropy configurations spontaneously occur in the disordered phase, systems whose solid phase exhibits high facet alignment (like truncated octahedra and rhombic dodecahedra) will tend to have lower transition free energy barriers than systems whose solid phase exhibits no such facet alignment (like octahedra). In fact, the latter systems will even tend to have higher transition free energy barriers than hard spheres since the spontaneously occurring facet aligned configurations in the isotropic phase are counterproductive toward forming the solid phase. Thus, the extent of “coherence” between local vs. global packing tendencies of such polyhedral systems during phase transition can lead to facilitated or impeded self-assembly.

In this work, we explore the disorder-to-order transition mechanism of hard cubes, an archetypal case of a system that exhibits strong coherence between local and global packing tendencies during ordering. Because hard cubes have equal facets and the ordered phase entails perfect facet alignment, it is expected that cubes would be one of the easiest systems to self-assemble. Cubes have been shown to possess an interesting phase behavior (see Fig. 1) with a disordered liquid phase at low pressure, a simple cubic crystal at high pressures, and a cubic mesophase in-between that merges continuously with the crystal phase.<sup>4</sup> This cubic mesophase could be seen as a state where the crystal phase contains a high concentration of mobile vacancies; in fact such

vacancies have been described as key contributors to the crystal stability,<sup>95</sup> and to result in diffusivities that are much larger than those of typical solids. For simplicity, we will henceforth refer to such mesophase state as ‘solid’ or ordered phase.

The rest of the paper is organized as follows. In Section 2, we explain our model, simulation methods, and analysis techniques including the order parameters used to track the progress of the transition. In Section 3.1, we analyze what happens when the isotropic phase spontaneously transitions into the crystal phase, revealing that a significant portion of the isotropic phase has particles that are in a locally ordered configuration. In Section 3.2 we further characterize the phase transition using umbrella sampling to determine the free energy barriers associated with different degrees of metastability of the disordered phase. In Section 3.3 we describe a computer experiment intended to illustrate the ability of cubes to resolve grain boundary conflicts through cooperative rearrangements. Finally, in Section 4 we provide our concluding remarks.

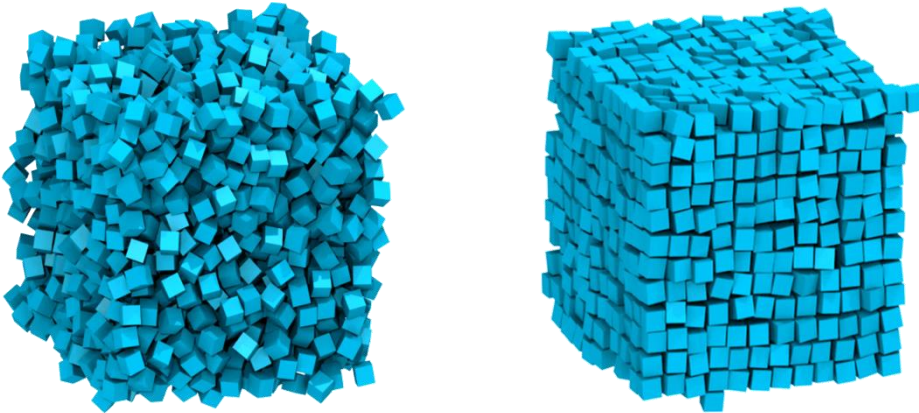


**Figure 8:** Sample snapshots of the disordered (left) and ordered (right) phases in hard cubes near the disorder-order transition.

## 2 Methods

### 2.1 Model

For a given pair of cubes  $i$  and  $j$ , we use hard pair-potential given by:

$$U_{ij} = \begin{cases} 0 & \text{if no overlap} \\ \infty & \text{if overlap} \end{cases} \quad (1)$$

The overlaps between any two cubes are detected using the separating axis theorem.<sup>49</sup>

### 2.2 Metropolis Monte Carlo

Metropolis<sup>55</sup> Monte Carlo (MC) simulations were performed in an isothermal-isobaric (NPT) ensemble where the number of particles ( $N$ ), the pressure, and the temperature of the system were kept constant. As per the conventions used in our previous studies<sup>4</sup>,

the dimensionless pressure is  $p = \beta p_a a_c^3$ , where  $p_a$  is the actual unscaled pressure and  $a_c$  is the radius of the circumscribing sphere for a cube (for a cube of unit edge, it would be  $\frac{\sqrt{3}}{2}$ ) and  $\beta = 1/k_B T$  with  $k_B$  = Boltzmann constant. Simulations were conducted using periodic boundary conditions, and each MC cycle consisting of N translation, N rotation, and 2 isotropic volume moves. Each move was accepted based on the Metropolis acceptance criteria. For each pressure, at least  $3 \times 10^6$  MC cycles were performed. All simulations were performed in a cubic box, and all system sizes had a perfect cube number of particles. For our ensuing discussions, we take the order-disorder phase transition of hard cubes to take place at  $p = p_{co} = 4.0$  as estimated in literature<sup>95</sup>. We note, however, that this value is only referential as the effective  $p_{co}$  in simulation will depend on system size, given the non-negligible finite-size effects known to particularly affect the ordered phase<sup>95</sup>.

## 2.3 Order Parameters

### 2.3.1 $q_4$ local translational order parameter

We use the  $q_4$  Steinhardt<sup>34,50</sup> translational order parameter defined as follows: For every particle  $i$ , the local bond order parameter,  $q_{l,m}(i)$  is

$$q_{l,m}(i) = \frac{1}{N_b(i)} \sum_{j=1}^l Y_{l,m}(\theta_{i,j}, \phi_{i,j}) \quad (2)$$

where  $N_b(i)$  is the number of neighbors of particle  $i$ ,  $Y_{l,m}(\vartheta,\phi)$  are the spherical harmonics,  $\vartheta_{ij}$  and  $\phi_{ij}$  are polar and azimuthal angles between particle  $i$  and its neighbor  $j$ , respectively,  $l$  is the symmetry index and the value of  $m$  ranges from  $-l$  to  $l$ . In this work we use  $l = 4$  to characterize cubatic order, henceforth using the symbol  $q_4$  to refer to the collection of all 9 components ( $2l + 1 = 9$ ). The neighbors of particle  $i$  are those particles whose centers of mass are within the cutoff distance  $r_c = 1.4\sigma$  of particle  $i$ . The translational-order correlation between particle  $i$  and its neighbor  $j$ ,  $d_q(i, j)$  is given by:

$$d_q(i, j) = \frac{\sum_{m=-4}^4 q_{4,m}(i) q_{4,m}^*(j)}{\left(\sum_{k=-4}^4 |q_{4,k}(i)|^2\right)^{\frac{1}{2}} \left(\sum_{l=-4}^4 |q_{4,l}(j)|^2\right)^{\frac{1}{2}}} \quad (3)$$

where the asterisk (\*) denotes the complex conjugate.

### 2.3.2 $i_4$ local orientational order parameter

In order to study local orientational order, we use the  $i_4$  orientational order parameter<sup>52</sup> that captures the symmetry in orientations of cubes in the ordered phase. It is defined in a very similar manner as  $q_4$  but instead of using the bond orientation vectors between two neighboring particles it uses the angles associated with individual particle axes orientations. In its normalized form it is evaluated for a given particle  $j$  as:

$$i_{4,m}(j) = \frac{\sum_{n=1}^3 Y_{4,m}(\theta_n, \phi_n)}{\sqrt{\sum_{m=-4}^4 \left| \sum_{n=1}^3 Y_{4,m}(\theta_n, \phi_n) \right|^2}} \quad (4)$$

where  $Y_{4,m}(\theta_n, \phi_n)$  are spherical harmonics with symmetry index 4, and  $\theta_n$  and  $\phi_n$  are polar and azimuthal angles of the 3 particles axis  $n$  with respect to the reference coordinate frame. Analogous to translational order, the orientation correlation between two particles  $k$  and  $l$  is defined as:

$$d_i(k, l) = \sum_{m=-4}^4 i_{4,m}(k) \cdot i_{4,m}^*(l) \quad (5)$$

where the asterisk (\*) implies complex conjugate. While we primarily use  $d_i$  to detect local correlations of neighboring particles for most of our calculations, we also use it in Section 3.1 to obtain the orientation correlation function over distance,  $d_i(\mathbf{r})$ , which is the average value of  $d_i(k, l)$  over all pairs of particles  $\{k, l\}$  whose centers lie at a distance  $r$  from each other.

### 2.3.3 Labelling of ordered particles

The orientational order parameters  $i_4$  and  $d_i(k, l)$  are used to identify ordered particles; the rationale for this choice is discussed in the Results Section. Two particles  $k$  and  $l$  within the first neighbor cutoff distance  $r_c = 1.4a$  are defined as connected if  $d_i(k, l) > 0.7$ . A particle with at least 3 connections is classified as ordered or solid-like. Solid clusters are identified by the condition that any two solid-like particles within  $r_c$  belong to the same cluster. The tunable parameters for the order parameters are set using criteria described in prior studies<sup>8,41</sup> for discriminating the disordered and ordered states; details on these calculations are provided in the SI (Fig. S1).

### 2.3.4 $P_4$ global orientational order parameter

To obtain an overall measure of orientational order among  $N$  particles, we used global orientational order parameter,  $P_4$  defined as:

$$P_4 = \max_{\mathbf{n}} \frac{3}{14N} \sum_i P_4(\mathbf{u}_i \cdot \mathbf{n}) = \max_{\mathbf{n}} \frac{3}{14N} \sum_i (35 \cos^4 \theta_{i,n} - 30 \cos^2 \theta_{i,n} + 3) \quad (6)$$

where,  $\mathbf{u}_i$  is the unit vector along a relevant particle axis and  $\mathbf{n}$  is a director unit vector which maximizes  $P_4$  (see details in John *et al.*<sup>51</sup>) and  $\theta_{i,n}$  is the angle contained by  $\mathbf{u}_i$  and  $\mathbf{n}$ . The summation is performed over all three axes for all  $N$  particles. A value of  $P_4 = 1$  describes perfect orientational order.

### 2.3.5 Particle orientation scatter plot

Particle orientations can be visualized by plotting as dots on the surface of a unit sphere, the unit vectors corresponding to the orientation axes of all or a selected subset of particles in the system (see SI in Agarwal *et al.*<sup>4</sup> The resulting plot reveals how correlated (clustered dots) or uncorrelated (diffused dots) those particle orientations are; e.g., in the perfect cubic crystal, all orientations will fall within 6 mutually orthogonal spots on the sphere, while in a fully isotropic phase the orientation dots will appear uniformly spread out over the whole spherical surface.

## 2.4 Umbrella Sampling (US)

Umbrella sampling (US) simulations<sup>8</sup> were performed to determine free energy barriers for the ordering transition. The total number of ordered particles ( $N_{ordered}$ ) in the system was chosen to be a suitable reaction coordinate to describe the disorder-order transition, as preliminary results revealed that the solid phase did not emerge from a single nucleus but rather from multiple regions in the entire system. The transition path along  $N_{ordered}$  from the disordered to the ordered state was divided into overlapping equal-sized windows. The size of each window was varied depending on the conditions and the size of the system. Each window is simulated separately with reflective walls and  $N_{ordered}$  was recorded every 2 MC cycles. Reflective walls are implemented such that any trajectory leaving the window at the end of 2 MC cycles is returned to the configuration prior to those 2 MC cycles, which is counted again. Statistics obtained from each window are used to obtain relative free energies for the  $N_{ordered}$  states within a window. Finally, individual sections are stitched together by matching values in the middle of the overlap between successive windows, keeping the value for the most frequent state in the disordered phase as the reference (zero point) for the calculation of the free energy barrier  $\Delta G^*$  as described in earlier work.<sup>8,59,96</sup> Values of  $\Delta G^*$  are scaled with respect to  $k_B T$ . We also implemented a version of US that allows mapping the free-energy surface over two order parameters despite using only a single order

parameter to bias or ‘drive’ the simulations; this is done by concurrently bookkeeping a 2<sup>nd</sup> “passenger” order parameter,<sup>30</sup> as further detailed in the SI (Fig. S3).

### 2.5 Facet Alignment Measure

To quantify the degree of facet alignment between a pair of neighboring cubes  $i$  and  $j$ , the *facet alignment measure*  $\Delta(i, j)$  introduced in an earlier study<sup>59</sup> was employed. In essence,  $\Delta$  is the overlap area of the nearest interparticle facets (defined by the minimum centroid to centroid distance) when one is projected onto the other. This measure and its implementation have been described in detail in a previous study<sup>59</sup>.

## 3 Results and Discussion

### 3.1 Spontaneous Phase Transition

Defining the degree of supersaturation (DSS) as the difference in chemical potentials between the isotropic and the solid phase<sup>40</sup>, the disorder-to-order first-order phase transition is spontaneous and the disordered phase metastable when DSS is positive. Such transitions are often characterized as following the mechanism of nucleation and growth<sup>57,97</sup> at low DSS (less than  $2 k_B T$ <sup>96</sup>), eventually leading into a spinodal decomposition regime at very high supersaturation<sup>64</sup>. In this study, we are only considering cases where DSS is much less than  $0.1 k_B T$ , for which a nucleation mechanism would be expected.

Upon compression of an isotropic system with stepwise pressure increments (starting with  $p = 1$ ), we observe a spontaneous disorder-to-order transition at  $p = 4.07$ . The distribution of orientational and translational correlations is shown in Figure 2 as the transition progresses. The distributions of ordered and disordered particles are farther apart along  $d_i$  than along  $d_q$ , indicating that the orientational correlation is a better metric to discriminate between the two states. We observed that even at coexistence ( $p = 4.0$ ), there is a non-negligible fraction of particles that are significantly more correlated than most particles in the disordered phase and experience a local environment that is akin to that of the ordered state. This amount of locally ordered particles is uncommon among polyhedral systems; for example, in case of octahedra<sup>59</sup> the population of such particles is comparatively insignificant as seen in Fig. 3. Of course, any such comparison provides only a rough guide since the count of ordered particles depends on the order parameter used.

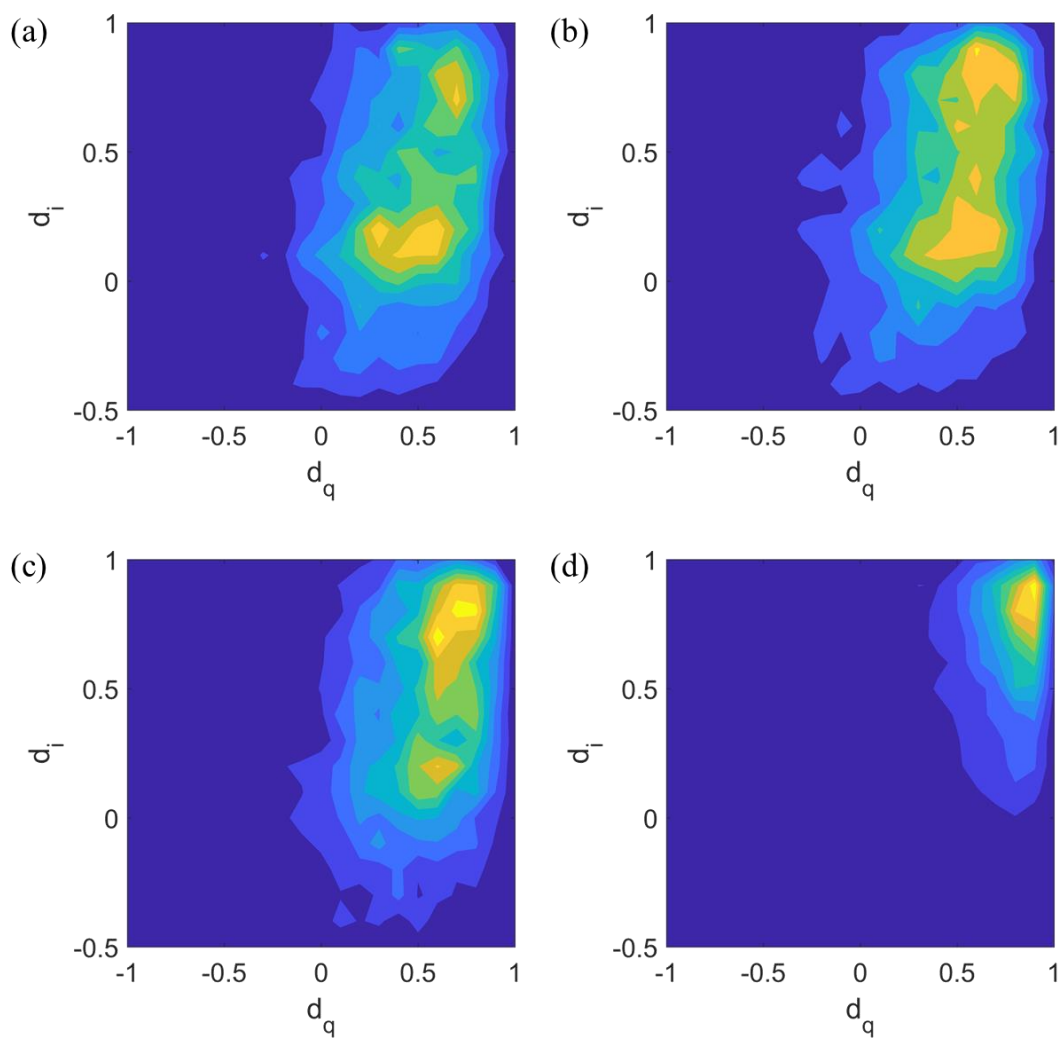


**Figure 9:** Contour plots for neighboring particle pair-correlations, as the system transitions from disordered (a) to ordered (d) state.  $d_q$  captures the translational correlation and  $d_i$  the orientational correlation for a system of 1728 particles at  $p = 4.07$ . Frequency increases from blue to yellow. The equilibrium disordered phase (a) contains a non-negligible population of particles-pairs that are near the same region of phase space that is frequented by the ordered state (d). The system transitions through stages (b,c) where the population of ordered pairs becomes more significant. In the ordered state all particles populate the top-right corner (d).

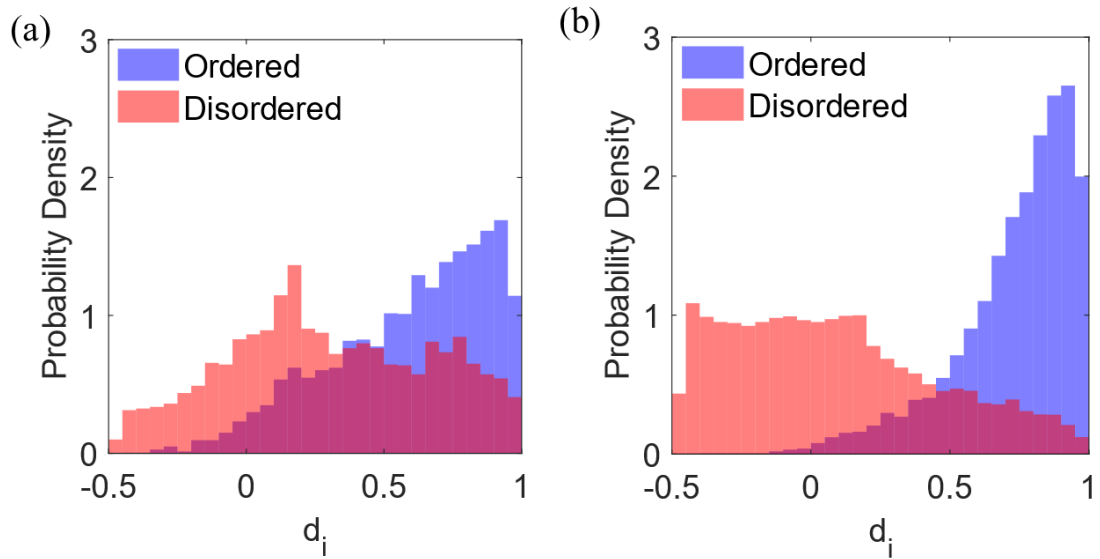


**Figure 10:** Orientational correlation distributions for (a) cubes and (b) octahedra<sup>59</sup> at liquid-solid coexistence conditions ( $p_{co,cubes} \approx 4.0$ ,  $p_{co,oct} \approx 6.93$ ). For cubes (octahedra), 65% (30%) of the particle population in the disordered phase have configurations occupying the same  $d_i$  region as the ordered phase.

We examined the spatial distribution of the locally ordered particles in the disordered phase to see if a large consolidated nucleus is distinguishable as the signature of a nucleation process as has been observed in other polyhedral particles.<sup>8,59</sup> Our clustering algorithm revealed that this is not the case; indeed, these particles were almost always sparsely distributed throughout the bulk disordered phase. For example, while about 4 percent of particles are ordered for  $p_{co} = 4$ , only one-tenth of them are consolidated in the largest cluster. Even during the disorder-to-order transition, we observe that the increase in the total number of ordered particles precedes their consolidation into a single spanning cluster (Figure 4(a)). In the metastable isotropic basin, we observe that clusters of ordered particles are largely uncorrelated as shown in Figure 4(b) for a

sample configuration and its corresponding spherical scatter plot for the orientation particle axes. As the transition progresses towards the ordered phase and 13% of the particles are ordered, we find that the clusters become more correlated, as evidenced in the scatter plot and snapshot of Figure 4(c). In this case we clearly see that the scatter plot has the characteristic symmetry with six orthogonal clusters. To further characterize this trend, we show in Fig. 5 the distance-dependent orientational correlation function of the ordered particles,  $d_i(r)$ , during a transition at  $p = 4.05$  for  $N = 8000$  particles. When only 6% of the particles are ordered, the correlation decays to a very low value over a distance of  $r \sim 10 a_c$ , revealing short-range order. For a 10.3% of ordered particles, which corresponds to the top of the free-energy barrier as discussed later in Section 3.4, the particles become correlated over longer distances (i.e., across the simulation box length). This long-range correlation becomes even stronger as the fraction of ordered particles increases (i.e., to 13% as shown in Fig. 5). Further, using an US calculation with the greatest cluster size as order parameter (which would be the appropriate reaction coordinate for a nucleation process) readily encounters multiple clusters of similar sizes coexisting in the system. This observation, which was common to simulations at all DSS values tested and for different definitions of solid-like particles making up the nuclei, indicates that the ordering process does not conform with the picture of classical nucleation. Hence, instead of the size of the largest consolidated nucleus, we chose the total number of ordered particles as an appropriate

order parameter for this transition. Indeed, we find that such ordered particles occur spontaneously at a given pressure (see Fig. 6), with their number increasing as the system's density slowly rises. For a  $N = 1728$  system and  $3 \times 10^6$  MC cycles per pressure point, on compression from the isotropic state a sudden jump in  $N_{ordered}$  occurs at  $p = 4.07$ , while upon expansion from the ordered crystal, a sharp drop in  $N_{ordered}$  occurs at  $p = 3.90$ . These results are only illustrative as the extent of hysteresis in the observable transition pressures around  $p_{co}$  depends on system size and the length of the simulation runs.

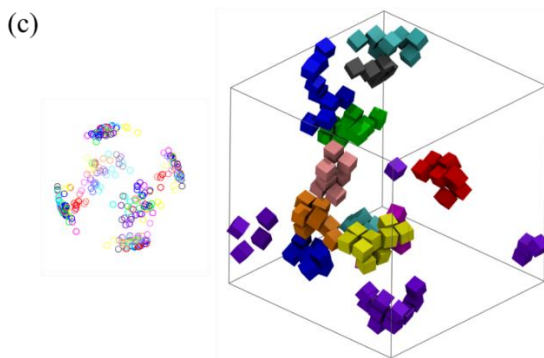
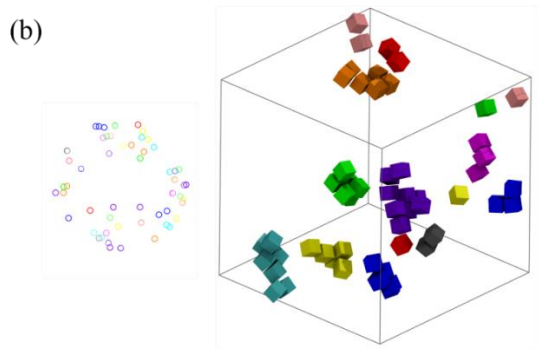
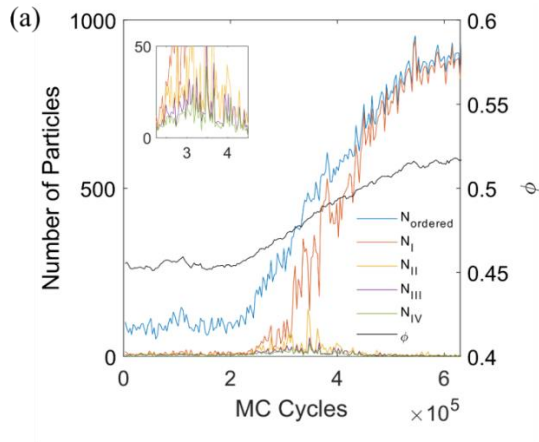


**Figure 11:** (a) Variation in number of ordered particles ( $N_{\text{ordered}}$ ) and largest cluster sizes ( $N_i$ : largest,  $N_{ii}$ : 2<sup>nd</sup> largest, etc.) during a spontaneous transition at  $p = 4.07$  and  $N = 1728$ . A steady increase in  $N_{\text{ordered}}$  precedes a rise in the size of the largest cluster  $N_i$  (after  $2 \times 10^5$  MC cycles). Before the consolidation, the relative size of various clusters is comparable (inset).  $\phi$  (black line) is the volume fraction of the cubes. (b,c) Visualization of ordered particles at two points during the transition: when 6% (b,  $2.1 \times 10^5$  MC cycles) and 13% (c,  $2.1 \times 10^5$  MC cycles) of the particles are ordered. The ten largest clusters are shown on the right, each with a different color that corresponds to those used in the scatter plot of particle orientation axes shown on the left.

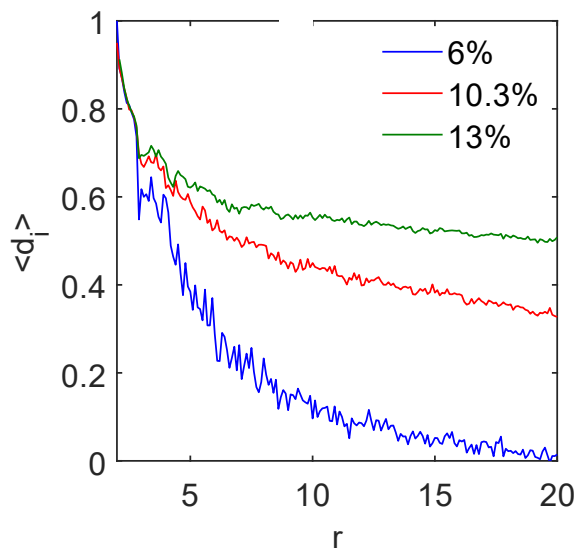


**Figure 12:** Mean  $d_i$  orientational correlation as a function of interparticle distance ( $r$ ) for all the ordered particles in a system at various percentages of ordered particles. Results for  $p = 4.05$  and  $N = 8000$ , for cubes of side of two units of length.

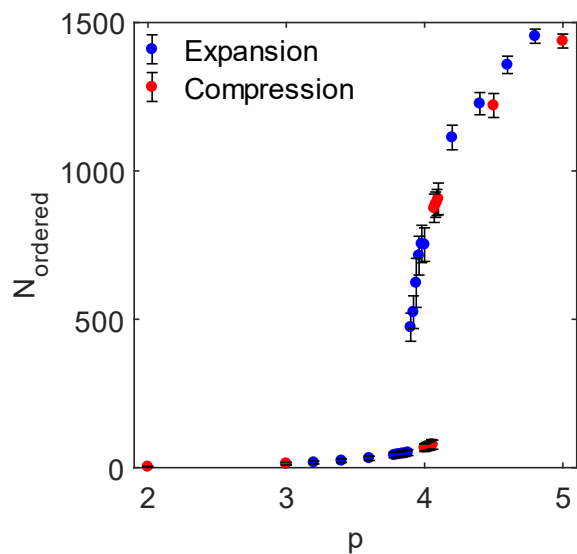


**Figure 6:** Number of spontaneously ordered particles ( $N_{ordered}$ ) as a function of pressure ( $p$ ) for a system of 1728 particles. Data points for compression from the isotropic phase in red and for expansion from the isotropic phase in blue. Error bars, representing one standard deviation from the mean, are shown as vertical bars on each point (as illustrated in the legend).

One contributing factor towards the presence of ordered domains in the disordered phase is the tendency of neighboring particles to align facets<sup>59</sup> (see Fig. 7). Since the final ordered structure has a very high population of facet-aligned particles compared to the disordered phase, it is expected that those local configurations in the latter with high facet alignment (high  $\Delta$  values) would bear an imprint of the final ordered structure. Since facet alignment is locally favored,<sup>59</sup> a local configuration that is disordered in  $d_i$  but has a typical  $\Delta \approx 0.5$  would be more likely to transition into an ordered configuration ( $d_i > 0.75$ ,  $\Delta > 0.7$ ). This is in contrast with the case of octahedra,<sup>59</sup> for which it was found that high- $\Delta$  disordered configurations hinder the ordering into the solid phase whose intrinsic low- $\Delta$  necessitates low- $\Delta$  configurations to precede the nucleation of translational order.

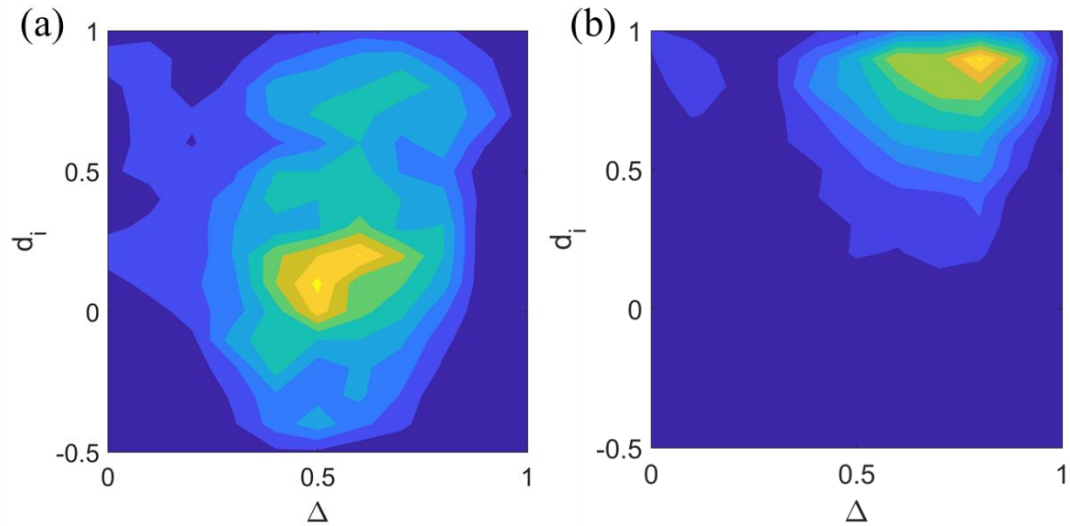


**Figure 7:** Contour plots describing the distribution of particle neighbor-pairs over the orientational correlation ( $d_i$ ) and facet alignment measure ( $\Delta$ ). The population moves towards a higher facet alignment as system goes from the disordered (a) to the ordered state (b). System of  $N = 1728$  hard cubes at  $p = 4$ .

CNT fails to describe the present ordering transition as it neglects inter-nuclei interactions and supposes bulk-average interfacial properties, assumptions that are inconsistent with the observed physical picture. Indeed, for all DSS tested hard cubes order via multiple spontaneously forming and spatially interacting nuclei, whose small size and irregular, fluctuating shapes create effects that are not properly accounted for by just the bulk average values of interfacial area and tension.

Thus, we hypothesized that at any given pressure above  $p_{co}$  an initially isotropic phase contains a certain fraction of particles forming multiple scattered ordered domains

which will increase as the ordering transition proceeds until such domains interact and consolidate. Such consolidation reduces the interfacial area and thus would be thermodynamically favored.

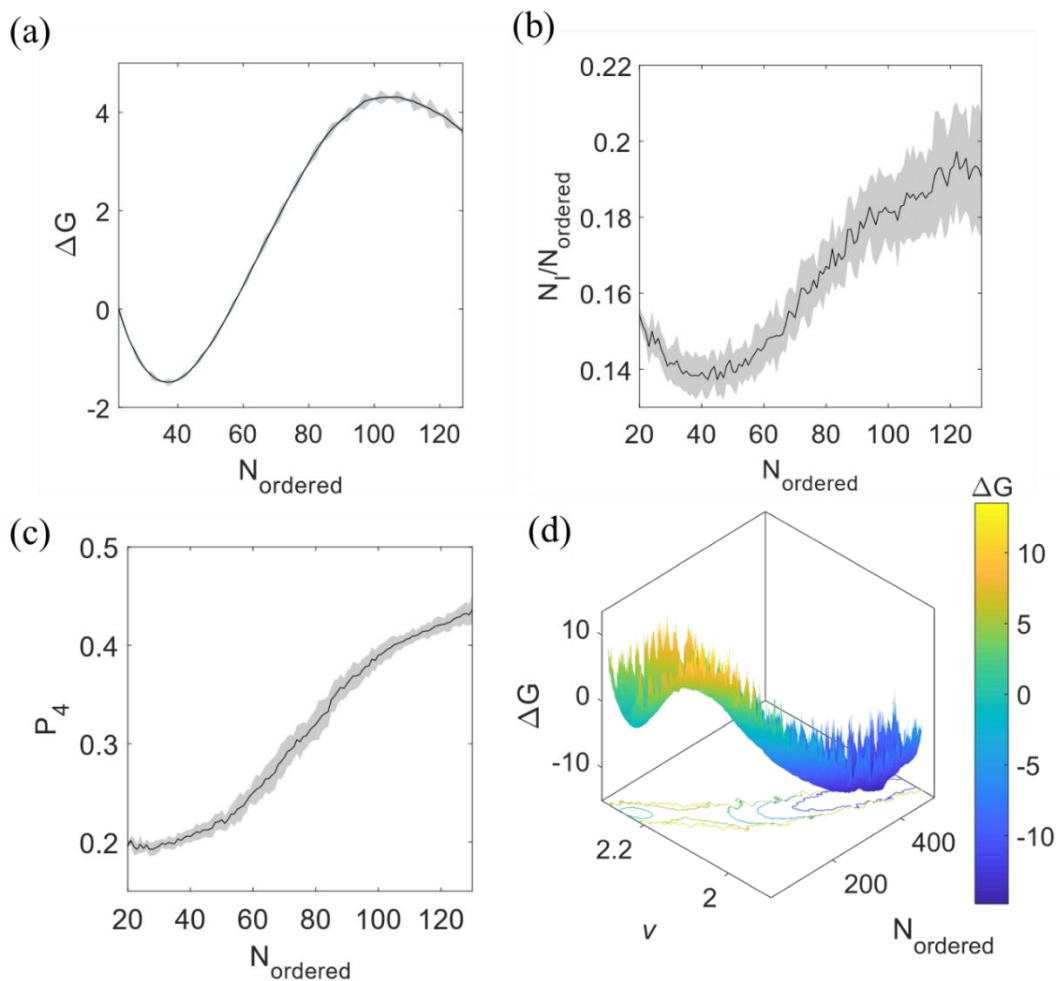
### 3.2 Free Energy Barriers

Figure 8(a) shows the US results for the free energy profile at  $p = 4$  for a system of 1000 particles. We observe that there is a well-defined well within which the disordered phase exists with about 38 ‘ordered’ particles (3.8% of total) present on average at a given time. Using US, we bias the system to explore rarer states with higher values of  $N_{ordered}$ . Eventually, we find that we attain a critical state, beyond which the system would be more likely<sup>57</sup> to spontaneously reach the ordered phase than the disordered phase. Figure 8(b) further shows that, overall, consolidation of the ordered domains increases with  $N_{ordered}$ . There exists, however, an initial decrease in the fraction of consolidated particles with  $N_{ordered}$ , indicating a regime where the ordered domains can grow while still being sufficiently dilute to avoid significant mutual interactions. Note that the  $N_{ordered}$  value where the free energy profile in Figure 8(a) has an inflexion point is close to where the minimum in Figure 8(b) occurs (i.e.,  $N_{ordered} \approx 55$ ). At this point additional ordered domains can be added to the system without any consolidation, which is unfavorable due to a concomitant increase in interfacial area. This is different from the behavior in the middle of the isotropic basin ( $N_{ordered} = 38$ ) where the number of domains decreases with  $N_{ordered}$ . For  $N_{ordered} > 55$ , however,

such merging of domains likely entails smaller changes in interfacial area so that the addition of newer domains leads to progressively smaller free energy increments. Interestingly, we find that even as the orientational correlation  $P_4$  (Fig. 8(c)) among the ordered particles gradually increases with  $N_{ordered}$ , the increase is particularly rapid during this region of consolidation ( $55 < N_{ordered} < 103$ ). Interestingly, at the top of the free energy barrier ( $N_{ordered} \approx 103$ ) less than 20% of all ordered particles have been consolidated into the largest cluster; the fact that the free energy decreases thereafter suggests that any further increase in  $N_{ordered}$  involves a net reduction in interfacial area; i.e., consolidation reduces its value more than new ordered particles can increase it.

Since the system undergoes a significant change in specific volume ( $v$ ) during the transition, we examined the relation between  $v$  and  $N_{ordered}$  by concurrently obtaining statistics for  $v$  while mapping the free energy landscape via US.<sup>30</sup> The resulting free energy surface, shown in Figure 8(d), reveals that  $N_{ordered}$  and  $v$  are strongly correlated. (Within errorbars, we obtained the same free-energy landscape when  $v$  is used as the primary order parameter in US while  $N_{ordered}$  is the “passenger” order parameter). We also performed another US simulation run in a reverse order (going from order to disorder) using the same  $N_{ordered}$  as order parameter and we found that the free-energy barrier heights (from the disordered basin to the barrier top and from the ordered basin to the barrier top) were essentially the same as those found in

the forward direction, indicating that this order parameter samples a reversible path across the transition. The values of the barriers determined from the 2D free energy surface of Fig. 8(d) or from the 1D free energy profile of Fig. 8(a) are nearly identical and thus we use the results from the latter approach for concreteness. The suitability of  $N_{ordered}$  as order parameter for the transition state region (around the free-energy barrier top) was further confirmed via the histogram test for the committor probability as described in the SI (Fig. S2).



**Figure 8:** Umbrella sampling (US) calculations at  $p = 4$  for  $N = 1000$  particles. (a)  $\Delta G$  profile along  $N_{ordered}$ ; disordered-phase basin is centered around  $N_{ordered} = 38$ . The top of the barrier corresponds to  $N_{ordered}^* = 103$ . Gray shaded regions represent error bars from the US calculation. (b) Relative proportion of ordered particles present in the largest cluster, averaged over each US window. A minimum occurs for  $N_{ordered} \in [30,55]$ , which precedes the inflexion point in (a)  $N_{ordered} \sim 60$ . (c) Global tetratic orientational order ( $P_4$ ) for the ordered particles as the transition progresses, averaged over each US window. Orientational order increases more rapidly for  $N_{ordered} \in [55,103]$ , likely due to the different ordered domains realigning as they merge. (d) 2-dimensional  $\Delta G$  landscape with respect to  $N_{ordered}$  and specific volume ( $v$ ).

To see whether the ordering transition is well described via a bulk phase property, we performed US calculations of the free energy barrier  $\Delta G^*$  for various system sizes using  $N_{ordered}$  as order parameter. Figure 9 shows that, for a given pressure, both properties scale linearly with system size  $N$ , and that the slope for a given pressure in Fig. 9(a), which would be equivalent to an “intensive” free energy barrier  $\Delta g^*$  in Fig. 9(a, inset), and to a fraction of ordered particles  $x_{ordered}^*$  in Fig. 9(b, inset), both remain nearly constant and decrease with pressure. Our hypothesis was that if the transition is a global or bulk process, both  $\Delta G^*$  and the critical number of ordered particles ( $N_{ordered}^*$ ) should scale linearly with respect to  $N$  (i.e., they would behave as “extensive” properties) with a prefactor that would be distinct from that expected for a nucleation process. Indeed, at the point when a classical nucleus of critical size  $N_c^*$  occurs, the total number of ordered particles in the system would be expected to follow a relation of the form:

$$N_{ordered}^* = n^* N_c^* + x_{ordered}^{iso} N \quad (7)$$

where  $x_{ordered}^{iso}$  is the fraction of ordered particles in the background, isotropic phase at the given DSS and  $n^*$  is the number of nuclei of size  $N_c^*$  in the system, which at equilibrium is given by  $\sim N e^{-\frac{\Delta G^*}{k_B T}}$ . Clearly,  $n^* < 1$  for a large barrier (say  $\Delta G^* > 10 k_B T$ ) and the system sizes used here  $10^3 \leq N < 10^4$ , but  $n^* = 1$  if a nucleus of size  $N_c^*$  is present. It follows then that for such nucleation scenario:

$$x_{ordered}^* = N_{ordered}^*/N \sim x_{ordered}^{iso} \quad (8)$$

As shown in the inset of Fig. 9,  $x_{ordered}^* \sim 0.1$ , a value significantly larger than  $x_{ordered}^{iso} \sim 0.04$  for the pressures considered, values largely independent of  $N$ . Hence, although  $N_{ordered}^*$  would increase linearly with  $N$  even if the transformation were to proceed via nucleation, the calculated slope  $x_{ordered}^*$  is inconsistent with such an interpretation. Note that our results are also inconsistent with a linear percolation behavior where  $N_{ordered}^*$  would be proportional to  $N^{\frac{1}{3}}$ .

We note that as  $N$  increases at fixed  $p (> p_{co})$  any long-range correlations that may have enhanced the stability of the ordered phase is weakened, leading to an increase in  $p_{co}$ , a reduction in  $(p - p_{co})$  and DSS, and hence to an increase in ordering transition barrier  $\Delta G^*$ . However, such finite size effects are expected to be significant only for small system sizes  $N < 10^3$  particles<sup>98</sup>, and be rather negligible for the range  $10^3 \leq N < 10^4$  under consideration (and unlikely to lead to a linear scaling  $\Delta G^* \propto N$ ). Note also that when the

top of the free energy barrier is reached most of our systems (~90%) are still in the isotropic phase where such finite size effects are minimal. We hence argue that the linear scaling on  $N$  that we observe for  $N_{ordered}^*$  and  $\Delta G^*$  are most consistent with a transition having a bulk-like behavior.

We further conjecture that the extrapolation of  $\Delta g^*$  to zero would mark a characteristic pressure ( $p_c$ ) at which the ordering transition would be unrestricted (i.e., barrier-less). Our linear extrapolation (see Figure 9(a), inset) indicates that  $p_c \approx 4.08$ , corresponding to  $DSS \approx 0.03$ . From a physical point of view,  $\Delta g^* > 0$  implies that in the large system limit (relevant to macroscopic experiments), the transition would be kinetically arrested. Only after the pressure is larger than a critical pressure ( $p_c$ ) at which  $\Delta g^* \leq 0$  can a spontaneous transition be kinetically viable. It should be pointed out, however, that our estimate of  $p_c$  is based on  $\Delta g^*$  values extrapolated from relatively small systems (Fig. 9(a)) that neglect the potential contributions to the transition of density and ordering fluctuations occurring over lengths scales larger than the simulation box size, implying that  $p_c \approx 4.08$  would be an overestimation.

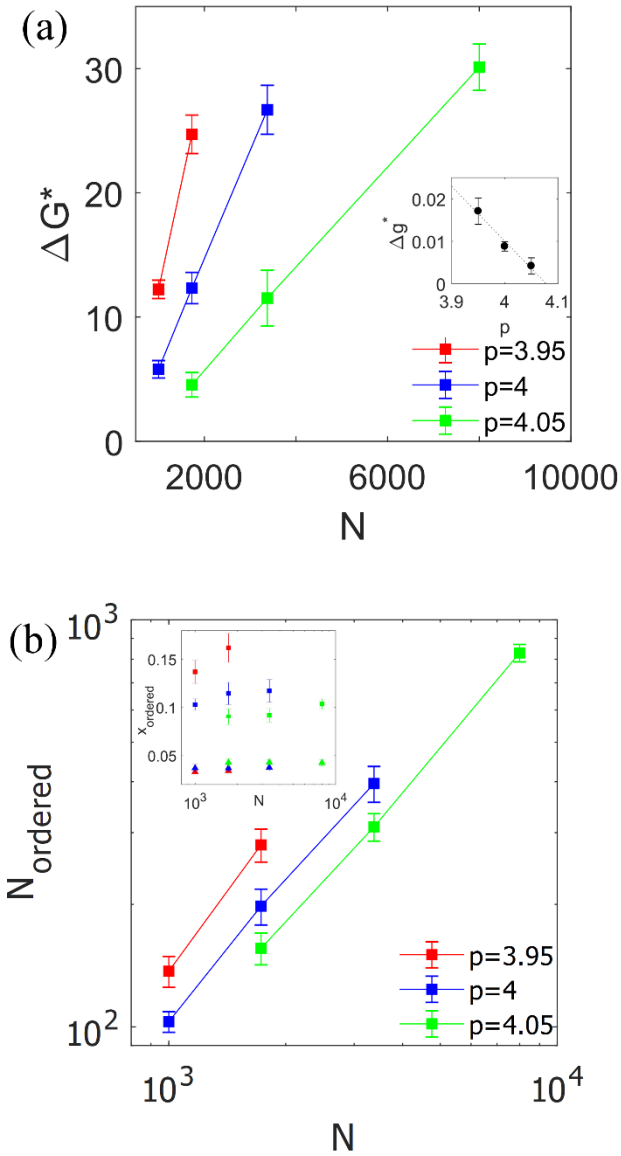


**Figure 9:** Free energy barriers for the disorder to order transition at various pressures and system sizes ( $N$ ). (a) Scaling of free energy barrier ( $\Delta G^*$ ); the slope of the lines can be interpreted as an “intensive” free energy barrier  $\Delta g^*$  which is shown in the inset for various pressures ( $p$ ), along with a linear fit (dotted line). (b) Scaling of critical number of ordered particles. Inset: The fraction of ordered particles at the critical point ( $x_{\text{ordered}}^*$ , squares) and in the isotropic basin ( $x_{\text{ordered}}^{\text{iso}}$ , triangles); colors correspond to the pressures in the legend.

The fact that cubes order via a process quite different from the nucleation mechanism that has been observed for other polyhedra (at comparable DSS),<sup>14</sup> including some from the truncated cube family,<sup>15</sup> could be traced to the unique characteristic of the mesophase-like solid that cubes form near the disorder-order transition (i.e., for  $0.5 < \phi < 0.55$ ). As discussed in the Introduction, such a solid phase could be seen as a mesophase not only because it contains an unusually large fraction of vacancies (~6.4%) for a crystal, but also because those vacancies are mobile and delocalized, spreading out over multiple lattice sites.<sup>17</sup> Indeed, the diffusivity of cubes is much larger than that of other polyhedra<sup>8</sup> or hard spheres in their solid states (near the ordering transition), which reflects the fast dynamics around the delocalized vacancies. The mobility of cubes in a solid-like cluster in contact with a disordered region is hence expected to be quite high and not too dissimilar to that of cubes in the disordered phase. The presence of ‘crystal’ vacancies must amplify density fluctuations in a solid cluster and facilitate interfacial rearrangements, effects that may translate into a small interfacial tension. Indeed, the latter would in turn explain the tendency to form multiple metastable ordered clusters (rather than a single nucleus) during the ordering transition, despite the concomitant increase in interfacial area. Ultimately, the extensive nature of  $\Delta G^*$  would largely arise from the fact that the interfacial area needed to consolidate the solid phase increases with system size.

### 3.3 Grain Boundary Dissolution

As shown in Figure 4(a), at early stages of the ordering process we always observe the presence of multiple, independent ordered domains in the system, which, if continued to grow without reorientation, would give rise to multiple grain boundaries. However, at least for the pressures and system sizes simulated, we never observe any (long-lived) polycrystallinity when the system fully transitions to the solid basin; the system always converges to a single-grain state. This ability to resolve domain misalignments likely plays a crucial role in facilitating the transition to the ordered phase. To gain some insight into the process of grain realignment, we created an artificial configuration consisting of two misaligned grains for  $N = 5544$  as shown in Figure 10(a). Grain 1 has particles with their faces aligned parallel to the box vectors, while grain 2 is rotated by  $45^\circ$  along the z-axis (pointing out of the page). We conducted NPT simulations at  $p = 5$  and tracked the evolution of the merging process. We observe that as the system is equilibrated, grain 1 tends to propagate (Figure 10(b)). However, in the final structure (obtained after  $6 \times 10^6$  MC cycles), both grains attain a final orientation that is intermediate between the original two orientations, albeit much closer to that of grain 1 (Figure 10(c)). Replicate simulations (not shown) exhibited a similar behavior, with the final orientation being intermediate, with varying proximity to the original orientation of either grain 1 or grain 2. If disparate-sized grains were to meet, the smaller grain would likely consistently experience the largest reorientation. The process is vaguely

reminiscent of Ostwald ripening, wherein one grain grows by the gradual dissolution and particle transfer from another grain, except that in this case the grains are not dispersed in a solution and can hence “push” against each other. This capability of hard cubes to reorganize quickly, even when large grains are involved (as in this example) helps explain the absence of polycrystallinity in the ordered phase, as multiple ordered domains would be able to conveniently merge. Once again, the high concentration of delocalized (dynamic) vacancies<sup>95</sup> and the high particle mobility<sup>4</sup> unique to hard cubes’ solid-phase provide the likely microscopic mechanisms that facilitate the cooperative rearrangement of particles near an interface, and the propagation of those changes through the grains. Indeed, Smalenburg et al.<sup>17</sup> found that spontaneous vacancies account for up to 6.4% (of lattice sites) which is several orders of magnitude larger than typically seen in colloidal crystals, including octahedra for which vacancies would not be observed in typical simulation system sizes (unless purposely implanted, in which case they would have minimal mobility).

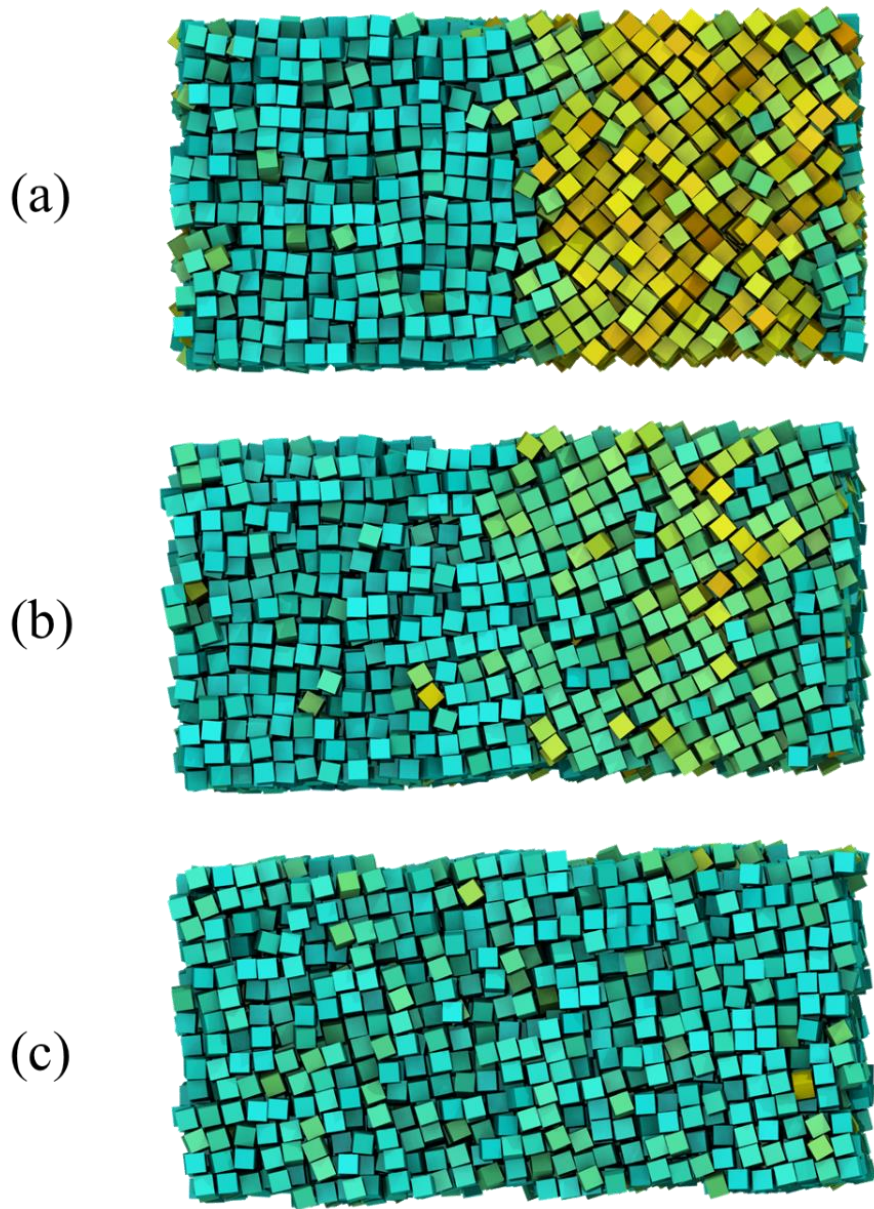


**Figure 10:** Dissolution of grain boundaries in hard cubes. (a) The initial system consists of two grains simulated at  $p = 5$ . Grain 2 (right) is rotated at  $45^\circ$  with respect to grain 1 (left), which is aligned with the simulation box axes. Cubes are colored based on their alignment: from blue for vertically aligned to yellow for  $45^\circ$  misalignment. (b) Grain 2 rotates driven by the facet alignment of particles at and around the grain boundaries. (c) Finally, the grains resolve into a single grain whose orientation is close to that of the original Grain 1.

## 4 Conclusions

Our analysis of the disorder-to-order phase transition of hard cubes reveals that due to high level of local facet alignment occurring in both the ordered phase and (to a lesser extent) in the disordered phase, there is a high propensity in the latter to contain small ‘ordered’ domains. At any given time, such domains are present in non-negligible quantities such that the total number of ordered particles describes the proximity to the ordered phase better than the size of the largest cluster alone. Analysis of unbiased simulations reveals that the transition involves an increase in the number of such domains, followed by their consolidation. Umbrella sampling calculations reveal that the free-energy transition barriers obtained from systems of different sizes are consistent with the view that the transition happens via a bulk process. Calculation of an ‘intensive’ free energy barrier allows us to extrapolate to a critical pressure  $p_c$  above which the transition in a macroscopic system would take place unhindered and spontaneously. The absence of polycrystallinity in the solid phase is linked to the ability of the system to dissolve grain boundaries via cooperative, correlated motions that propagate through the grains as demonstrated by the simulation of misaligned grains that realigned by simultaneously changing their original orientations. Indeed, ordered domains that spontaneously arise and come in contact during the disorder-to-order process readily resolve any grain boundaries, resulting in a final single-grain ordered phase.

The existence of such a global ordering mechanism for hard cubes brings up the question about what other systems might exhibit a similar mechanism. Clearly, truncated cubes with a small amount of truncation<sup>13</sup> or rounded cubes (described via superball<sup>99</sup> or polybead models<sup>52</sup>) which undergo a similar transition into a cubic ordered phase should closely approach the behavior of the hard cubes studied here. More generally, systems with a strong coherence in their tendencies for local packing (in disordered phase) and global packing (in ordered phase) may exhibit a similar mechanism. For practical applications, it would be of interest to quantify the effect on the ordering mechanism of soft interparticle attractions<sup>21</sup> and size polydispersity,<sup>30</sup> two factors which are ubiquitous in experimental systems. Further studies can focus on finding theoretical models that can describe the general features of the phase transition mechanism studied here, incorporating the key elements that we observed in hard cubes, such as a high concentration of locally ordered particles in the isotropic phase basin and the proliferation and consolidation of ordered domains before reaching the solid phase basin. Also, studies employing methods designed to sample the disorder-to-order transition kinetics and rates<sup>14,28</sup> would provide complementary insights into the microstructure changes along transition pathways.

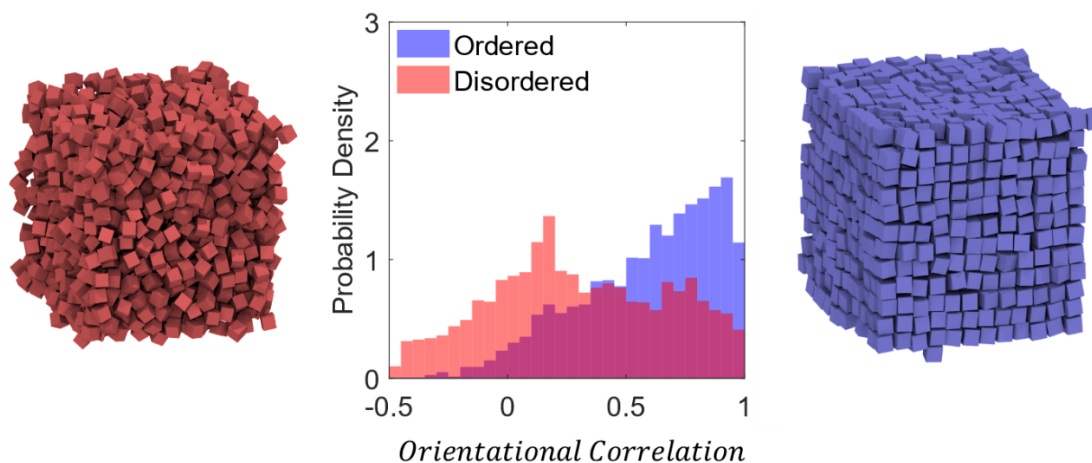
## 5 Acknowledgements

Funding support from NSF awards DMR-1609997 and CBET-1402117 are gratefully acknowledged. The authors are grateful to Dr. Vikram Thapar for valuable discussions and sharing the base simulation code.

### Supplementary Information

Further discussion on order parameter optimization and umbrella sampling methodology is provided in the supplementary information (SI).

### TOC Graphic



## 6 Supplementary Information

### 6.1 Order Parameter Optimization

The tunable parameters used to evaluate  $N_{ordered}$  were set based on values reported for similar calculations<sup>8,59,96</sup> and by visual inspection of the results in representative configurations. However, they can be optimized further based on different criteria. Here we suggest an approach that ensures a suitable discrimination between the ordered and disordered states. The tunable parameters can be hierarchically optimized to match false positives with false negatives<sup>68</sup>, such that the probability of falsely labelling a disordered particles as ordered is equal to the probability of falsely labelling an ordered particles as disordered. The cutoff for the orientational correlation  $d_i$  for a pair of neighboring particles to be identified as ‘connected’ can be obtained using the mislabeling distribution for sample ordered and disordered states. For example, for hard cubes at  $p = 4.0$  (Figure S1), the cutoff at  $d_i = 0.63$  provides the best discrimination with mislabeling fraction of 0.245. If we use this optimized cutoff to observe the distribution of mislabeling with respect to the number of connections, we find that the minimum mislabeling fraction of 0.248 is achieved at a cutoff of  $\zeta = 2$ . These optimal values, however, will vary depending on pressure and are slightly different from the ones we use in the main text ( $d_c = 0.7, \zeta_c = 3$ ), which were chosen to render a stricter criterion to assign order, i.e., to mislabel fewer disordered particles than ordered particles.

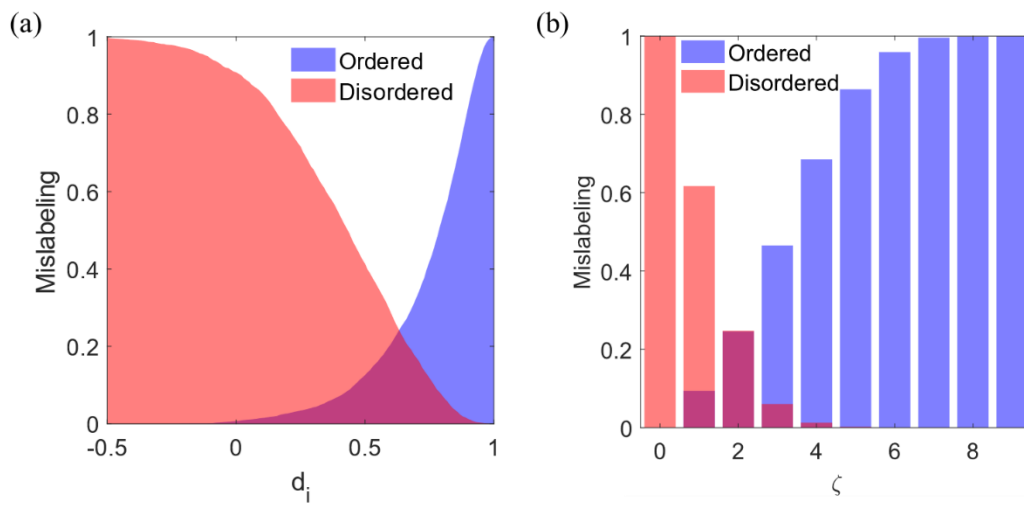


**Figure S13:** Distribution of fraction of mislabeled particles for various cutoff values for (a) the orientational correlation  $d_i$  and (b) the number of connections  $\zeta$  for the order parameter of hard cubes in ordered and disordered phases at  $p = 4.0$  and  $N=1728$ .

Nevertheless, the main predictions in the text with respect to the phase behavior and transition barriers are largely unaffected by the choice of  $d_c$  and  $\bar{\mu}_c$  for values encompassed by those given above. Specifically, the free-energy barrier height is expected to exhibit little sensitivity to such fine tuning (as demonstrated before for a similar formulation of order parameters<sup>41</sup>) but the number of ordered particles were the barrier top occurs can change significantly due to the variability in assigning order to interfacial particles (those between ordered and disordered domains). For example, if the optimized values were used, it would increase the fraction of ordered particles in the isotropic phase at coexistence from 4% to 25%; hence, the spontaneous presence of ordered particles would still be observed, albeit with a seemingly unrealistic high value.

## 6.2 Umbrella Sampling (US)

While performing US simulations with respect to order parameter  $N_{ordered}$ , the following window sizes were used for various system sizes:

**Table S5:** Window sizes for umbrella sampling

System Size (N)	Window Size
1000	10
1728	20

3375	40
------	----

In practice, we generally kept an overlap of half of the window size between successive windows. For example, in a specific case it may go like [50, 70], [60, 80] and so on. The data from pairs of successive windows was combined by matching the values in the middle of the overlap region.

To test the quality of the ordered parameter  $N_{ordered}$  in describing the region around the transition state determined using umbrella sampling, we performed a committor probability analysis by obtaining statistics for the growth of microstates belonging to the transition state ensemble.<sup>6</sup> For this we chose a 8000 particle system at a pressure  $p = 4.05$  whose relatively flat free-energy barrier top lies in the range  $N_{ordered} \in [790, 860]$ . For  $N_{ordered} = 810$ , we ran 10 trajectories each for 55 uncorrelated microstates to estimate their growth probability  $p_{growth}$  and plot the distribution shown in Figure S2. The average  $p_{growth}$  is 0.58 is rather close to the expected 0.5 value (the operational definition of the transition state) and, importantly, the  $p_{growth}$  histogram shows a tendency toward a central peak (despite the statistical noise). While an ideal reaction coordinate would give a histogram that is sharply peaked around  $p_{growth} = 0.5$ , the shape of the histogram in Fig. S2 is sufficiently centrally biased to

confirm the suitability of  $N_{ordered}$  as order parameter, especially considering the relatively flatness of the free-energy barrier top.

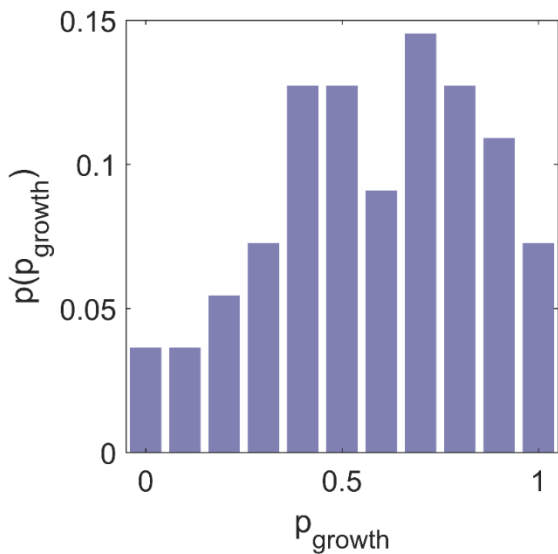


**Figure S14:** Normalized histogram of committor probability  $p_{growth}$  of 55 uncorrelated configurations with  $N_{ordered}=810$  for a system of  $N=8000$  hard cubes.

### 6.3 Specific Volume as an Order Parameter

In order to test the robustness of  $N_{ordered}$  as an order parameter and see if it correlates with specific volume ( $v$ ), we kept track of  $v$  data as a ‘passenger’ order parameter.<sup>7</sup> Using these data we were able to obtain the two dimensional free energy landscape as shown in Figure 8 (d) of the main text, obtaining results consistent with barriers obtained with  $N_{ordered}$  alone. As a further consistency test, we performed the US calculation with specific volume ( $v$ ) as the primary order parameter and  $N_{ordered}$  as the passenger order parameter. The window size was set at 0.01 along specific volume. The results from

these two US calculations are shown side by side in Figure S3. As can be observed, all the properties of interest (transition barrier heights, positions of the disordered/ordered phase wells) are essentially the same within statistical errors.

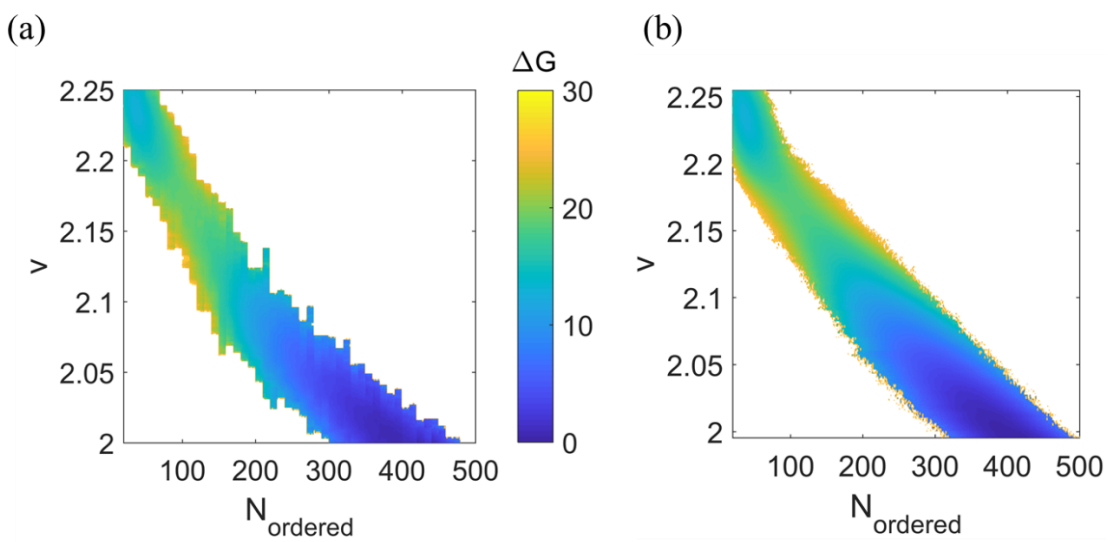


**Figure S3:** 2D Free energy landscapes calculated using umbrella sampling for a system ( $N=1000$ ) hard cubes at  $p = 4.0$  using  $N_{\text{ordered}}$  and  $v$  as order parameters. (a) Primary OP:  $N_{\text{ordered}}$ , passenger OP:  $v$  (b) Primary OP:  $v$ , passenger OP:  $N_{\text{ordered}}$ .

## CHAPTER 4: LOW INTERFACIAL FREE ENERGY DESCRIBES BULK ORDERING TRANSITION IN COLLOIDAL CUBES

Abhishek K. Sharma and Fernando A. Escobedo\*

*R. F. Smith School of Chemical and Biomolecular Engineering, Cornell University, Ithaca,  
New York 14853, USA.*

*\*) Corresponding author Email: fe13@cornell.edu*

### **Abstract**

Many hard faceted nanoparticles are known to undergo disorder-to-order phase transitions following a classical nucleation and growth mechanism. In a previous study [*J. Phys. Chem. B* **2018**, *122*, 9264-9273] it was shown that hard cubes undergo a non-classical phase transition with a bulk character instead of originating from consolidated nuclei. Significantly, an unusually high fraction of ordered particles was observed in the metastable basin of the disordered phase, even for very low degrees of supersaturation. This work aims to substantiate the conjecture that these unique properties originate from a comparatively low interfacial free energy between the disordered and ordered phases for hard cubes relative to other hard particle systems. Using the cleaving wall method to directly measure the interfacial free energy for cubes, it is found that its

values are indeed small, e.g., at phase coexistence conditions it is only one fifth that for hard spheres. A theoretical nucleation model is used to explore the broader implications of low interfacial tension values and how this could result in a bulk ordering mechanism.

## 1 Introduction

Recent advancements in chemical synthesis<sup>17,94,100</sup> have enabled an unprecedented control of the shape and monodispersity of nanoparticles. Such tailored nano-scale colloids are important as building blocks for bottom-up materials design<sup>1,89–91,101</sup> with potential applications in photonics<sup>102</sup> and plasmonics.<sup>103,104</sup> In the absence of strong, ligand- or patch-mediated energetic interactions, the self-assembling properties of colloidal nanoparticles can be largely traced to their shape and have been predicted through ‘hard’ particle models, e.g., the formation of different crystalline structures,<sup>6</sup> and mesophases,<sup>4,7,10,83,99</sup> and the occurrence of phase transitions.<sup>8,40,41,59,96,105,106</sup> To date, many of these predictions have been confirmed through experiments.<sup>13,73,94,107–</sup>

109

Computer simulations have revealed that hard colloidal nanoparticles generally undergo first-order, disorder-to-order phase transitions in 3D space.<sup>8,59,105</sup> One of the first cases studied through simulations was that of hard spheres,<sup>55</sup> which form a face-centered cubic (FCC) lattice *via* nucleation and growth.<sup>40,105</sup> Adding anisotropy to the shape of the particle, say by adding facets, alters the phase behavior by favoring

ordered structures that enhance packing entropy.<sup>4,6</sup> As for the phase transition kinetics, the faceted particles studied thus far have been found to generally order via nucleation and growth.<sup>8,59,96,110</sup>

Remarkably, simulations of hard cubic nanoparticles reveal both unusual phase behavior<sup>4,95,111</sup> and ordering kinetics. Upon compression, they form an ordered phase with orientationally aligned particles arranged in a simple cubic lattice. Near the phase transition, this ordered phase has an unusually high diffusivity and concentration of vacancies for a crystalline phase when compared to that for other particle shapes. In a recent study<sup>106</sup> where the disorder-to-order transition of hard cubes was tracked and free-energy barriers mapped via umbrella sampling, we observed that the kinetic pathway toward ordering was also unusual. Unlike most other polyhedra that have been studied in literature,<sup>8,59</sup> the phase transition in cubes is not well described by classical nucleation and growth. Instead, it undergoes a 'bulk-like' transition behavior with the following features:

- (i) A large number of sparse, small clusters of ordered particles are present in the disordered phase. The concentration of ordered particles increases with supersaturation and, at a given supersaturation, is much higher when compared to other polyhedra that undergo nucleation and growth.

- (ii) The apparent free energy barrier for the ordering transition was found to scale linearly with system size, which would imply that in a system of macroscopic size the transition would be practically impossible.
  
- (iii) At no or minimal degree of supersaturation, a critical concentration of ordered cubes – rather than a critically-sized ordered nucleus - needs to be attained for the transition to proceed. During the transition, the fraction of ordered particles gradually increases, leading to consolidation of ordered domains and an eventual transition to the ordered phase.

It is well established that any stable or metastable phase will exhibit local fluctuations in structural order where motifs associated with another phase may occur.<sup>112</sup> While these fluctuations will largely be transient, they will also encompass the seeds of an incipient (stable) phase as it nucleates and grows within a metastable phase. Of course, that such fluctuations also exist in a stable phase – albeit fewer and too small to initiate any phase transition. The presence of a significant fraction of ordered particles in a disordered phase reflects the ease of creating interfaces in the system, i.e., a small interfacial free energy between ordered and disordered phases. Hence, we hypothesize that the abundance of such fluctuations that resemble the ordered phase (henceforth simply referred to as *cubic fluctuations*) in the disordered phase of cubes could be attributed to a low surface tension. In this paper we conduct direct measurements of

the interfacial free energy of a disorder-order interface for hard cubes and compare the resulting values to those of other hard-core systems. We also present a mass action-derived classical nucleation theory (MADCNT) model to qualitatively understand how the extent of cubatic fluctuations depends on interfacial free energy.

The paper is structured as follows: In Section 2 we outline the implementation of the cleaving walls method in Monte Carlo simulations. In Section 3 we present our results and discuss them in the context of a theoretical model to explore the consequences of low surface tensions on concentration of cubatic fluctuations. In Section 4 we provide a summary and outlook of our results.

## 2 Methods

### 2.1 Model

For any two cubic particles  $i$  and  $j$ , we use a hard pair-potential given by:

$$U_{ij} = \begin{cases} 0 & \text{if no overlap} \\ \infty & \text{if overlap} \end{cases} \quad (1)$$

The overlap is detected by using the separating axis theorem.<sup>49</sup>

### 2.2 Monte Carlo Simulations

We use Metropolis<sup>55</sup> Monte Carlo (MC) simulations in either the canonical ( $NVT$ ) or the isothermal-isobaric ( $NpT$ ) ensemble as necessary, where  $N$  is the total number of

particles,  $V$  is the volume of the system,  $p$  is the pressure, and  $T$  is the temperature. We use scaled units consistent with our previous studies,<sup>4</sup> with lengths scaled by the circumradius ( $a_c$ ) of the polyhedron. Thus, the dimensionless pressure is given by  $p = \beta p_a a_c^3$ , where  $p_a$  is the unscaled pressure and  $\beta = \frac{1}{k_B T}$ , where  $k_B$  is Boltzmann's constant. The chemical potential  $\mu$  and free energy ( $\Delta G$ ) are scaled by  $k_B T$  and the dimensionless interfacial free energy is given by  $\gamma = \beta \gamma_a a_c^2$  where  $\gamma_a$  is the unscaled interfacial free energy. For comparison among different particle shapes we tried to remove the dependence on the choice of length scale  $a_c$ , by defining a reduced dimensionless interfacial free energy as  $\bar{\gamma} = \frac{\gamma}{\rho_s^{2/3}}$ , where  $\rho_s$  is the density of the solid/ordered phase. This definition is identical to that in an earlier study,<sup>8</sup> and is consistent with the dimensionless surface component of free energy in classical nucleation theory. The supersaturation is defined as  $\Delta\mu_{od} = \mu_o - \mu_d$ , where  $\mu_o$  and  $\mu_d$  are chemical potentials associated with ordered and disordered phases, respectively. The coexistence pressure  $p_{co}$  for hard cubes under this scaling is  $p = 4.0$  as reported in literature.<sup>95</sup> The simulations used periodic boundary conditions to mimic bulk behavior. Each MC cycle included  $N$  translation,  $N$  rotation, and 2 isotropic volume moves (for  $NpT$  ensemble runs only).

## 2.3 *Cleaving Walls Method*

### 2.3.1 Outline

The cleaving walls method used in this study is a Monte Carlo adaptation of an existing method<sup>113</sup> typically implemented using molecular dynamics simulations. While there have been several modifications of the method over the years<sup>88</sup> to improve accuracy, we use an early, simple implementation which proved to be sufficiently accurate for our purposes. To the best of our knowledge this is the first implementation of the method using Monte Carlo simulations.

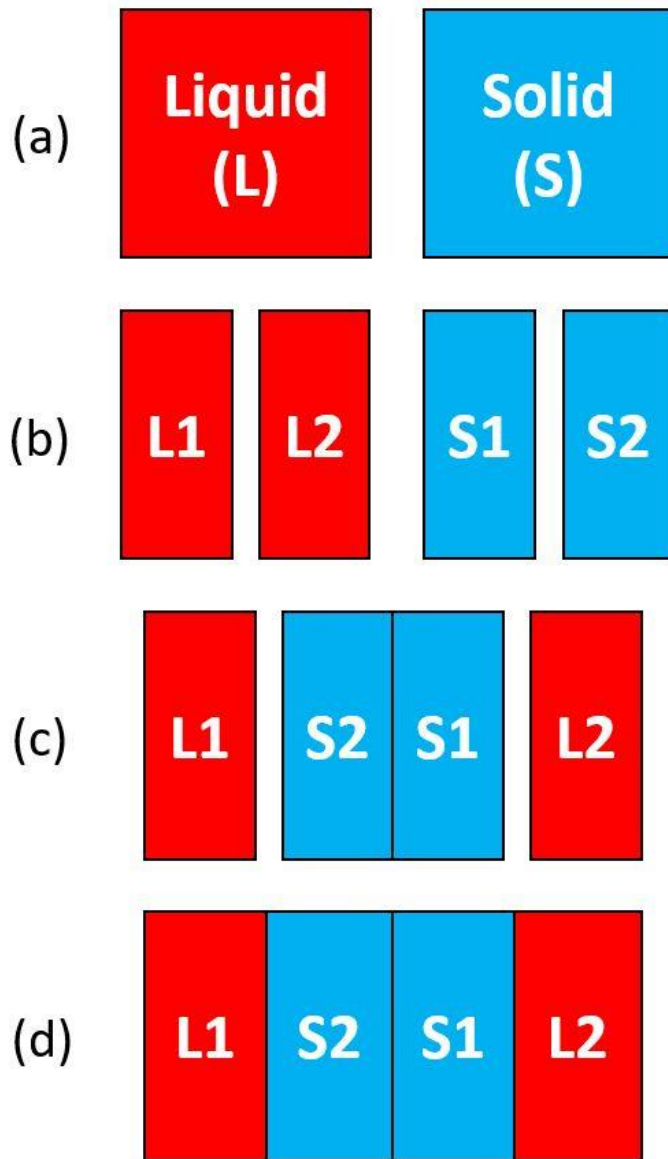


**Figure 15:** Schematic illustration of steps in the cleaving walls method. (a) Bulk simulation boxes of solid and liquid phases with three-dimensional periodic boundary conditions at the desired pressure. (b) Phases cleaved at the midplanes. (c) Transposed simulation boxes with dissimilar phases facing each other. (d) Final two-phase state with the gap closed and the two interfaces created.

The method involves three steps:

- I. Cleaving: Start from independent simulation boxes of the two phases at a given pressure (Figure 1a). The two boxes need to have the same cross-sectional dimensions along the cleaving plane and satisfy periodic boundary conditions. Move the cleaving walls to create a gap in the midplane of the simulation box such that particles do not interact across the gap (Figure 1b).
- II. Transposition: Rearrange the boxes as shown in Figure 1c to create a larger simulation box with two gaps with dissimilar phases facing each other.
- III. Merging: Recede the two pairs of cleaving walls to close the gaps, creating two interfaces (Figure 1d).

The interfacial free energy is then defined as the work done through these steps per unit area of the interface created. Since the interfacial particles do not undergo any change in energy at Step II, the interfacial free energy  $\gamma$  is given by the following expression:

$$\gamma = w_I + w_{III} \tag{2}$$

Where  $w_I$  is the work done per unit area on both systems in Step I, and  $w_{III}$  is the work done per unit area on the transposed system in Step III. The latter is negative and smaller in magnitude, resulting in a positive value for  $\gamma$ .

The pressure faced by the cleaving wall is measured throughout steps I and III and it is crucial to move the wall very gradually to minimize hysteresis. The values were verified by also conducting the process in reverse, i.e., by cleavage of an interface. The initial set up, definition of the cleaving wall, and the pressure calculation are described in the next subsection.

### 2.3.2 Initial Setup

We performed all the calculations at the estimated bulk coexistence pressure  $p = 4.0$ . As described in previous studies, the ordered phase of hard cubes at coexistence was generated by sequential NpT runs of  $3 \times 10^6$  MC cycles each, starting from a high pressure ( $p = 20$ ) and gradually reducing the pressure to  $p = 4.0$ . For the (100) crystal plane, configurations with  $N=1000$  were prepared on a simple cubic lattice aligned with the box vectors of a cubic box. The configurations presenting the (110) crystal plane were obtained in a cuboidal box with  $N=1024$  particles.

To obtain the disordered phase simulation box, the ordered phase simulation box was melted at  $p = 1.0$  with anisotropic volume moves along the  $z$  direction (orthogonal to the cleaving plane) to maintain the cross sectional ( $x$ - $y$ ) dimensions consistent for transposition in Step II. The system was then compressed to  $p = 4.0$  to obtain the equilibrium disordered phase at coexistence. To circumvent the finite-size effect of the interfacial region propagating into bulk-phase structure, longer boxes with  $N = 2000$

were primarily studied; these systems were obtained by duplicating the box along the  $z$  direction, followed by equilibration for  $3 \times 10^6$  MC cycles.

### 2.3.3 Cleaving Walls

We implemented the cleaving walls as hard planes that only interact with the centroids of the particles (see Supporting Information for discussion on walls that interact with the full particle shapes). There are two walls, one which moves in  $+z$  and the other in  $-z$  direction. For a given simulation box, both walls start at the midplane along the  $z$ -axis and particles are disallowed from crossing the midplane or the wall. A given wall only interacts with particles in the direction of its movement during Step I. The simulation is conducted in the NVT ensemble and at the end of each MC cycle, walls are moved in either direction by small increments ( $< 10^{-4}$ , in reduced units) with smaller increments used in cases where a particle would obstruct the wall. For example, if a movement of  $10^{-4}$  would lead to an overlapping particle, a movement of  $10^{-5}$  would be considered. This process is continued until we have achieved a separation of at least one particle circumradius, ensuring that the particles do not interact across the gap. Throughout the process we output configurations at various separations to perform pressure calculations as described later.

After transposing the two phases with dissimilar phases facing each other across the gaps, the two gaps are closed in small steps corresponding to separations at which the

pressure will be calculated ( $< 10^{-3}$ ). Each time the separation is reduced the system is given  $10^3$  MC Cycles to relax. Eventually the gap is entirely closed, and the system has two interfaces of area equal to the box cross section.

### 2.3.4 Pressure and Work Calculation

We calculate the pressure on the wall using virtual perturbations of the wall position following similar well-known volume perturbation methods.<sup>114</sup>

$$p = \left( \frac{\partial F}{\partial V} \right)_{N,T} = \frac{\ln(\langle e^{-\beta \Delta U} \rangle)}{\Delta V} \quad (3)$$

where  $F$  is the free energy,  $V$  is the volume of box,  $U$  is the configurational energy, and the changes ( $\Delta U$ ,  $\Delta V$ ) are obtained upon virtual movements of the wall. Let the initial wall position from the midplane be  $z$  and the cross-sectional area in the  $xy$  plane be  $A$ . If the wall is moved by  $\delta z$  then the change in volume  $\Delta V = -A\delta z$ , and we can write down Equation (3) as

$$p(z) = - \frac{\ln(\langle e^{-\beta \Delta U(z)} \rangle)}{A\delta z} \quad (4)$$

The expression  $\langle e^{-\beta \Delta U} \rangle$  in our case can be interpreted as the ensemble-average probability of overlap between the wall and any particle upon perturbation. For cubes we generally use  $\delta z = 0.001$  (see Supporting Information).

To accurately determine the pressure at a given separation, we conduct an NVT simulation with the initial configurations as described previously. Each simulation was conducted for  $10^6$  MC cycles and overlap with a virtual perturbation was checked every 10 cycles. The statistics thus obtained were analyzed to calculate the pressure  $p(z)$  for Steps I and III. Assuming a reversible process, the work done per unit area was calculated with the following expression that integrates pressure (force per unit area on the plane) over the displacement of the wall:

$$w = \int_{z_i}^{z_f} p(z) dz \quad (5)$$

where  $z_i$  and  $z_f$  are the initial and final distance of the wall from the midplane. The work per unit area thus calculated was used to obtain  $\gamma$  using Equation 2.

### 2.3.5 Corrugated Cleaving Walls

To measure the interfacial free energy of the (110) plane in hard cubes crystal we needed to implement corrugated walls<sup>88</sup> compatible with the zigzagging interface, or else the crystal would spontaneously reorient during the cleaving and merging processes. Here we present a simplified implementation for corrugated walls that only interact with the centroids of the particles.

Let the plane be corrugated along the y-axis. The corrugated wall was simulated through a triangular wave given by the following function for the z coordinate of the wall ( $z_{wall}$ ) at a given y-coordinate and position of the wall z:

$$z_{wall,\pm}(y, z) = \left| y \bmod \lambda - \frac{\lambda}{2} \right| - \frac{\lambda}{4} \mp \frac{\lambda}{4} + z \quad (6)$$

where  $\pm$  refers to different walls based on the direction of movement during Step I, and  $\lambda$  is the wavelength of corrugation along the y-axis. Note that the position of the wall z is defined as the z-coordinate of the leading peaks of the triangular wave facing the direction of movement during Step I. In this way, at  $z = 0$  neither wall interacts with any particle at the beginning of the simulation.

The final positions of the walls at the end of Step I was kept conservatively at  $z_{final,\pm} = \pm \left( a_c + \frac{\lambda}{2} \right)$  to ensure that particles cannot interact across the gap. The pressure calculations for the corrugated wall are identical to those for the flat wall. The wavelength  $\lambda$  is determined by the initial conditions of the crystal simulation box and was chosen such that the box length along y-axis  $L_y = n_p \lambda$  where  $n_p$  is the number of particle layers along the y-axis. This choice ensures compatibility with the periodic boundary conditions and cleaves the systems in a manner conforming with the crystal plane. In principle this approach can be generalized to other topographies with an appropriate wall function.

## 2.4 Interfacial potential of mean force (PMF)

We calculated the PMF experienced by a free particle interacting with a perfect interface of particles in a crystalline arrangement. NVT simulations were conducted comprising a single immobile layer of crystalline particles and a free particle. The spacing of the crystalline particles was chosen to be consistent with the volume fraction of the coexistence conditions. Statistics for free particle position were obtained through  $10^7$  MC cycles. The coordinates of the free particles were histogrammed with a resolution of  $0.05a_c$ . The *PMF* experienced at a given bin  $i$  is given by:

$$PMF_i = -k_B T \ln\left(\frac{f_i}{f_\infty}\right) \quad (7)$$

where  $f_i$  and  $f_\infty$  are the visiting frequencies for the  $i^{th}$  bin and a distant bin where the particle is not interacting with the immobile particles, respectively. The statistics were sufficient to obtain states with  $PMF \sim 7 k_B T$ . For comparison across different systems, the “effective” position of the interface was chosen to correspond to the point where  $PMF = 5 k_B T$ .

## 2.5 Measurement of Interfacial Thickness

We estimate the thickness of the interface using the final configuration at the end of Step III of the cleaving process. The interface thickness  $\delta$  is defined in a manner analogous to phase field models:<sup>115</sup>

$$\phi(z) = \frac{1}{2} \left( 1 + \tanh \frac{z}{2\delta} \right) \quad (8)$$

where  $\phi$  is a scalar order parameter and  $z$  is the position with respect to the interface.

For our analysis we define  $\phi$  as:

$$\phi = \frac{\rho_s - \rho(z)}{\rho_s - \rho_l} \quad (9)$$

where  $\rho_s$ ,  $\rho_l$ , and  $\rho(z)$  are the densities of the bulk solid, bulk liquid, and system at position  $z$ . Thus,  $\phi = 0$  for the bulk solid, and  $\phi = 1$  for the bulk liquid. The starting interfacial configurations are simulated further for  $10^6$  MC cycles in an NVT ensemble to obtain statistics for  $\phi(z)$ . Equation 8 is fitted to the  $z$  vs.  $\phi(z)$  data using a least squares method to obtain  $\delta$ , which is reported in circumradius units ( $a_c$ ).

### 3 Results and Discussion

#### 3.1 Interfacial Free Energy

The calculation was carefully performed to ensure that the process does not significantly alter the bulk behavior of either phase (e.g., by ordering of the disordered phase or disordering of the ordered phase). The process was conducted for various system lengths, and it was observed that the cleaving process influences the structure of a layer  $\sim 3$  particles deep into the bulk phases. Hence a system size of  $N = 2000$  particles ( $\sim 20$  layers) on each phase was chosen. Sample configuration at the end of

Step III for the case that the interfacial plane faces the (100) crystal plane is shown in **Figure 16a**. Intermediate configurations at other steps are shown in the Supporting Information. The pressure profiles for cleaving and merging cubes at coexistence pressure  $p_{co} = 4.0$  are shown in **Figure 16b** and **Figure 16c** for the ordered and disordered phase, respectively.

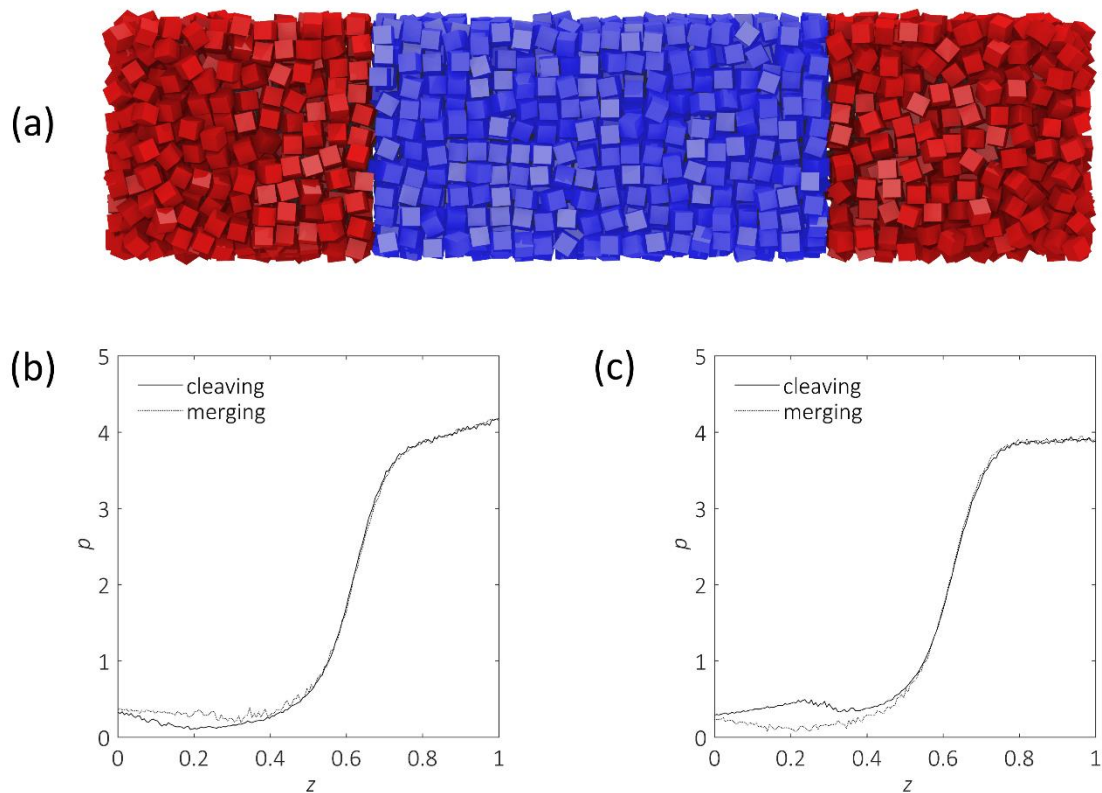


**Figure 16:** Cleaving walls for hard cubes (100) plane at coexistence pressure  $p = 4.0$ . (a) Sample configuration at the end of Step III. Ordered and disordered phase particles are colored blue and red, respectively. Intermediate configurations at other steps are shown in the Supporting

Information. (b, c) Pressure variation with the position of the cleaving walls with respect to the midplane (quantifying the gap width) for (b) ordered and (c) disordered phase. Step I-Cleaving is shown with a solid line and Step II-Merging is shown with gray line. Scaling for the axes is described in Section 2.2.

The interfacial free energy for the (100) orientation of the ordered phase was determined as  $\gamma_{100} = 0.042 \pm 0.007$ . Attempts to calculate the interfacial tension for the (110) orientation  $\gamma_{110}$  with a flat (i.e., non-corrugated) cleaving wall resulted in the ordered phase reorienting in the (100) direction upon merging. This rapid reorienting is rather unique to cubes as we have tested a variety of orientations of other polyhedral crystals without facing the same problem. There could be several reasons for this. The tendency to reorientation indicates that  $\gamma_{100} < \gamma_{110}$ , so that the system relaxes toward the more stable interface. The short time scale of this process is likely facilitated by the unusually high diffusivity<sup>4</sup> and vacancy concentration<sup>95,111</sup> in the ordered phase for cubes. Fast crystal domain reorientation is consistent with our observations in a previous study<sup>106</sup> that hard cubes exhibit fast grain resolution dynamics. Also, because the disordered phase is cleaved by a flat wall, the cubes in the closest layers tend to align parallel to it, which in turn tend to realign (flatten) the closest zigzag (110) layer of the ordered phase during the merging step. This limitation was resolved with implementation of a corrugated cleaving wall<sup>88</sup> as described in the Section 2.3.5. This approach allows for the disordered phase to be cleaved with a zigzag presentation of the particles compatible with the (110) crystal plane. The final configuration with (110)

interfaces at the end of Step III and pressure profiles for both phases are shown in **Figure 17**.

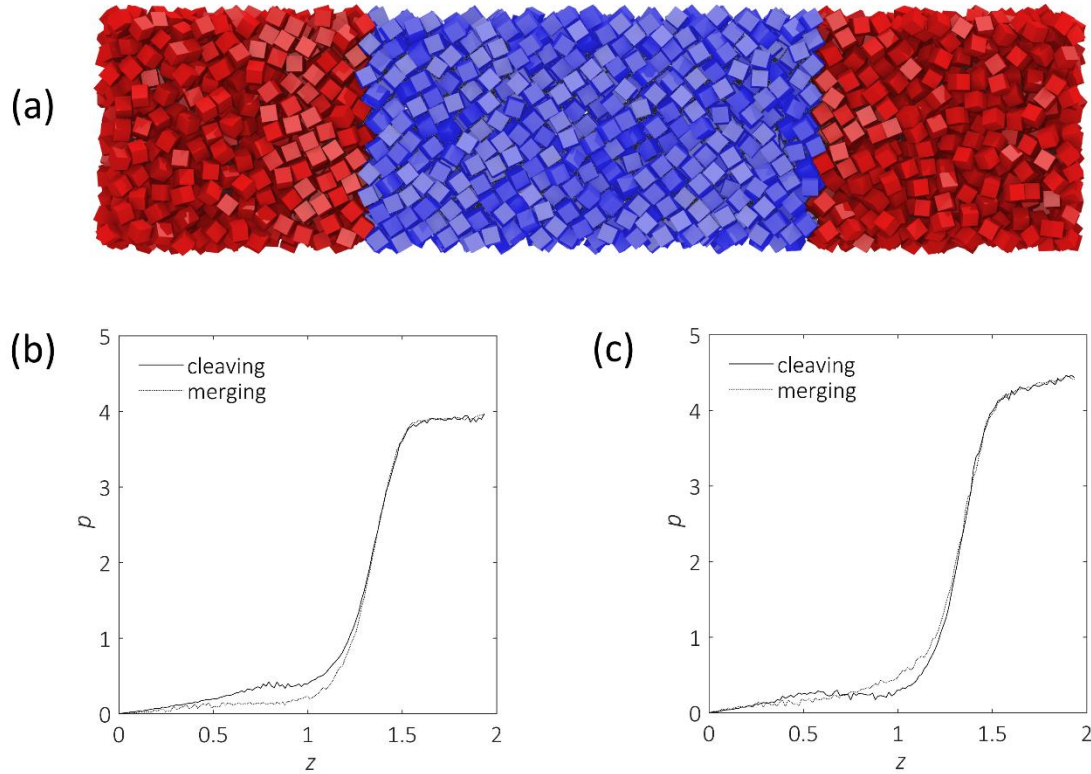


**Figure 17:** Cleaving walls for hard cubes (110) plane at coexistence pressure  $p=4.0$ . (a) Sample configuration at the end of Step III. Ordered and disordered phase particles are colored blue and red, respectively. Intermediate configurations at other steps are shown in the Supporting Information. (b, c) Pressure variation with the position of the cleaving walls defined by the leading peak of the corrugated wall (see Section 2.3.5) with respect to the midplane (quantifying the gap width) for (b) ordered and (c) disordered phase. Step I-Cleaving is shown with a solid line and Step II-Merging is shown with dotted line. Scaling for the axes is described in Section 2.2.

The interfacial free energy for the (110) orientation of the ordered phase was determined as  $\gamma_{110} = 0.090 \pm 0.010$ . This value is more than twice  $\gamma_{100}$ , confirming

that this difference is the main force driving the crystal reorientation with a flat wall observed earlier. The physical reason for why  $\gamma_{100} < \gamma_{110}$  can be rationalized by examining the entropic and enthalpic effects associated with the particles in the disordered region in contact with the different ordered planes, to be referred here as *wetting layer*. The pV component of the enthalpy (and free energy) favors smaller volumes or denser packing (due to closer contact) of the wetting layer; likewise, a more efficient packing (attained by partial lateral alignment) would favor packing entropy of that layer. As the potential of mean force (PMF) calculations reveal (**Figure 18**), the (110) plane produces a longer-range repulsive field, which is a consequence of its rougher and more intrusive profile (**Figure 18** inset). This also translates into a thicker wetting layer as shown in **Figure 19**. These observations are consistent with a larger free energy penalty in the 110 wetting layer and hence  $\gamma_{110} > \gamma_{100}$ . Based on these physical considerations, we further anticipate that  $\gamma_{111} > \gamma_{110} > \gamma_{100}$ .

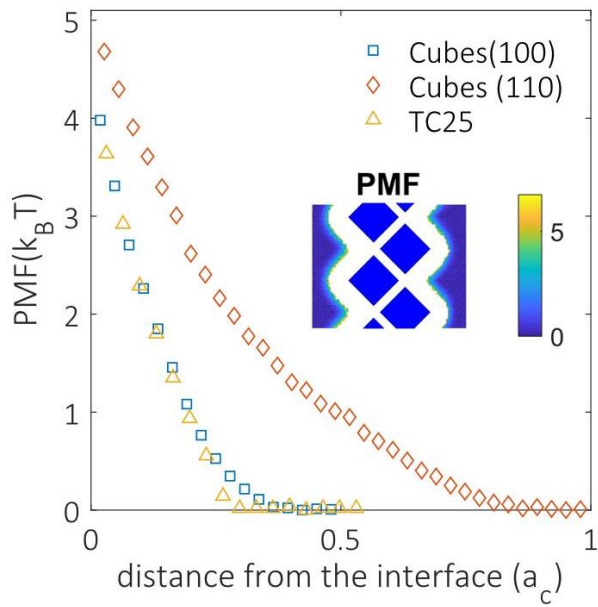


**Figure 18:** Interfacial potentials of mean force (PMF) at coexistence for various cases. Inset: two-dimensional PMF surface for (110) plane of hard cubes, where crystalline cubes (blue) are placed in the middle at their fixed positions in the calculation. Details on the calculation are provided in Section 2.4.

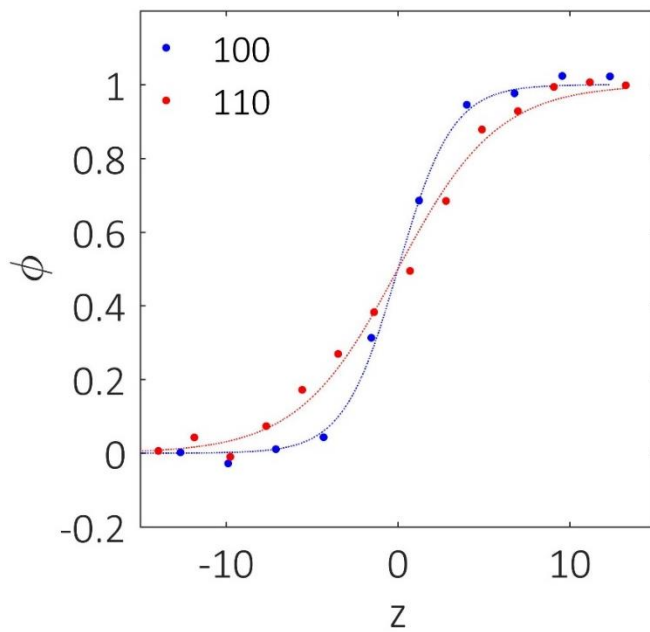


**Figure 19:** Scalar order parameter  $\phi$  as a function of position with respect to the interface ( $z$ , in circumradius  $a_C$  units) for various crystal planes of hard cubes. The interfacial thickness of (100) and (110) crystal planes were found to be  $\delta_{100} = 1.6 \pm 0.2$  and  $\delta_{110} = 2.9 \pm 0.3$ , respectively. Details on the calculation are provided in Section 2.5.

Based on the  $\gamma$  values thus calculated, a Wulff construction<sup>116–119</sup> could be performed to obtain information about the nucleus geometry. The governing principle of Wulff construction states that the length  $h$  of a perpendicular to a crystal plane passing through the centroid is proportional to its interfacial free energy  $\gamma$ . Based on this principle, the perpendiculars of (100) and (110) facets should be related as  $h_{110} = 2.14h_{100}$ . This relation would put the (110) plane outside the inner volume enclosed by (100) plane since  $h_{110} > \sqrt{2}h_{100}$ . This implies that, if we restrict ourselves to the closed-packed facets,<sup>119</sup> the (110) should not show up in an equilibrium nucleus geometry. Regardless, since the (100) facet is the most closed-packed<sup>119</sup> facet for this crystal,  $\gamma_{100}$  can be used as a representative value for comparison across different shapes.

We use reduced interfacial free energies  $\bar{\gamma}$  as defined in Section 2.2 for comparison across different shapes. In most studies of hard polyhedra the interfacial free energy has been calculated indirectly through nucleation free energy barrier calculations<sup>8,105</sup> leveraging classical nucleation theory (CNT). These approaches are sensitive to the definition of the order parameter used to ascertain the interface of the nucleus.<sup>120</sup> Nevertheless, these indirect estimates for hard spheres are very much comparable to those obtained from direct methods including the cleaving walls approach.<sup>67</sup> Hence we

use CNT estimates for comparison among shapes when results from any direct method is unavailable.

At coexistence, the value of the reduced interfacial free energy for the (100) crystal facet in cubes ( $\bar{\gamma}_{100} = 0.088$ ) is about one sixth the value for hard spheres ( $\bar{\gamma}_{HS} \sim 0.52$  for all closed packed orientations). For comparison, orientationally-average interfacial free energies reported for faceted particles (at the disorder-order phase transition) have been at most 20% lower than that of hard spheres (e.g., for cuboctahedra, truncated octahedra and rhombic dodecahedra),<sup>8</sup> and often higher than that (e.g., for octahedra and gyrobifastigia).<sup>59,96</sup> We illustrate these observations in **Figure 20** where we plot reduced interfacial free energy  $\bar{\gamma}$  at a given supersaturation  $\Delta\mu_{od}$  for a number of shapes as reported in the literature. It is evident that cubes have by far the lowest value of reduced interfacial free energy, which generally increases with  $\Delta\mu_{od}$ .

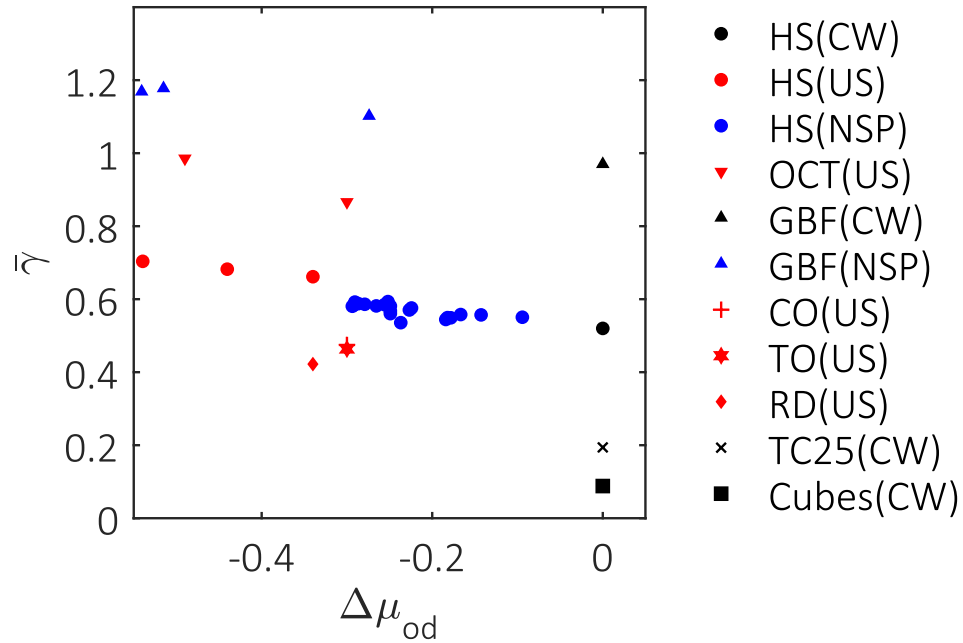


**Figure 20:** Reduced interfacial free energy  $\bar{\gamma}$  at a given supersaturation  $\Delta\mu_{od}$  for various shapes (HS: hard spheres, OCT: octahedra, GBF: gyrobifastigia, CO: cuboctahedra, TO: truncated octahedra, RD: rhombic dodecahedra, TC25: truncated cubes with  $s=0.25$ , and Cubes) reported in literature using a variety of methods (CW: cleaving walls, US: umbrella sampling and classical nucleation theory, NSP: nucleus-size pinning with classical nucleation theory). Data sources: HS(CW)<sup>88</sup>, HS(US)<sup>40</sup>, HS(NSP)<sup>96</sup>, OCT(US)<sup>59</sup>, GBF(CW)<sup>121</sup>, GBF(NSP)<sup>96</sup>, CO-TO-RD(US),<sup>8</sup> Cubes and TC25: this work.

Physically, the small  $\bar{\gamma}$  for hard cubes implies a small penalty for creating solid-liquid interfaces, which correlates with the observation of a relatively high incidence of ordered and disordered domains co-existing next to each other in both the disordered and ordered phase. This results in a significant concentration of ordered domains in the disordered phase and hence a high fraction of ordered particles (about 3% at coexistence compared to less than 0.05 % for hard spheres). Likewise, the high content (>6%) of mobile vacancies in the solid phase<sup>95</sup> connotes some localized liquid-like

behavior. This similarity between some local configurations from its disordered and ordered phases means that both phases share a fraction of the same phase space in the terms of translational and orientational order, which enhance their interfacial affinity.

The low  $\gamma$  could also be indicative of the proximity between the binodal and spinodal conditions for cubes, as a zero interfacial tension is a characteristic of the spinodal point in other systems.<sup>122,123</sup> This hypothesis is strengthened by the fact that the orientational correlation length diverges with pressure (see SI). We attempted a calculation of  $\gamma$  for cubes at finite degrees of supersaturation, but the results were inconclusive due to large statistical variations associated with a significant tendency for ordering in the disordered phase. A more complete picture of the consequences of low  $\bar{\gamma}$  values is provided in the next section through a theoretical analysis.

We also examined the effect of a small perturbation to the cubic shape on interfacial tension by computing  $\bar{\gamma}_{100}$  for truncated cubes with truncation parameter<sup>7</sup>  $s = 0.25$ , hereafter referred to as TC25. The phase behavior is similar to that of hard cubes, with a first order transition from a disordered phase to a simple cubic crystal. Moreover, the disordered phase also has abundance of cubatic fluctuations, and the ordering transition progresses spontaneously at very low supersaturations. We also calculated the free energy barrier for the TC25 disorder to order transition at coexistence through umbrella sampling as described elsewhere<sup>106</sup> (see crucial details in the Supporting

Information). The free energy profile as a function for fraction of ordered particles ( $x_{ordered}$ ) at coexistence pressure for TC25 is shown in **Figure 21**, along with previously reported<sup>106</sup> results for hard cubes. At coexistence, the free energy barrier for TC25 is over three times larger than that of hard cubes. While there is no clear theoretical framework that can describe the exact relationship between  $\bar{\gamma}$  and  $\Delta G^*$  for this non-classical phase transition, the much higher barrier would indicate a correspondingly higher value for interfacial free energy. Indeed, we find that the interfacial free energy for the (100) plane of TC25 using the cleaving walls method at the coexistence pressure<sup>10</sup>  $p_{co} = 3.64$  is  $\bar{\gamma}_{100,TC25} = 0.194$ , which is about two times that for hard cubes. Another important observation is that  $x_{ordered}$  at both the disordered-state basin and the top of the barrier is much higher for TC25 compared to cubes. We note, however, that the order parameter definitions (see Supporting Information) are not identical for hard cubes and TC25 and hence the  $x_{ordered}$  for the two systems cannot be unambiguously compared. While the PMF for cubes and TC25 (associated with the 100 plane) are expectedly comparable, the densities of the coexistence phases are higher for TC25 than those for cubes, which would be expected to increase  $\gamma$ .

An interesting trend in **Figure 20** is that particles shapes having more similarity to cubes tend to have lower  $g$  (e.g., TC25 and CO). This could reflect the fact that a preference of local ordered motifs with 6-fold coordination and smaller unit cells are easier to generate than structures requiring the coordination for more nearest-neighbor

particles (like 8 or 12) and larger unit cells. The low coordination number of cube-like shapes is a likely contributor to low  $g$  values by promoting low-free-energy-cost 6-fold configurations in route to the ordered phases they form (even if not a simple cubic). Since no other hard particle is able to order with a smaller coordination number and unit cell, we surmise that hard cubes likely possess the lowest  $g$  value of all athermal systems at the order-disorder transition (note that we exclude the case of tetrahedra whose isotropic phase does not transition into a simple-unit-cell solid<sup>124</sup>).

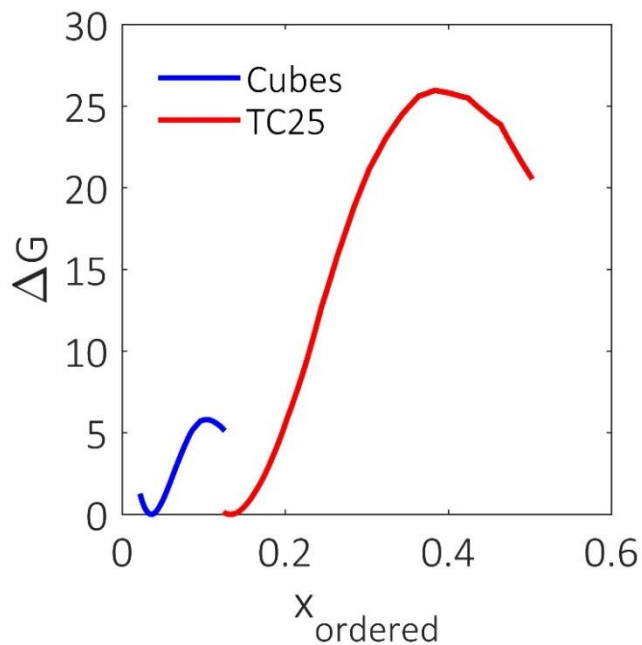


**Figure 21:** Free energy ( $\Delta G$ ) profile calculated as function of fraction of ordered particles ( $x_{\text{ordered}}$ ) for TC25 via umbrella sampling at coexistence  $p = 3.64$ . Previously reported<sup>106</sup> free energy profile for a hard cubes system of identical size ( $N=1000$ ) is also shown for comparison. Free energy is in  $k_B T$  units.

### 3.2 Theoretical quantification of cubatic fluctuations

We aim to provide a simple description of how the fraction of ordered particles ( $x_{ordered}$ ) compounding the local solid-like fluctuations in the disordered phase is related to  $\bar{\gamma}$  at a given supersaturation  $\Delta\mu_{od}$ . In this model, the cubatic fluctuations are in the form of nuclei which are non-interacting with each other and distributed uniformly throughout the bulk.<sup>125</sup> Let  $\Delta G(n)$  be the free energy change associated with the formation of an ordered cluster of size  $n$  (analogous to  $n$  particles), the classical nucleation theory (CNT) provides the following expression:

$$\Delta G(n) = \Delta\mu_{od}n + A\bar{\gamma}n^{2/3} \quad (10)$$

where  $A$  is a geometric factor capturing the shape of the nucleus assuming that its surface area scales with the two-thirds power of the volume. For simplicity, we assume that both the inner and the interfacial regions of a cluster can be described by  $\mu_o$  and  $\bar{\gamma}$ . This is not true for clusters smaller than a characteristic length and there are models that could be used to account for such an effect.<sup>126–128</sup> As such, our model will overestimate  $x_{ordered}$  if  $\bar{\gamma}$  is higher for smaller clusters than larger ones in the system being considered, such as in hard spheres.<sup>129</sup>

For steady state conditions for a system evolving from the metastable disorder-phase basin, the distribution of fraction of particles  $x_n$  belonging to clusters of size  $n$  can be described by the law of mass action<sup>130</sup> as:

$$x_n = nx_0^n e^{-\Delta G(n)} \quad (11)$$

where  $x_0$  is the fraction of disordered particles. We note that such a formulation assumes no inter-cluster interactions, that is, the effect of impingements between clusters is neglected so that each cluster is independent from others and only surrounded by disordered cubes. Further, the ordered clusters exhibiting a range of representative sizes are assumed to be well mixed (uniformly distributed) throughout a “continuous” phase of disordered cubes. Despite the limitations imposed by these assumptions (i.e., a scenario of relatively dilute clusters), this model forms a good basis for illustrating the consequences of interfacial tension on the concentration of ordered particles in the metastable disordered basin. We define the metastable basin as a disordered phase that may contain clusters up to the critical cluster size at the top of the barrier defined as:

$$n^* = \left( \frac{2A\bar{\gamma}}{3|\Delta\mu_{od}|} \right)^3 \quad (12)$$

The fraction of ordered particles in the basin can then be evaluated as an integral over various sizes of ordered clusters described by Equation 11:

$$x_{ordered} = \int_{0^+}^{n^*} x_n dn \quad (13)$$

A discrete version of the model could also be formulated considering only integer nucleus sizes (see Supporting Information). We favor here the continuous version of the

model as it avoids discontinuous jumps in values and makes trends easier to follow.

Applying mass balance on all particles:

$$x_0 + x_{ordered} = 1 \quad (14)$$

Since the left-hand side of Equation 14 (when coupled to Equations 12 and 13) consists of continuous functions and takes a value of zero for  $x_0 = 0$  and a value greater than unity for  $x_0 = 1$ , then the intermediate value theorem ensures that a solution for  $x_0 \in [0, 1]$  exists where the equality of Equation (14) holds. We can then numerically solve for this value of  $x_0$  at any given conditions of  $\Delta\mu_{od}$  and  $\bar{\gamma}$ .

We can follow the consequences of this mass action-derived classical nucleation theory (MADCNT) model in the context of the cubatic fluctuations observed in the disordered phase of hard cubes by evaluating  $x_{ordered}$  as a function of  $\Delta\mu_{od}$  and  $\bar{\gamma}$  for a particular case. For simplicity, if the ordered clusters are spherical, the geometric factor will be:

$$A = (36\pi)^{\frac{1}{3}} \quad (15)$$

As an example, **Figure 22a** shows a plot of  $x_{ordered}$  as a function of  $\Delta\mu_{od}$  and  $\bar{\gamma}$ .

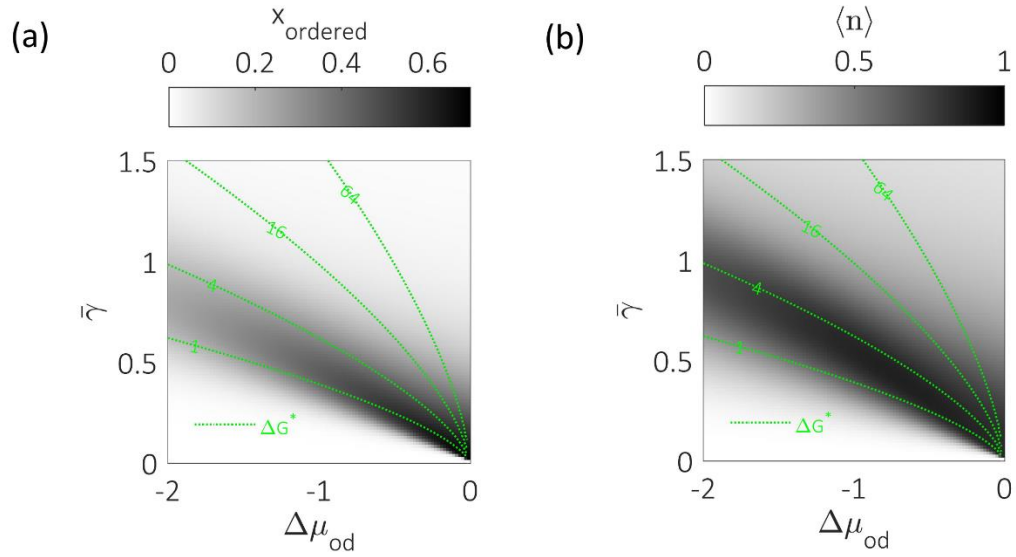


**Figure 22:** Predictions from the MADCNT model for spherical ordered clusters. (a) Fraction of ordered particles  $x_{ordered}$  and (b) Average cluster size  $\langle n \rangle$  as a function of  $\Delta\mu_{od}$  and  $\bar{\gamma}$ . The isolines for the nucleation barrier  $\Delta G^*$  are shown in green. The calculations were performed with a resolution of 100 points along each axis.

In general,  $x_{ordered}$  remains relatively low ( $< 0.01$ ) except for a diagonal ‘band’ where it can get as high as 0.697. The model also allows us to extract information about the cluster size distribution. Sample distributions  $x_n$  at coexistence as a function of cluster size  $n$  are shown in **Figure 23**. Ordered clusters predominantly exist in clusters of small sizes, with the spread of cluster sizes generally decreasing with increasing  $\bar{\gamma}$ . It is informative to evaluate the average cluster size:

$$\langle n \rangle = \frac{x_{ordered}}{\int_{0^+}^{n^*} x_0^n e^{-\Delta G(n)} dn} \quad (16)$$

**Figure 22b** reveals that the average cluster size generally correlates with  $x_{ordered}$ , also attaining higher values along the diagonal band.

The trends in these MADCNT predictions can be understood by considering two effects at play relating to the metastable basin: its depth (embodied by  $\Delta G(n^*)$ ) and its width (embodied by  $n^*$ ). The width of the basin,  $n^*$  determines the upper limit to the integral in Equation 13. A larger  $n^*$  would imply that more numerous ordered species are competing against the disordered particles, resulting in a larger  $x_{ordered}$ . Hence the width contributes positively to  $x_{ordered}$ . On the other hand, the depth of the basin is related to the nucleation barrier:

$$\Delta G(n^*) = \Delta G^* = \frac{4(A\bar{\gamma})^3}{27|\Delta\mu_{od}|^2} \quad (17)$$

and since  $\Delta G(n) < \Delta G(n^*)$ , larger values will translate into smaller exponential factors within the integral in Equation 13, making the larger clusters rare. Hence an increased depth of the metastable basin contributes negatively to  $x_{ordered}$ . Since both width and depth of the metastable basin increase with  $\bar{\gamma}$  and decrease with  $\Delta\mu_{od}$ , the following three distinct regions in the plot can be identified depending on whether one effect dominates or both effects are in play:

- I. Bottom-left triangular region: This region has very low  $x_{ordered} \ll 1$  due to narrow metastable basins ensuing from a low  $\bar{\gamma}$  and high  $|\Delta\mu_{od}|$ . In practice, it would be very difficult to sustain a metastable state located in this region due to the very small critical nucleus sizes and barriers (see isolines in Figure 8),

which will likely manifest as a spinodal decomposition. Interestingly, the line for  $n^* = 1$  demarcates the boundary of this region where  $n^* < 1$ .

- II. Top-right triangular region: This region also has a low  $x_{ordered} \ll 1$  but due to reasons different from those for region I. Due to the high  $\bar{\gamma}$ , the basins are wide and deep. This would result in a rather robust metastable state with rare occurrence of nuclei akin to systems where nucleation and growth is the mechanism of phase transition. Generally,  $x_{ordered}$  decreases as  $\bar{\gamma}$  increases (interfaces become more expensive) and/or as  $\Delta\mu_{od}$  increases (ordered phase becomes less stable). In contrast with region I,  $\langle n \rangle$  is slightly higher because larger clusters are being considered. In this region we can sufficiently describe the fraction of ordered particles through MADCNT, since a low fraction implies the nuclei are not likely to interact with each other. The values of  $x_{ordered}$  predicted by the model in this scenario have been validated for specific conditions for hard spheres, and are consistent with predictions of models that use appropriate corrections for interfacial tension as a function of nucleus size.<sup>129</sup>
- III. Downward diagonal band: In this region neither of the effects dominate, leading to a metastable basin that is neither too narrow nor too deep. This results in a non-negligible  $x_{ordered}$  that could take up values greater than 0.5, especially

near the lower-right corner (low  $\bar{\gamma}$ ,  $|\Delta\mu_{od}|$ ). This is a scenario that MADCNT is ill-suited to describe since beyond a certain  $x_{ordered}$  the ordered clusters are likely to interact with each other and form motifs that are not described by Equation 10. Indeed, at sufficiently high  $x_{ordered}$ , a percolating network of ordered cluster might form. We refrain from assigning a percolation threshold as it will depend on the cluster size distribution which varies with conditions  $\bar{\gamma}$ ,  $|\Delta\mu_{od}|$ . For example, for completely uncorrelated ordered particles distributed throughout the bulk, the three-dimensional percolation threshold for site percolation of the intrinsic crystal lattice might be an appropriate bound. The band becomes more diffused as we go to higher supersaturations, eventually connecting regions I and II.

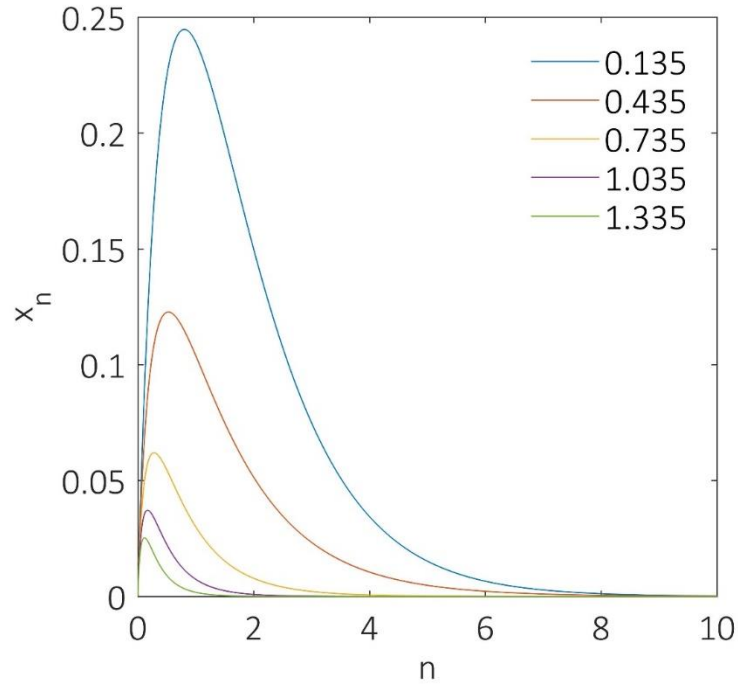


**Figure 23:** Sample distributions ( $x_n$ ) of ordered particles over various cluster sizes ( $n$ ) at coexistence for various values of  $\bar{\gamma}$  as predicted by MADCNT model.

While  $\bar{\gamma}$  and  $\Delta\mu_{od}$  are easy-to-interpret physical properties, the trends get simplified when we evaluate  $x_{ordered}$  as a function of  $\Delta G^*$  and  $n^*$ , surrogates of depth and width of the metastable basin respectively, as shown in **Figure 24**. We notice that regions I and II are mapped into a single triangular region (light area in **Figure 24**), and  $x_{ordered}$  generally increases with increasing  $n^*$  and/or decreasing  $\Delta G^*$ . Thus, the fraction of ordered particles in the metastable phase increases with shallower and wider basins. We note that this alternative mapping preserves the general trends described earlier but it shrinks certain areas of **Figure 22** and expands others, with certain regions involving infeasible/unusual conditions.

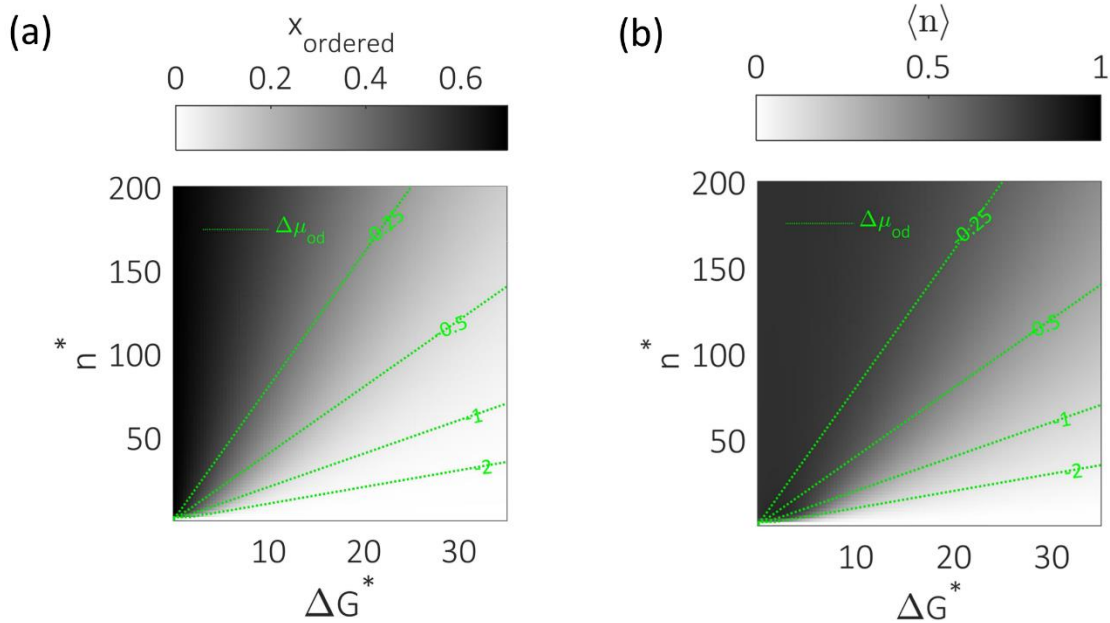


**Figure 24:** Predictions from the MADCNT model for spherical ordered clusters with: (a) Fraction of ordered particles  $x_{ordered}$  and (b) Average cluster size  $\langle n \rangle$  as a function of  $n^*$  and  $\Delta G^*$ . The isolines for the supersaturation  $\Delta\mu_{od}$  are shown in green. The calculations were performed with a resolution of 100 points along each axis.

It is instructive to compare Figure 8a with Figure 6. While direct quantitative comparison may be difficult since the geometric factor  $A$  is system specific, it can be observed that most shapes would likely be placed in region II given the relatively low concentration of ordered particles observed in the metastable disordered phases of those systems. On the other hand, both cubes and TC25 could be placed in region III by the virtue of their low  $\bar{\gamma}$ , which is corroborated by the observation of non-negligible  $x_{ordered}$  in their metastable phases in simulations and can be associated with a wide, shallow metastable basin.

The validity of a nucleation scenario rests on the basic assumption that at the early stages of phase transformation the nuclei of the incipient phase are rare and grow without interacting with other nuclei before approaching their critical size. This would largely hold for the region II but would eventually not be true for systems in region III. For cubes, an abundance of cubatic fluctuations of the incipient ordered phase (as predicted for lower interfacial free energy) would violate this assumption. Under such circumstances, the dominant mechanism cannot be nuclei growth by conversion of disordered particles at the interface since there would also exist interfaces between ordered domains of non-negligible size. Usually, such impingement of nuclei leads to a halt in growth<sup>131</sup> and a final polycrystalline state. However, as illustrated in our previous publication,<sup>106</sup> hard cubes exhibit fast dynamics of grain resolution by quickly reorienting intermediate layers along the boundary of two grains and then propagating a uniform alignment. Hence, any two impinging clusters could merge in a process similar to Oswald ripening. An increase in concentration of ordered clusters would increase instances of such growth mechanisms. There would be a critical concentration beyond which such instances of consolidation (or ripening) would become more probable than the breaking of clusters into smaller clusters. This would be consistent with our observation in a previous report<sup>106</sup> of a critical concentration of ordered cubes being required to effect the disorder-to-order phase transition. Indeed, we found that cubes

exhibit a transition that involves ordered phase nuclei gradually consolidating by resolving grain boundaries through local reorientation events.

#### **4 Conclusion and Outlook**

In this study, we implemented the cleaving-walls method to directly measure order-disorder interfacial free energy for the (100) and (110) crystal planes of hard cubes. We found them to be substantially lower than those for other reported cases of hard-core particles where nucleation and growth is reported. Our MADCNT model predicts that a lower interfacial tension gives rise to more abundant ordered clusters in the disordered phase, which could explain the abundance of cubatic fluctuations in the disordered phase for hard cubes. We also find that hard truncated cubes (TC25) have a higher  $\bar{\gamma}_{100}$  than hard cubes which also translates into higher free energy barriers at comparable coexistence conditions.

There are however many open questions regarding the non-classical characteristics of the ordering phase transition of hard cubes. It would be of interest to attain a deeper understanding of why hard cubes have a lower surface tension than other shapes. Given that TC25 also has a smaller  $\bar{\gamma}$  compared to other particle shapes points to the cubic lattice structure of the ordered phase, and its known peculiarities, as playing a central role. Of course, cubic symmetry may not be a sufficient condition for a low  $\bar{\gamma}$ ; indeed, we expect that if interparticle attractions are enacted among cubes,  $\bar{\gamma}$  could be made

significantly larger. In this context, interfacial tension calculations for other hard-core shapes and crystal planes would be informative and could help illuminate any trends therein. For example, while we found that truncation of the cubes increases the interfacial free energy (i.e., going from perfect cubes to TC25), it would be worthwhile to explore if larger perturbations can alter the behavior to the point where the classical nucleation and growth picture becomes a valid description. In assessing the role of  $\gamma$  in the ordering of cubes and concomitant theories, it is also important to keep in mind that since most cubatic fluctuations are small and encompass only ten or fewer particles, bulk-like domains and their interfaces are not well defined. Further, as we have noticed in our simulations, the effect of the interface could reach  $\sim 3$  particles deep into either phase. There are interesting approaches to address these effects<sup>128,129,132,133</sup> and describe the free energy of small clusters. Even in cases where nuclei are large enough to have well defined geometries, it would be interesting to investigate the morphology of the nuclei through Wulff construction,<sup>116,119</sup> especially in cases with aspherical nuclei<sup>96</sup> as this would help evaluating the geometric factor ( $A$ ) in CNT-like theories.

Further studies could aim to provide a more rigorous theoretical treatment that is applicable to region III described in Section 3.2. The key element would be a description of ordered motifs that are preferred when the classical theory predicts the presence of too many ordered nuclei. At high  $\bar{\gamma}$  there would be a preference to make compact

motifs like nuclei but at lower  $\bar{\gamma}$  the ordered domains could comprise loose dendritic structures. Also needed description is a mechanism that captures how the ordered motifs grow, analogous to nucleus growth in CNT. For non-compact ordered domains, the interfacial contribution to the free energy would not necessarily grow monotonously with concentration of ordered particles (see SI), hence leading to more complex free energy landscapes.

### **Supporting Information**

Additional details pertaining to the cleaving walls method, the truncated cube system, and the MADCNT model.

## **5 Acknowledgements**

Funding support from NSF award CBET-1907369 is gratefully acknowledged. We would also like to acknowledge Dr. Vikram Thapar for sharing base simulation code, Dr. Karthik Nayani for sharing useful literature, and Prof. Donald Koch and Prof. Marjolein Dijkstra for insightful discussions.

## 6 Supporting Information

### 6.1 Optimizing Pressure Calculation

The value of the virtual cleaving wall perturbation  $\delta z$  used to calculate the pressure (see Equation 4 in main text) can influence the accuracy of the pressure and hence of  $\gamma$  values. To assess this effect, for a simple case of  $N=1000$  hard cubes at coexistence we evaluated  $\gamma$  for various values of  $\delta z$  (Figure S1(a)). We notice some systematic variation, more so for small  $\delta z$ . For good accuracy, the quantity inside the logarithm in Eq. (4) i.e., the probability of overlap, should not be too close to either zero (correlated sampling) or one (sparse sampling). Furthermore, since the work integrals are dominated by larger

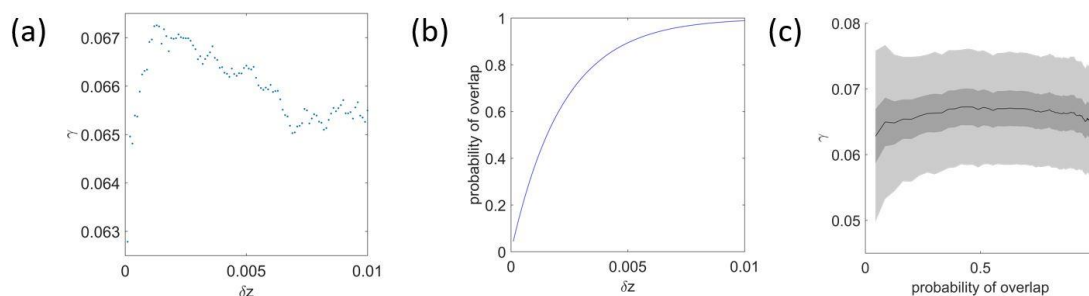


**Figure S1:** Effect of perturbation size  $\delta z$  on pressure calculation for cubes with  $N=1000$  at coexistence. (a)  $\gamma$  as a function of  $\delta z$ . (b) maximum probability of overlap vs.  $\delta z$ . (c) Error estimate in  $\gamma$  using block averages. Lighter shade corresponds to the standard deviation while the darker refers to the standard error for 10 blocks.

pressures, their accuracy directly influences the value of  $\gamma$ . Larger pressures imply the maximum probability of overlap should be near 0.5. Figure S1(b) shows how the probability of overlap quickly increases with increase in  $\delta z$ , crossing 0.5 around  $\delta z \sim 0.001$ . This is also reflected in the values of  $\gamma$  that plateau around the maximum

probability of overlap being around 0.5. Further analysis using block averages reveals that this variation is not that significant and is within error bars of the method itself.

## 6.2 Cleaving Walls Configurations for Cubes

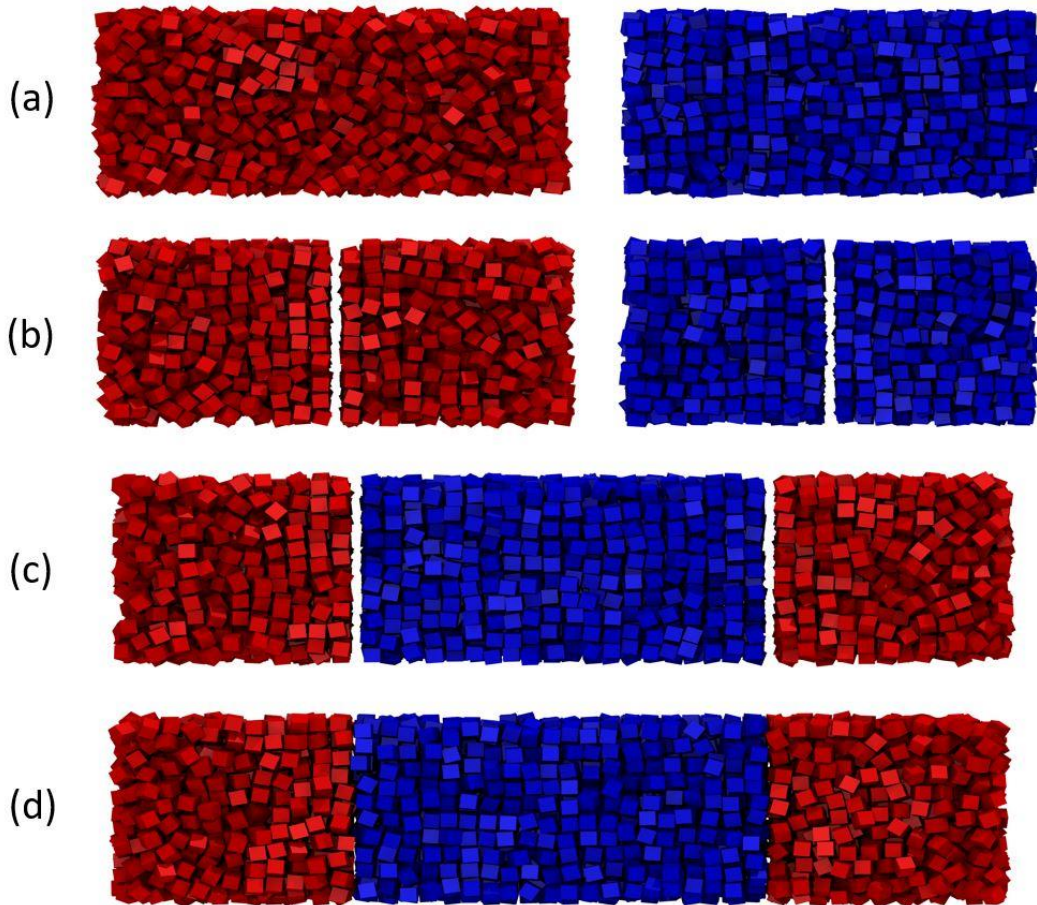


**Figure S2:** Simulation renderings at key steps in the cleaving walls method for  $\{100\}$  crystal plane (a) Bulk simulation boxes of solid and liquid phases with three-dimensional periodic boundary conditions at  $\mathbf{p} = \mathbf{4.0}$ . (b) Phases cleaved at the midplanes. (c) Transposed simulation boxes with dissimilar phases facing each other. (d) Final two-phase state with the gap closed and the two interfaces created.

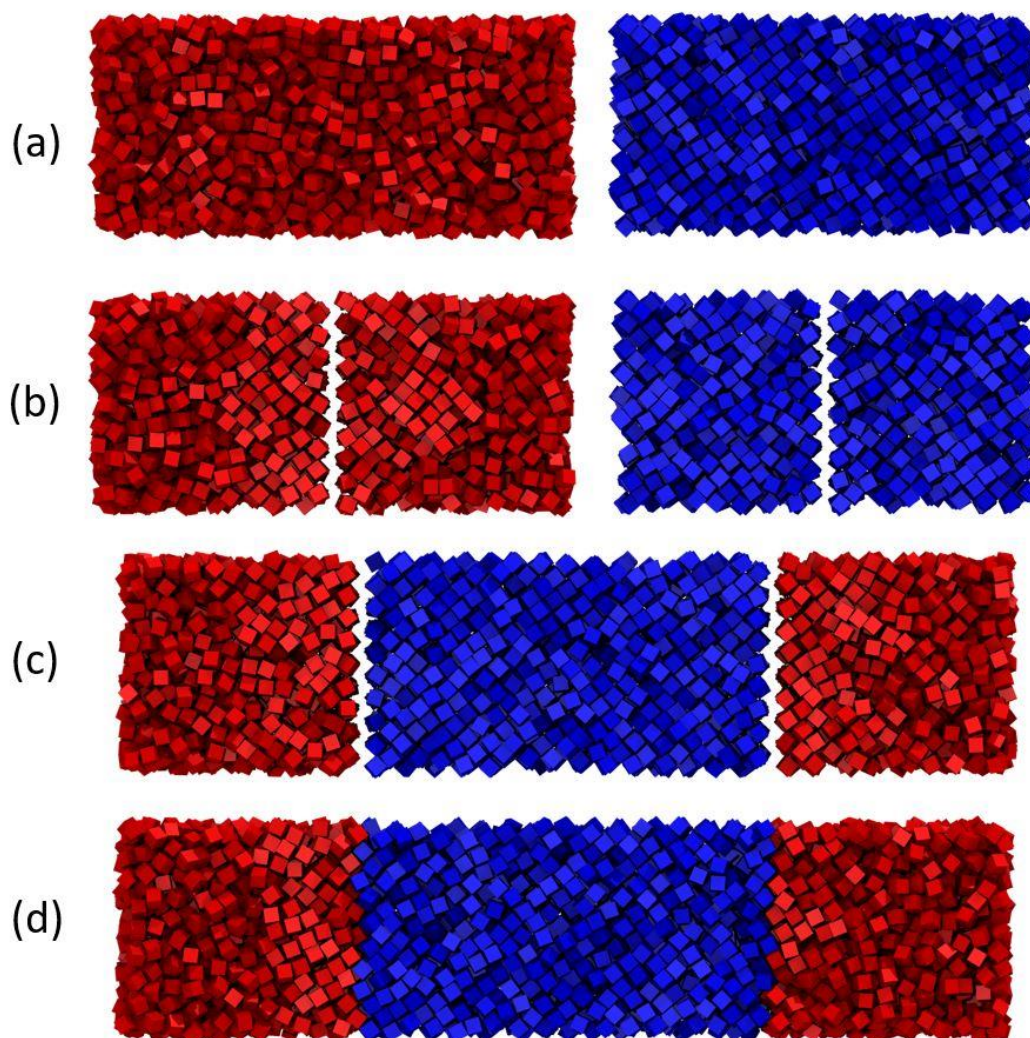


**Figure S3:** Simulation renderings at key steps in the cleaving walls method for  $\{110\}$  crystal plane using corrugated walls. (a) Bulk simulation boxes of solid and liquid phases with three-dimensional periodic boundary conditions at  $p=4.0$ . (b) Phases cleaved at the midplanes. (c) Transposed simulation boxes with dissimilar phases facing each other. (d) Final two-phase state with the gap closed and the two interfaces created.

### 6.3 Hard Truncated Cubes (TC25)

The length scaling for TC25 was also done with respect to its circumradius  $a_c$ .

#### 6.3.1 Umbrella Sampling

The umbrella sampling calculations for truncated cubes were performed largely following the procedure described in an earlier publication.<sup>106</sup> The only difference is the optimized cutoff for the orientational correlation  $d_i > 0.5$  for connection between two particles (Figure S4(a)). For a system of  $N = 1000$  particles, windows 40-particles wide were used with half-width overlap. The calculated free energy barrier at coexistence pressure  $p = 3.64$  is  $\Delta G = 26.0 \pm 2.0 k_B T$  and the critical number of ordered particles is  $N_{ordered}^* = 385$ .

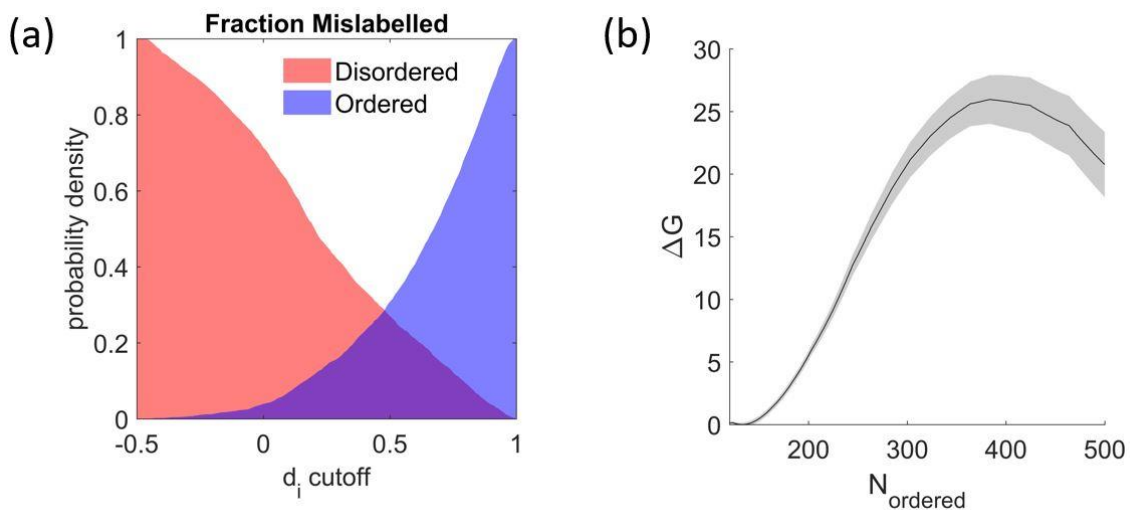


**Figure S4:** (a) Optimization of orientational correlation cutoff for the order parameter. (b) Free energy profile calculated via umbrella sampling for TC25 at coexistence.

### 6.3.2 Interfacial Free Energy Calculation

For TC25 pressure calculation,  $\delta z = 7 \times 10^{-4}$  was found to be the most appropriate for the starting cubic simulation boxes with  $N=1000$  particles. The pressure profiles for cleaving walls method for TC25 at coexistence are shown in Figure S5.

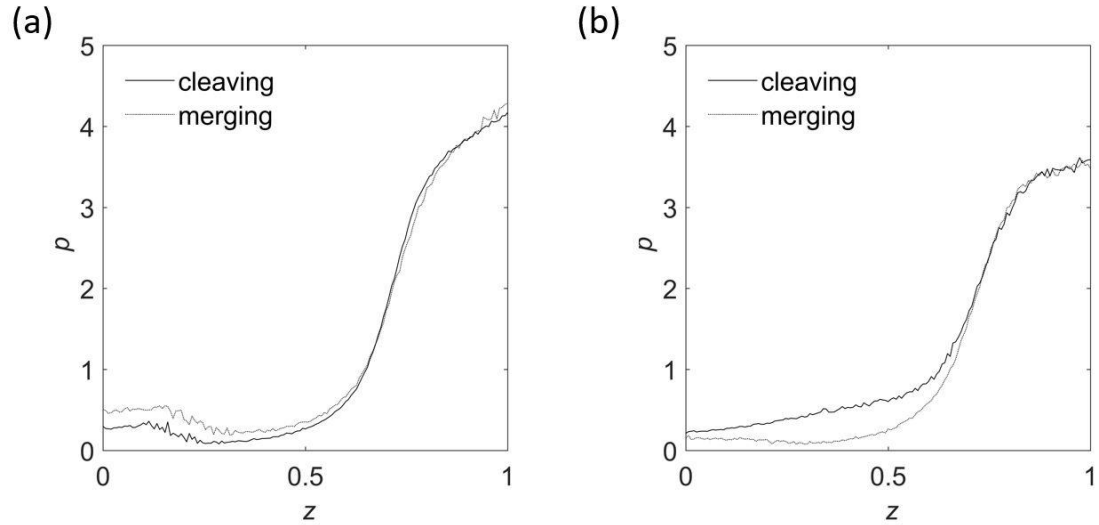


**Figure S5:** Pressure profiles for cleaving walls method for TC25. (a) ordered phase. (b) disordered phase.

### 6.4 Discrete MADCNT

We also solved the MADCNT model where only integer cluster sizes were considered.

We took a floor function to determine the critical nucleus size  $n^* = \left\lfloor \left( \frac{2A\bar{\gamma}}{3|\Delta\mu_{od}|} \right)^3 \right\rfloor$ . The

results are shown in Figure S6. This model introduces discrete jumps as  $n^*$  only takes

integer values corresponding to specific ratios  $\frac{\bar{\gamma}}{|\Delta\mu_{od}|}$ . Hence the jumps correspond to

straight lines with varying slopes passing through the origin. The lower left triangular

region corresponds to  $n^* = 1$  and is the zone of spinodal decomposition. The results are qualitatively similar to those of the continuous case presented in the main text, with the main difference being that the metastable basin is entirely absent for  $n^* < 1$ , leading to  $x_{ordered} = 0$  and an undefined  $\langle n \rangle$  for region I.

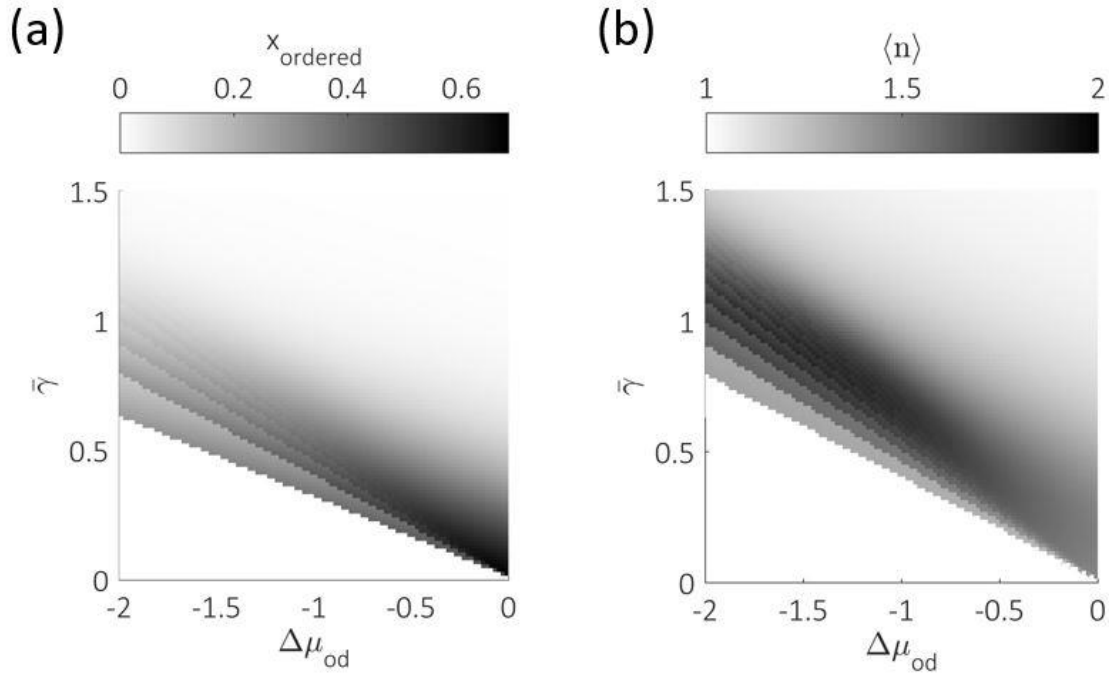


**Figure S6:** Predictions from the discrete MADCNT model for spherical ordered clusters with  $n_{max} = n^*$ . (a) fraction of ordered particles  $x_{ordered}$  and (b) average cluster size  $\langle n \rangle$  as a function of  $\Delta\mu_{od}$  and  $\bar{\gamma}$ . The calculations were performed with a resolution of 100 points along each axis.

### 6.5 Example of a non-monotonous interfacial contribution

A simple lattice model can be used to illustrate how interfacial contribution to the free energy may be a non-monotonous function of the fraction of ordered particles. Let the system consist of  $N$  sites and  $n_{ordered}$  randomly distributed ordered sites. Any unlike

neighbors on a lattice are considered forming one unit of interface. Let the interfacial area per site be  $a_{site}$  (this will be half the coordination number of the lattice). Then on average the fraction of neighbors being ordered is the same as the fraction of sites being ordered in general, i.e.,  $x_{ordered} = \frac{n_{ordered}}{N}$ . As a result, the average fraction of neighbors being disordered is  $(1 - x_{ordered})$ . The interfacial area per ordered site is then given by  $\bar{a} = a_{site}(1 - x_{ordered})$ , and the interfacial area per site is given by:

$$a_i = a_{site}x_{ordered}(1 - x_{ordered})$$

This expression by itself is non monotonous with a maximum at  $x_{ordered} = 0.5$ . An expression for the total intensive free energy for the system  $\Delta g = \frac{\Delta G}{N}$  can be constructed as:

$$\Delta g = \Delta\mu_{od}x_{ordered} + \gamma a_i$$

$$\Delta g = \Delta\mu_{od}x_{ordered} + \gamma a_{site}x_{ordered}(1 - x_{ordered})$$

This function has a maximum at  $x_{ordered}^* = \frac{1}{2} \left( 1 + \frac{\Delta\mu_{od}}{\gamma a_{site}} \right)$ . This model predicts the following cases:

A.  $\Delta\mu_{od} \leq 0$ : supersaturation:

1.  $\gamma a_{site} \geq |\Delta\mu_{od}|$ :  $x_{ordered}^* \in \left[0, \frac{1}{2}\right]$  there is a critical fraction and  $\Delta g$  is non-monotonous with  $\Delta g^* > 0$ .
2.  $\gamma a_{site} < |\Delta\mu_{od}|$ :  $x_{ordered}^* < 0$  : since this  $x_{ordered}^*$  is unphysical, there is no critical fraction,  $\Delta g$  is monotonically decreasing,  $\Delta g^* = 0$

B.  $\Delta\mu_{od} > 0$ : subsaturation:

1.  $\gamma a_{site} > |\Delta\mu_{od}|$ :  $x_{ordered}^* \in \left[\frac{1}{2}, 1\right]$ : there is a critical fraction and  $\Delta g$  is non-monotonous with  $\Delta g^* > 0$ .
2.  $\gamma a_{site} < |\Delta\mu_{od}|$ :  $x_{ordered}^* > 1$ : there is no critical fraction and  $\Delta g$  is monotonically increasing.

Since usually  $\gamma > 0$  and  $\Delta\mu_{od} = 0$  at some condition and the latter varies continuously, cases A1 and B1 are bound to occur.

This model could perhaps describe the intensive free energy barrier observed in hard cubes<sup>106</sup> for both supersaturated and subsaturated conditions encompassing cases A1 and B1. We also notice that  $x_{ordered}^*$  remains consistent over various system sizes. Further, the barrier calculations indicate that case A2 might indeed occur at a specific pressure (a surrogate for supersaturation) above which a metastable disordered phase

is impossible to sustain due to the absence of a barrier. Case B2 is simply a stable disordered phase.

### 6.6 *Shape-Interacting Cleaving Walls*

We have considered different approaches to implement cleaving walls, one of which is having walls that interact with the actual particle shape (instead of particle centroid as used in the main text). The implementation for cubes is relatively straightforward and involves calculating the relative position of cube vertices with respect to the wall. These walls start receded at one circumradius distance into the side of the box they do not interact with, hence the position of the wall ( $z_{wall\pm}$ ) is different from the convention used in the plots as  $z_{wall\pm} = z \mp a_c$ . At the end of Step I the walls are both located at the midplane. For a system of  $N=1000$  cubes at the coexistence pressure we performed benchmark calculations for both a centroid-interacting wall and a shape-interacting wall. The pressure change with wall position for the shape-interacting wall is shown in Figure S7. The shapes of curves are qualitatively different from the usual centroid-interacting wall, but the resulting value of  $\gamma_{shape} = 0.0654$  was within 1% of the value calculated for  $\gamma_{centroid} = 0.0650$ . Given this agreement, we favored the use of the centroid-interacting wall as it is more readily transferable to other particle shapes, it does not induce facet alignment on interfacial particles, and it simplifies pressure calculations.

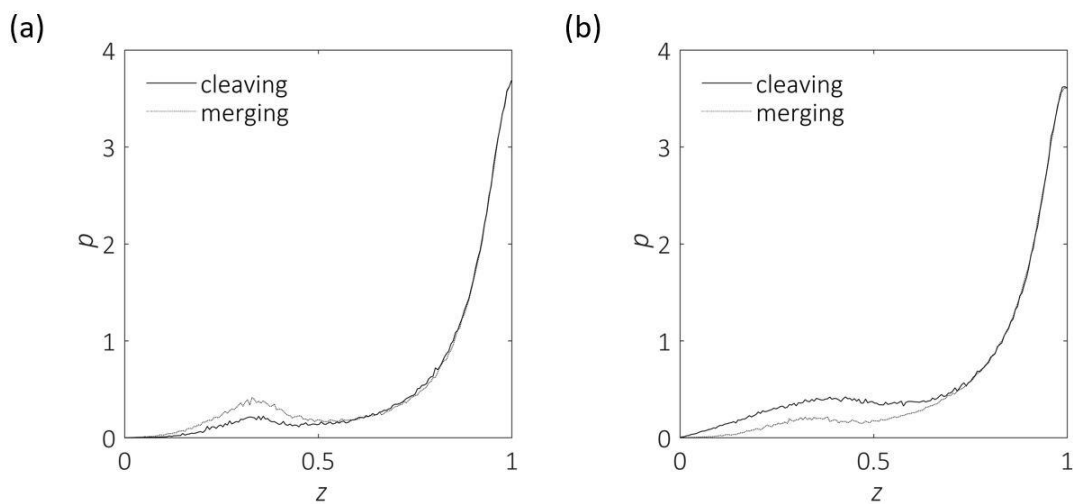


**Figure S7:** Pressure variation as a function of wall position for a particle-interacting wall for (a) solid and (b) liquid.

### 6.7 *Orientational Correlation in Disordered Phase*

The orientational correlation as a function of distance between two particles was calculated in the disordered phase using  $d_i$  as described in a previous study.<sup>106</sup>  $d_i$  as a function of distance  $r$  was calculated at various pressures as shown in Figure S8. While a correlation function of the form  $e^{-r/l_c}/r$  (where  $l_c$  is the correlation length) did not provide a good fit due to non-monotonous decay of  $d_i$ , the general trend is that  $l_c$  increases drastically with pressure. This could be attributed to an increase in concentration of ordered domains in the system, indicative that the system is close to the conditions of spinodal decomposition.

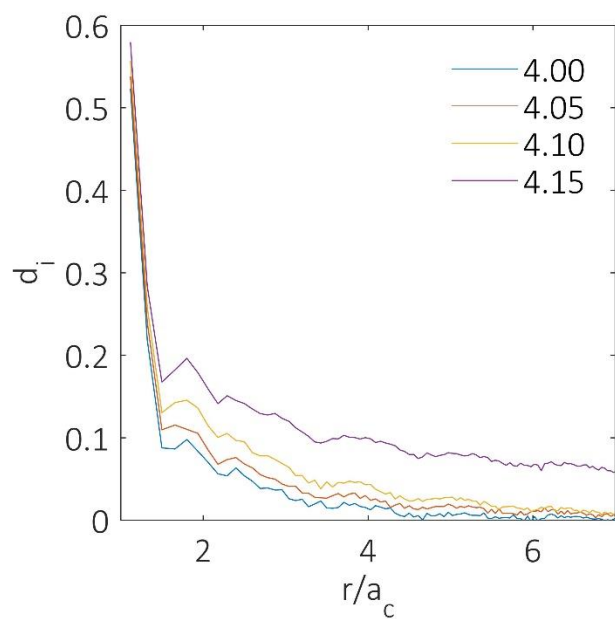


**Figure S 3:** Decay of orientational correlation ( $d_i$ ) as a function of interparticle distance ( $r$ ) for various pressures,  $p_{co} = 4$ .

TOC Graphic



## CHAPTER 5: KINETICS OF ROTATOR-CRYSTAL TRANSITION OF TRUNCATED CUBES

Abhishek K. Sharma and Fernando A. Escobedo\*

### Abstract

Rotationally symmetric faceted particles can form rotator mesophases which are translationally ordered and orientationally disordered. In this study we explore the possibility and mechanism of rotator-crystal transitions. Monte Carlo simulations are conducted for two selected truncations of cubes ( $s = 0.527$  and  $s = 0.572$ ) that are known to form rotator phases. The two truncations are chosen because  $s = 0.527$  has dissimilar rotator and crystal lattices, whereas  $s = 0.572$  has an identical lattice. These differences set the stage for a qualitative difference in rotator-crystal transition. Our simulations reveal that significant lattice deviatoric effects could hinder the rotator-crystal transition. We improve the sampling of orientational space by introducing specialized rotation moves. In case of  $s = 0.527$  we found that upon compression the rotator phase transitions to an orientational salt. This study paves the way for further analysis of diffusionless transformations in nanoparticle systems, and what features of lattice-distortion could influence the kinetics.

## 1 Introduction

Particles in the truncated cubes family exhibit a rich phase behavior as a function of truncation  $s$ .<sup>4,6,7,10</sup> Previous studies have focused on the isotropic to rotator transition that takes place via nucleation and growth.<sup>8,59</sup> In this paper we complement those studies by investigating the rotator-to-crystal phase transitions. These transitions have been studied in the past for other shapes,<sup>134</sup> revealing interesting influence of similarity/dissimilarity between local directional entropic forces (DEFs) and crystal lattice on the nature of the transition.

We focus on two specific truncations:  $s = 0.527$  (TC52) and  $s = 0.572$  (TC57) whose phase behavior and coexistence conditions are well established. (Figure 1)

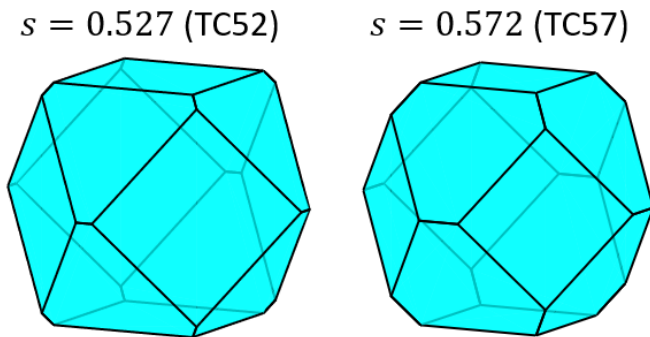


**Figure 25:** Shapes from the truncated cubes family studied in this work.

These particular shapes are selected because their preferred orientations in the rotator phase are of the same symmetry. Furthermore, despite being quite proximal in truncation space ( $s$ ), the lattice geometry for rotator and crystal phases is nearly

identical for TC57 but is different for TC52. This difference allows us to study the influence of lattice distortion on the rotator-to-crystal phase transition mechanism.

This paper is organized as follows: Section 2 describes the simulation methods and order parameters employed in this study. Section 3 reports the observations and Section 4 discusses the results.

## 2 Methods

### 2.1 Model

For any two particles  $i$  and  $j$ , we use a hard pair-potential given by:

$$U_{ij} = \begin{cases} 0 & \text{if no overlap} \\ \infty & \text{if overlap} \end{cases}$$

The overlap is detected by using the separating axis theorem.<sup>49</sup> Particle shape for a given value of truncation parameter can be obtained through formulae described in an earlier study.<sup>10</sup>

### 2.2 Monte Carlo Simulations

Metropolis<sup>55</sup> Monte Carlo (MC) simulations are performed in the isothermal-isobaric ( $NpT$ ), where  $N$  is the total number of particles,  $p$  is the pressure, and  $T$  is the temperature. All lengths scaled by half-side ( $a_{1/2}$ ) of the original cube the particles are

truncated from. Thus, the dimensionless pressure is given by  $p = \beta p_a a_{1/2}^3$ , where  $p_a$  is the unscaled pressure and  $\beta = \frac{1}{k_B T}$ , where  $k_B$  is Boltzmann's constant. The supersaturation is defined as  $\Delta\mu_{od} = \mu_o - \mu_d$ , where  $\mu_o$  and  $\mu_d$  are chemical potentials associated with ordered and disordered phases, respectively. The coexistence volume fraction were obtained courtesy of the authors of an earlier study.<sup>95</sup> The simulations used periodic boundary conditions to mimic bulk behavior. Unless specified otherwise, each MC cycle included  $N$  translation,  $N$  rotation (along box coordinate axes), and 2 volume moves. Isotropic and anisotropic (triclinic) volume moves were used for isotropic and translationally ordered phases, respectively. To accelerate the exploration of different particle orientations in the rotator phase, we perform additional  $N$   $60^\circ$  rotations along the particle's body-diagonal. These rotations facilitate rotation between orientations with similar facet presentation.

The crystal phase is initiated with configurations close to the best packing of the crystal phase previously reported.<sup>10</sup> The configuration is then equilibrated at  $p = 9.0$  and gradually expanded until it *orientationally* melts into the rotator phase. For TC52, such a melting nearly always results in grain boundaries. To circumvent any grain boundaries, we pick the lowest pressure where the crystal phase was observed, and gradually expand it without any translational moves. The triclinic volume moves allow for proper distortion of the lattice to result in a rotator phase with defect-free lattice. This lattice is equilibrated with the standard NpT simulations and compressed gradually.

## 2.3 Order Parameters

### 2.3.1 Definitions

We use Steinhardt<sup>50</sup> order parameters to capture both local translational and orientational order. For translational order we use  $q_6$  since it is found to be suitable for BCC-like arrangements.<sup>59</sup> For orientational order we employ  $i_4$  as it can effectively capture  $O_h$  symmetry for all particles in the truncated cubes family.<sup>59,106</sup> These parameters are evaluated for each particle in the system.  $q_6$  is dependent upon the neighbor cutoff distance  $r_c = 8$ . More details on these order parameters are provided in the previous studies.<sup>59,106</sup>

### 2.3.2 Correlations

In any given context, the order parameters of any two particles can be used to evaluate a correlation function akin to a dot product used to measure alignment among two vectors. The translational-order correlation between particle  $i$  and its neighbor  $j$ ,  $d_q(i, j)$  is given by:

$$d_q(i, j) = \frac{\sum_{m=-6}^6 q_{6,m}(i) q_{6,m}^*(j)}{\left(\sum_{k=-6}^6 |q_{6,k}(i)|^2\right)^{\frac{1}{2}} \left(\sum_{l=-6}^6 |q_{6,l}(j)|^2\right)^{\frac{1}{2}}}$$

Analogous to translational order, the orientation correlation between two particles  $k$  and  $l$  is defined as:

$$d_i(k, l) = \sum_{m=-4}^4 i_{4,m}(k) \cdot i_{4,m}^*(l)$$

where the asterisk (\*) denotes the complex conjugate in both cases.

## 2.4 Visualization of Configurations

Simulation configurations are visualized using Visual Molecular Dynamics (VMD) software.<sup>135</sup> Particles were colored based on their alignment with the box axis. For any particle, the dot product of its three axes unit vectors is taken with respect to the box x-axis. This dot product has a theoretical minimum of  $\frac{1}{\sqrt{3}}$  and a maximum of one. A colormap is then used to color the particles red if the dot product equals  $\frac{1}{\sqrt{3}}$  and blue if it equals one, with shades of yellow and green in between. In essence, this coloring measures the ‘orthogonality’ of the particle with respect to the box coordinate system. The configurations snapshots shown may have been reorientated for clarity, so apparent coloring of particles in the figures may not be comparable to other panels or figures.

## 3 Results and Discussions

### 3.1 Equations of State and Phase Behavior

#### 3.1.1 TC52

Equations of state regimes for TC52 ( $N = 1000$ ) are shown in Figure 2. While we observe the previously reported<sup>10</sup> isotropic, rotator, and crystal phases, (Figure 3(a,b,d)) upon compression the rotator phase spontaneously transitions into a novel

*orientational* salt composed of two distinct orientations (Figure 3(c)). Like the cesium chloride (CsCl) crystal, TC52 particles are arranged in the body centered tetragonal (BCT) lattice with one orientation occupying the body center and the other occupies the corners of the unit cell. We suspect this configuration might have been missed in previous studies due to absence of rotations that allow for rotation between different orientational sectors in the rotator phase. We note that the salt formation is not observed if insufficient rotation moves are conducted in the simulations, where the rotator transitions to the crystal phase spontaneously.

The coexistence pressure for between the rotator and crystal phases is  $p_{co,rc} \approx 2.9$  and between the isotropic and rotator phases is  $p_{co,ir} \approx 1.1$ .

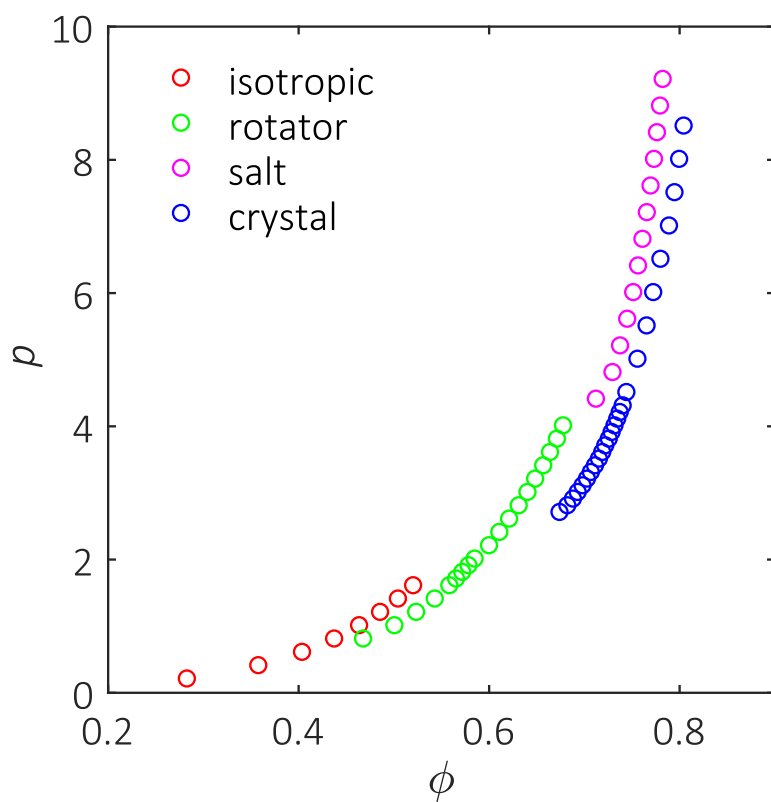


**Figure 26:** Equation of state for TC52 obtained from various simulation runs.

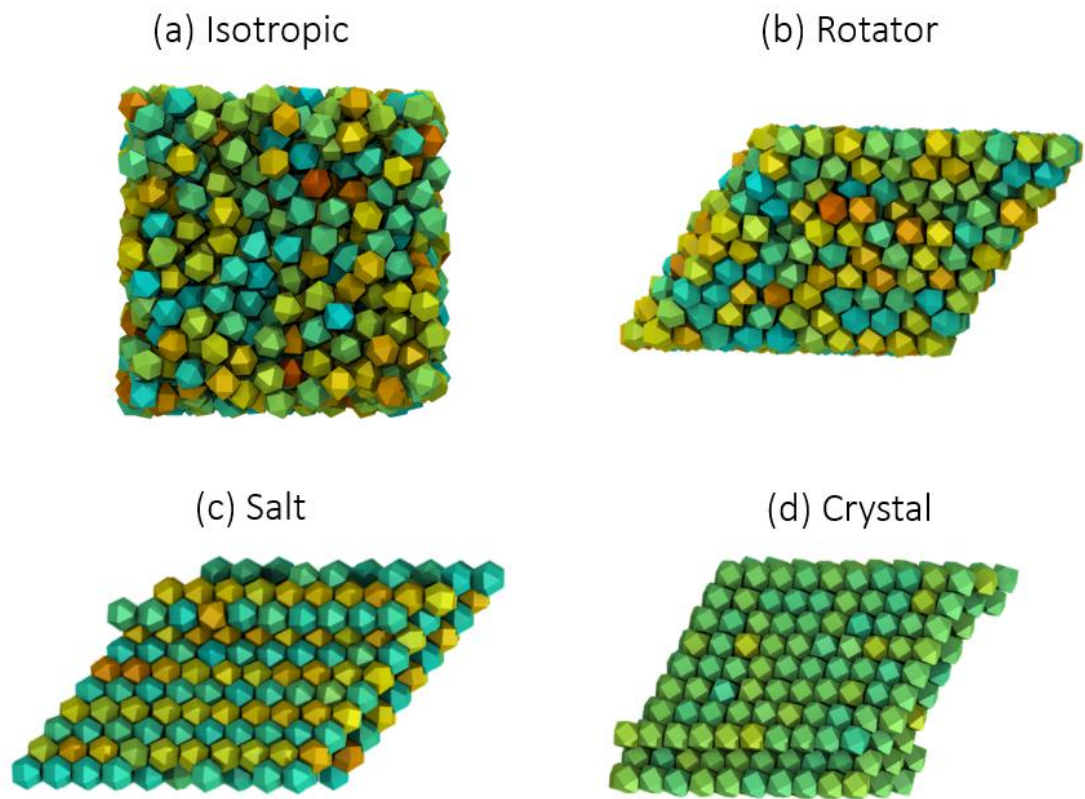


**Figure 27:** Sample configurations for various phases obtained for TC52. (a) Isotropic phase at  $p=1.0$ ; (b) Rotator phase at  $p=4.5$ ; (c) Orientational Salt at  $p=4.8$ ; (d) Crystal phase at  $p=4.5$ . Particle coloring correlates with their alignment with respect to the box coordinate as described in Section 2.4.

### 3.1.2 TC57

Equations of state for TC57 ( $N = 2304$ ) are shown in Figure 4. In this case we observe the isotropic, rotator and crystal phases (Figure 5). The coexistence pressures between isotropic and rotator phases  $p_{co,ir} \approx 1.1$  and between rotator and crystal phases is  $p_{co,rc} \approx 4.5$ .

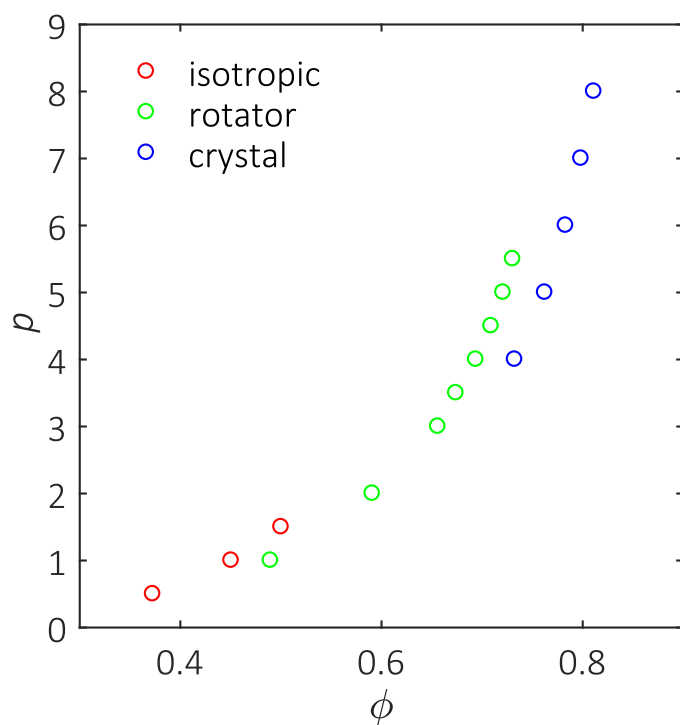


Figure 28: Equation of state for TC57 obtained from various simulation runs.

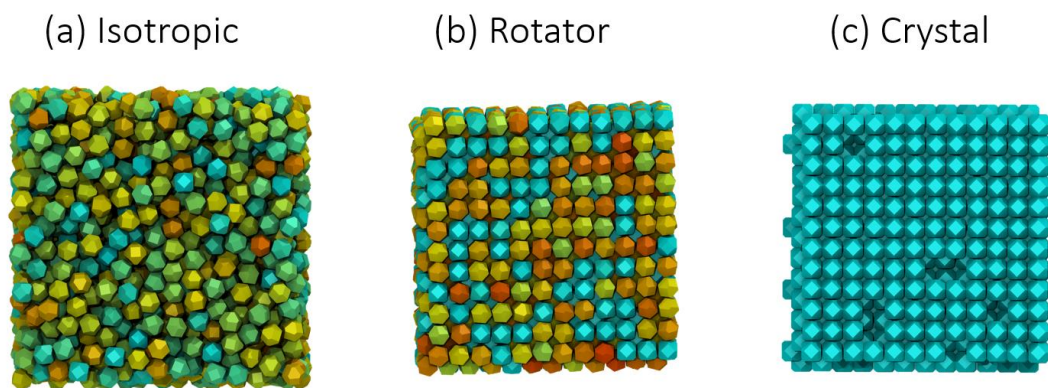


Figure 29: Sample configurations for various phases observed for TC57: (a) Isotropic phase at  $p=1.0$ ; (b) Rotator phase at  $p=4.5$ ; (c) Crystal phase at  $p=5.0$ . Particle coloring correlates with their alignment with respect to the box coordinate as described in Section 2.4.

## 3.2 *Analysis of Phases*

### 3.2.1 Crystal and Rotator Lattices

The rotator phases for both shapes are reported to be positioned on a body centered tetragonal (BCT) lattice. The crystal phase for TC52 is a distorted BCT lattice whereas the TC57 lattice remains BCT.<sup>10</sup>

We can illustrate the lattices by analyzing the coordination shells. Figure 6(a) shows coordination number as a function of distance for TC52 among the two phases at  $p =$

3.4.

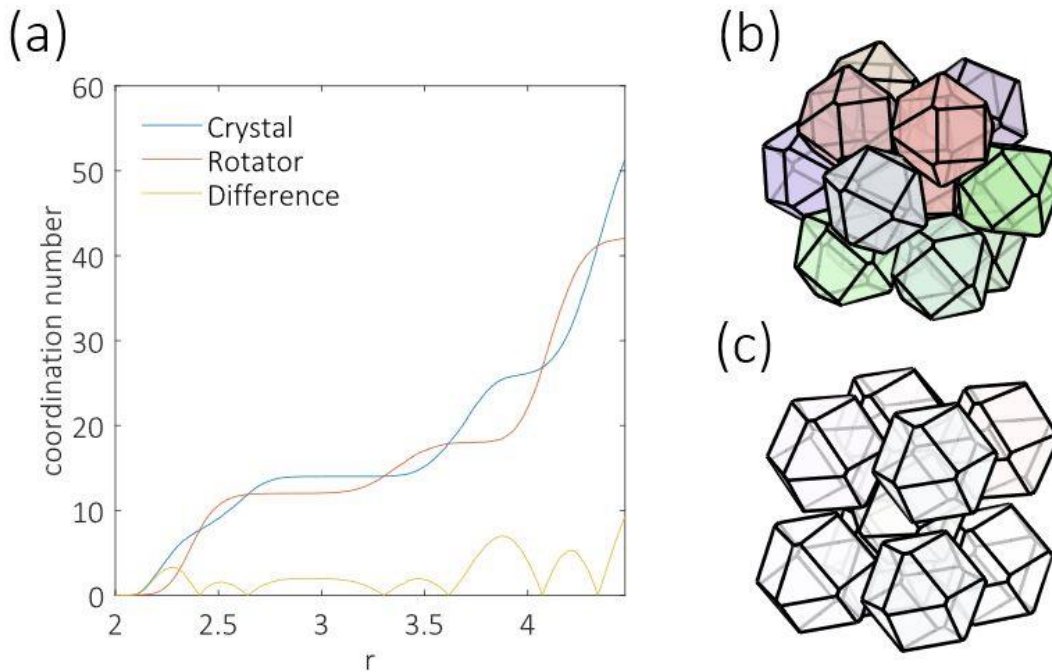


**Figure 30:** Analysis of coordination shell for TC52 rotator and crystal phases at  $p=3.4$ : (a) Coordination number as a function of distance. (b) Nearest neighbors for the rotator phase. (c) Nearest neighbors for the crystal phase. Particle coloring described in Section 2.4.

We find that there is a qualitative difference between the two phases in that the rotator phase has 12 nearest neighbors situated at roughly the same distance whereas the crystal phase has 8 nearest neighbors. The arrangement of the nearest neighbors for rotator and crystal phase is shown in Figure 6(b) and Figure 6 (c) respectively. The rotator phase's nearest neighbors are quite similar in their arrangement to a face centered cubic lattice, which is not unexpected given that FCC and BCC are related.<sup>136</sup> The crystal phase has the neighbors arranged as if the original particle is placed at the

body center and the rest are arranged at corners, albeit not on a cubic cell (hence distorted).

In contrast, we find that the coordination shell for both rotator and crystal phases is identical (Figure 7), with both having a nearest coordination shell with 12 neighbors arranged on a BCT lattice.

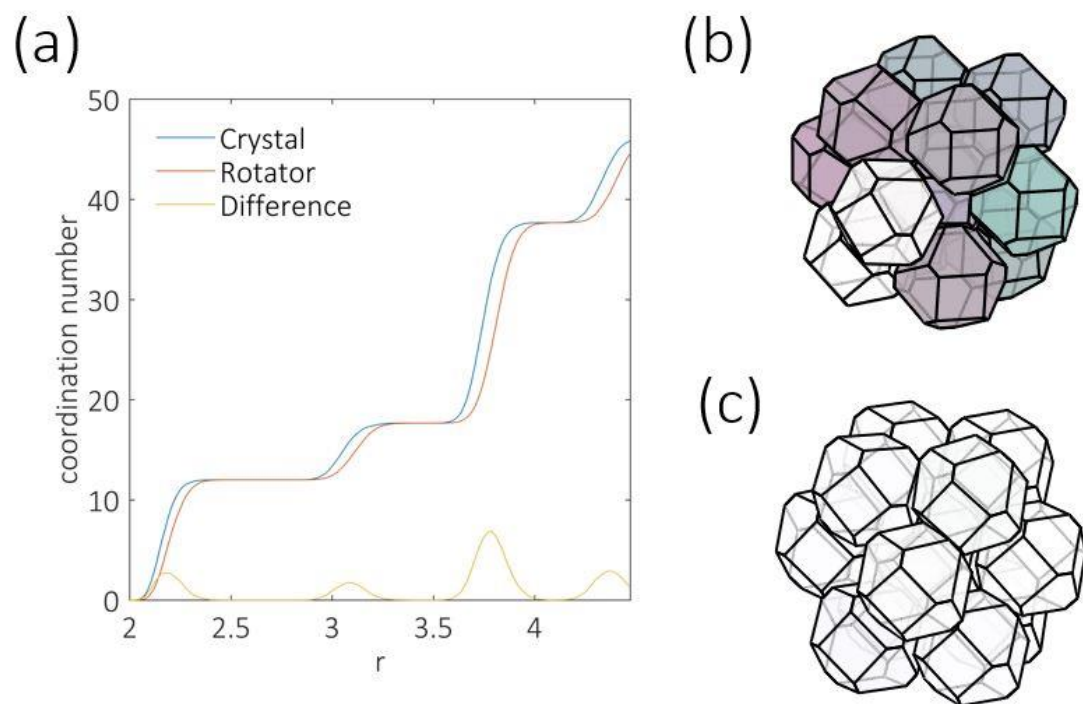


**Figure 31:** Analysis of coordination shell for TC57 rotator and crystal phases at  $p=5.0$ : (a) Coordination number as a function of distance. (b) Nearest neighbors for the rotator phase. (c) Nearest neighbors for the crystal phase. Particle coloring described in Section 2.4.

### 3.2.2 Rotator Phase Orientational Sectors

The rotator phases for both shapes have similar distribution of orientations. Figure 8 shows the arrangement of orientation vectors. The particles prefer 18 orientational sectors. These 18 sectors can be understood as a consequence of three distinct orientations and their  $O_h$  symmetry as three sets of six orthogonal sectors can be identified. These orientations do not particularly align with the bond vectors with the neighbors. Interestingly for TC57, the three distinct orientations all could form a perfect BCT crystal if all particles attain a single orientation. The same is not true for TC52 since the lattice is distorted relative to the orientation of the particles.

At low densities, the particles can ‘travel’ between different sectors continuously. However, beyond a certain density such rotations can become rare. To accelerate and properly sample particle orientations, we use special  $60^\circ$  rotations along body-diagonals as described in the Methods section. Please note that our recipe is not unique, as other symmetries of the particle may be leveraged. For instance, similar results could be obtained with a  $90^\circ$  rotation along edge diagonals.

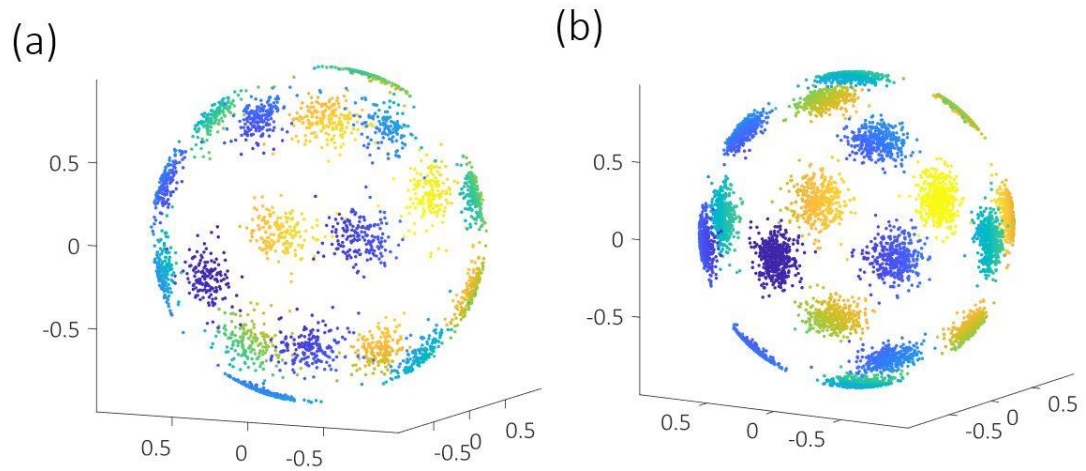


**Figure 32:** Preferred orientational sectors for rotator phases: (a) TC52 at  $p=4.0$ ,  $N=1000$  (b) TC57 at  $p=4.5$ ,  $N=2304$ . Points colored as a function of x-axis, blue in the foreground and yellow in the background.

### 3.2.3 Orientational Salt for TC52

Compression of the TC52 rotator phase beyond  $p = 4.0$  results in the formation of the orientational salt. The analysis of coordination shells and sample arrangement of nearest neighbors is shown in Figure 9. We notice that the salt has the same number of nearest neighbors as the rotator phase, and the variation of coordination number as a function of distance is qualitatively similar to that of the rotator phase, except for a small ‘bump’ near  $r = 3.1$ . The visualization of the nearest neighbors reveals an interesting arrangement of the two orientations. From the standpoint of the BCT lattice, one could describe the orientational salt as one orientation occupying the corners and the other orientation occupying the body centers. This 1:1 salt is reminiscent to cesium chloride (albeit being BCT instead of BCC). This arrangement manifests in an

orientational distribution shown in Figure 10. It has 12 preferred orientations instead of 18 observed for the rotator. The spontaneous formation of this salt, instead of the crystal might be born out of kinetic considerations, with a transformation to the salt structure requiring a minimal lattice distortion while transformation to crystal structure requiring a significant lattice distortion and overcoming a larger concomitant free-energy barrier.

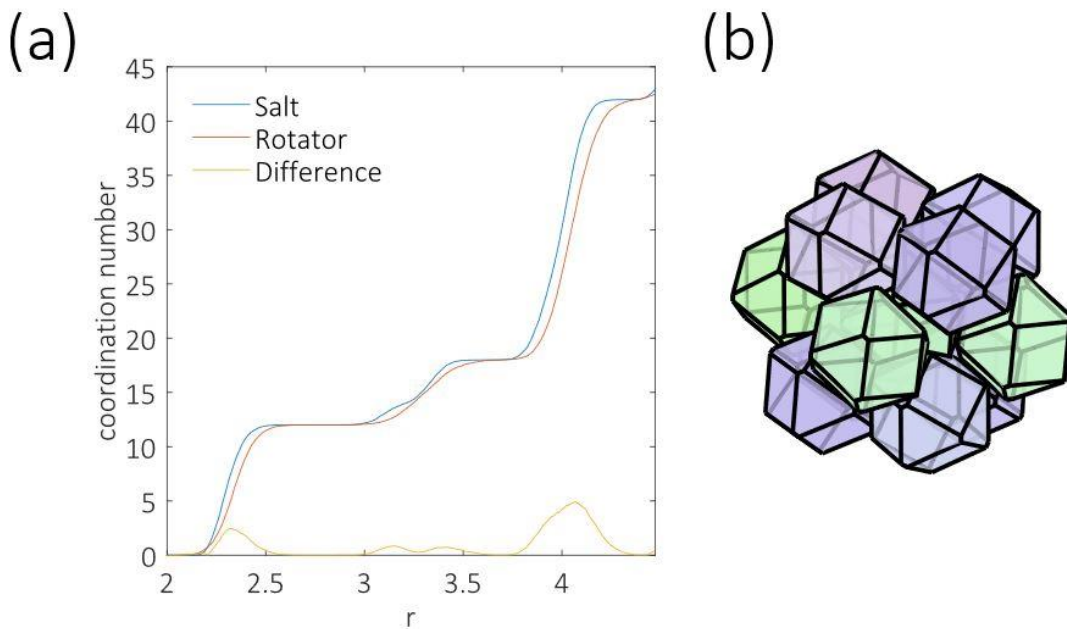


**Figure 33:** Analysis of coordination shell for TC57 orientational salt at  $p=4.8$ : (a) Coordination number as a function of distance. (b) Nearest neighbors. Particle coloring described in Section 2.4.

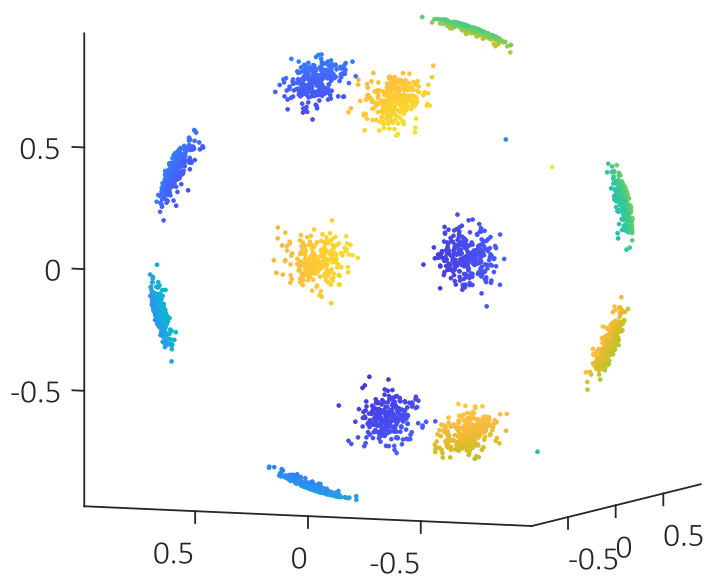


**Figure 34:** Particle orientations for the orientational salt at  $p=4.8$ . Points colored as a function of x-axis, blue in the foreground and yellow in the background.

### 3.2.4 Diffusionless Transformations

As particles do not migrate great distances (compared to lattice spacing) in transitioning from rotator to crystal phase and vice versa, the phase transitions can be termed as diffusionless. As there is an abrupt change in volume fractions, these are also first-order transitions. We can borrow the classification from the literature on diffusionless/displacive transformations in metals and alloys.<sup>137,138</sup>

A transformation is called *lattice-distortive* if the shape of the unit cell is distorted in the process. In contrast, if particles rearrange within the unit cell, then it is termed as a *shuffle* transformation. The lattice-distortive transformations can further be composed of a *dilational* and *deviatoric* components, where the former refers to expansion or contraction of the lattice, and the latter refers to transformations where the lattice may have an undistorted line (such as a rotation or shear). Dilation itself could be homogeneous (isotropic) or heterogenous (anisotropic). These classifications are not sharp, as there can be transformations that may not fit clearly in one category.

The rotator-crystal transitions are inherently lattice-dilational, given the change in volume fraction and distances between the nearest neighbors. For TC52 (and not so much for TC57), there is a significant difference in the lattice structure of rotator and crystal, and one may expect a significant deviatoric component to the transformation.

### 3.2.5 Visualization of Lattice Displacements

The visualization of lattice displacements between two configurations could be useful in characterizing the transformations. In order to do this, we take two configurations (C1, C2) and pick a particle as the origin (i.e., shift and rewrap the configurations according to periodic boundary conditions such that a particular particle is at the origin). Then we calculate the displacements of all particles needed to go from C1 to C2. These displacements also need to be rewrapped. We can then plot the lattice displacements

in a quiver plot. The visualization is thus relative to one particle; hence you should expect larger displacement for distant particles as the effect adds up.

Lattice displacements for a TC52 rotator-crystal transition are plotted in Figure 11. The average magnitude of displacement is  $\sim 1.97$  which is less than but comparable to the lattice spacing ( $\approx 2.2$ ). Note that the average displacement may not be a suitable measure if system sizes ( $N$ ) are quite different as the displacements generally increase in magnitude moving away from the origin. The quiver plot has been rotated to clearly show the elongation/contraction of the lattice. This pattern is similar to a uniaxial contraction flow.

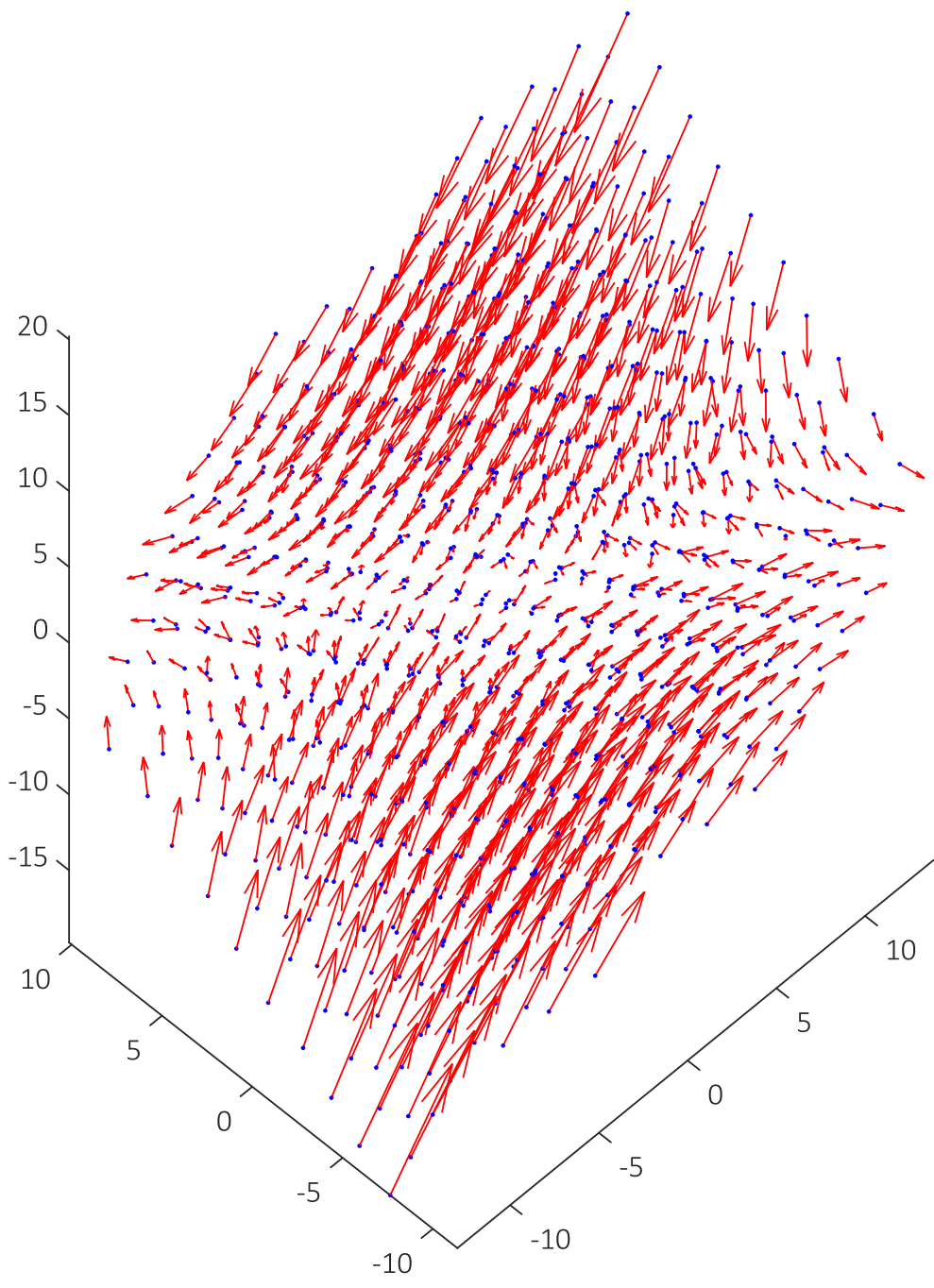


**Figure 35:** Lattice displacements for rotator-crystal transformation in TC52 at  $p=3.4$ . The rotator lattice is shown with blue points and red arrows terminate at the position of the particle in the crystal.

In contrast, the transformation from rotator to the orientational salt does not lead to a significant lattice displacement (Figure 12). The average displacement in this case was found to be 0.3952, which is much less than that for rotator to crystal transition. Interestingly, the displacements could be described as a part of a rotation. There also exists a line along into the page where the displacements are very small, indicating the presence of an undistorted line.

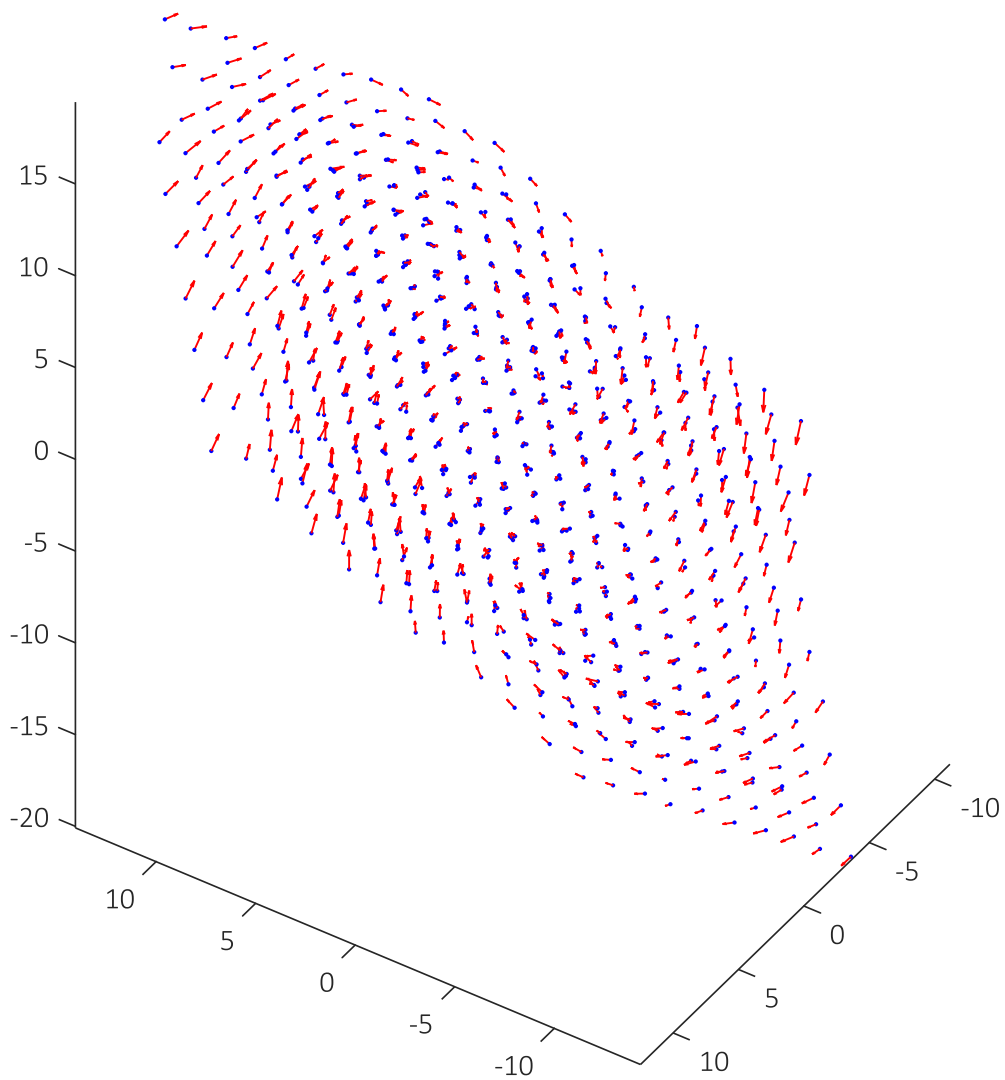


**Figure 36:** Lattice displacements for rotator-salt transformation in TC52 at  $p=4.4$ . The rotator lattice is shown with blue points and red arrows terminate at the position of the particle in the salt.

Finally, lattice displacements for TC57 from rotator to crystal are shown in Figure 13.

The average displacement is 0.3697 (though note that the number of particles here is

2304 instead of 1000 for TC52). The displacements largely seem to be isotropically compressing the lattice.

Based on this classification, we can describe the transformations as follows:

- TC52 rotator-crystal transformation is dilational and considerably deviatoric, with a significant elongational-contraction.
- TC52 rotator-salt transformation is dilational and deviatoric, with some rotational component.
- TC57 rotator-crystal transformation is mostly dilational.

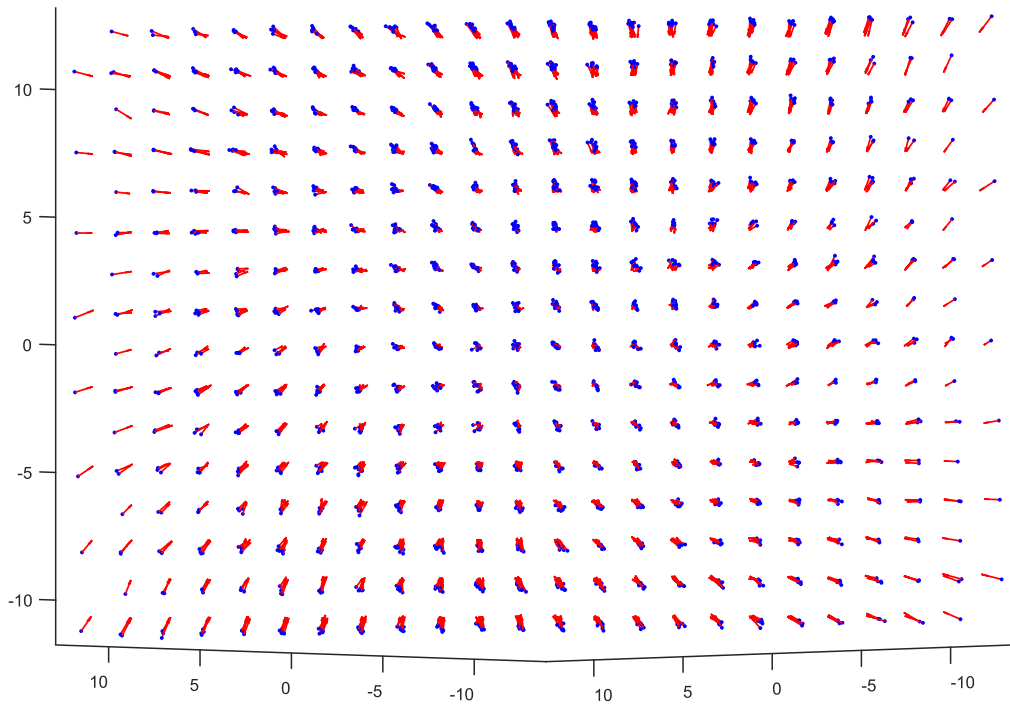


**Figure 37:** Lattice displacements for rotator-crystal transformation in TC57 at  $p=5.0$ . The rotator lattice is shown with blue points and red arrows terminate at the position of the particle in the crystal.

### 3.3 Order Parameter Development

#### 3.3.1 TC52 Rotator-Crystal

While we do not observe a spontaneous transition from the rotator to crystal phase, it is useful to evaluate orientational and translational correlations in the two phases. We do this by evaluating the mislabeling of neighboring particles (within  $r_c = \sqrt{8}$  of each

other) from either phase for a given cutoff correlation value. We perform this analysis at  $p = 3.4$ .

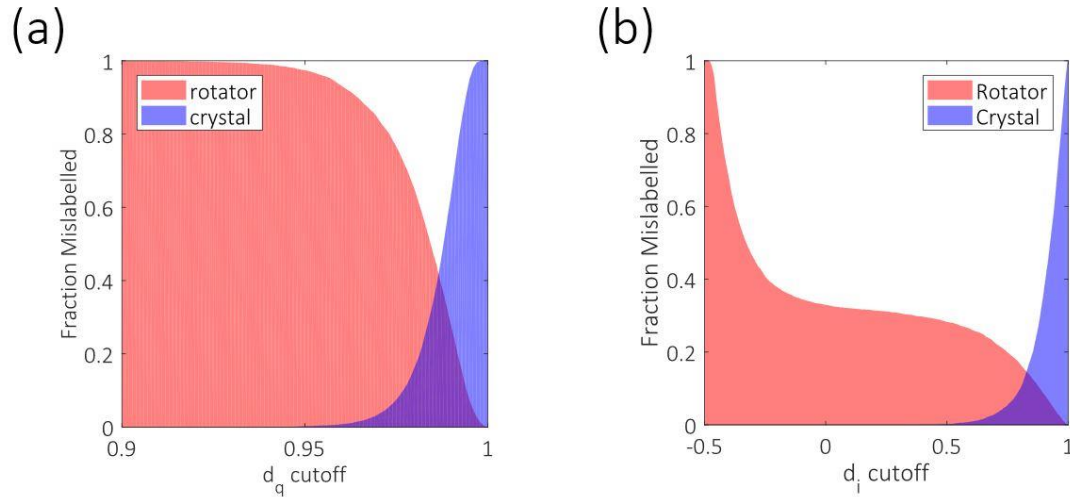


**Figure 38:** Mislabeleding of neighbors as correlated/uncorrelated a function of cutoff for (a) translational and (b) orientational order for rotator and crystal phases of TC52 at  $p=3.4$ .

We find that for translational correlation  $d_q$  (Figure 14(a)) there is only minimal contrast among the two phases, with optimal mislabeling of roughly 40%. This implies that there is not a significant change in the relative translational order (particularly for  $q_6$ ) with both phases occupying a high  $d_q$  space. On the other hand, there is an interesting contrast between the two phases in terms of orientational correlation  $d_i$  (Figure 14(b)). It appears that while most crystal phase neighbor-pairs are aligned with respect to each other, there is a bimodality in the distribution for rotator phase neighbors, with nearly 1/3 of them occupying a high  $d_i$  space like the crystal phase. This number could be rationalized in that as the particles occupy three distinct orientations in the rotator

phase, and if they are present in equal proportions, we can expect one-third of the neighbors to be aligned at any given point. Hence, we can use  $d_i$  to effectively discriminate between the two phases. In addition, we also know that there is a lattice distortion that takes place, and the discrepancy in the number of nearest neighbors could also be leveraged to identify particles belonging to the crystalline phase.

### 3.3.2 TC52 Rotator-Salt

Like the preceding case, we can compare the rotator phase with the orientational salt. At  $p = 4.4$ , the results are shown in Figure 15. Interestingly, there was an appreciable contrast we could achieve through  $d_q$  (Figure 15(a)). The salt seems to occupy a much higher  $d_q$  space than the rotator. Note that the pressure here is much higher than the pressure at which we compared rotator and crystal phases. As for orientational correlation there is no appreciable contrast between the two phases, and it appears that both phases have nearly identical bimodal distributions with a given particle aligned with 1/3 of its neighbors. This is much simpler to explain for the salt, given that only the four body centered particles are aligned out of 12 nearest neighbors.

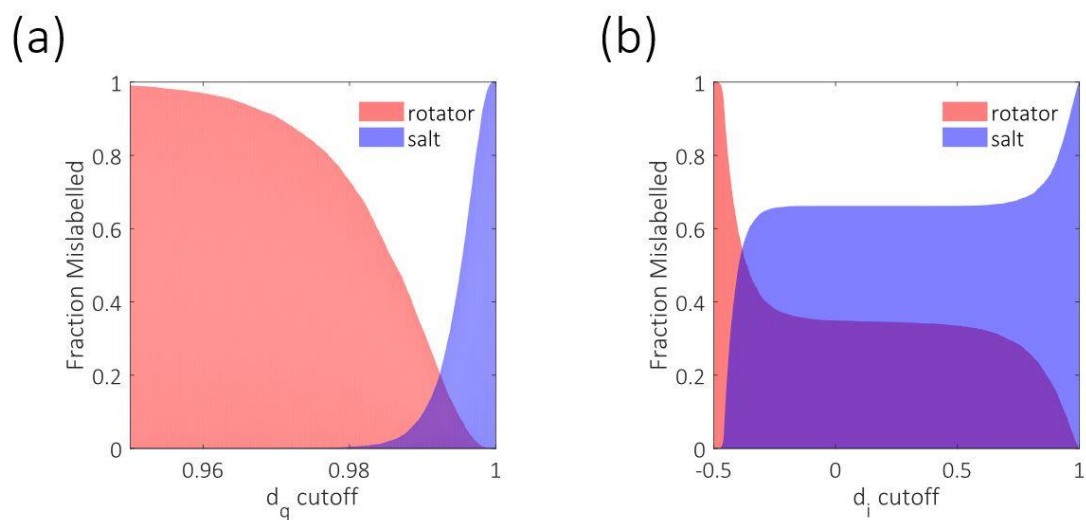


**Figure 39:** Mislabeled neighbors as correlated/uncorrelated as a function of cutoff for (a) translational and (b) orientational order for rotator phase and orientational salt of TC52 at  $p=4.4$

### 3.3.3 TC57 Rotator-Crystal

We also performed similar analysis for TC57 at  $p = 4.5$  (Figure 16).

Similar to TC52, the phases are indistinguishable from each other in terms of translational order with minimum achievable mislabeling being near 50%. The orientational correlation however reveals significant contrast between the two phases. Interestingly, it reveals that in the rotator phase there seems to be a preference to nearly 45% of the neighbors being aligned, indicating some level of affinity of the orientations with themselves.

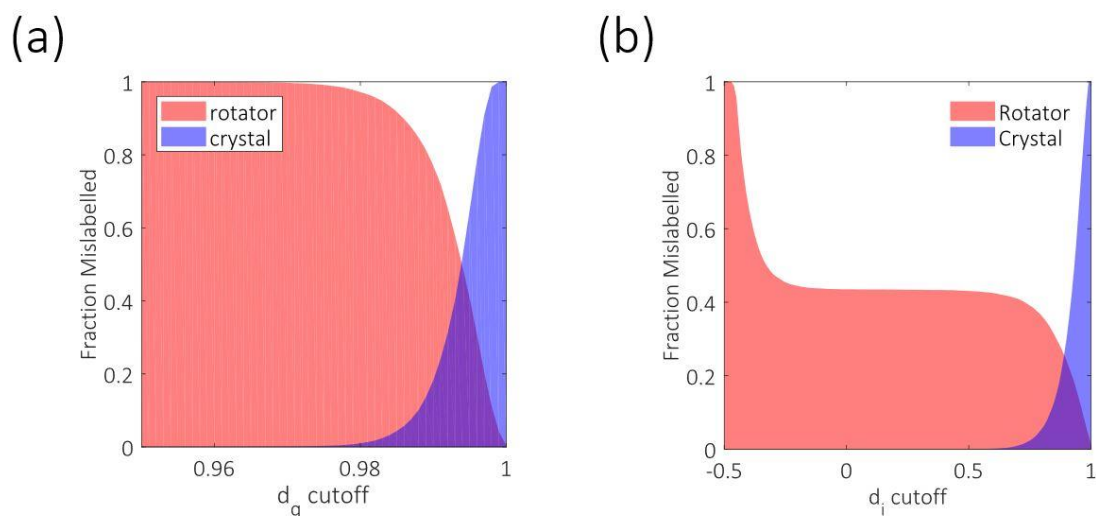


**Figure 40:** Mislabeled neighbors as correlated/uncorrelated as a function of cutoff for (a) translational and (b) orientational order for rotator and crystal phases of TC57 at  $p=4.5$ .

#### 4 Conclusions and Future Work

In this paper we have investigated the rotator-crystal transition for two truncations of cubes (TC52 and TC57). We found existence of a novel orientational salt that forms upon compression of the TC52 rotator phase. We conducted analysis of these phase in terms of their coordination shells that reveals interesting differences and similarities among the lattices. Particularly, for TC52 we find that the coordination shell for rotator is much closer to that of the orientational salt than that of the crystal, which could be the reason why the rotator phase prefers transitioning to the orientational salt. In comparison, the relative similarity of rotator and crystal phase coordination shells for TC57 lead to a spontaneous rotator-crystal transition.

We also analyze the transition in the context of established classification of lattice-distortive transformations using 3D quiver plots. Finally, we established order parameters for various transformations. This characterization of the phase behavior and spontaneous transformations sets up the stage for investigation of the phase transitions. Next steps include the following ideas:

1. Utilize the developed order parameters to study spontaneous phase transitions. Are there unique motifs that arise (e.g., nuclei)?
2. Perform umbrella sampling<sup>40</sup> to calculate free energy barriers and characterize transition states.
3. Investigate the role of shear in formation of orientational salt vs. crystal.
4. Study the formation of salt with odd number of layers to break the periodicity (currently we have only studied systems with even number of layers).
5. Characterize lattice distortions further by fitting transformation matrices.

## **5 Acknowledgements**

We are thankful to Anjan Gantapara for sharing the coexistence data for various truncations of cubes.

## CHAPTER 6: INFLUENCE OF PARTICLE ASPECT RATIO ON KINETICS

Abhishek K. Sharma and Fernando A. Escobedo\*

### Abstract

We study the influence of particle aspect ratio on the kinetics and phase behavior of hard gyrobifastigia through Monte Carlo simulations. We explain the formation of a highly anisotropic nucleus during isotropic to crystal transition in regular GBF through a direct measurement of interfacial free energies of various crystal planes through cleaving walls method and performing a Wulff construction to predict the nucleus geometry. We also study GBF-related shapes with various aspect ratios, revealing an easing of the kinetic barrier for isotropic-crystal transition upon increase in aspect ratio. At much higher aspect ratios, we find stabilization of an intermediate nematic phase. We calculate the equations of state and determine coexistence conditions using interfacial pinning method. Finally, develop order parameters to distinguish the isotropic, nematic, and crystalline phases and track the decay of correlation in respective phases.

### 1 Introduction

Particle aspect ratio (AR) is known to be an important determinant of the phase behavior of colloidal nanoparticles.<sup>4,6</sup> Generally speaking, a higher particle anisotropy

stabilizes liquid crystalline phases.<sup>83</sup> For example, cuboids of very large or very small aspect ratios can stabilize a myriad of mesophases, such as nematic, smectic, columnar, and cubatic phases.<sup>51,139,140</sup> For low anisotropy, if the particle asphericity is low it leads to stabilization of rotator mesophases (e.g. cuboctahedra, truncated cubes, rhombic dodecahedra).<sup>7,8</sup> For aspherical shapes with low particle anisotropy, such as regular triangular prisms,<sup>4</sup> octahedra,<sup>10,19</sup> and gyrobifastigia (GBF),<sup>4</sup> no mesophases are observed. When it comes to kinetics of disorder to order phase transitions, this category of shapes exhibits the highest nucleation free energy barriers ( $\Delta G^*$ ) at a given supersaturation ( $\Delta\mu_{od}$ ). In fact, for high enough barriers no spontaneous transition to ordered phases is observed when disordered phases are compressed in unbiased simulations.<sup>4</sup> This leads to a conjecture that the existence of a mesophase can kinetically ease the transition. This conjecture has been supported by observations made for mesophases of hard polyhedra<sup>8,59,106</sup> and mesophases associated with block copolymers.<sup>141</sup>

In this study we focus on the phase behavior and kinetics of disorder-order phase transition in hard gyrobifastigia (GBF). It is one of the few regular convex space-filling polyhedra but is quite an outlier in that it forms an ABCD lattice and is a quite asymmetric shape. In a previous study<sup>96</sup> we calculated very large  $\Delta G^*$  for isotropic-crystal transition (compared to other shapes at a given  $\Delta\mu_{od}$ ). This observation was partly explained by the discord between the locally favored structures and the

arrangement of particles in the crystal. Further, nucleus-size pinning revealed a highly anisotropic nucleus shape with aspect ratio of approximately two. In this study we investigate those results by first performing direct measurement of disorder-order interfacial free energy of various crystal planes using the cleaving walls method.<sup>88,113</sup> We then use these results perform a Wulff construction to predict a nucleus geometry to corroborate our earlier predictions.

The kinetics of self-assembly of anisotropic particles have also been of great interest in the literature.<sup>26,43,84,123</sup> Colloidal rods for instance have interesting kinetics: short rods ( $AR = 2$ ) may follow nucleation and growth at moderate supersaturations, but will get kinetically arrested with large number of crystallites at higher supersaturations.<sup>123</sup> At extremely high supersaturation the system gets arrested in a glassy state. For longer rods ( $AR = 3.4$ ), it was reported that isotropic-smectic transition is suppressed due to spinodal instability. This motivates us to study selected aspect ratios of GBF to investigate the effect of particle anisotropy on the kinetics of isotropic-crystal transition, and possible alteration in the mesophase behavior.

This paper is organized as follows: Section 2 describes the simulation model, cleaving walls method and order parameters employed in this study, and Section 3 discusses the results.

## 2 Methods

### 2.1 Model

For any two particles  $i$  and  $j$ , we use a hard pair-potential given by:

$$U_{ij} = \begin{cases} 0 & \text{if no overlap} \\ \infty & \text{if overlap} \end{cases}$$

The overlap is detected by using the separating axis theorem.<sup>49</sup> A gyrobifastigium is composed of two regular triangular prisms (*fastigium* pl. *fastigia* meaning roof) attached at a square base with a twist. This aspect ratio (AR) is defined as

$$AR = \frac{h}{a}$$

where  $h$  is the height of GBF and  $a$  is the side of the square base. For a regular gyrobifastigium, the aspect ratio is  $\sqrt{3}$ . The particle aspect ratio in the study is varied by elongating the triangular faces into isosceles triangles while keeping square base of attachment unaltered. If the side of the square base is two units, then the height of the triangular facet is equal to the aspect ratio. We study four shapes (Figure 1): regular gyrobifastigium (GBF,  $AR = \sqrt{3}$ ), oblate gyrobifastigium (oGBF,  $AR = 1$ ), prolate gyrobifastigium (pGBF,  $AR = 2\sqrt{3} - 1$ ), and long gyrobifastigium (lGBF,  $AR = 3$ ).

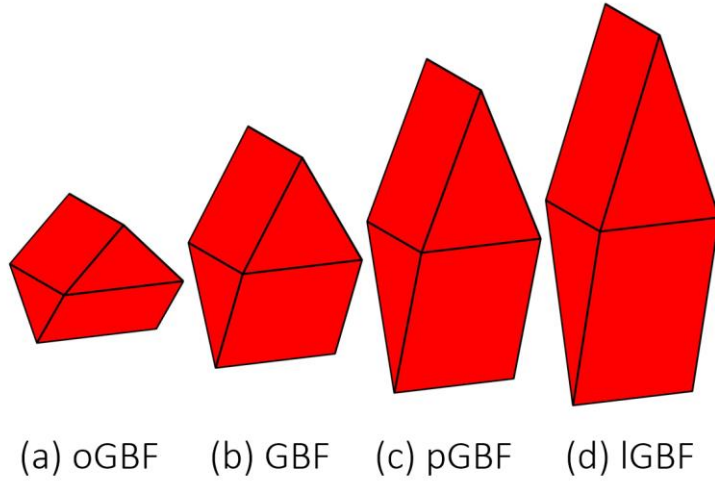


**Figure 41:** Shapes from the GBF family being considered in this work: (a) oblate gyrobifastigium (oGBF,  $AR = 1$ ), (b) regular gyrobifastigium (GBF,  $AR = \sqrt{3}$ ), (c) prolate gyrobifastigium (pGBF,  $AR = 2\sqrt{3} - 1$ ), and (d) long gyrobifastigium (IGBF,  $AR = 3$ ).

## 2.2 Monte Carlo Simulations

Metropolis<sup>55</sup> Monte Carlo (MC) simulations conducted in either the canonical ( $NVT$ ) or the isothermal-isobaric ( $NpT$ ) ensemble as necessary, where  $N$  is the total number of particles,  $V$  is the volume of the system,  $p$  is the pressure, and  $T$  is the temperature. We use scaled units consistent with our previous studies,<sup>4</sup> with lengths scaled by the circumradius ( $a_c$ ) of the shape. Thus, the dimensionless pressure is given by  $p = \beta p_a a_c^3$ , where  $p_a$  is the unscaled pressure and  $\beta = \frac{1}{k_B T}$ , where  $k_B$  is Boltzmann's constant. The chemical potential  $\mu$  and free energy ( $\Delta G$ ) are scaled by  $k_B T$  and the dimensionless interfacial free energy is given by  $\gamma = \beta \gamma_a a_c^2$  where  $\gamma_a$  is the unscaled interfacial free energy. For comparison among different particle shapes we tried to remove the dependence on the choice of length scale  $a_c$ , by defining a reduced dimensionless

interfacial free energy as  $\bar{\gamma} = \frac{\gamma}{\rho_s^{2/3}}$ , where  $\rho_s$  is the density of the solid/ordered phase.

The supersaturation is defined as  $\Delta\mu_{od} = \mu_o - \mu_d$ , where  $\mu_o$  and  $\mu_d$  are chemical potentials associated with ordered and disordered phases, respectively. The simulations used periodic boundary conditions to mimic bulk behavior. Each MC cycle included  $N$  translation,  $N$  rotation,  $N$  flip (flips the particle along its long axis) and 2 isotropic volume moves (for  $NpT$  ensemble runs only). Unless otherwise stated, all configurations were originally obtained for a cuboidal simulation box with  $N = 1728$  particles containing 12 layers of  $12 \times 12$  particles arranged in an ABCD crystal lattice of the GBF honeycomb.

### 2.3 *Cleaving Walls Method*

We use cleaving walls method<sup>113</sup> to directly calculate  $\gamma$  for various crystal planes. The method essentially calculates the reversible work done per unit area of interface created. In this study, we used flat walls that interact with particle centroids, and performed all calculations at disorder-order coexistence pressures. More details on the method implementation and initial setup in Monte Carlo simulations is described in a previous study.<sup>142</sup>

## 2.4 Coexistence Pressures

The isotropic-crystal coexistence pressure for GBF under this scaling is  $p_{ic,GBF} = 10.8$  as calculated in a previous study.<sup>95</sup> For non-regular GBFs we calculate the isotropic-crystal coexistence pressures using the interfacial pinning method.<sup>78</sup>

## 2.5 Order Parameters

Steinhardt<sup>50</sup> order parameters are used to capture both local translational and orientational order. We use  $q_6$  to quantify the translational order.  $q_6$  is dependent upon the neighbor cutoff distance  $r_c$ . More details on our use of this order parameter is provided in previous studies.<sup>8,96</sup>  $q_6$  values for any two particles ( $i$  and  $j$ ) can be used to evaluate translational correlation  $d_q(i, j)$ :

$$d_q(i, j) = \frac{\sum_{m=-6}^6 q_{6,m}(i) q_{6,m}^*(j)}{\left(\sum_{k=-6}^6 |q_{6,k}(i)|^2\right)^{\frac{1}{2}} \left(\sum_{l=-6}^6 |q_{6,l}(j)|^2\right)^{\frac{1}{2}}}$$

where the asterisk (\*) denotes the complex conjugate in both cases.

We use  $P_2$  orientational order parameter<sup>143</sup> to measure the orientational correlation between two particles ( $i$  and  $j$ ):

$$P_2(i, j) = \frac{3 \cos^2 \theta_{ij} - 1}{2}$$

where  $\theta_{ij}$  is the angle between the long-axis unit vectors.

### 3 Results and Discussion

#### 3.1 GBF

##### 3.1.1 Crystal Planes of Interest

A given crystal may have several closed packed crystal planes.<sup>119</sup> Based on results from nucleus-size pinning and umbrella sampling, we could narrow down the relevant crystal planes that are prominently present in the nucleus shape (Figure 2). We choose three crystal planes (100), (001) and  $(\sqrt{12} 0 1)$ . The last plane will henceforth be referred to as the *s* (slant) plane.

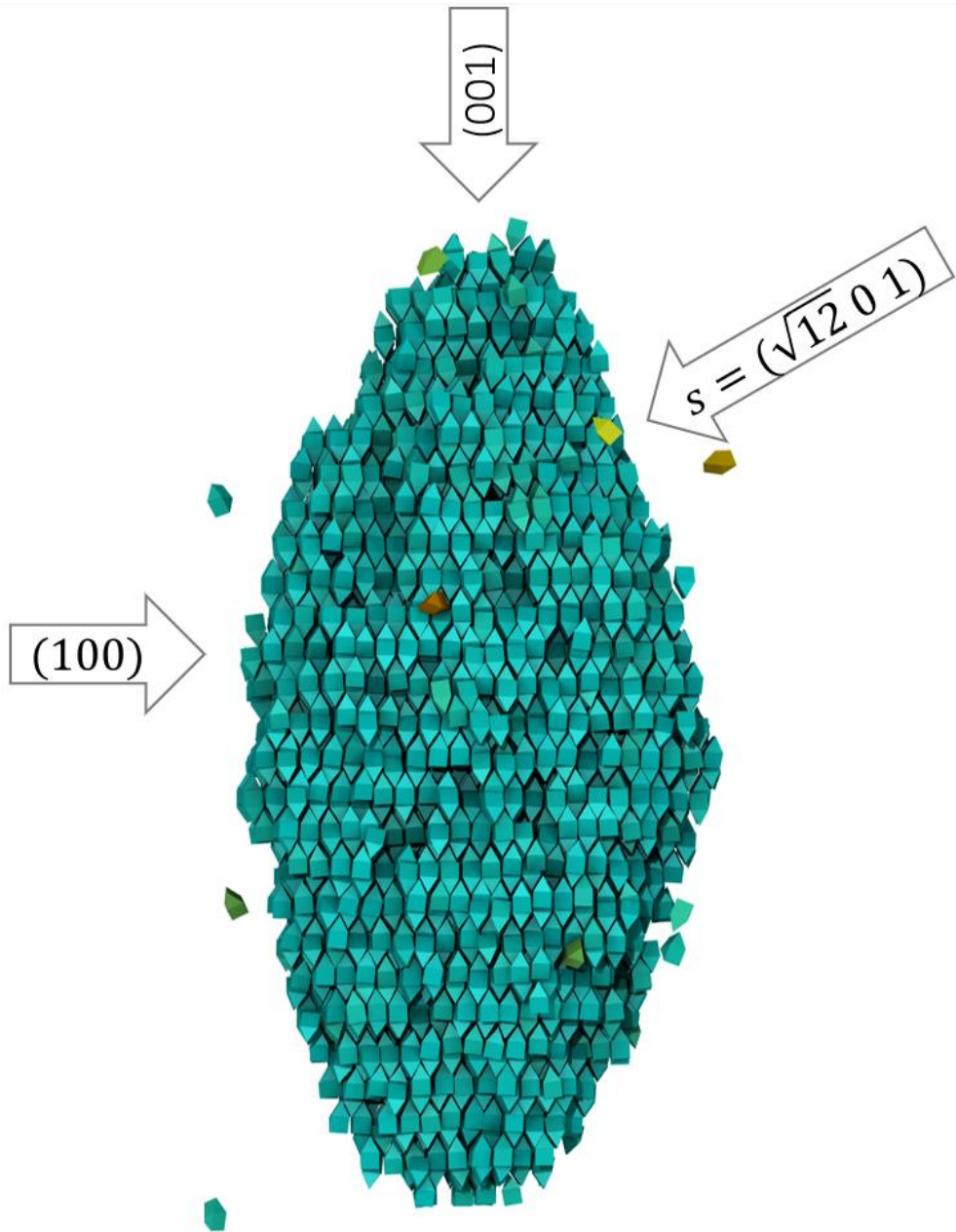


**Figure 42:** Crystal planes of interest based on their prominence in the nucleus of crystal phase of GBF.

### 3.1.2 Interfacial Free Energy Calculations

We needed to use different system sizes for various crystal planes to have a proper cleaving walls calculation without any artifacts. All interfacial free energies were calculated at coexistence pressure  $p_{ic,GBF} = 10.8$ .

- For (001) crystal plane, we used  $N = 1728$  particles for each phase.  $\gamma_{001} = 1.60$ . (Figure 3)
- For (100) crystal plane, we used  $N = 1728$  particles for the isotropic phase and  $N = 3456$  particles for the crystal. A longer crystal phase was required in order to avoid warping of crystal lattice.  $\gamma_{100} = 1.13$ . (Figure 4)
- For  $s = (\sqrt{12} \ 0 \ 1)$  crystal plane we had to specially create a new crystal configuration with  $N = 1872$  particles. Isotropic phase of the same size was generated by melting the crystal.  $\gamma_s = 0.76$ . (Figure 5)

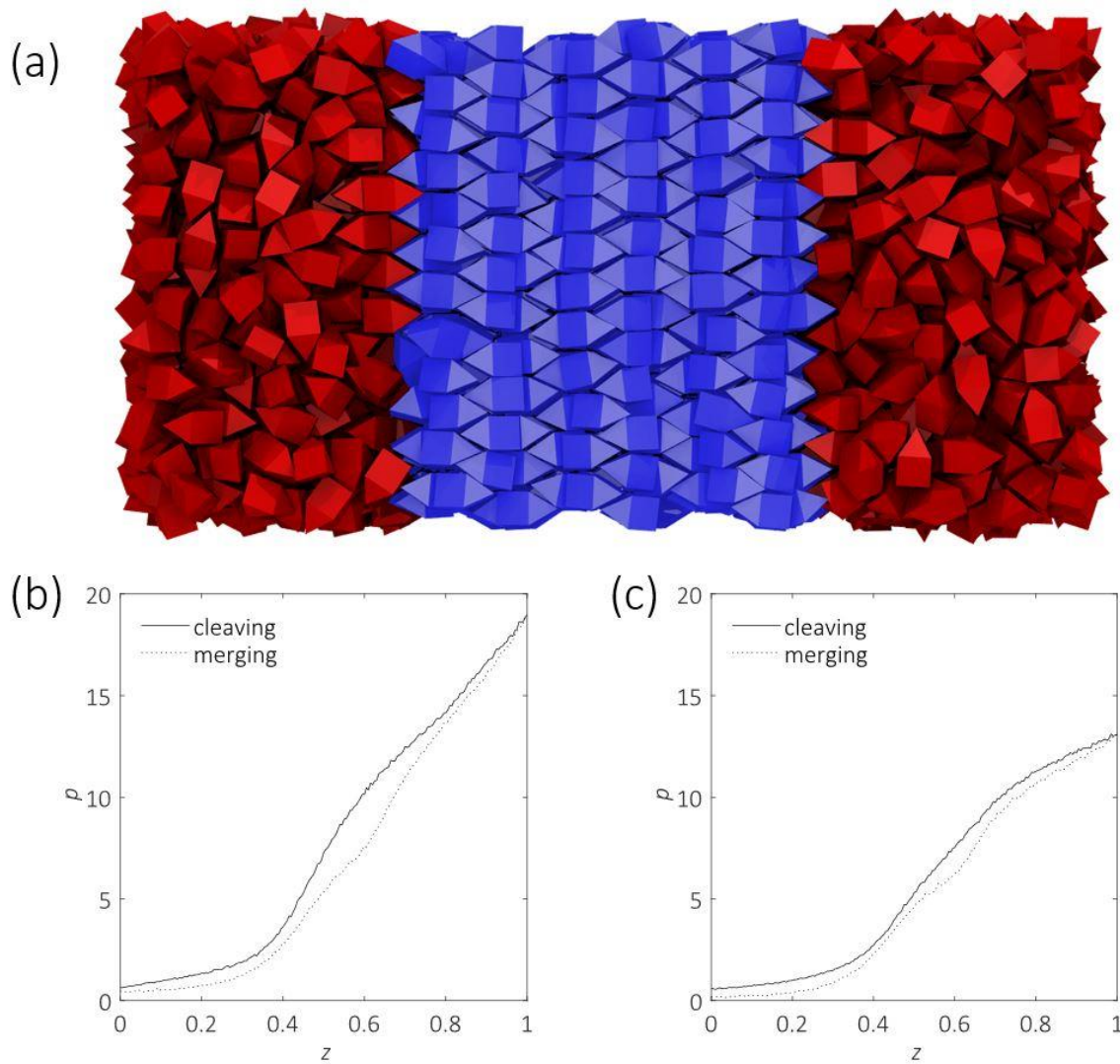


**Figure 43:** Cleaving walls for GBF (100) plane at coexistence pressure  $p=10.8$ . (a) Sample configuration at the end of the procedure. Ordered and disordered phase particles are colored blue and red, respectively. (b, c) Pressure variation with the position of the cleaving walls with respect to the midplane (quantifying the gap width) for (b) ordered and (c) disordered phase. Cleaving is shown with a solid line and merging is shown with dotted line. Scaling for the axes is described in Section 2.2.

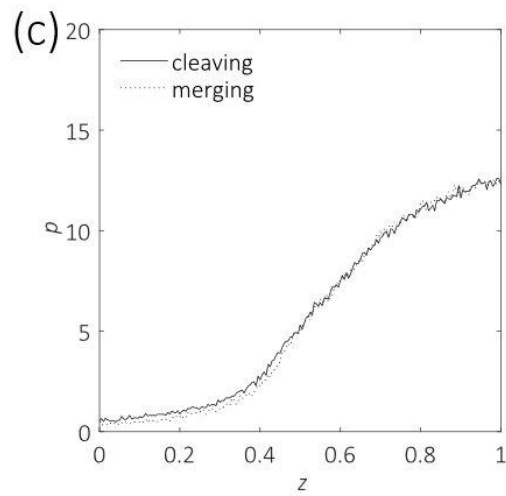
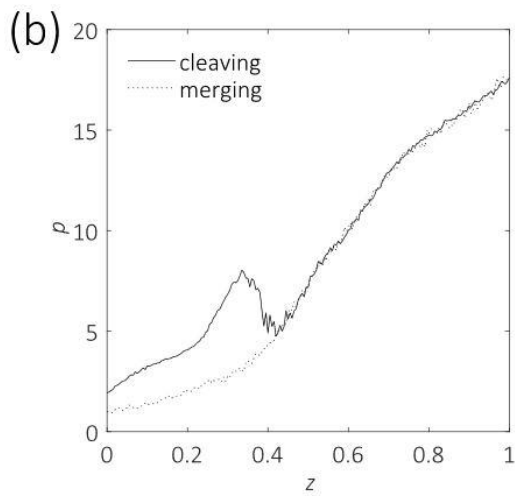
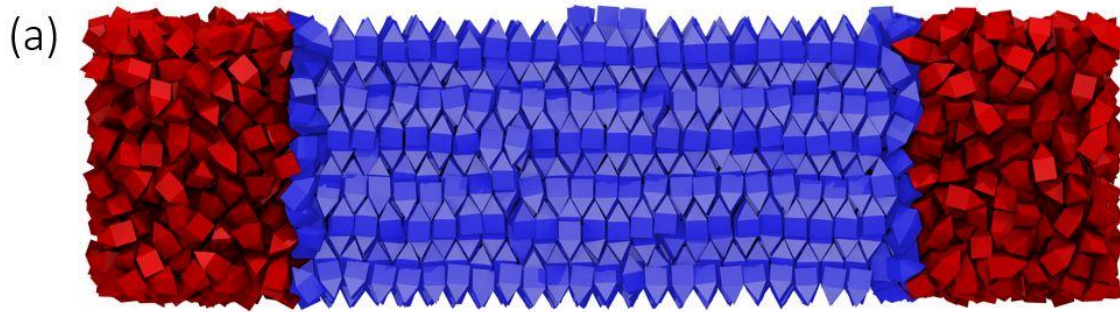


**Figure 44:** Cleaving walls for GBF (001) plane at coexistence pressure  $p=10.8$ . (a) Sample configuration at the end of the procedure. Ordered and disordered phase particles are colored blue and red, respectively. (b, c) Pressure variation with the position of the cleaving walls with respect to the midplane (quantifying the gap width) for (b) ordered and (c) disordered phase. Cleaving is shown with a solid line and merging is shown with dotted line. Scaling for the axes is described in Section 2.2.

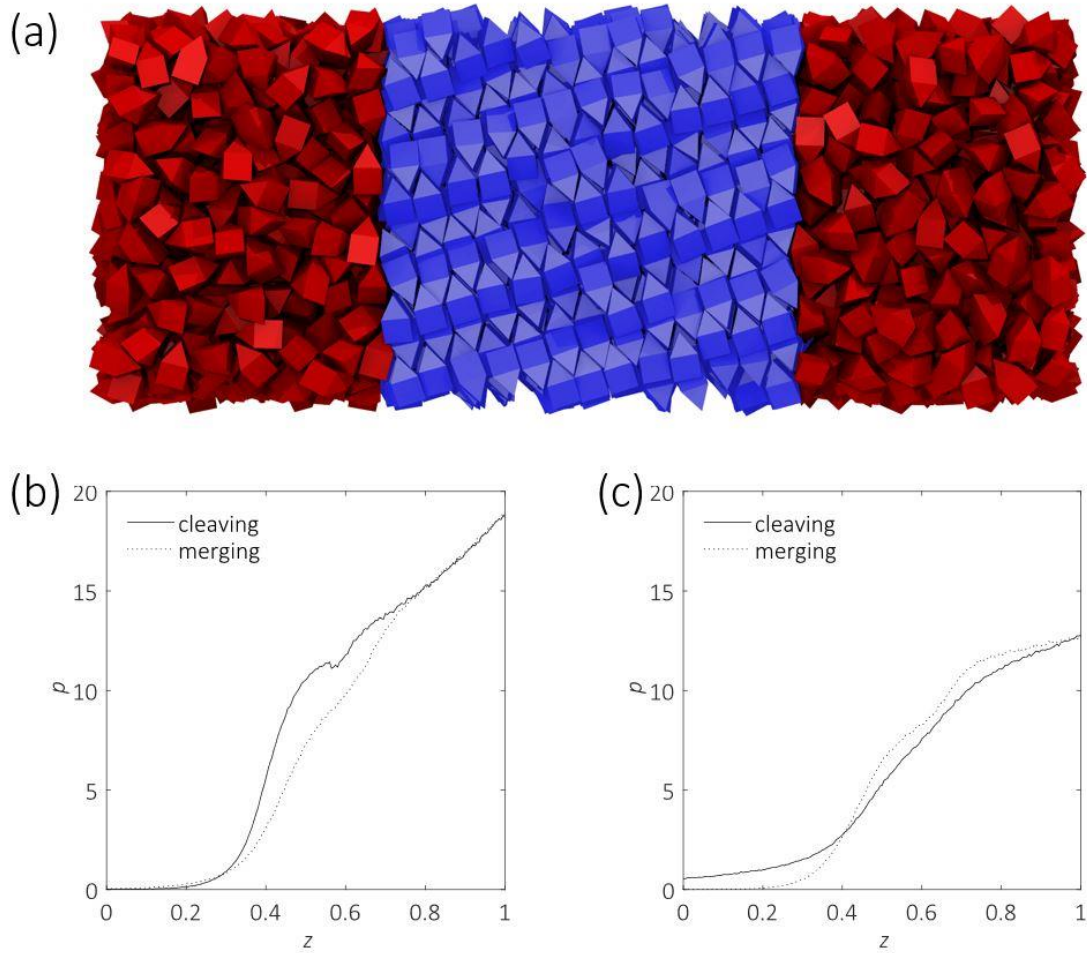


**Figure 45:** Cleaving walls for GBF  $s = (\sqrt{12} \ 0 \ 1)$  plane at coexistence pressure  $p=10.8$ . (a) Sample configuration at the end of the procedure. Ordered and disordered phase particles are colored blue and red, respectively. (b, c) Pressure variation with the position of the cleaving walls with respect to the midplane (quantifying the gap width) for (b) ordered and (c) disordered phase. Cleaving is shown with a solid line and merging is shown with dotted line. Scaling for the axes is described in Section 2.2.

### 3.1.3 Relation of Interfacial Roughness and Interfacial Free Energy

In an earlier study we conjectured if the interfacial free energy correlates with the roughness of the crystal surface. The results from GBF crystal planes substantiate that conjecture as visual inspection (Figure 6(a)) places the roughness of facets in the order:  $(001) > (100) > s$ , which is the same as the order for  $\gamma$ . This could be understood by considering how much excluded volume for the isotropic phase a given crystal interface creates due to its roughness. This effect can be captured by calculating interfacial potential of mean force (PMF) experienced by a free particle at a given distance from a perfect crystal interface. The distance from the interface ( $x$ ) here is defined with respect to the point where  $PMF = 7 k_B T$ . This choice is based on the intuition that the surface at a certain point entirely forbids a particle from occupying a space i.e.,  $PMF \rightarrow \infty$ . Since we cannot measure infinite PMFs, we use this threshold as a surrogate. More details of the method are provided in an earlier study.<sup>142</sup> The interfacial PMF calculations are shown in Figure 6(b). We find that the  $s$  facet unequivocally has the shortest range of influence. The  $(001)$  has higher PMF at short distances ( $x < 0.5$ ) than  $(100)$ , but decays to zero quicker at longer distances, indicative shorter range of disruption overall.

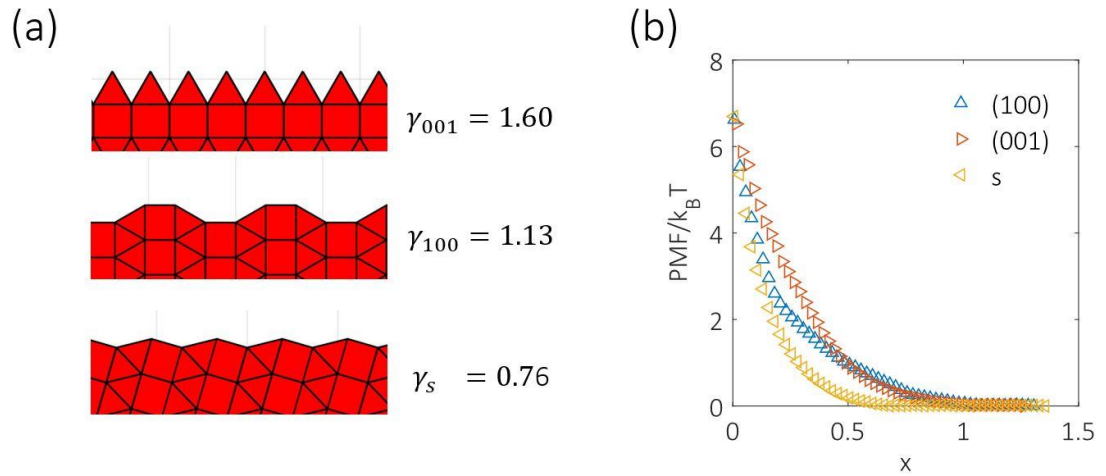


**Figure 46:** Correlation of surface roughness and interfacial free energy. (a) Surface topographies of various crystal planes. (b) Interfacial potentials of mean force (PMF) experienced by a free particle at a distance  $x$  from the interface (defined by  $\text{PMF}=7k_B T$ ).

### 3.1.4 Wulff Construction

We can utilize the interfacial free energy calculated for the three crystal planes to perform a Wulff construction.<sup>117–119</sup> The construction is based on the derived relation that in a steady state nucleus of a crystalline phase, the perpendicular distance of a crystal facet  $i$  from the center of mass ( $h_i$ ) is proportional to its interfacial free energy  $\gamma_i$ , i.e.  $h_i \propto \gamma_i$ . This relation can be used to determine the relative positions of crystal planes, with the enclosed volume representing the nucleus shape. Wulff construction for GBF is shown in Figure 7(a), where we take perpendicular distance to the energetically most inexpensive facet  $s$  as  $h_s = 1$ . We also leverage the symmetry of the crystal to find the 3D volume enclosed by all the crystal planes for which we know  $\gamma$  (Figure 7(b)). We find that the crystal plane (100) does not appear in the predicted

nucleus shape, resulting in a shape we could describe as an elongated octahedron with truncated vertices along the elongated axis. The aspect ratio of this predicted nucleus geometry is calculated to be 2.05, which is quite close to the nucleus size-pinning estimates between 1.9 and 2.1. Based on relative areas of  $s$  and  $(001)$  facets in the Wulff construction, we calculated the average interfacial free energy of the nucleus at coexistence to be  $\gamma_{avg} = 0.79$ , which is also in agreement with the previous predictions.

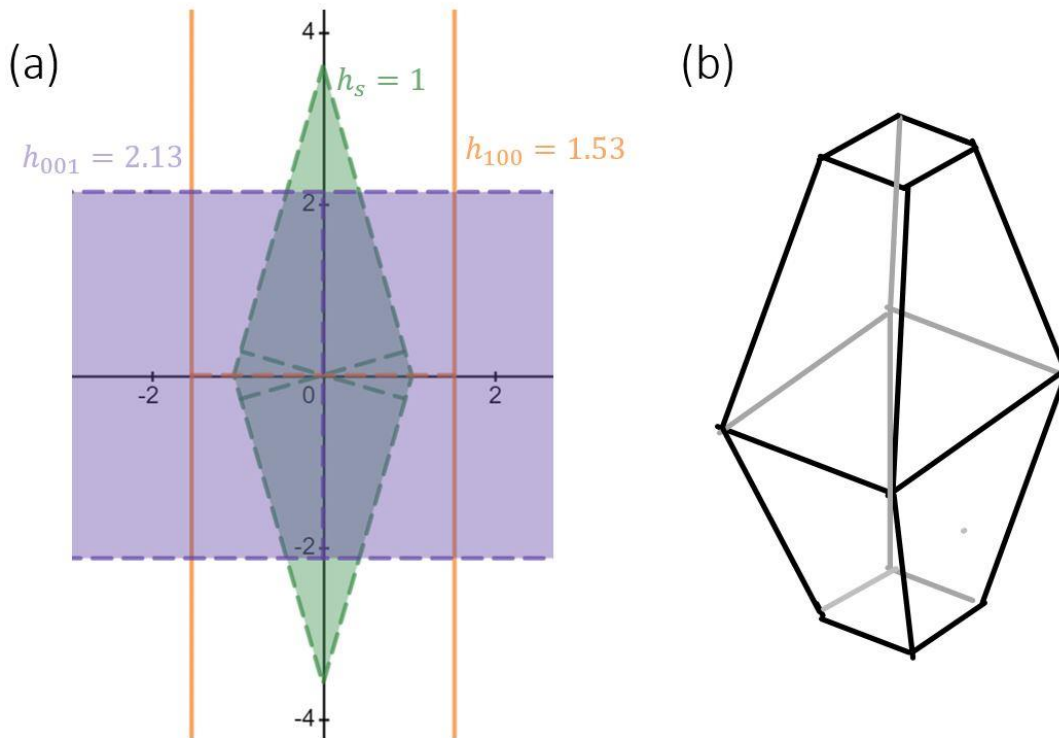


**Figure 47:** Wulff construction for GBF at coexistence. (a) Geometric construction. Generated using Desmos online graphing calculator<sup>144</sup> (b) Schematic sketch of the 3D polyhedral shape predicted.

### 3.2 Oblate GBF (oGBF)

The equation of state calculated for  $N = 1728$  of oGBF particles is shown in Figure 8. The phase behavior and kinetics are qualitatively similar to those of GBF. We find that there is an isotropic and a crystal branch, with a spontaneous melting of the crystal into the isotropic phase with minimal hysteresis. On the other hand, the isotropic branch does not spontaneously transition to the crystal phase upon compression, and instead enters a glassy state. This could indicate a higher  $\Delta G^*$  compared to GBF at a given  $\Delta\mu$ . The isotropic-crystal coexistence pressure for oGBF calculated by interfacial pinning method is  $p_{ic,oGBF} \approx 7.06$ .

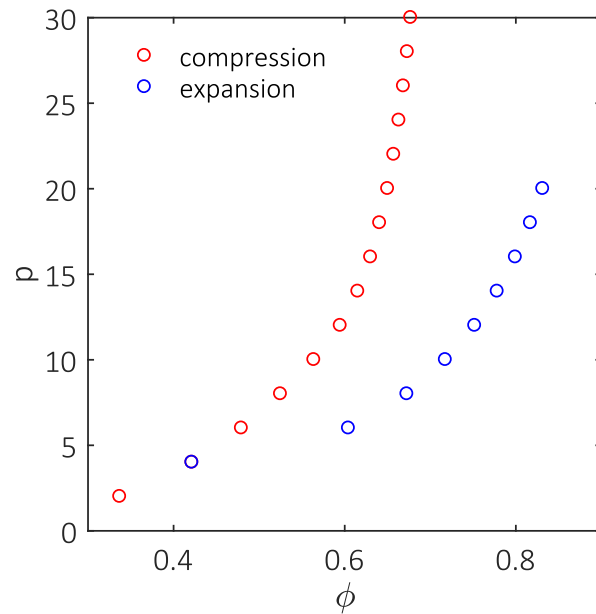
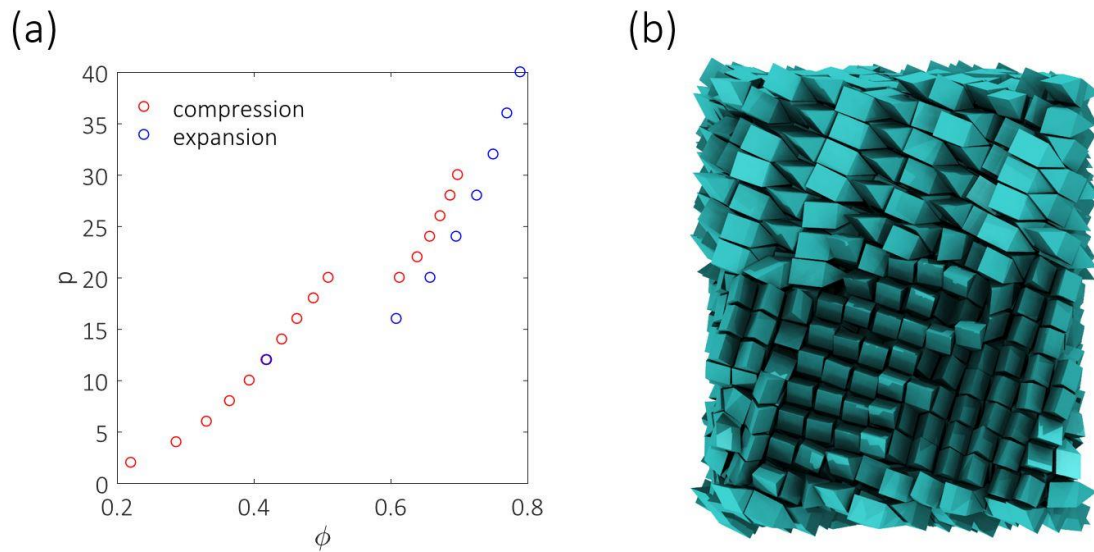


Figure 48: Equation of state for oGBF.

### 3.3 Prolate GBF (pGBF)

The equation of state for pGBF calculated for  $N = 1728$  particles is shown in Figure 9(a). Similar to GBF, we observe an isotropic branch and a crystal branch, with the crystal spontaneously melting into the isotropic phase upon expansion with minimal hysteresis. Interestingly, unlike GBF, at  $p = 20$  the isotropic phase spontaneously transitions to the crystal phase. The crystal phase thus formed is not perfect and contains multiple grains (Figure 9(b)), hence a small discrepancy is observed between the two branches. This suggests that the  $\Delta G^*$  for the isotropic-crystal transition for pGBF would be lower than that for GBF at a comparable degree of supersaturation i.e., it is inversely related to the aspect ratio, perhaps consistent with inability of the oGBF to spontaneously crystallize. The isotropic-crystal coexistence pressure for pGBF calculated by interfacial pinning method is  $p_{ic,pGBF} \approx 15.6$ .



**Figure 49:** (a) Equation of state for pGBF. (b) Imperfect crystal formed upon compression of the isotropic phase. The snapshot is equilibrated at  $p=30.0$ .

### 3.4 Long GBF (IGBF)

#### 3.4.1 Equation of State and Phase Behavior

The equation state for IGBF reveals major qualitative differences in phase behavior (Figure 10) relative to the previous cases. Apart from the standard isotropic and crystal branches, we found the existence of an orientationally ordered but translationally disordered (nematic) phase. Sample configurations of the three phases at  $p = 19$  are shown in Figure 11(a-c). The nematic phase can be obtained from both compression of the isotropic phase (at  $p = 19$ ) and expansion of the crystal (at  $p = 18.5$ ). The nematic phase also spontaneously transitions to isotropic phase upon expansion at  $p = 18.5$  (although a lower transition pressure was observed from nematic phase obtained from

the crystal). The hysteresis in nematic-isotropic transition is minimal, implying that the coexistence pressure  $p_{in,IGBF} \in [18.5,19.0]$ .

Upon compression to  $p = 22.5$ , the nematic phase spontaneously transitions to the crystal with a slight discrepancy in volume fraction (Figure 11(d)). The discrepancy is much smaller when compared to pGBF, with nearly all particles constituting a single grain in the present case.

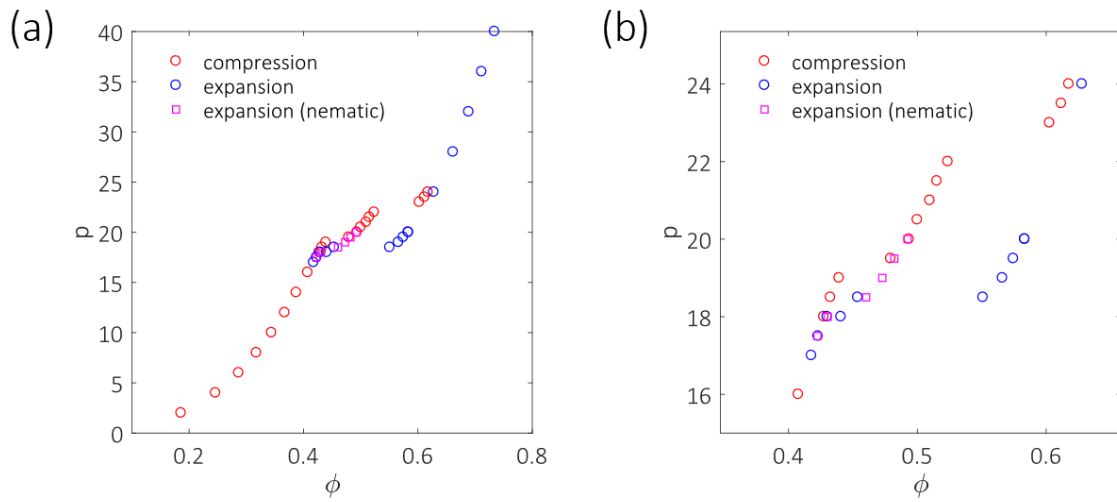
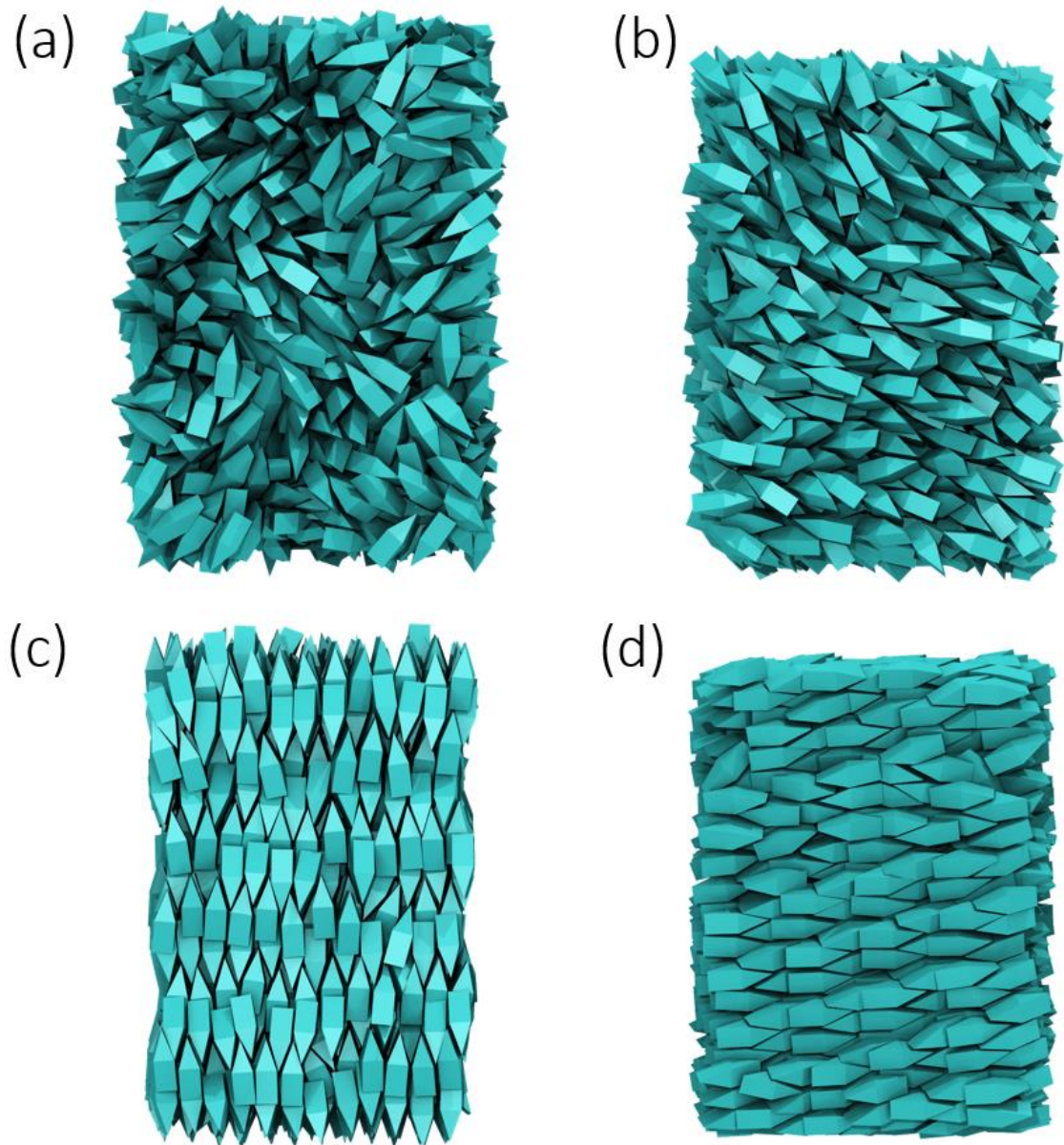


Figure 50: (a) Equation of state for IGBF (b) Zoomed-in for clarity.



**Figure 51:**(a-c) Sample configurations of various phases of IGBF particles at  $p=19$  (a) Isotropic phase, (b) Nematic phase, (c) Crystal. (d) Sample configuration of crystal obtained upon compression of nematic phase, equilibrated at  $p=24$ .

### 3.4.2 Translational and Orientational Correlations

We characterize the three phases and the transitions between them by calculating the correlations of translational and orientational order as a function of distance between the particles  $r$  at  $p = 19$ . The orientation correlation ( $P_2$ ) is shown in Figure 12(a). We find that at all distances there is a clear distinction between the three phases with  $P_2^{crystal} > P_2^{nematic} > P_2^{isotropic}$ . There is nearly no decay in orientational correlation for the crystal phase with distance. The orientational correlation in the nematic phase decays with distance to a moderate value ( $\sim 0.5$ ), while it decays quicker and to a lower value ( $\sim 0.0$ ) for the isotropic phase. Note that the minimum possible value for  $P_2$  is -0.5.

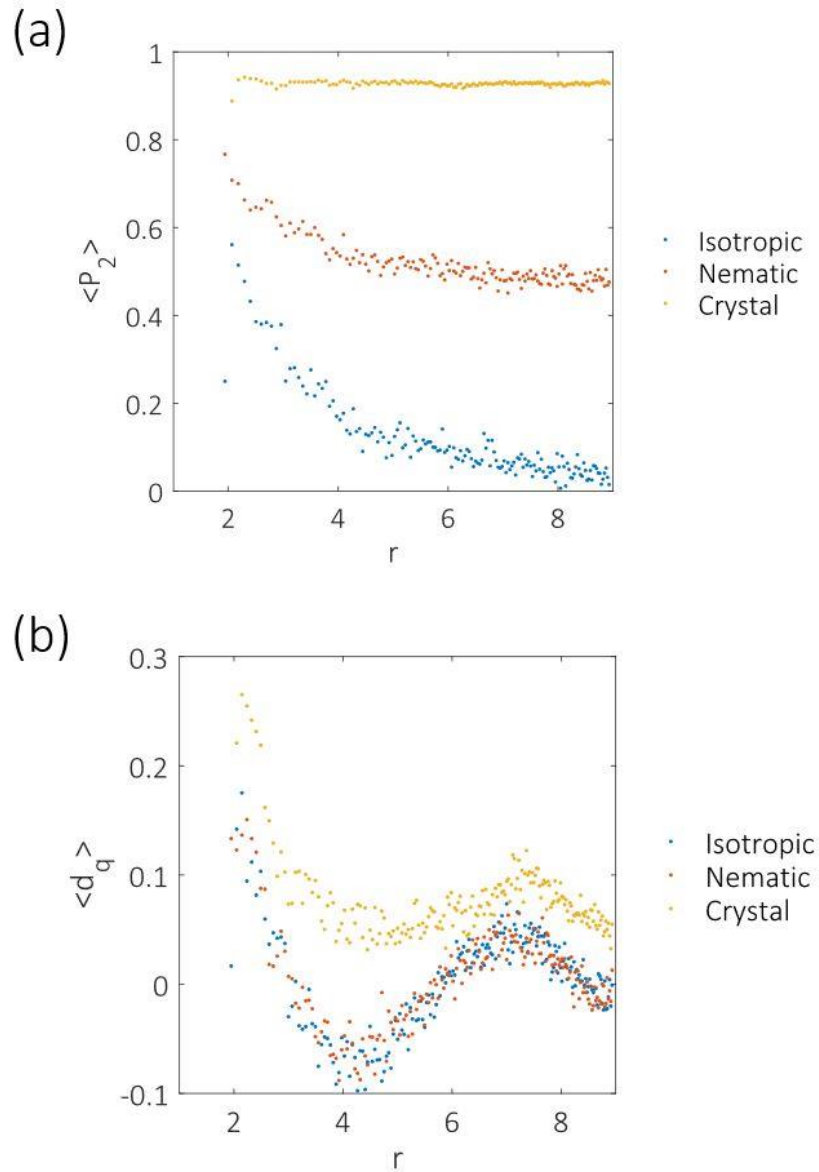


**Figure 52:** Average correlation of order for IGBF phases as a function of interparticle distance ( $r$ , unscaled for base side = 2 units) at  $p=19$ . (a) orientational correlation ( $P_2$ ); (b) translational order ( $d_q$ ).

The translational correlation function  $d_q$  for the three phases is shown in Figure 12(b).

This correlation can clearly distinguish crystal from other phases, which look nearly

identical. Note that  $d_q$  is impacted by the choice of  $r_c$  (chosen here to be  $\sqrt{2}$  in scaled units), hence the distinction would likely become sharper for a smaller  $r_c$ .

### 3.4.3 Visualization of Order

The IGBF system also presents a unique opportunity to develop visualizations that can reflect the presence of concurrent translational and orientational order. One way to achieve that is to plot the centroids of all particles in a plane that passes through a given particle, and color them according to orientational correlation. An example of such a visualization is shown in Figure 13 for the three phases at  $p = 19$ .

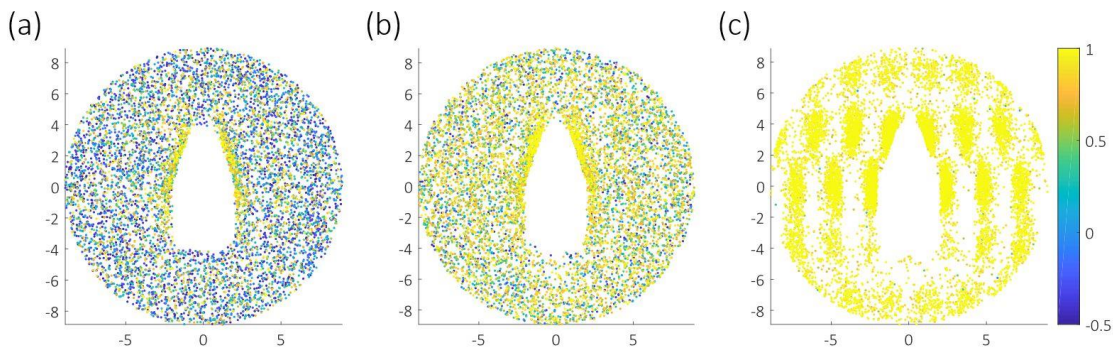


**Figure 53:** Visualization of orientational and translational order around a particle within its plane. Coordinate axes are unscaled, with the particle square base with side = 2. The color bar corresponds to  $P_2$  value.

For isotropic phase, we find using this visualization that neighboring particles are generally spread uniformly and are only aligned with the central particle when in close proximity (especially near the rectangular faces). For the nematic phase we observe a

general increase in orientational order and a slight clustering of particles close to the central particle. For the crystal, we find a clear periodic clustering of highly aligned neighbors on a lattice.

#### **4 Conclusions and Future Work**

In this paper we have studied the origins of anisotropic nuclei in GBF through a direct measurement of interfacial free energy and predicted the nucleus shape and average interfacial free energy in agreement with independent estimates. Our calculations reveal a trend that the surface roughness correlates with the interfacial free energy. We then focus on related shapes with varying aspect ratio. It is revealed that changing the aspect ratio significantly alters both kinetics and phase behavior for GBF like particles. The key results are summarized in Figure 14. We find that while shortening the GBF does not alter the kinetics and phase behavior, elongating it makes the transition easier (i.e., lowers the barrier). For pGBF we observe that upon compression the isotropic phase spontaneous transition to a crystal (albeit with defects). Further elongation results in stabilization of a nematic phase, which can be formed by both expansion of crystal and compression isotropic phase. Further the nematic phase also compresses into the crystal with minimal defects. Finally, we studied how orientational and translational correlations distinguish various phases.

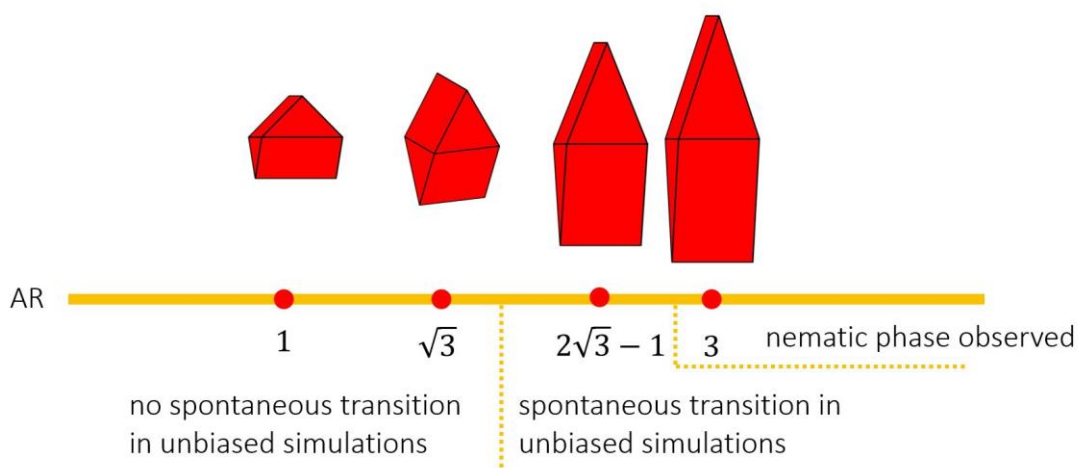


**Figure 54:** Key observations regarding the change of phase behavior and kinetics for GBF like particles.

These results set up the stage for some very interesting questions and directions that could be pursued:

- Development of order parameters to track the spontaneous and rare transitions.<sup>43,123,145</sup>
- Umbrella sampling and nucleus size pinning simulations to calculate  $\Delta G^*$  for various transitions.
- How does the nucleus shape change with aspect ratio?
- How do the interfacial free energies at coexistence vary with aspect ratio?
- Calculation of nematic-crystal coexistence pressure for IGBF.
- Development of a measure for surface roughness similar to sinuosity or skew.
- Investigating existence long-range structures, such as helices, in the orientational field for the nematic phase of IGBF particles.

## **5 Acknowledgements**

We would like to thank Marjolein Dijkstra for insightful discussions.

## REFERENCES

- (1) Whitesides, G. M.; Boncheva, M. Beyond Molecules: Self-Assembly of Mesoscopic and Macroscopic Components. *Proc. Natl. Acad. Sci. U. S. A.* **2002**, *99*, 4769–4774.
- (2) Burda, C.; Chen, X.; Narayanan, R.; El-Sayed, M. A. Chemistry and Properties of Nanocrystals of Different Shapes. *Chemical Reviews*. 2005, pp 1025–1102.
- (3) Glotzer, S. C.; Solomon, M. J. Anisotropy of Building Blocks and Their Assembly into Complex Structures. *Nat. Mater.* **2007**, *6*, 557–562.
- (4) Agarwal, U.; Escobedo, F. A. Mesophase Behaviour of Polyhedral Particles. *Nat. Mater.* **2011**, *10*, 230–235.
- (5) Damasceno, P. F.; Engel, M.; Glotzer, S. C. Crystalline Assemblies and Densest Packings of a Family of Truncated Tetrahedra and the Role of Directional Entropic Forces. *ACS Nano* **2012**, *6*, 609–614.
- (6) Damasceno, P. F.; Engel, M.; Glotzer, S. C. Predictive Self-Assembly of Polyhedra into Complex Structures. *Science (80-. )*. **2012**, *337*, 453–457.
- (7) Gantapara, A. P.; De Graaf, J.; Van Roij, R.; Dijkstra, M. Phase Diagram and Structural Diversity of a Family of Truncated Cubes: Degenerate

- Close-Packed Structures and Vacancy-Rich States. *Phys. Rev. Lett.* **2013**, *111*, 1–5.
- (8) Thapar, V.; Escobedo, F. A. Localized Orientational Order Chaperones the Nucleation of Rotator Phases in Hard Polyhedral Particles. *Phys. Rev. Lett.* **2014**, *112*, 048301.
- (9) Khadilkar, M. R.; Escobedo, F. A. Heuristic Rule for Binary Superlattice Coassembly: Mixed Plastic Mesophases of Hard Polyhedral Nanoparticles. *Phys. Rev. Lett.* **2014**, *113*, 165504.
- (10) Gantapara, A. P.; De Graaf, J.; Van Roij, R.; Dijkstra, M. Phase Behavior of a Family of Truncated Hard Cubes. *J. Chem. Phys.* **2015**, *142*, 054904.
- (11) Manna, L.; Milliron, D. J.; Meisel, A.; Scher, E. C.; Alivisatos, A. P. Controlled Growth of Tetrapod-Branched Inorganic Nanocrystals. *Nat. Mater.* **2003**, *2*, 382–385.
- (12) Chen, S.; Wang, Z. L.; Ballato, J.; Foulger, S. H.; Carroll, D. L. Monopod, Bipod, Tripod, and Tetrapod Gold Nanocrystals. *J. Am. Chem. Soc.* **2003**, *125*, 16186–16187.
- (13) Sun, Y.; Xia, Y. Shape-Controlled Synthesis of Gold and Silver Nanoparticles. *Science (80-. )*. **2002**, *298*, 2176–2179.

- (14) Malikova, N.; Pastoriza-Santos, I.; Schierhorn, M.; Kotov, N. A.; Liz-Marzán, L. M. Layer-by-Layer Assembled Mixed Spherical and Planar Gold Nanoparticles: Control of Interparticle Interactions. *Langmuir* **2002**, *18*, 3694–3697.
- (15) Cho, K. S.; Talapin, D. V.; Gaschler, W.; Murray, C. B. Designing PbSe Nanowires and Nanorings through Oriented Attachment of Nanoparticles. *J. Am. Chem. Soc.* **2005**, *127*, 7140–7147.
- (16) Dendukuri, D.; Pregibon, D. C.; Collins, J.; Hatton, T. A.; Doyle, P. S. Continuous-Flow Lithography for High-Throughput Microparticle Synthesis. *Nat. Mater.* **2006**, *5*, 365–369.
- (17) Seo, D.; Ji, C. P.; Song, H. Polyhedral Gold Nanocrystals with Oh Symmetry: From Octahedra to Cubes. *J. Am. Chem. Soc.* **2006**, *128*, 14863–14870.
- (18) Compton, O. C.; Osterloh, F. E. Evolution of Size and Shape in the Colloidal Crystallization of Gold Nanoparticles. *J. Am. Chem. Soc.* **2007**, *129*, 7793–7798.
- (19) Henzie, J.; Grünwald, M.; Widmer-Cooper, A.; Geissler, P. L.; Yang, P. Self-Assembly of Uniform Polyhedral Silver Nanocrystals into Densest Packings and Exotic Superlattices. *Nat. Mater.* **2012**, *11*, 131–137.

- (20) Martin, B. R.; Dermody, D. J.; Reiss, B. D.; Fang, M.; Lyon, L. A.; Natan, M. J.; Mallouk, T. E. Orthogonal Self-Assembly on Colloidal Gold-Platinum Nanorods. *Adv. Mater.* **1999**, *11*, 1021–1025.
- (21) Roh, K. H.; Martin, D. C.; Lahann, J. Biphasic Janus Particles with Nanoscale Anisotropy. *Nat. Mater.* **2005**, *4*, 759–763.
- (22) Zhang, G.; Wang, D.; Möhwald, H. Decoration of Microspheres with Gold Nanodots - Giving Colloidal Spheres Valences. *Angew. Chemie - Int. Ed.* **2005**, *44*, 7767–7770.
- (23) Jackson, A. M.; Hu, Y.; Silva, P. J.; Stellacci, F. From Homoligand- to Mixed-Ligand- Monolayer-Protected Metal Nanoparticles: A Scanning Tunneling Microscopy Investigation. *J. Am. Chem. Soc.* **2006**, *128*, 11135–11149.
- (24) Yu, Y. Y.; Chang, S. S.; Lee, C. L.; Wang, C. R. C. Gold Nanorods: Electrochemical Synthesis and Optical Properties. *J. Phys. Chem. B* **1997**, *101*, 6661–6664.
- (25) Peng, X.; Manna, L.; Yang, W.; Wickham, J.; Scher, E.; Kadavanich, A.; Alivisatos, A. P. Shape Control of CdSe Nanocrystals. *Nature* **2000**, *404*, 59–61.
- (26) Van Der Kooij, F. M.; Kassapidou, K.; Lekkerkerker, H. N. W. Liquid

- Crystal Phase Transitions in Suspensions of Polydisperse Plate-like Particles. *Nature* **2000**, *406*, 868–871.
- (27) Mohraz, A.; Solomon, M. J. Direct Visualization of Colloidal Rod Assembly by Confocal Microscopy. *Langmuir* **2005**, *21*, 5298–5306.
- (28) Allen, R. J.; Warren, P. B.; Ten Wolde, P. R. Sampling Rare Switching Events in Biochemical Networks. *Phys. Rev. Lett.* **2005**, *94*, 018104.
- (29) Allen, R. J.; Frenkel, D.; Ten Wolde, P. R. Forward Flux Sampling-Type Schemes for Simulating Rare Events: Efficiency Analysis. *J. Chem. Phys.* **2006**, *124*, 194111.
- (30) Meadley, S. L.; Escobedo, F. A. Thermodynamics and Kinetics of Bubble Nucleation: Simulation Methodology. *J. Chem. Phys.* **2012**, *137*, 074109.
- (31) Torrie, G. M.; Valleau, J. P. Nonphysical Sampling Distributions in Monte Carlo Free-Energy Estimation: Umbrella Sampling. *J. Comput. Phys.* **1977**, *23*, 187–199.
- (32) Van Duijneveldt, J. S.; Frenkel, D. Computer Simulation Study of Free Energy Barriers in Crystal Nucleation. *J. Chem. Phys.* **1992**, *96*, 4655–4668.
- (33) Ten Wolde, P. R.; Ruiz-Montero, M. J.; Frenkel, D. Numerical Evidence

- for Bcc Ordering at the Surface of a Critical Fcc Nucleus. *Phys. Rev. Lett.* **1995**, *75*, 2714–2717.
- (34) Ten Wolde, P. R.; Ruiz-Montero, M. J.; Frenkel, D. Numerical Calculation of the Rate of Crystal Nucleation in a Lennard-Jones System at Moderate Undercooling. *J. Chem. Phys.* **1996**, *104*, 9932–9947.
- (35) Dellago, C.; Bolhuis, P. G.; Csajka, F. S.; Chandler, D. Transition Path Sampling and the Calculation of Rate Constants. *J. Chem. Phys.* **1998**, *108*, 1964–1977.
- (36) Dellago, C.; Bolhuis, P. G.; Chandler, D. On the Calculation of Reaction Rate Constants in the Transition Path Ensemble. *J. Chem. Phys.* **1999**, *110*, 6617–6625.
- (37) Van Erp, T. S.; Moroni, D.; Bolhuis, P. G. A Novel Path Sampling Method for the Calculation of Rate Constants. *J. Chem. Phys.* **2003**, *118*, 7762–7774.
- (38) van Erp, T. S.; Bolhuis, P. G. Elaborating Transition Interface Sampling Methods. *J. Comput. Phys.* **2005**, *205*, 157–181.
- (39) Peters, B.; Trout, B. L. Obtaining Reaction Coordinates by Likelihood Maximization. *J. Chem. Phys.* **2006**, *125*, 054108.

- (40) Auer, S.; Frenkel, D. Numerical Prediction of Absolute Crystallization Rates in Hard-Sphere Colloids. *J. Chem. Phys.* **2004**, *120*, 3015–3029.
- (41) Fillion, L.; Hermes, M.; Ni, R.; Dijkstra, M. Crystal Nucleation of Hard Spheres Using Molecular Dynamics, Umbrella Sampling, and Forward Flux Sampling: A Comparison of Simulation Techniques. *J. Chem. Phys.* **2010**, *133*, 244115.
- (42) Auer, S.; Frenkel, D. Prediction of Absolute Crystal-Nucleation Rate in Hard-Sphere Colloids. *Nature* **2001**, *409*, 1020–1023.
- (43) Cuetos, A.; Sanz, E.; Dijkstra, M. Can the Isotropic-Smectic Transition of Colloidal Hard Rods Occur via Nucleation and Growth? *Faraday Discuss.* **2009**, *144*, 253–269.
- (44) Schöpe, H. J.; Bryant, G.; Van Meegen, W. Two-Step Crystallization Kinetics in Colloidal Hard-Sphere Systems. *Phys. Rev. Lett.* **2006**, *96*, 175701.
- (45) Russo, J.; Tanaka, H. Nonclassical Pathways of Crystallization in Colloidal Systems. *MRS Bulletin*. 2016, pp 369–374.
- (46) Karthika, S.; Radhakrishnan, T. K.; Kalaichelvi, P. A Review of Classical and Nonclassical Nucleation Theories. *Cryst. Growth Des.* **2016**, *16*, 6663–6681.

- (47) Smeets, P. J. M.; Finney, A. R.; Habraken, W. J. E. M.; Nudelman, F.; Friedrich, H.; Laven, J.; De Yoreo, J. J.; Rodger, P. M.; Sommerdijk, N. A. J. M. A Classical View on Nonclassical Nucleation. *Proc. Natl. Acad. Sci. U. S. A.* **2017**, *114*, E7882–E7890.
- (48) Lutsko, J. F.; Nicolis, G. Theoretical Evidence for a Dense Fluid Precursor to Crystallization. *Phys. Rev. Lett.* **2006**, *96*.
- (49) Gottschalk, S.; Lin, M. C.; Manocha, D. OBB Tree: A Hierarchical Structure for Rapid Interference Detection. *Proc. 23rd Annu. Conf. Comput. Graph. Interact. Tech. SIGGRAPH 1996* **1996**, No. 8920219, 171–180.
- (50) Steinhardt, P. J.; Nelson, D. R.; Ronchetti, M. Bond-Orientational Order in Liquids and Glasses. *Phys. Rev. B* **1983**, *28*, 784–805.
- (51) John, B. S.; Juhlin, C.; Escobedo, F. A. Phase Behavior of Colloidal Hard Perfect Tetragonal Parallelepipeds. *J. Chem. Phys.* **2008**, *128*, 044909.
- (52) Escobedo, F. A. Effect of Inter-Species Selective Interactions on the Thermodynamics and Nucleation Free-Energy Barriers of a Tessellating Polyhedral Compound. *J. Chem. Phys.* **2016**, *145*, 211903.
- (53) Van Anders, G.; Klotsa, D.; Ahmed, N. K.; Engel, M.; Glotzer, S. C. Understanding Shape Entropy through Local Dense Packing. *Proc. Natl.*

*Acad. Sci. U. S. A.* **2014**, *111*, E4812–E4821.

- (54) Scott, R.; Allen, M. P.; Tildesley, D. J. *Computer Simulation of Liquids.*; 1991; Vol. 57.
- (55) Metropolis, N.; Rosenbluth, A. W.; Rosenbluth, M. N.; Teller, A. H.; Teller, E. Equation of State Calculations by Fast Computing Machines. *J. Chem. Phys.* **1953**, *21*, 1087–1092.
- (56) Auer, S.; Frenkel, D. Suppression of Crystal Nucleation in Polydisperse Colloids Due to Increase of the Surface Free Energy. *Nature* **2001**, *413*, 711–713.
- (57) White, G. M. Steady-State Random Walks with Application to Homogeneous Nucleation. *J. Chem. Phys.* **1969**, *50*, 4672–4678.
- (58) Kashchiev, D. Interrelation between Cluster Formation Time, Cluster Growth Probability, and Nucleation Rate. *J. Chem. Phys.* **2007**, *127*, 064505.
- (59) Sharma, A. K.; Thapar, V.; Escobedo, F. A. Solid-Phase Nucleation Free-Energy Barriers in Truncated Cubes: Interplay of Localized Orientational Order and Facet Alignment. *Soft Matter* **2018**, *14*, 1996–2005.
- (60) Allen, R. J.; Valeriani, C.; Rein Ten Wolde, P. Forward Flux Sampling for

- Rare Event Simulations. *J. Phys. Condens. Matter* **2009**, *21*, 463102.
- (61) Thapar, V.; Escobedo, F. A. Simultaneous Estimation of Free Energies and Rates Using Forward Flux Sampling and Mean First Passage Times. *J. Chem. Phys.* **2015**, *143*, 244113.
- (62) Giberti, F.; Salvalaglio, M.; Parrinello, M. Metadynamics Studies of Crystal Nucleation. *IUCrJ* **2015**, *2*, 256–266.
- (63) Laio, A.; Parrinello, M. Escaping Free-Energy Minima. *Proc. Natl. Acad. Sci. U. S. A.* **2002**, *99*, 12562–12566.
- (64) Trudu, F.; Donadio, D.; Parrinello, M. Freezing of a Lennard-Jones Fluid: From Nucleation to Spinodal Regime. *Phys. Rev. Lett.* **2006**, *97*, 105701.
- (65) Bai, X. M.; Li, M. Differences between Solid Superheating and Liquid Supercooling. *J. Chem. Phys.* **2005**, *123*, 151102.
- (66) Ter Horst, J. H.; Kashchiev, D. Determination of the Nucleus Size from the Growth Probability of Clusters. *J. Chem. Phys.* **2003**, *119*, 2241–2246.
- (67) Espinosa, J. R.; Vega, C.; Valeriani, C.; Sanz, E. Seeding Approach to Crystal Nucleation. *J. Chem. Phys.* **2016**, *144*, 034501.
- (68) Espinosa, J. R.; Vega, C.; Valeriani, C.; Sanz, E. The Crystal-Fluid Interfacial Free Energy and Nucleation Rate of NaCl from Different

Simulation Methods. *J. Chem. Phys.* **2015**, *142*, 194709.

- (69) Lifanov, Y.; Vorselaars, B.; Quigley, D. Nucleation Barrier Reconstruction via the Seeding Method in a Lattice Model with Competing Nucleation Pathways. *J. Chem. Phys.* **2016**, *145*, 211912.
- (70) Sun, Y.; Song, H.; Zhang, F.; Yang, L.; Ye, Z.; Mendeleev, M. I.; Wang, C. Z.; Ho, K. M. Overcoming the Time Limitation in Molecular Dynamics Simulation of Crystal Nucleation: A Persistent-Embryo Approach. *Phys. Rev. Lett.* **2018**, *120*, 1709.00085.
- (71) Suh, D.; Yasuoka, K. Nanoparticle Growth Analysis by Molecular Dynamics: Spherical Seed. *J. Phys. Chem. B* **2011**, *115*, 10631–10645.
- (72) Suh, D.; Yasuoka, K. Nanoparticle Growth Analysis by Molecular Dynamics: Cubic Seed. *J. Phys. Chem. B* **2012**, *116*, 14637–14649.
- (73) Gasser, U.; Weeks, E. R.; Schofield, A.; Pusey, P. N.; Weitz, D. A. Real-Space Imaging of Nucleation and Growth in Colloidal Crystallization. *Science (80-. )*. **2001**, *292*, 258–262.
- (74) Gasser, U. Crystallization in Three-and Two-Dimensional Colloidal Suspensions. *J. Phys. Condens. Matter* **2009**, *21*, 203101.
- (75) O'Malley, B.; Snook, I. Crystal Nucleation in the Hard Sphere System.

*Phys. Rev. Lett.* **2003**, *90*, 4.

- (76) Koß, P.; Statt, A.; Virnau, P.; Binder, K. Free-Energy Barriers for Crystal Nucleation from Fluid Phases. *Phys. Rev. E* **2017**, *96*, 042609.
- (77) Zaragoza, A.; Conde, M. M.; Espinosa, J. R.; Valeriani, C.; Vega, C.; Sanz, E. Competition between Ices Ih and Ic in Homogeneous Water Freezing. *J. Chem. Phys.* **2015**, *143*, 134504.
- (78) Thapar, V.; Escobedo, F. A. Extensions of the Interfacial Pinning Method and Application to Hard Core Systems. *J. Chem. Phys.* **2014**, *141*, 124117.
- (79) Pedersen, U. R. Direct Calculation of the Solid-Liquid Gibbs Free Energy Difference in a Single Equilibrium Simulation. *J. Chem. Phys.* **2013**, *139*, 174502.
- (80) Pedersen, U. R.; Hummel, F.; Kresse, G.; Kahl, G.; Dellago, C. Computing Gibbs Free Energy Differences by Interface Pinning. *Phys. Rev. B - Condens. Matter Mater. Phys.* **2013**, *88*, 094101.
- (81) Zimmermann, N. E. R.; Vorselaars, B.; Quigley, D.; Peters, B. Nucleation of NaCl from Aqueous Solution: Critical Sizes, Ion-Attachment Kinetics, and Rates. *J. Am. Chem. Soc.* **2015**, *137*, 13352–13361.

- (82) Zahn, D. Thermodynamics and Kinetics of Prenucleation Clusters, Classical and Non-Classical Nucleation. *ChemPhysChem* **2015**, *16*, 2069–2075.
- (83) Onsager, L. The Effects of Shape on the Interaction of Colloidal Particles. *Ann. N. Y. Acad. Sci.* **1949**, *51*, 627–659.
- (84) Schilling, T.; Frenkel, D. Self-Poisoning of Crystal Nuclei in Hard-Rod Liquids. *J. Phys. Condens. Matter* **2004**, *16*, 085505.
- (85) Shapiro, S. S.; Wilk, M. B. An Analysis of Variance Test for Normality (Complete Samples). *Biometrika* **1965**, *52*, 591.
- (86) Moroni, D.; Ten Wolde, P. R.; Bolhuis, P. G. Interplay between Structure and Size in a Critical Crystal Nucleus. *Phys. Rev. Lett.* **2005**, *94*, 235703.
- (87) Davidchack, R. L.; Morris, J. R.; Laird, B. B. The Anisotropic Hard-Sphere Crystal-Melt Interfacial Free Energy from Fluctuations. *J. Chem. Phys.* **2006**, *125*, 094710.
- (88) Davidchack, R. L. Hard Spheres Revisited: Accurate Calculation of the Solid-Liquid Interfacial Free Energy. *J. Chem. Phys.* **2010**, *133*, 234701.
- (89) Whitesides, G. M.; Grzybowski, B. Self-Assembly at All Scales. *Science* (80-. ). **2002**, *295*, 2418–2421.

- (90) Manoharan, V. N. Colloidal Matter: Packing, Geometry, and Entropy. *Science* **2015**, *349*, 1253751.
- (91) Cademartiri, L.; Bishop, K. J. M. Programmable Self-Assembly. *Nat. Mater.* **2015**, *14*, 2–9.
- (92) Zeravcic, Z.; Manoharan, V. N.; Brenner, M. P. Colloquium: Toward Living Matter with Colloidal Particles. *Rev. Mod. Phys.* **2017**, *89*, 1–14.
- (93) Frenkel, D. Order through Entropy. *Nat. Mater.* **2015**, *14*, 9–12.
- (94) Henzie, J.; Grünwald, M.; Widmer-Cooper, A.; Geissler, P. L.; Yang, P. Self-Assembly of Uniform Polyhedral Silver Nanocrystals into Densest Packings and Exotic Superlattices. *Nat. Mater.* **2012**, *11*, 131–137.
- (95) Smallenburg, F.; Fillion, L.; Marechal, M.; Dijkstra, M. Vacancy-Stabilized Crystalline Order in Hard Cubes. *Proc. Natl. Acad. Sci. U. S. A.* **2012**, *109*, 17886–17890.
- (96) Sharma, A. K.; Escobedo, F. A. Nucleus-Size Pinning for Determination of Nucleation Free-Energy Barriers and Nucleus Geometry. *J. Chem. Phys.* **2018**, *148*, 184104.
- (97) Kashchiev, D. Forms and Applications of the Nucleation Theorem. *J. Chem. Phys.* **2006**, *125*, 014502.

- (98) Carignano, M. A.; Kachmar, A.; Hutter, J. Thermal Effects on CH<sub>3</sub>NH<sub>3</sub>PbI<sub>3</sub> Perovskite from Ab Initio Molecular Dynamics Simulations. *Journal of Physical Chemistry C*. 2015, pp 8991–8997.
- (99) Ni, R.; Gantapara, A. P.; De Graaf, J.; Van Roij, R.; Dijkstra, M. Phase Diagram of Colloidal Hard Superballs: From Cubes via Spheres to Octahedra. *Soft Matter* **2012**, *8*, 8826–8834.
- (100) Tao, A. R.; Habas, S.; Yang, P. Shape Control of Colloidal Metal Nanocrystals. *Small* **2008**, *4*, 310–325.
- (101) Cademartiri, L.; Bishop, K. J. M.; Snyder, P. W.; Ozin, G. A. Using Shape for Self-Assembly. *Philosophical Transactions of the Royal Society A: Mathematical, Physical and Engineering Sciences*. 2012, pp 2824–2847.
- (102) Kempa, T. J.; Kim, S. K.; Day, R. W.; Park, H. G.; Nocera, D. G.; Lieber, C. M. Facet-Selective Growth on Nanowires Yields Multi-Component Nanostructures and Photonic Devices. *J. Am. Chem. Soc.* **2013**, *135*, 18354–18357.
- (103) Bian, K.; Schunk, H.; Ye, D.; Hwang, A.; Luk, T. S.; Li, R.; Wang, Z.; Fan, H. Formation of Self-Assembled Gold Nanoparticle Supercrystals with Facet-Dependent Surface Plasmonic Coupling. *Nat. Commun.* **2018**, *9*.
- (104) Pietrobon, B.; McEachran, M.; Kitaev, V. Synthesis of Size-Controlled

Faceted Pentagonal Silver Nanorods with Tunable Plasmonic Properties and Self-Assembly of These Nanorods. *ACS Nano* **2009**, *3*, 21–26.

(105) Auer, S.; Frenkel, D. Prediction of Absolute Crystal-Nucleation Rate in Hard-Sphere Colloids. *Nature* **2001**, *409*, 1020–1023.

(106) Sharma, A. K.; Escobedo, F. A. Disorder Foreshadows Order in Colloidal Cubes. *J. Phys. Chem. B* **2018**, *122*, 9264–9273.

(107) Tao, A.; Sinsermsuksakul, P.; Yang, P. Polyhedral Silver Nanocrystals with Distinct Scattering Signatures. *Angew. Chemie - Int. Ed.* **2006**, *45*, 4597–4601.

(108) Gong, J.; Newman, R. S.; Engel, M.; Zhao, M.; Bian, F.; Glotzer, S. C.; Tang, Z. Shape-Dependent Ordering of Gold Nanocrystals into Large-Scale Superlattices. *Nat. Commun.* **2017**, *8*.

(109) Shukla, N.; Liu, C.; Roy, A. G. Oriented Self-Assembly of Cubic FePt Nanoparticles. *Mater. Lett.* **2006**, *60*, 995–998.

(110) Lee, S.; Teich, E. G.; Engel, M.; Glotzer, S. C. Entropic Colloidal Crystallization Pathways via Fluid–Fluid Transitions and Multidimensional Prenucleation Motifs. *Proc. Natl. Acad. Sci. U. S. A.* **2019**, *116*, 14843–14851.

- (111) van der Meer, B.; van Damme, R.; Dijkstra, M.; Smalenburg, F.; Filion, L. Revealing a Vacancy Analog of the Crowdion Interstitial in Simple Cubic Crystals. *Phys. Rev. Lett.* **2018**, *121*, 258001.
- (112) James, D.; Beirsto, S.; Hartt, C.; Zavalov, O.; Saika-Voivod, I.; Bowles, R. K.; Poole, P. H. Phase Transitions in Fluctuations and Their Role in Two-Step Nucleation. *J. Chem. Phys.* **2019**, *150*, 074501.
- (113) Davidchack, R. L.; Laird, B. B. Direct Calculation of the Hard-Sphere Crystal/Melt Interfacial Free Energy. *Phys. Rev. Lett.* **2000**, *85*, 4751–4754.
- (114) De Miguel, E.; Jackson, G. The Nature of the Calculation of the Pressure in Molecular Simulations of Continuous Models from Volume Perturbations. *J. Chem. Phys.* **2006**, *125*, 1–11.
- (115) Boettinger, W. J.; Warren, J. A.; Beckermann, C.; Karma, A. Phase-Field Simulation of Solidification. *Annu. Rev. Mater. Sci.* **2002**, *32*, 163–194.
- (116) Ogura, T.; Hayami, R.; Kadota, M. Kinetics and Mechanism of Crystallization of Lithium Silicate Glasses. *J. Ceram. Assoc. Japan* **1968**, *76*, 277–284.
- (117) Tutton, A. E. H.; Hilton, H. Mathematical Crystallography and the Theory of Groups of Movements. *Math. Gaz.* **1904**, *2*, 387.

- (118) Bealing, C. R.; Baumgardner, W. J.; Choi, J. J.; Hanrath, T.; Hennig, R. G. Predicting Nanocrystal Shape through Consideration of Surface-Ligand Interactions. *ACS Nano* **2012**, *6*, 2118–2127.
- (119) Frank, F. C. Crystal Growth and Dislocations. *Adv. Phys.* **1952**, *1*, 91–109.
- (120) Zimmermann, N. E. R.; Vorselaars, B.; Espinosa, J. R.; Quigley, D.; Smith, W. R.; Sanz, E.; Vega, C.; Peters, B. NaCl Nucleation from Brine in Seeded Simulations: Sources of Uncertainty in Rate Estimates. *J. Chem. Phys.* **2018**, *148*.
- (121) Sharma, A. K.; Escobedo, F. A. Determination of Interfacial Free Energy for Gyrobifastagia. *Under Prep.* **2021**.
- (122) Fortini, A.; Dijkstra, M.; Schmidt, M.; Wessels, P. P. F. Wall-Fluid and Liquid-Gas Interfaces of Model Colloid-Polymer Mixtures by Simulation and Theory. *Phys. Rev. E - Stat. Nonlinear, Soft Matter Phys.* **2005**, *71*, 1–13.
- (123) Ni, R.; Belli, S.; Van Roij, R.; Dijkstra, M. Glassy Dynamics, Spinodal Fluctuations, and the Kinetic Limit of Nucleation in Suspensions of Colloidal Hard Rods. *Phys. Rev. Lett.* **2010**, *105*, 7–10.
- (124) Haji-Akbari, A.; Engel, M.; Glotzer, S. C. Phase Diagram of Hard

- Tetrahedra. *J. Chem. Phys.* **2011**, *135*, 194101.
- (125) Cheng, B.; Ceriotti, M. Bridging the Gap between Atomistic and Macroscopic Models of Homogeneous Nucleation. *J. Chem. Phys.* **2017**, *146*, 034106.
- (126) Wilemski, G. The Kelvin Equation and Self-Consistent Nucleation Theory. *J. Chem. Phys.* **1995**, *103*, 1119–1126.
- (127) Ford, I. J. Statistical Mechanics of Nucleation: A Review. *Proc. Inst. Mech. Eng. Part C J. Mech. Eng. Sci.* **2004**, *218*, 883–899.
- (128) Kalikmanov, V. I. Nucleation Theory. *Lect. Notes Phys.* **2013**, *860*, 1–331.
- (129) Cacciuto, A.; Auer, S.; Frenkel, D. Solid-Liquid Interfacial Free Energy of Small Colloidal Hard-Sphere Crystals. *J. Chem. Phys.* **2003**, *119*, 7467–7470.
- (130) Israelachvili, J. N. Thermodynamic Principles of Self-Assembly. In *Intermolecular and Surface Forces*; Elsevier, 2011; pp 503–534.
- (131) Riedel, M. R.; Karato, S. I. Microstructural Development during Nucleation and Growth. *Geophys. J. Int.* **1996**, *125*, 397–414.
- (132) Heermann, D. W. Classical Nucleation Theory with a Tolman Correction. *J. Stat. Phys.* **1982**, *29*, 631–640.

- (133) Montero De Hijes, P.; Espinosa, J. R.; Bianco, V.; Sanz, E.; Vega, C. Interfacial Free Energy and Tolman Length of Curved Liquid-Solid Interfaces from Equilibrium Studies. *J. Phys. Chem. C* **2020**, *124*, 8795–8805.
- (134) Karas, A. S.; Dshemuchadse, J.; Van Anders, G.; Glotzer, S. C. Phase Behavior and Design Rules for Plastic Colloidal Crystals of Hard Polyhedra: Via Consideration of Directional Entropic Forces. *Soft Matter* **2019**, *15*, 5380–5389.
- (135) Humphrey, W.; Dalke, A.; Schulten, K. VMD: Visual Molecular Dynamics. *J. Mol. Graph.* **1996**, *14*, 33–38, 27–28.
- (136) Kauffmann-Weiss, S.; Kauffmann, A.; Niemann, R.; Freudenberger, J.; Schultz, L.; Fähler, S. Twinning Phenomena along and beyond the Bain Path. *Metals (Basel)*. **2013**, *3*, 319–336.
- (137) Delaey, L. Diffusionless Transformations. In *Phase Transformations in Materials*; Wiley-VCH Verlag GmbH & Co. KGaA: Weinheim, FRG, 2005; pp 583–654.
- (138) Christian, J. W.; Olson, G. B.; Cohen, M. Classification of Displacive Transformations : What Is a Martensitic Transformation ? *Le J. Phys. IV* **1995**, *05*, C8-3-C8-10.

- (139) John, B. S.; Stroock, A.; Escobedo, F. A. Cubatic Liquid-Crystalline Behavior in a System of Hard Cuboids. *J. Chem. Phys.* **2004**, *120*, 9383–9389.
- (140) John, B. S.; Escobedo, F. A. Phase Behavior of Colloidal Hard Tetragonal Parallelepipeds (Cuboids): A Monte Carlo Simulation Study. *J. Phys. Chem. B* **2005**, *109*, 23008–23015.
- (141) Kumar, A.; Molinero, V. Why Is Gyroid More Difficult to Nucleate from Disordered Liquids than Lamellar and Hexagonal Mesophases? *J. Phys. Chem. B* **2018**, *122*, 4758–4770.
- (142) Sharma, A. K.; Escobedo, F. A. Low Interfacial Free Energy Describes Bulk Ordering Transition in Colloidal Cubes. *J. Phys. Chem. B* **2021**, Accepted.
- (143) Dalmolen, L. G. P.; Picken, S. J.; de Jong, A. F.; de Jeu, W. H. The Order Parameters  $\langle P_2 \rangle$  and  $\langle P_4 \rangle$  in Nematic P-Alkyl-p'-Cyano-Biphenyls : Polarized Raman Measurements and the Influence of Molecular Association. *J. Phys.* **1985**, *46*, 1443–1449.
- (144) Desmos. Desmos Online Graphing Calculator  
<https://www.desmos.com/calculator>.
- (145) Cuetos, A.; Dijkstra, M. Kinetic Pathways for the Isotropic-Nematic Phase

Transition in a System of Colloidal Hard Rods: A Simulation Study. *Phys. Rev. Lett.* **2007**, 98, 095701.